



DISSERTATION

From liquid crystalline building blocks to semicrystalline photopolymers

carried out for the purpose of obtaining the degree of Doctor technicae (Dr. techn.)

under supervision of

Univ.Prof. Dipl.-Ing. Dr.techn. Robert Liska

Univ.Ass.in Dr.in techn. Katharina Ehrmann, MSc

at the

Institute of Applied Synthetic Chemistry Faculty for Technical Chemistry TU Wien

by

Dipl.-Ing. Michael Göschl, BSc

01425491



Signature: _____

"Wenn ihr jedes Gift recht wollt auslegen, was ist, das nicht Gift ist? Alle Dinge sind Gift, und nichts ohne Gift, allein die Dosis macht, dass ein Ding kein Gift ist."

-Theophrastus Bombast von Hohenheim (Paracelsus)

Danksagung

Robert, als Leiter dieser Forschungsgruppe hast du es geschafft, eine Arbeitsatmosphäre zu schaffen, die ihresgleichen sucht. Diverse "Zuckerl" in Form von Feiern und dem MC-Retreat sorgen dafür, dass jeder sofort in die Gemeinschaft integriert wird. Mit einem Händchen für interessante Themen und Projekte und wichtigem Rat bei jedem Gespräch ist man auch auf wissenschaftlicher Seite bestens betreut.

Kathi, mit deiner Betreuung hat das Wort "gründlich" für mich eine neue Bedeutung bekommen. Durch dich habe ich gelernt, Dinge mit einem kritischen Auge zu betrachten, und bei wissenschaftlichen Fragen über den Tellerrand zu schauen. Zu jeder Zeit konnte ich mich bei dir melden, und mir sicher sein, dass du dich mit jeder meiner Fragen intensiv auseinandersetzt. Bleib weiterhin so wissbegierig!

Dominik, mithilfe deiner Motivation und Ausdauer in 3D-Druckexperimenten sind im letzten Jahr die besten Ergebnisse dieser Arbeit entstanden, und das Ganze in einer entspannten und optimistischen Zusammenarbeit.

Zeitperioden des besonders großen Fortschritts in dieser Arbeit sind mit der tatkräftigen Unterstützung meiner Bachelorstudenten Lorenz und Clemens und WahlpraktikantInnen Selina und Felix entstanden. Danke für euer Mitwirken!

Abseits von der rein wissenschaftlichen Seite dürfen Dagi, Jürgen, Walter und auch Bekira nicht vergessen werden, die gemeinsam in unserem Stockwerk alles wie geschmiert laufen lassen. Ebenso zu schätzen ist die immer bemühte Hilfe von unserem Felsen in der Brandung Thomas Koch, der neben zahlreichen Werkstofftests für mich eine ganze Messmethode etabliert hat, um das meiste aus meinen Materialien herauszuholen.

Unsere Forschungsgruppe ist über die Jahre für mich zu einem zweiten Zuhause geworden, und ich habe unzählige Erfahrungen gemacht, an die ich mich lange erinnern werde. Gleich von Anfang an bin ich von den damaligen PhD-StudentInnen, vor allem Lisa, Babsi, Larissa und Anna, meinen Labornachbarn Stefan, Jakob und später David, und natürlich meinem anfänglichen Betreuer Ricky, bestens aufgenommen worden und habe gemeinsam mit den Otex Bois Flo, Fitzi und Pontus meine Diplomarbeit mit viel Freude verbracht.

Ich möchte den Mitstreitern meiner Generation, Dani, Flo, Carola, meinem Co-Bonkel Klausi, Toni, Miri und Tina, die für fast fünf Jahre wertvolle Begleiter waren, meinen Dank für die tolle Zusammenarbeit aussprechen. Wir haben diese Hütte in unserer Zeit bestens zusammengehalten! wo ist Jo?

Besonders hervorzuheben sind in jüngerer Zeit meine Lab-Besties, Lieblingstratschtanten und -trashtalker Björn, Kaja, Edma und Schmiddi, die für viele lustige Stunden innerhalb und außerhalb des Laboralltags gesorgt haben.

Danke an jedes einzelne Mitglied dieser Gruppe! Davide, Knäcksi, Stefan, Daniel, Gigi, Flippo, Jen, Seli, Kristina, Toni, Mina, Chrissie, Harshi, Theresa, Olja und alle Oldies, die schon abgeschlossen haben. Durch euch alle bin ich jeden Tag gerne hierhergekommen!

Danke an meine Freunde außerhalb der Forschungsgruppe, der "Zustand", Männer von Flake und alle anderen, die mich seit vielen Jahren in meinem Leben begleiten und mit denen ich viele unvergessliche Erlebnisse gemacht habe.

Ein großes Dankeschön an meine Familie, vor allem natürlich meine Mutter Verena, meine Großeltern und meinen Onkel Thomas, die mich mein ganzes Leben unterstützt haben und jederzeit mit offenen Armen empfangen!

Shilpa, it's been almost three exciting years of being married and we've already been through thick and thin together. With your excitement for new experiences and appreciation for the small things you have made my life much more colorful than it would have been without you. I love you!

Abstract

Hot Lithography is a 3D printing technique that enables additive manufacturing of photocurable polymers at high temperature. This technology greatly expands the spectrum of monomers to include those that are too unreactive, viscous or simply solid at room temperature.

In this work, multiple liquid crystalline (LC) monomers were synthesized to be polymerized using the photoinitiated thiol-ene click reaction. An extensive literature search was conducted to gain information about the LC phase behavior of certain structures and derive promising LC motifs for dithiol or diene monomer and addition-fragmentation chain transfer (AFCT) agent design. While polymer networks derived from AFCT agents failed to cause crystallinity in polymers, they still exhibited efficient chain transferring capabilities during polymerization.

The synthesis of liquid crystalline thiol monomers proved unfeasible due to oligomerization of the functional chain ends. Synthesis of the chosen liquid crystalline terminal alkene monomer structures was successful and they were combined with a variety of comonomers to obtain photoreactive formulations, most of which exhibited LC phases in narrow temperature ranges. A heated polymerization chamber was built to polymerize precisely within the LC temperature windows.

The resulting polymer networks exhibited high degrees of crystallinity, which resulted in high mechanical strength and toughness. Additionally, multiple materials were found to have shape memory properties with excellent shape imprintability and recovery. One combination of monomers exhibited fully controllable polymer crystallinity based on the curing parameters. Moderate curing temperatures within the LC temperature window resulted in opaque, hard, crystalline polymers while high temperatures above the LC temperature window led to transparent, soft, amorphous polymers.

This was successfully utilized to print multi-material parts via Hot Lithography. The highly tunable mechanical and optical properties were proven to be variable pixel to pixel, within each printed layer.

The research performed during this thesis opens effective new ways of introducing crystallinity into rather densely crosslinked polymer networks to significantly enhance mechanical and functional properties, which are complimented by the ability to 3D print them.

Kurzfassung

Hot Lithography ist eine 3D-Drucktechnik, die additive Fertigung von lichthärtenden Polymeren bei hoher Temperatur ermöglicht. Dadurch wird die Bandbreite von 3Ddruckbaren Monomeren um solche erweitert, die bei Raumtemperatur fest, zu viskos oder zu unreaktiv sind.

Das Ziel dieser Arbeit war die Synthese mehrerer flüssigkristalliner Monomere und deren Polymerisation mithilfe der Thiol-En-Klickreaktion. Zuerst wurde die Literatur durchsucht, um Informationen über das Phasenverhalten flüssigkristalliner Stoffe zu gewinnen und vielversprechende flüssigkristalline Strukturen zur Herstellung von Monomeren und Kettentransferreagenzien abzuleiten. Obwohl die Kettentransferreagenzien zwar keinen Erfolg zeigten, Kristallinität in Polymeren zu erzeugen, zeigten sie trotzdem effiziente Fähigkeiten, die Polymerisation zu steuern. Die Synthese flüssigkristalliner Monomere mit Thiol-Endgruppen konnte aufgrund von Oligomerisation der Endgruppen nicht erfolgreich durchgeführt werden.

flüssigkristallinen Alkenmonomere Die erfolgreich synthetisierten wurden in photoreaktiven Formulierungen mit Thiol-Comonomeren kombiniert. flüssigkristalline Phasen in meist engen Temperaturbereichen bildeten. Eine beheizte Polymerisationskammer wurde gebaut, um diese Bedingungen exakt einzuhalten. Viele der so hergestellten Polymere besaßen hohe Kristallinitätsgrade, die sie zu festen, zähen Werkstoffen machten. Einige der Materialien zeigten außerdem ein Formgedächtnis mit nahezu perfekter Wiederherstellbarkeit der Ursprungsform nach einer Verformung.

Eine Kombination von Monomeren ergab bei niedrigeren Belichtungstemperaturen einen harten, kristallinen Werkstoff, während bei hohen Temperaturen ein weiches, amorphes Material entstand. Dieses Verhalten wurde erfolgreich mithilfe von Heißlithographie-3D-Druck reproduziert, was die Herstellung von Multimaterial-Werkstücken aus einer einzigen Formulierung mit pixelgenauer Einstellung von mechanischen Eigenschaften ermöglichte.

Die Ergebnisse dieser Arbeit eröffnen effektive neue Möglichkeiten, Kristallisation in stark vernetzten Polymeren einzuleiten, was zu einer deutlichen Verbesserung mechanischer und funktioneller Eigenschaften führt, welche durch die erfolgreiche Anwendung des 3D-Drucks noch weiter verbessert werden.

Table of contents

Introduction		1	1	
1	Additive manufacturing technologies	1		
2	Radical photopolymerization	4		
2.1	Mechanism	4		
2.2	Chain transfer for polymer tuning	5		
2.2.1	Thiols as chain transfer agents	6		
2.2.2	Addition Fragmentation Chain Transfer	6		
2.2.3	Thiol-ene step growth polymerization	7		
2.3	Photoinitiation of free radical polymerization	8		
2.4	Toughening photopolymers	10		
2.4.1	Microphase separation	11		
2.4.2	Semicrystallinity in photopolymers	12		
2.4.3	Multi-material approach	13		
3	Liquid crystallinity	13		
Objective		16		
State of the art		17		
1	3D-printable thiol-ene photopolymers	17		
2	Liquid crystalline networks and elastomers	18		
3	Mechanically strong crystalline photopolymers	19		
4	Liquid crystalline phase behavior	19		
		Recults	Evn	

Results and discussion & Experimental part		Results	Exp.	
		27	162	
1	Studies with AFCT agents	27	162	
1.1	Synthesis of AFCT agents	30	162	
1.1.1	Mesogen-containing chain transfer agent BPVS	30	162	
1.1.1.1	Synthesis of precursor TDP	30	162	
1.1.1.2	Synthesis of BPVS	31	163	
1.1.2	Mesogen-containing chain transfer agent C12VS	32	164	
1.1.2.1	Synthesis of precursor C12DP	32	164	
1.1.2.2	Synthesis of C12VS	32	165	
1.1.3	Reference chain transfer agent DVS	33	166	
1.2	Selection of	34	168	
1.3	Photoreactivity study	36	170	

1.4	Thermomechanical behavior	41	170
1.5	Mechanical tests	43	171
2	Synthesis and characterization of monomers	46	172
2.1	Synthesis of liquid crystalline monomers	46	172
2.1.1	LCM5	47	172
2.1.2	LCM6	50	174
2.1.2.1	Synthesis of precursor HBE	53	174
2.1.2.2	Synthesis of intermediate HBA	54	176
2.1.2.3	Synthesis of monomer LCM6	55	177
2.1.3	LCM7	58	178
2.1.3.1	Synthesis of precursor HOEBA	59	178
2.1.3.2	Synthesis of intermediate AEBA	59	179
2.1.3.3	Synthesis of monomer LCM7	60	180
2.1.4	Liquid crystalline dithiol LCDT	62	182
2.2	Synthesis of thiol crosslinkers	65	183
2.2.1	Trithiol crosslinker CHTT	66	183
2.2.1.1	Synthesis of precursor	66	183
2.2.1.2	Synthesis of CHTT	67	185
2.2.2	Trithiol crosslinker MTSH	68	186
3	Synthesis and characterization of LCM-based polymers	71	188
3.1	LCM5-based polymers	71	188
3.1.1	Pre-screening experiment	71	188
3.1.1.1	Thermomechanical evaluation	74	188
3.1.1.2	Phase analysis	76	189
3.1.2	Design of heated polymerization chamber	77	189
3.1.3	Optimization of polymerization parameters	79	189
3.1.3.1	Single light source	80	190
3.1.3.2	Combination of two light sources	85	192
3.1.3.3	Polymerization experiment with aromatic crosslinker	94	193
3.1.4	3D printing experiments	95	194
3.1.4.1	Initial crystalline and amorphous print test	96	194
3.1.4.2	Thermomechanical tests of multi-material printed parts	99	195
3.1.4.3	3D printing of functional multi-material parts	104	197
3.1.4.4	Printing of complex structure	106	197
3.2	LCM6-based polymers	108	198

3.2.1	Photoinitiator study	109	198
3.2.2	Qualitative evaluation	111	198
3.2.4	Thermomechanical evaluation	114	200
3.2.5	Evaluation of crystallinity	116	200
3.2.6	Mechanical tests	120	202
3.2.7	Micro- and nanostructural evaluation	122	202
3.2.8	Shape memory evaluation	126	204
3.2.9	3D printing experiments	128	205
3.2.10	Linear polymer conversion study	130	205
3.2.10.1	Variation of photoinitiator and curing temperature	130	205
3.2.10.2	Variation of irradiation parameters and stoichiometry	134	207
3.3	LCM7-based polymers	137	209
3.3.1	Linear polymerization test	137	209
3.3.2	LCM7-based polymer networks	139	209
3.3.4	Thermomechanical evaluation	143	211
3.3.5	Mechanical tests	146	211
3.3.6	Evaluation of crystallinity	149	212
3.3.7	Shape memory evaluation	152	212
3.3.8	3D printing experiments	153	212
Methods		21	13
1	Gel permeation chromatography	21	13
2	Polarized optical microscopy procedure	21	13
3	Thiol-ene formulating procedure	21	13
4	Photo-DSC measurements	21	14
5	RT-NIR-photorheology measurements	21	15
6	DMTA measurements	21	16
7	Tensile test procedure	21	16
8	DSC measurements	21	16
9	Optimized polymer curing	21	17
10	Shape memory evaluation procedure	21	19
11	3D printing procedure	22	20
Materials		22	22
Instruments		22	23
Abbreviati	ons	22	26

Appendix		228	
1	DSC measurement graphs	228	
2	Shape memory measurements	229	
3	Liquid crystalline molecule list	231	
References		244	

Introduction

Polymer networks containing liquid crystalline groups are at the forefront of the development of programmable, stimuli-responsive materials. Depending on the crosslinking density, stiff liquid crystalline networks or flexible liquid crystalline elastomers are formed.² Both of these material classes have shown uniquely tunable mechanical³, optical⁴ and even electrical⁵ properties as the liquid crystalline groups in the material can be aligned through various methods, after which certain stimuli can change the behavior of the material. Combined with the advantages of 3D printing, which allows the arrangement of materials into any desired shape, a variety of possible applications can be derived, from stimuli-responsive micromotors and optical elements to mechanically strong structural materials with low shrinkage.^{2,6-16}

1 Additive manufacturing technologies

Additive manufacturing technologies (AMT), nowadays commonly called 3D printing, is an overarching term for all technologies that produce parts by joining or making volume elements. For modern applications, a computer aided design (CAD) model is used, which is sliced into the layers that make up the part. The model may be built using CAD software or imported using a 3D scanner.¹⁷

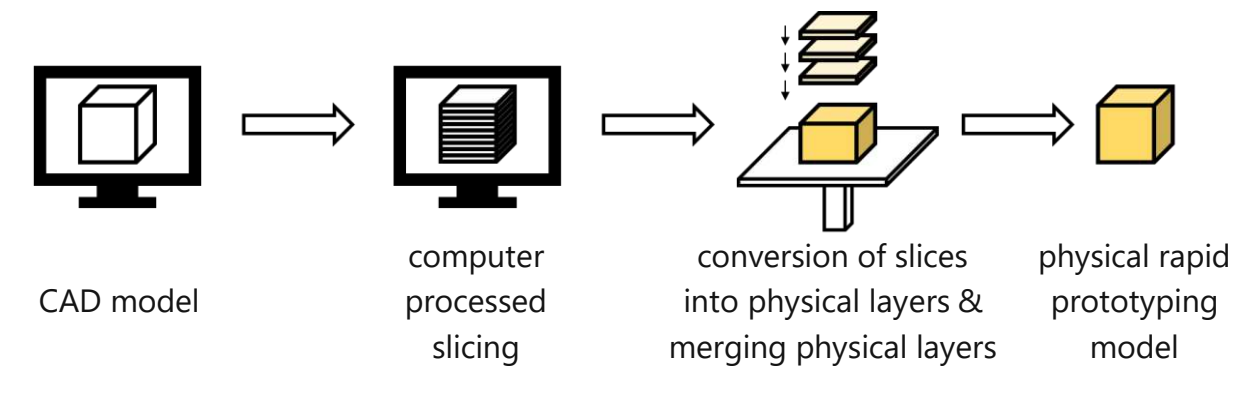


Figure 1: Typical AMT process. 17

A major advantage of AMT is the low entry-barrier of producing one piece of a certain kind as opposed to other manufacturing methods like injection molding, where expensive molds must be manufactured before the production of a part. This enables the main application of AMT, Rapid Prototyping, which allows for simple testing of the shape of a part before the final model is built using expensive and time-consuming methods.

A multitude of AMT processes for various materials exist, including fusing pre-cut layers (layered manufacturing), precipitation from the gas phase (chemical/physical vapor deposition), sintering or melting of powders (powder bed fusion, selective laser sintering), extrusion of a molten material (fused deposition modeling), or photopolymerization of liquid monomer formulations to form solid polymer parts (stereolithography).¹⁷ For consumer applications, FDM printers are most common, since their lower price, relative ease of modification of devices, and the absence of harmful UV light makes them more accessible.18

Stereolithography (SL) is a powerful AMT subtype often used for more advanced prototyping and manufacturing applications due to its ability to manufacture a variety of materials in great detail, including hard, stiff materials for dental or other structural applications, or hydrogels for biological applications. 19 Top-down and bottom-up processes exist. The top-down process employs a resin vat filled with a photoreactive formulation, in which the building platform, and subsequently, the printed part is repeatedly dipped, followed by irradiation of each layer. The first developed type of stereolithography is laser-SL (Figure 2). By using a laser to induce polymerization, it is the most accurate process, especially when two-photon technology is employed. However, its drawback is the necessity for the laser to scan over the full surface that should be polymerized, which makes it a relatively slow process. An increase in laser intensity, scanning speed and layer thickness speeds up the printing process, but leads to a more inaccurate print and potentially weaker part. 17

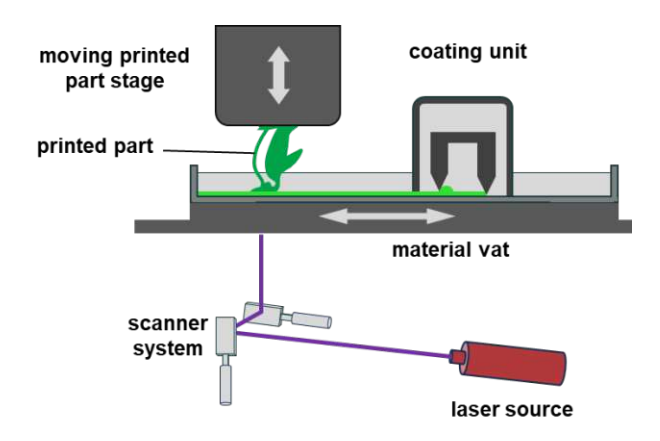


Figure 2: Top-down laser stereolithography setup.

Digital light processing (DLP) works similarly to laser-SL, but uses a digital micromirror device (DMD)-chip to project pixels onto the formulation. The main advantage of this method is an increase in printing speed over the laser-based method, as the entire layer may be irradiated at once. However, the resolution of this method is limited to the pixel size of the projector, which is typically much larger than a laser's diameter.²⁰ A recent addition to light-based AMTs is Hot Lithography, which employs a heated resin vat and building platform.²¹ This enables the processing of a much larger variety of materials, e.g., viscous prepolymers with high molecular weight that enhance material toughness, monomers with high melting points like liquid crystals, or simply building blocks that are unreactive at room temperature, such as epoxy- or oxazoline-monomers.^{22,23}

One of the drawbacks of stereolithography is related to the polymer network structure. Popular commercially available formulations polymerize acrylates or methacrylates, which often cause dense, inhomogeneous networks that lead to brittle materials.²⁴ The formulation also includes a photoinitiator to start the polymerization with light, which is typically a small molecule that may leach out of the material over time, or react further, causing discoloration or even damage to the polymer network, especially when exposed to sunlight. Various methods have been developed to reduce these drawbacks, like using different polymerization mechanisms or attempting to modify the polymer network to be more homogeneous.²⁵

2 Radical photopolymerization

Radical polymerization is a polymerization process that utilizes unpaired electrons, also called free radicals, to propagate polymer chain growth. This widely utilized method can rapidly produce polymers from various reactive substrates, but is typically relatively uncontrolled compared to catalyzed polymerization. To better control radical polymerization, various methods to slow down and homogenize the process are utilized, such as chain transfer agents.²⁶ By employing a photoinitiator, free radical polymerization may be initiated by irradiation with light.²⁷

2.1 Mechanism

Radical polymerization is typically initiated by a thermal initiator or photoinitiator, which generate radicals upon exposure to heat or light, respectively (Scheme 1 A). Other initiation routes include redox initiation or spontaneous initiation by the monomer. The radical is then transferred to a monomer, creating an active center (B). In the actual polymerization reaction, other monomers react with the active center, which results in growth of the polymer chain and the shift of the active centers to a new location (C). During polymerization, side reactions may occur in the form of chain transfer within one polymer chain (D) or between two separate polymer chains (E). In both cases, this leads to branching of the chain. Termination of the reaction occurs by recombination of radicals (F) or by disproportionation reactions, where a hydrogen atom is abstracted from the active site.²⁶

$$I \xrightarrow{h\nu/\Delta T} I \cdot (A)$$

$$I \cdot + R \xrightarrow{I} R \qquad (B)$$

$$I \stackrel{\cdot}{\longrightarrow} R + R \xrightarrow{(R')_n \stackrel{\cdot}{\longrightarrow} R} \qquad (C)$$

$$(R)_n \stackrel{\cdot}{\longrightarrow} (R)_n \stackrel{\cdot$$

Scheme 1: Steps of free radical polymerization: (A) radical generation, (B) initiation, (C) propagation, (D) intramolecular chain transfer, (E) intermolecular chain transfer, (F) termination by radical recombination.²⁶

In the case of the commonly used (meth)acrylate terminated monomers, use of purely monofunctional monomers results in a linear polymer and use of di- or multifunctional monomers results in a crosslinked network as each radical can attack another double bond. This crosslinking often happens rapidly and highly localized, resulting in microgel formation and hence inhomogeneities in the network between densely crosslinked areas and unreacted end groups (dangling ends). This can lead to leftover unreacted monomers and brittle mechanical behavior.²⁴ Further drawbacks of free radical polymerization are oxygen inhibition and instability of the monomers under ambient conditions. To circumvent these drawbacks, additives like radical inhibitors are used.²⁸

2.2 Chain transfer for polymer tuning

Chain transfer reactions during radical polymerization cause branching of chains and lower the overall molecular weight in linear polymers. In polymer networks, a large number of chain transfer reactions causes a lower density of crosslinking, a more defined glass transition within a narrower temperature range, and a delayed gel point. These effects may be desirable as they allow polymer network modification towards networks

with higher toughness, more predictable properties, and fewer unreacted monomers. One approach to modify the architecture of polymer networks is to purposefully increase the number of chain transfer reactions occurring, which can be achieved using chain transfer agents (CTA).²⁹ CTAs induce chain transfer by deactivating the original radical center in the growing polymer chain and creating a new radical center on the CTA, which is subsequently transferred to a different location.

The effectiveness of CTAs is given as the chain transfer constant (C_{tr}), which is the ratio of the reaction constant for chain transfer to the reaction constant for chain propagation. This value is not constant throughout the polymerization process as it changes with conversion and temperature of the reaction. Traditionally, thiols were used as CTAs and are still frequently employed. More specialized approaches to chain transfer include addition fragmentation chain transfer (AFCT), reversible addition fragmentation chain transfer (RAFT) and atom transfer radical polymerization (ATRP).

2.2.1 Thiols as chain transfer agents

Thiols are commonly used as CTAs to enhance the toughness of polymers.³⁰ They are highly suitable for this purpose due to the weakness of the S-H bond and the high reactivity of the thiyl radical, which is formed when the hydrogen atom is abstracted.³¹ Utilizing the same traits that make thiols efficient chain transfer agents, the thiol-ene click reaction started to see widespread use as a polymerization mechanism (chapter 2.2.3).³²

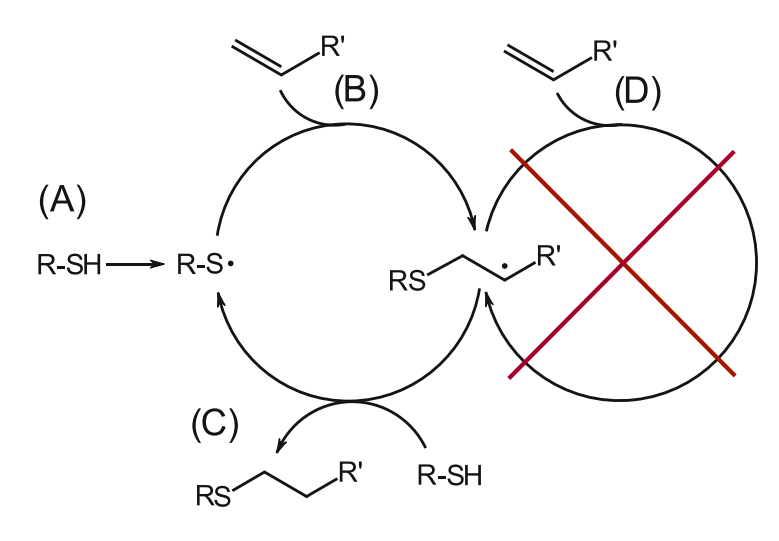
2.2.2 Addition Fragmentation Chain Transfer

Addition fragmentation chain transfer (AFCT) agents are a newly discovered type of CTA, which exhibit high reactivity with chain transfer constants close to 1.33 The chain transfer agents capable of this mechanism have distinct advantages over other advanced techniques like RAFT and ATRP as they do not slow down the polymerization significantly and do not exhibit high UV absorbance while they are still capable of modifying a radical polymerization to proceed in a controlled and homogeneous fashion. Advantages over thiol reagents are higher reactivity, enhanced storage stability and no unpleasant odor. Specifically, β-allyl sulfones (Generation 1 AFCT agent, Figure 3 a) were found to significantly enhance homogeneity and double bond conversion in methacrylate systems due to the similarity in reaction speed compared to the methacrylate monomers.³⁴ Vinyl sulfonate esters (Generation 2 AFCT agent, Figure 3 b) exhibit further improved properties over β-allyl sulfones. A relative increase in reactivity is achieved as the formation of a lowreactive double bond intermediate is prevented. This leads to reaction speeds close to those of a neat methacrylate system while the properties are tuned through chain transfer.35

Figure 3: a) Generation 1 AFCT agent with β -allyl sulfone group. b) Generation 2 AFCT agent with vinyl sulfonate group.

2.2.3 Thiol-ene step growth polymerization

By utilizing the chain transferring capabilities of thiols combined with terminal alkene (ene) monomers that, unlike (meth)acrylates, do not have the capability to homopolymerize, a step-growth polymerization reaction takes place in the presence of radicals (Scheme 2). Herein, after the usual initiation (A) and radical addition of a terminal alkene (B) steps, a chain transfer reaction (C) occurs after every monomer addition to the chain end. Homopolymerization of the terminal alkene monomer (D) must not take place to avoid unreacted thiol groups. This type of polymerization enables the preparation of linear, thermoplastic polymers if difunctional thiols and difunctional enes are used, and formation of crosslinked networks if tri- or multifunctional monomers of either type are used. The thiol-ene click reaction can also be used to crosslink existing polymers with unsaturated sites, like butadiene rubbers or other purposefully functionalized polymers.^{32,36}



Scheme 2: Radical thiol-ene step growth polymerization. (A) Hydrogen abstraction on the thiol and formation of a thiyl radical. (B) Propagation by radical addition of a terminal alkene monomer. (C) Chain transfer by quenching of the radical on the active chain by a hydrogen from a thiol and formation of another thiyl radical. (D) Terminal alkene homopolymerization. When thiol-ene step growth is desired, non-homopolymerizable terminal alkenes must be used.32

Reactivity of the thiol-ene click reaction is highest when a high ring strain and high electron density is present on the ene substrate (Figure 4). Non-homopolymerizable substrates for step-growth polymerization are vinyl ethers, allyl ethers, allyl esters and aliphatic terminal alkenes.³⁷

$$R > O R >$$

Figure 4: Various (terminal) alkene groups in order of reactivity in the thiol-ene click reaction.³⁷

2.3 Photoinitiation of free radical polymerization

Light-initiated polymerization of monomers using radicals was utilized soon after the first preparation of photoinitiating molecules. Between 1960 and 1970, a large number of photoinitiators were developed and, because of the speed and low cost of their

application, immediately employed for commercial applications like coating of manufactured parts and devices, fabrication of composites and adhesives.²⁷

To achieve light-initiation, the initiator molecule must be elevated from its ground state S₀ into its excited singlet state S₁ by absorption of light, from which intersystem crossing can take place to reach the excited triplet state T₁. From the triplet state, photochemical processes typically begin (Figure 5).^{27,38}

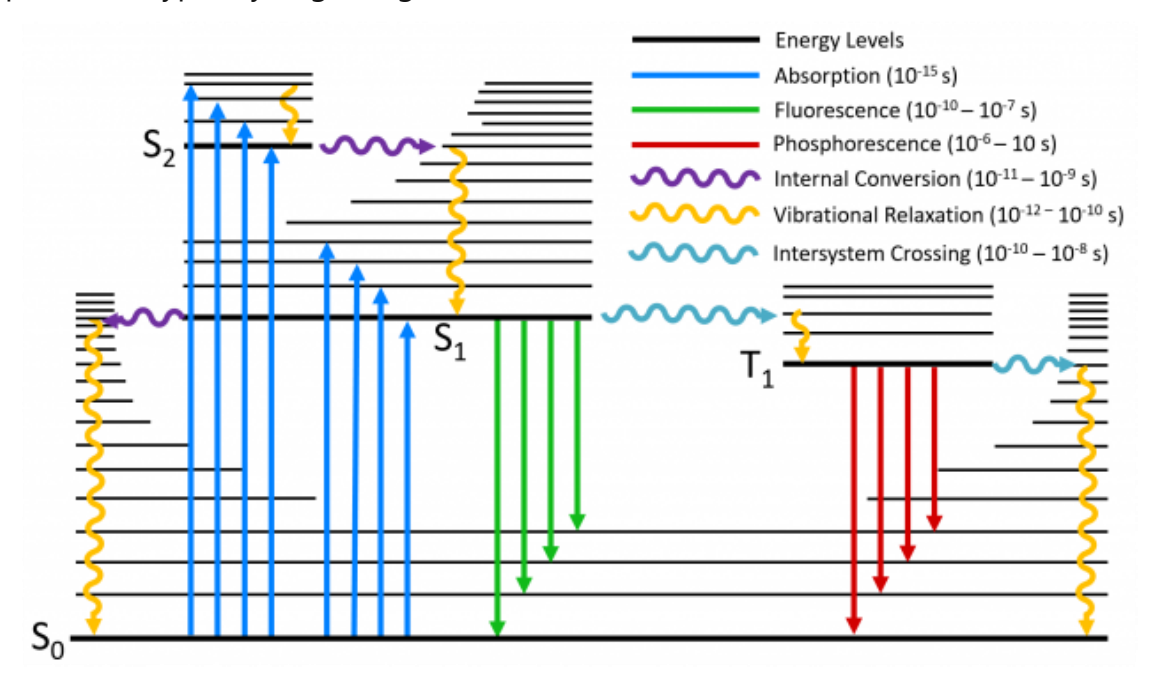


Figure 5: Jablonski diagram showing different types of excitations, state transfers and relaxations through various energy levels.³⁹

Traditionally, highly energetic ultraviolet (UV) light was needed to elevate the initiator into its excited state. Nowadays, many initiators have been developed that enable the use of less harmful visible light, which broadens the scope of application significantly towards medical and biological applications.⁴⁰

Two main types of radical initiators exist: Norrish Type I and Type II. Type I initiators undergo homolytic cleavage upon irradiation, generating radicals. Type II initiators are used in conjunction with a coinitiator. Upon irradiation, they undergo an electron transfer followed by a slower proton transfer, which generates a stable radical site on the initiator

and a reactive radical site on the coinitiator. Factors like cost, biocompatibility, solubility and photobleaching capability typically influence the choice between Type I and Type II photoinitiators, and which specific initiator is used. 41-44 Examples for typical Type I and Type II initiation systems are given in Figure 6.

Figure 6: Radical photoinitiators: a) Commonly used Norrish Type I initiator diphenyl (2,4,6-trimethylbenzoyl)phosphine oxide (TPO). b) Visible light Type I photoinitiator Ivocerin, developed for dental applications. c) Type II initiator benzophenone. d) Type II co-initiator triethylamine. 42-44

2.4 Toughening photopolymers

Toughness is the ability of a material to absorb energy through plastic deformation before fracture, which is achieved through a combination of high strength and high ductility. Typical monomers used in radical polymerization lead to inhomogeneous and brittle polymer networks with poor impact resistance (Figure 7). Tough materials are able to absorb large amounts of energy before fracturing. To achieve this, high strength must be combined with ductility. An important factor for the toughening of materials is crack formation and propagation, which is extensively studied by the field of fracture mechanics.45

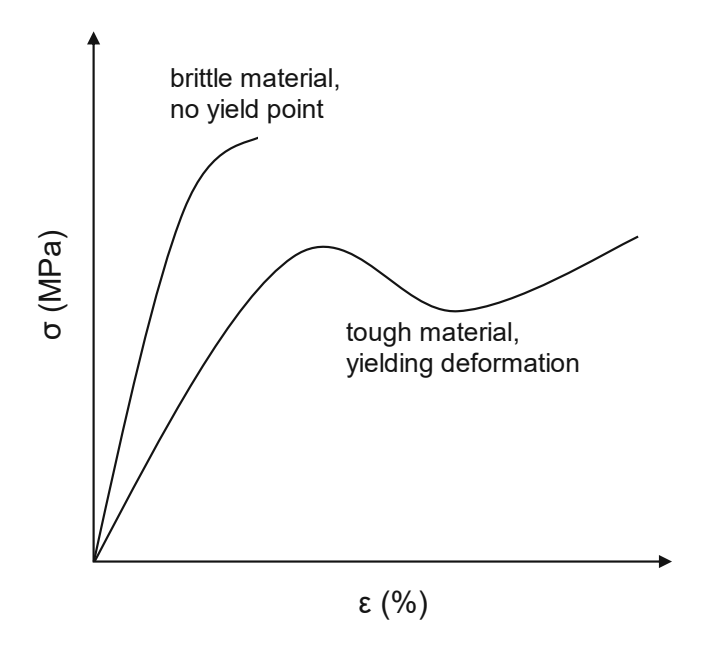


Figure 7: Exemplary tensile test curve of a brittle material and a tough material.

For (meth)acrylate systems, the previously mentioned chain transfer agents (chapter 2.2) are a popular strategy to increase impact resistance. Other strategies for toughening polymers include the introduction of microphase separation into the polymer, the copolymerization with reactive end group-functionalized prepolymers that enhance toughness through supramolecular bonding (e.g., functionalized poly(tetrahydrofuran), poly(ε-caprolactone) or oligomerized urethane (meth)acrylates), the introduction of hyperbranched polymers, multi-material networks like composites or interpenetrating polymer networks, or the introduction of crystallinity. Most of these approaches attempt to hinder crack propagation by closely connecting materials with contrasting properties.²⁴

2.4.1 Microphase separation

Various benefits can be achieved with phase separation in polymers. An established phase separated thermoplastic is acrylonitrile-butadiene-styrene (ABS), in which a styreneacrylonitrile matrix surrounds butadiene rubber particles. The polymer exhibits an excellent balance between hardness, toughness, chemical resistance and processability. In this material, acrylonitrile exhibits highly polar interactions, which gives ABS its hardness and chemical resistance. The elastomeric butadiene rubber lends toughness and increases elongation at break even at low temperatures. Lastly, styrene lends gloss and stiffness and has a comparatively low price.⁴⁶

To induce phase separation in photopolymer systems, the initially homogeneous formulation must be phase separated during the polymerization process (polymerizationinduced phase separation). Two main mechanisms exist: nucleation and growth, which results in droplet-like morphologies, and spinodal decomposition, which occurs in unstable systems that undergo composition fluctuations during polymerization. The resulting separated phases exhibit greatly enhanced mechanical strength and toughness. 47,48

2.4.2 Semicrystallinity in photopolymers

Crystalline domains, which are commonly observed in certain thermoplastics, enhance toughness by hindering crack propagation through the material, which causes a yielding fracture behavior instead of brittle fracture. Full crystallization is not possible. Instead, crystalline and amorphous domains alternate, forming semicrystalline lamellar structures, and from these, sphere-shaped structures called spherulites. 49 These materials exhibit a glass transition and a melting transition, and their typical temperature range of application is between the two. To analyze the crystalline microstructure of these materials, small angle X-ray scattering (SAXS) or polarized optical microscopy may be used.50

In photopolymers, crystallinity is much less common. In polymer networks, crystallinity competes with crosslinking, and from a certain degree of crosslinking on, the polymers are typically fully amorphous, and crystallinity is only achieved with a minor quantity of crosslinker. 51,52 In linear photopolymers, crystallinity can cause a significant increase in mechanical strength and toughness.⁵³ However, the occurrence of crystallization is highly dependent on the monomer structure.⁵⁴

2.4.3 Multi-material approach

One promising approach to toughening and material property tuning is the use of composites, wherein crack propagation is hindered by a densely packed combination of materials with different properties.⁵⁵ A modern method to achieve composite toughening is the creation of multi-material parts through additive manufacturing. Although it often comes with difficult engineering challenges, the potential benefits of freely arranging materials with certain properties in three-dimensional space are nearly limitless. Multinozzle printing and multi-vat printing are two examples where two distinct formulations may be polymerized within one printed part. 56,57 In gradient printing, the resin composition is modified during the print, which leads to a smoother transition between properties.⁵⁸ Another strategy to manufacture multi-material parts is greyscale printing.⁵⁹ Herein, varying light intensity is used to create harder and softer areas with more and less intense irradiation. By use of an orthogonal crosslinking reaction during post-curing, the initial soft/hard separation is not disrupted. In multi-color printing two separate light colors are used to first cure a soft (meth)acrylate network followed by a hard epoxy network. This results in a 3D printed interpenetrating polymer network (IPN).⁶⁰

3 Liquid crystallinity

Liquid crystals (LC) are molecules that are able to form a state of matter between the unordered structure of a liquid and the ordered structure of a solid. They can flow like a liquid but exhibit long-distance ordering typically found in crystalline solids. LC phases occur in certain organic molecules upon melting (thermotropic LC phase), in aqueous solutions of amphiphilic molecules (lyotropic LC phase) or in certain molten metal halide mixtures (metallotropic LC phase).^{61,62} Molecules that are able to form a thermotropic LC phase (also called mesophase) are called mesogens, which typically consist of a rigid mesogenic core, in many cases a structure of closely connected aromatic rings, and one or more linear spacer chains.⁶³ Terminal reactive groups can be attached if the liquid crystalline structure should be built into a polymer (Figure 8 a).⁶⁴

Figure 8: Two commercially available liquid crystalline molecules. a) Liquid crystalline monomer with a phenylester mesogenic core and terminal acrylate groups. b) Cyanobiphenyl liquid crystal "5CB" with a saturated five-carbon spacer chain.64

The liquid crystal's molecular structure defines the type of mesophase formed after melting. In many cases, a highly ordered LC phase that occurs after melting turns into a less ordered LC phase at a higher temperature before forming an isotropic melt. The classical types of mesogenic groups are cholesteric (cholesterol-containing), calamitic (column-shaped) and discotic (disc-shaped) mesogens.⁶⁵ The most loosely ordered LC phase is the nematic phase, which typically presents as a colorful schlieren texture under a polarized optical microscope with crossed polarizing filters. Cholesteric LC phases are also called twisted nematic phases. Smectic phases are more highly ordered, as the molecules are aligned in a certain direction and in distinct layers.⁶¹

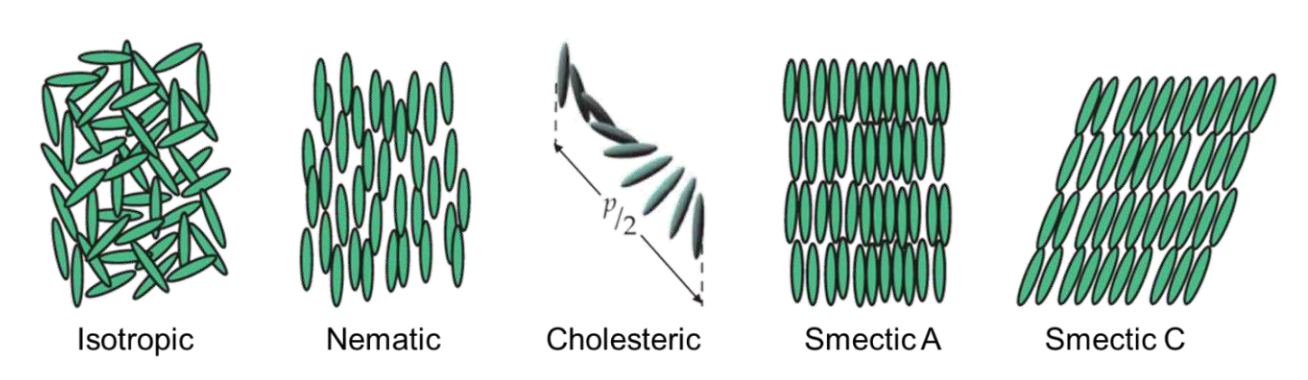


Figure 9: Different types of thermotropic liquid crystalline phases and the arrangement of molecules forming them.61

The most popular and widespread use for liquid crystals is in flat panel displays (LCD).⁶⁶ Other uses include optical devices, thermoplastic liquid crystalline polymers, wherein aromatic groups are aligned into a type of liquid crystalline phase through stretching, and liquid crystalline network polymers, wherein liquid crystalline monomers are incorporated into a polymer network, which can then react to certain stimuli. 7,67-69

Objective

The aim of this work is the synthesis of crystalline photopolymers. To achieve this, liquid crystalline (LC) building blocks should be used that can induce a pre-ordered structure in a monomer formulation, from which the polymerization can take place. As a primary method of polymer synthesis, the thiol-ene click reaction should be used. Herein, the LC component should be the terminal alkene, while low-molecular weight thiol comonomers serve as crosslinkers and chain extenders.

Based on a literature search, an overview of the phase transition behavior of liquid crystals depending on their molecular structures should be determined. This information, in particular the melting point and the liquid crystalline temperature range, should be used to design and synthesize LC monomers. Ideally, the preparation should be relatively simple, with no more than two complex synthesis steps and start from affordable source materials. The monomers should form an LC phase that is not fully disrupted by the presence of an impurity in form of a comonomer. As an end group, an aliphatic terminal alkene or an allyl group should be utilized as they polymerize readily in conjunction with thiol comonomers and do not homopolymerize.

A variety of thiol comonomers has to be be selected to be polymerized with the LC monomers. The formulations should be investigated based on their LC phase behavior and polymerized from the liquid crystalline phase, if one is present.

Additionally, the introduction of LC building blocks into an acrylate/methacrylate system should be investigated, in which polymerization is controlled using an addition fragmentation chain transfer mechanism. Herein, the LC groups should be built into the chain transfer agents.

The resulting polymers should be characterized regarding their crystallinity, and thermomechanical properties. Crystalline structures found in the polymers shall be investigated using micro- and nanoscale analysis. Lastly, 3D printing experiments should be performed.

State of the art

The initial focus of literature review was light-initiated 3D printing using thiol-ene click chemistry. Since the aim of this work is the incorporation of liquid crystalline building blocks into polymers, an overview of polymer networks incorporating liquid crystalline groups was compiled. Therein, only few publications focusing on the enhancement of mechanical properties were found. Thus, special attention was given to literature containing mechanically strong polymers of the aforementioned classes. Finally, an extensive overview of structure-property relationships of various liquid crystalline structures was created. The search was focused on structures suitable for incorporation into the main chain of thiol-ene polymers as difunctional alkene or difunctional thiol monomers.

1 3D-printable thiol-ene photopolymers

The thiol-ene click reaction has been proposed as a polymerization mechanism that can substitute the use of (meth)acrylates in a variety of applications, especially when low toxicity, low shrinkage and toughness are a priority. The step-growth polymerization mechanism leads to low shrinkage and homogeneous networks with predictable properties. 3D printing applications are particularly attractive as the reaction is well suited to being photoinitiated. 32,70-72

In recent years, dynamic networks that can be reshaped from their 3D printed shape have played an increasingly large role in research, as they may be recycled without losing the benefits of a thermosetting network, like strength and stiffness. Herein, thiol-ene chemistry may be combined with disulfide bonds to form networks that rearrange upon a certain stimulus, usually heat. 73,74

2 Liquid crystalline networks and elastomers

Liquid crystalline networks (LCN), or liquid crystalline thermosets, are densely crosslinked polymer networks that incorporate mesogenic groups. Their properties are similar to conventional thermoset polymers made from (meth)acrylate monomers as they are usually present in a glassy state due to their high crosslinking density. 40 Through alignment of the mesogenic groups before polymerization, directional anisotropy can be induced, leading to high strength in the direction of the alignment. However, most stimuli-responsive "smart material" applications are limited by their high crosslinking density and low crystallinity. Usually, no more than five percent programmable strain is achieved.2,75,76

In contrast, liquid crystalline elastomers (LCE) are highly programmable materials due to their loosely crosslinked network structure, in which mesogenic groups are pre-aligned. The typical preparation procedure involves a mesogen-containing pre-polymer, which is oriented along an axis using stretching, magnetic or electrical fields, special surfaces, or other methods. The polymer is crosslinked in this ordered state, while the directional order in the polymer network is maintained.² The mesogenic groups are either built into the polymer backbone (main-chain LCE)⁷⁷ or present as pendant groups (side-chain LCE).⁷⁸

Unique properties of these materials include reversible shape changes with elongations up to 400% or programmable color or opacity changes upon a certain stimulus. These stimuli can be mechanical stress, light, electricity or temperature changes.^{2,4,6-12}

A multitude of implementations spanning electronics, (micro)robotics and medical applications is predicted for these materials.^{2,79} However, one main limitation of functional LCE materials is that they are typically soft and elastic and therefore unsuitable for structural applications, in which strong, stiff materials are required.^{2,80,81}

3 Mechanically strong crystalline photopolymers

Bowman et al. have employed a simple system comprising a difunctional terminal alkene monomer and difunctional thiols of varying chain lengths to achieve strong, tough semicrystalline thermoplastics.⁵³ They found strong structure-property relationships depending on the chain length of the thiol monomer, wherein even numbered chain lengths led to crystallization of the polymer, and odd numbered chains caused the polymer to remain amorphous. Significantly higher tensile strengths were found for the crystalline polymers.⁵⁴ Light-based 3D printing of these materials was successful despite their linear structure, as they formed high molecular weight polymers that did not dissolve in the surrounding monomer mixture. One proposed application would be cast molds for other materials that could be selectively molten by introducing chromium oxide that is susceptible through heating by induction.⁸² By lightly crosslinking these materials, their crystallinity and mechanical properties remain, while their ability to be 3D printed using light-based methods is improved significantly. However, the advantage of recyclability that comes with a linear, meltable structure, is lost.^{51,83,84}

Liquid crystalline polymer networks are only rarely used in applications that require high mechanical strength. When they are reported in literature for these purposes, they are often suggested for dental applications due to their low polymerization shrinkage. A low shrinkage is crucial for tooth fillings since shrinkage during polymerization leaves gaps under the filling, in which bacteria can grow, damaging the tooth further. 13-16

4 Liquid crystalline phase behavior

While reviewing literature on liquid crystalline molecules, a lack of comprehensive comparisons between mesogenic groups with different spacer chains with respect to their liquid crystalline behavior (melting point, liquid crystalline temperature range) was identified. Most available reviews and papers that did have a broad overview of chain lengths focused on a specific type of mesogenic groups or functionalities. To make an

informed decision on what mesogenic groups to focus on for future synthesis, a thorough literature review was performed to gain a better overview of the effects of molecular architecture on liquid crystalline phase formation and transition temperatures. Therein, the focus was laid on biphenyl and phenylester central groups (Figure 10), as they typically have manageable melting points and are used in applications where specific mechanical properties are required.

a) b)
$$R_1 = \text{spacer chain + reactive group}$$
 c) $R_1 = \text{spacer chain + reactive group}$ $R_2 = CH_3$, H

Figure 10: Commonly used mesogenic groups: a) biphenyl mesogen, b) two-ring phenylester mesogen, c) three-ring phenylester mesogen.

Additionally, cyclohexane and bicyclo(2.2.2)octane groups were explored as partial or full substituents for the commonly used phenyl group in these motifs (Figure 11). The goal was to potentially modify the liquid crystalline phases to be broader or more stable while keeping the melting point equal to phenylester systems, or to lower the melting point of the monomer while keeping the liquid crystalline phase stable within a large temperature range.

a) b)
$$R_2$$
 R_1 R_2 R_2 R_3 R_4 R_4 R_4 R_5 R_7 R_8 R_8 R_8 R_8 R_8 R_8 R_9 R_9

 R_1 = spacer chain + reactive group

 $R_2 = CH_3, H$

Figure 11: a-c) Mesogens containing cyclohexane groups; d) mesogen containing bicyclo[2.2.2]octane

Primarily, mesogens connected to linear aliphatic methyl-terminated spacer chains were investigated as a way to gain an understanding of the correlation of spacer length with liquid crystalline behavior of different mesogenic groups. Furthermore, alkene- and thiolterminated chains were examined because of their potential to be used directly as new monomer options. Acrylate-, methacrylate- and epoxide-terminated liquid crystals were recorded when they appeared in relevant literature but no extensive search was carried out for these reactive groups.

A list of various mesogenic group-containing and liquid crystalline molecules was compiled, including their melting temperatures and LC temperature ranges (appendix, chapter 3). From this list, a number of significant correlations were deferred:

Two-ring phenylester systems (Figure 12) exhibit low melting points along with relatively narrow or no liquid crystalline phases, which mostly appear from C₄ spacer lengths onwards.85-89 Especially with reactive groups attached to the spacer chains, liquid crystalline phases rarely span further than a temperature range of 15 °C.⁴²

- Figure 12: Two-ring phenylester liquid crystal.
- Three-ring phenylester systems lead to broad, stable liquid crystalline phases across a wide range of spacer lengths. However, their melting points are rarely under 100 °C unless long spacer chains are used. Attachment of a methyl group to the central aromatic ring leads to lower melting points at the cost of slightly lower LC phase stability.⁸⁹ A relatively predictable trend of decreasing melting points with higher spacer chain lengths is observed (Figure 13), with a decrease in melting point depression per carbon atom towards longer chains. 16,90,91

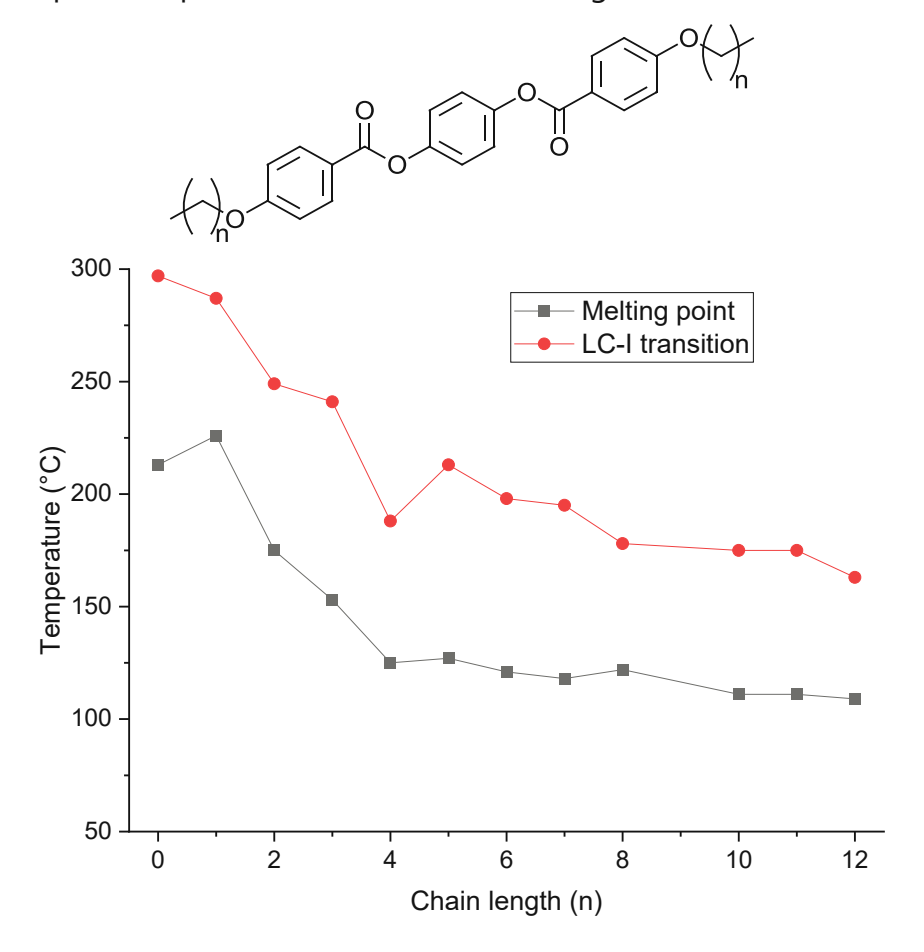


Figure 13: Correlation of chain lengths with melting points and liquid crystalline (LC) to isotropic liquid phase (I) transition for the three-ring phenylester system. 16,90,91

Four-ring phenylester systems exhibit even broader liquid crystalline phases but their melting points are significantly higher than the manageable limits for laboratory-scale monomer processing (Figure 14). 92-94

Figure 14: Four-ring phenylester liquid crystal with epoxide reactive group.

Biphenyl mesogens have highly spacer-dependent liquid crystalline phases. Depending on the type of the spacer (functionalized vs. saturated), LC phases may occur starting at four-carbon chain lengths. Highly ordered smectic phases are frequently encountered but generally, LC temperature ranges broader than 40 °C occur only rarely and are often not present outside of a specific window of chain lengths.95-103 For monofunctional monomers, cyanobiphenyl mesogens (Figure 15 c) are suitable, as they exhibit broad liquid crystalline phases along with low melting points. The nitrile group appears to contribute to the column-shape of the mesogen while only marginally increasing the molecular weight and therefore the melting point.¹⁰⁴ However, as this work is focused on difunctional monomers for application of the thiol-ene click reaction, they were not considered further.

a)
$$\downarrow_{n}
\downarrow_{n}
\downarrow_{$$

Figure 15: Types of biphenyl liquid crystals: a) without ether bridge, b) with ether bridge, and c) cyanobiphenyl with ether bridge.

- A three-ring mesogenic core is less dependent on spacer chains regarding presence and stability of an LC phase. Stable liquid crystalline phases can already be obtained at very low spacer lengths (1-3 carbon atoms). However, such short spacer chains often lead to melting points above 150 °C. 89-92,105
- For biphenyl systems, a steady melting point decrease with increasing chain length is not always found. An initial decline of melting points with increasing carbon chain lengths of 1 to 5 is often followed by a sharp increase in melting points at higher chain lengths. 98-103,106
- Ether bridges connecting the mesogenic core to the spacers lead to massive increases in melting points compared to chains directly connected to the ring with a carbon-carbon bond. A biphenyl core with an etherified spacer chain of five carbon atoms exhibits a melting point over 100 °C higher than a C-C bond connected chain while simultaneously not significantly affecting the LC temperature range. The same trends are found for phenylester systems, with tworing systems showing differences in melting points of 30-40 °C depending on the connector between LC core and aliphatic chain and three-ring systems showing differences of 20-30 °C. Compared to simple etherification reactions to form the ether bridges, sp²-sp³-coupling reactions using transition metal catalysts are

usually needed for the synthesis of C-C coupled chains but may be worthwhile exploring since the higher synthetic effort may lead to a monomer with significantly lower melting point. 98-103,107-113

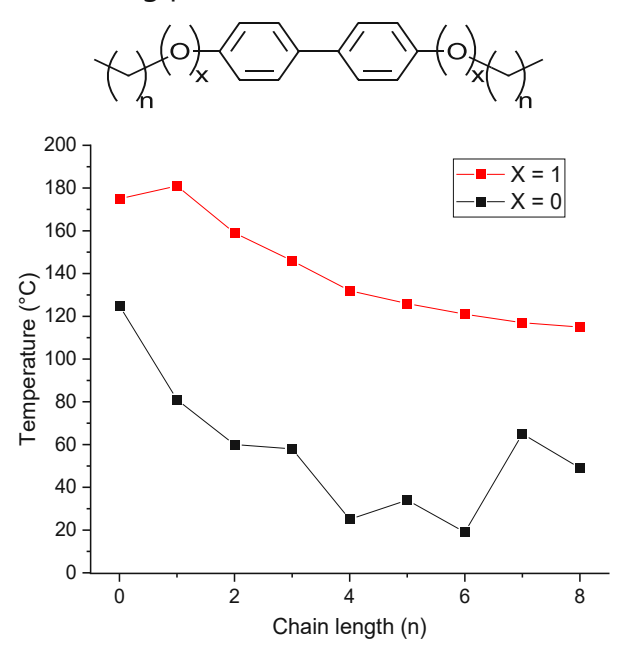


Figure 16: Melting points of biphenyl mesogens with and without an ether bridge connecting the spacer chain to the mesogenic core.

Destrade et al. tested various rigid core groups using a depolarized Rayleigh scattering setup. The resulting JA22-value gives valuable information about the potential of a central group to result in a liquid crystalline phase: If the JA₂₂-value is around 0.5 (values for the tested groups ranged from -0.17 to 1.08), a liquid crystalline phase is likely to form with appropriate spacers, usually linear aliphatic chains containing 5-10 carbon atoms. Noteworthy observations include that a cyclopropyl linker between two phenyl rings, though rigid and quasi-linear, is completely unsuitable as a mesogenic group. This is likely caused by the different angle between the cyclopropyl and phenyl rings compared to the more commonly used ester bridge. Additionally, the measurements showed that cyclohexylbenzene cores have the same JA22-value as biphenyl cores, making them a possible (although more difficult to synthesize) substitute. 114

- Side chains on the middle phenyl ring are an effective way to reduce melting points of three-ring phenylester mesogens. However, they also cause a significant narrowing of the liquid crystalline phase temperature range. For most compounds, from a side chain length higher than four carbons, only a monotropic LC phase (present upon cooling but not heating) was found. Weissflog et al. have performed extensive studies with a variety of side chain lengths and structures.⁸⁹
- A mesogenic compound with a terminal double bond is likely to have a lower melting point than a saturated aliphatic chain, approximately leading to a similar decrease as increasing the chain length by 1-2 carbon atoms. Additionally, reactive end groups in general (terminal double bond, (meth)acrylate, epoxide, thiol) usually cause a narrowing or complete disappearance of the LC phase. In two-ring phenylester mesogens, only very specific chain lengths form LC phases when terminal reactive groups are present. Three-ring mesogens appear less affected by this disrupting effect. 92,105,115-117
- Partially substituting phenyl rings with bicyclo[2.2.2]octane leads to LC phases over broad temperature ranges. However, the melting points of resulting compounds are also typically higher compared to pure phenyl systems, and the bicyclo[2.2.2]octane group is often more difficult to synthesize and incorporate into mesogens.^{88,114,118}
- Partially or fully substituting phenyl rings with cyclohexane groups lowers the melting point of the resulting liquid crystalline compounds but also decreases the width of the liquid crystalline phase significantly. 116,118,119

Results and discussion

1 Studies with AFCT agents

The use of chain transfer agents was proposed for the preparation of crystalline, homogeneous acrylate or methacrylate polymers. The AFCT method was reported in literature to be highly effective in regulating radical polymerization.^{34,120}

This combination could enable controlled curing of linear (meth)acrylate systems or networks from the liquid crystalline phase, which could result in low-stress semicrystalline thermoplastics or networks, respectively. If the influence of the chain transfer agent (CTA) is not sufficient to cause the entire formulation to become liquid crystalline, the formation of semicrystallinity in the polymer is still possible. The melting point of the CTA should be no higher than 50 °C. A much higher melting point could cause problems due to the occurrence of spontaneous polymerization of methacrylate monomers at such high temperatures. The melting point of these chain transfer agents is difficult to predict, as it may be affected by multiple factors (flexibility of the spacer chain, molecular weight, influence of the mesogenic groups). Two- and three-ring ester systems as well as biphenyl based mesogenic groups were considered for synthesis (Figure 18).

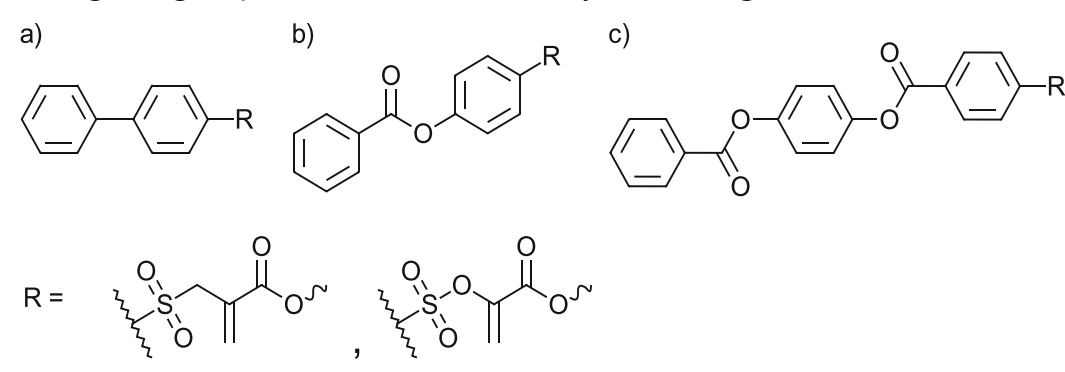


Figure 17: Possible mesogenic groups for synthesis of liquid crystalline AFCT-agent: a) biphenyl; b) two-ring phenylester; c) three-ring phenylester. On the R position, the chain transferring group is attached.

Generation 1 CTAs (β -allyl sulfones) are synthesized from methacrylates and sulfonic acid iodides (Scheme 3 a).34, while Generation 2 CTAs (vinyl sulfonates) are derived from sulfonic acid chlorides and pyruvic acid esters (Scheme 3 b).

Scheme 3: General synthesis procedure of AFCT agents. a) Generation 1 chain transfer agents synthesized from methacrylates and sulfonic acid iodides via a multi-step procedure. b) Generation 2 chain transfer agents synthesized from sulfonic acid chlorides and pyruvic acid esters using 1,4-diazabicyclo(2.2.2)octan (DABCO).

Synthesis options for both known types of AFCT agents were considered, with a focus on generation 2. The initial plan was to synthesize a monofunctional CTA with two terminal mesogenic groups (Figure 18).

Figure 18: Proposed monofunctional liquid crystalline CTA.

However, an asymmetric molecule would have required a one-sided esterification of the oligoethylene glycol, which was expected give very low yields and subsequent difficult purification. Therefore, the scope was set to a symmetrical, difunctional CTA similar to the ones reported by Gorsche et al (Figure 19a).³⁵ Instead of tosyl groups, mesogenic groups would be used. Due to the synthetic accessibility as well as commercial availability of 4biphenylsulfonyl chloride, the biphenyl mesogenic group was chosen for the first synthesis of a liquid crystalline CTA (Figure 19b).

Figure 19: a) AFCT chain transfer agent reported by Gorsche et al.; b) Biphenyl based liquid crystalline chain transfer agent.

Depending on results concerning the liquid crystalline behavior of the CTAs, a range of adjustments can be made. If the melting point of the CTA is too high, the phenylesterbased CTA (Figure 20a) is expected to have a lower melting point. If no liquid crystalline phase is observed, a less flexible spacer chain, e.g., a purely aliphatic chain (Figure 20b) or a shorter oligoethylene glycol chain (Figure 20c) may aid the molecular arrangement in the liquid phase.

Figure 20: a) Phenylester mesogen containing chain transfer agent. b) Aliphatic chain transfer agent. c) Shorter oligoethylene glycol chain transfer agent.

If a liquid crystalline phase is observed in the pure CTA but not in a formulation, a liquid crystalline methacrylate monomer could be chosen for part of the formulation.

1.1 Synthesis of AFCT agents

To aid in the crystallization of (meth)acrylate networks while causing effective network regulation, mesogenic group-containing addition fragmentation chain transfer (AFCT) agents were synthesized. The biphenyl group was chosen for this purpose due to its wide availability. Initially, a difunctional chain transfer agent (CTA) around a tetraethylene glycol spacer was chosen. If crystallinity was not sufficient, an adjustment towards a purely aliphatic spacer was planned. Additionally, a previously published CTA was required to be synthesized as a reference compound. A publication by Gorsche et al. was followed for the synthesis of all CTAs, and the CTA reported therein was chosen as the reference. 120

1.1.1 Mesogen-containing chain transfer agent BPVS

A two-step synthesis according to Gorsche et al. 120 was laid out for the preparation of the liquid crystalline difunctional chain transfer agent 11-[1-(4-biphenylylsulfonyloxy) ethenylcarbonyloxy]-3,6,9-trioxaundecyl 2-(4-biphenylylsulfonyloxy)acrylate (BPVS).

Figure 21: Liquid crystalline difunctional vinyl sulfonate chain transfer agent 11-[1-(4-Biphenylylsulfonyloxy) ethenylcarbonyloxy]-3,6,9-trioxaundecyl 2-(4-biphenylylsulfonyloxy)acrylate (BPVS).

1.1.1.1 Synthesis of precursor TDP

The AFCT agent precursor ((oxybis(ethane-2,1-diyl))bis(oxy))bis(ethane-2,1-diyl) bis(2oxopropanoate) (TDP) was synthesized in a Steglich esterification (Scheme 4). 13.12 g (35%) of the product were isolated after purification by column chromatography. When the synthesis of the compound was repeated, yields could be improved to up to 45% by using an excess of pyruvic acid in combination with a proportional increase in the amount of DCC.

Scheme 4: Synthesis of pyruvate ester intermediate ((Oxybis(ethane-2,1-diyl))bis(oxy))bis(ethane-2,1-diyl) bis(2-oxopropanoate) (TDP).

1.1.1.2 Synthesis of BPVS

To obtain the first chain transfer agent BPVS, the precursor TDP and 4-biphenylsulfonyl chloride (Scheme 5) were combined.

Scheme 5: Synthesis of BPVS.

The synthesis afforded 8.9 g (32%) of the product as a clear oil. However, full conversion could not be confirmed as the double bond integrals in the NMR spectrum of the product were significantly lower than expected. When using the aromatic protons of the biphenyl group as a reference, the integrals of the double bond peaks were at 28% of the expected value. After thorough analysis using advanced NMR-spectroscopy methods (COSY, HSQC, HMBC, APT), it was concluded that some oligomerization of the chain transfer agent had likely occurred. In addition, the product did not exhibit crystallinity at room temperature. Therefore, changes to the synthesis and the molecular design of the product were implemented as described in the next section.

1.1.2 Mesogen-containing chain transfer agent C12VS

To obtain the more crystalline chain transfer agent 12-[1-(4-biphenylylsulfonyloxy) ethenylcarbonyloxy]dodecyl 2-(4-biphenylylsulfonyloxy)acrylate (C12VS), an aliphatic spacer chain was implemented instead of an oligoethylene glycol chain.

Due to potential oligomerization of the chain transfer agent during the synthesis as described in the previous chapter, an adjustment of the reaction conditions was made, in which butylhydroxytoluene (BHT) was used as a stabilizer throughout the entire synthesis, and keeping the reaction under dry air instead of argon, as BHT is an aerobic radical inhibitor.

1.1.2.1 Synthesis of precursor C12DP

Aside from the aforementioned changes, the synthesis was again carried out as described previously according to the procedure published by Gorsche et al., 120 resulting in 13.33 g (36%) of the intermediate product 12-(acetylcarbonyloxy)dodecyl pyruvate (C12DP), a slightly yellow solid (Scheme 6).

Scheme 6: Synthesis of chain transfer agent precursor C12DP.

1.1.2.2 Synthesis of C12VS

The second step was performed in analogy to the synthesis of BPVS with the use of C12DP instead of TDP (Scheme 7). The radical stabilizer BHT was added at the start of the synthesis and the reaction was kept under air atmosphere for its full duration. After purification by column chromatography, 6.0 g (72.6%) of the pure product were obtained as a white solid. NMR analysis proved that the double bonds were fully formed and that no oligomerization took place during the synthesis or purification. Purity was further confirmed by high performance liquid chromatography (HPLC, Figure 22).

Scheme 7: Synthesis of mesogen-containing AFCT chain transfer agents C12VS.

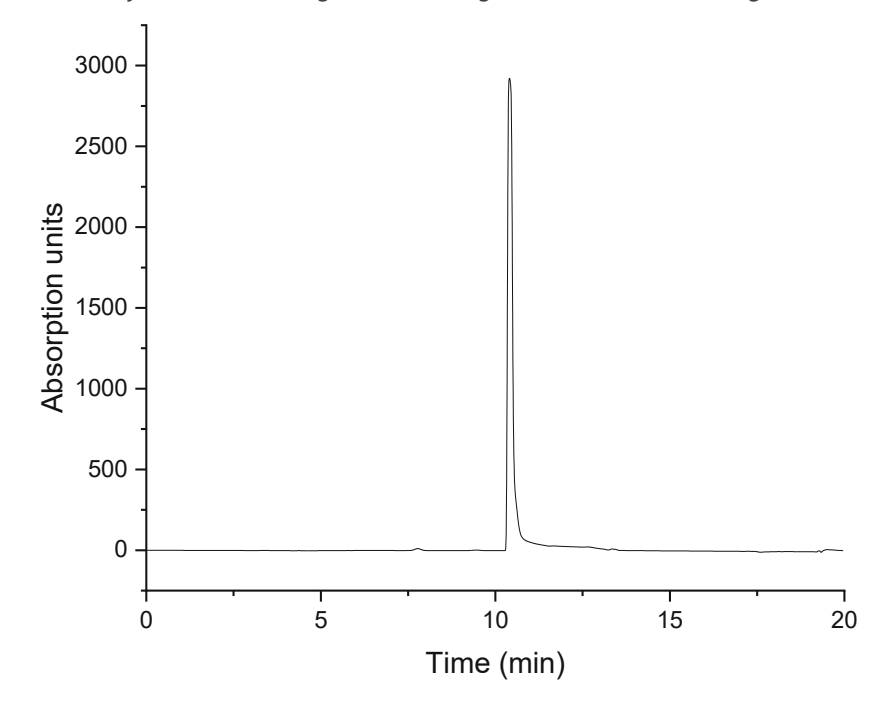


Figure 22: HPLC chromatogram of C12VS.

1.1.3 Reference chain transfer agent DVS

(11-[1-(4-Methylphenylsulfonyloxy)ethenylcarbonyloxy]-3,6,9-trioxaundecyl 2(4methylphenylsulfonyloxy)prop-2-enoate) (DVS) was synthesized as a reference chain transfer agent.

The synthesis was again performed based on the procedure reported by Gorsche et al.³⁵ under air atmosphere (Scheme 8). The reaction was performed under conditions identical to the chain transfer agent C12DP with the precursors TDP (chapter 1.1.1.1) and 4toluenesulfonyl chloride. 3.54 g (34%) of the product were obtained as a clear oil.

Scheme 8: Synthesis of reference chain transfer agent DVS.

To evaluate the efficacy of the newly synthesized chain transfer agent, it was tested in a commercially available acrylate/methacrylate system along with a reference chain transfer agent.

1.2 Selection of crosslinker

12-[1-(4-Biphenylylsulfonyloxy)ethenylcarbonyloxy]dodecyl 2-(4-biphenylylsulfonyloxy) acrylate (C12VS, Figure 23 a) was planned to be tested and compared to the reference agent (11-[1-(4-methylphenylsulfonyloxy)ethenylcarbonyloxy]-3,6,9trioxaundecyl 2(4-methylphenylsulfonyloxy)prop-2-enoate) (DVS, Figure 23 b) in a commercially available monomer system (Figure 23 c-e). As a monofunctional acrylate monomer, Sartomer SR531 was chosen. To improve the strength of the material, two difunctional crosslinkers were considered: a difunctional polyester urethane methacrylate Bomar XR-741MS ("Bomar") and an aliphatic dimethacrylate crosslinker (D3MA). 0.5 mol% of the photoinitiator Ivocerin were added to all formulations.

Figure 23: a) Newly synthesized mesogen-containing chain transfer agent C12VS. b) reference chain transfer agent DVS. c) Monofunctional acrylate monomer Sartomer SR531. d) Polyester urethane methacrylate crosslinker Bomar XR-741MS. e) Aliphatic difunctional methacrylate crosslinker 1,10-decanediol dimethacrylate (D3MA).

An initial experiment was performed to determine the crosslinker that would be used for further tests. Both crosslinkers, Bomar and D3MA were compared by polymerizing a mixture of the monofunctional acrylate monomer SR531 in formulations containing 0, 5 and 10 double bond-% (db%) of each crosslinker separately. Irradiation was performed at room temperature using a Uvitron Intelli-Ray 600 UV floodlight.

To determine which crosslinker is better suited for future experiments, DMTA measurements were performed (Figure 24). In these tests, the Bomar-containing polymers displayed a higher storage modulus and a higher increase in glass transition temperature at the same concentration. Additionally, the presence of D3MA caused brittleness, which was noticeable already when handling the samples, which was not the case in Bomarcontaining samples. Therefore, Bomar was selected as the crosslinker for all future tests of the new chain transfer agent.

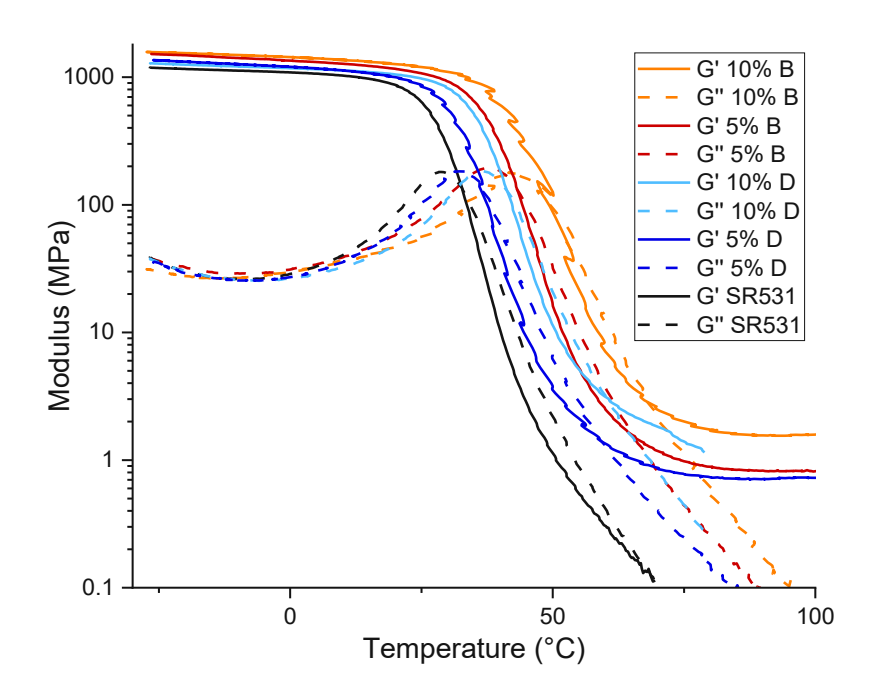


Figure 24: Storage and loss moduli (G' and G", respectively), recorded during DMTA measurements of samples SR531 (grey), SR531 with 5 db% D3MA (5% D, pink), 10 db% D3MA (10% D, green), SR531 with 5 db% Bomar XR-741MS (5% B, blue), SR531 with 10 db% Bomar XR-741MS (10% B, orange).

1.3 Photoreactivity study

To screen the effectiveness of C12VS as a chain transfer agent (CTA), as well as its influence on general polymer properties, a series of eight monomer formulations was created, all of which were based on the SR531 monomer (Table 1). The influence of the crosslinker Bomar on sample properties was tested by polymerizing it together with the reactive diluent SR531. The mixture was tested without any CTA, and with 2.5 and 10 db% of the mesogen-containing C12VS and reference DVS separately. Additionally, the linear SR531 formulation was tested with 2.5 db% of CTAs C12VS and DVS. A concentration of 10% CTA in non-crosslinked samples was initially made, but not tested further as the resulting polymer was highly brittle and weak, which was likely a result of the polymer chain length being reduced to very low lengths.

The naming convention of the formulations, and subsequently the resulting polymers, was chosen based on the crosslinker and chain transfer agent used in double bond percentage with the formula n(crosslinker)n(CTA). Therefore, the formulation containing 10 db% of the crosslinker Bomar and 2.5 db% of the CTA C12VS will be referred to as "10B2.5C12VS" (Table 1, first column). The formulation containing only the reactive diluent SR531 along with the photoinitiator will be referred to simply as SR531. These polymers were subsequently analyzed with respect to their reactivity and thermomechanically, which is described in the following chapters.

Table 1: Formulations for polymerization experiments comparing C12VS to the reference chain transfer agent DVS. All formulations contain SR531 as the base monomer. The formulation containing neither crosslinkers nor chain transfer agents was simply named after the base monomer, while all other formulations were named after the crosslinker and/or CTA used.

Formulation name	Crosslinker Bomar (db%)	CTA C12VS (db%)	CTA DVS (db%)
SR531	0	0	0
10B	10	0	0
2.5C12VS	0	2.5	0
2.5DVS	0	0	2.5
10B2.5C12VS	10	2.5	0
10B2.5DVS	10	0	2.5
10B10C12VS	10	10	0
10B10DVS	10	0	10

The polymerization behavior of SR531 in combination with crosslinker Bomar and chain transfer agents C12VS and DVS was tested via the photo-DSC (Table 2, Figure 25).

Table 2: Photo-DSC results for formulations containing varying amounts of chain transfer agent and crosslinker. t_{max} is the time at which maximum conversion takes place after the start of irradiation, t_{95} is the time at which 95% conversion has been achieved.

Formulation name	C12VS (db%)	DVS (db%)	Bomar XR (db%)	t _{max} (s)	t ₉₅ (s)	Peak area (J g ⁻¹)	Peak area (kJ mol ⁻¹)
SR531	/	/	/	8.1±0.1	60±4	481±13	96.3±2.6
10B	/	/	10	8.5±0.1	64±8	386±8	88.9±1.8
2.5C12VS	2.5	/	/	8.2±0.2	60±4	457±26	93.6±5.3
2.5DVS	/	2.5	/	8.2±0.3	65±5	475±8	96.5±1.6
10B2.5C12VS	2.5	/	10	8.7±0.2	52±1	373±4	87.6±4
10B2.5DVS	/	2.5	10	8.7±0.1	59±3	373±22	87.0±5.1
10B10C12VS	10	/	10	8.9±0.1	43±2	347±5	86.4±1.2
10B10DVS	/	10	10	9.1±0.3	49±4	344±14	83.4±3.4

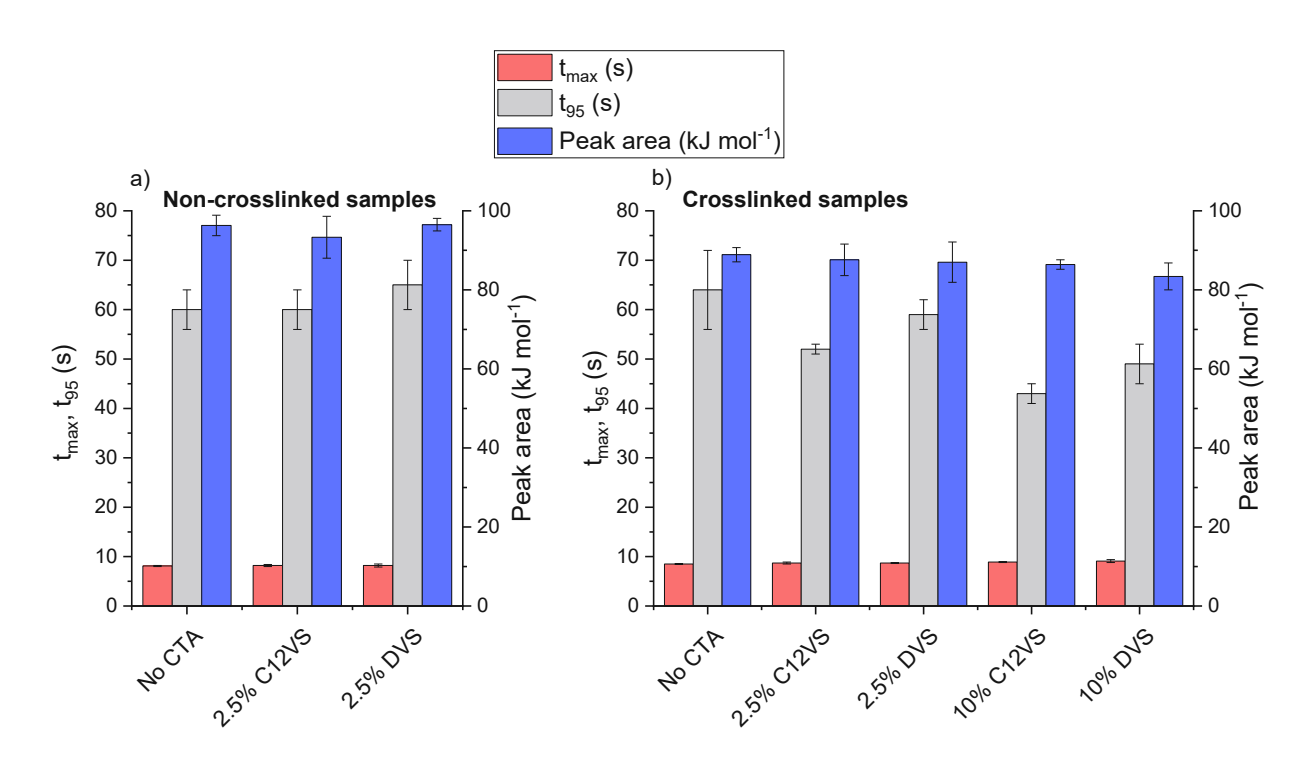


Figure 25: Results of photo-DSC measurements: time of maximum conversion after start of irradiation (t_{max}), time at 95% conversion (t_{95}) and peak area of formulations containing mesogen-based chain transfer agent C12VS and reference chain transfer agent DVS compared to non-CTA containing samples for a) noncrosslinked samples, b) crosslinked samples. Percentages of chain transfer agent content are given in double bond percent.

The fastest reaction times by t_{max} as well as the highest peak areas were observed in the linear samples SR531, 2.5C12VS and 2.5DVS. This is likely a result of the higher mobility of polymer chains due to the absence of crosslinking, as well as the density of reactive double bonds in the samples due to a lower average monomer molecular weight. Among the non-crosslinked samples, no statistically significant differences in values were found.

Crosslinked samples showed ~10% lower peak areas than the linear SR531 polymer, most likely due to the earlier gel points, which result from immobility of polymer chains upon network formation.

Among the crosslinked samples, use of chain transfer agents resulted in a very minor, but statistically still significant delay of t_{max} and a decrease in t₉₅ and peak area across samples, indicating that the chain transfer agents effectively rearrange the network, but also in a slightly lower conversion. Another explanation for the lower conversions could be that the addition of a reactive acrylate chain onto the active double bond of the chain transfer agent is less exothermal compared to an acrylate-acrylate polymerization.

To further elucidate photoreactivity, RT-NIR-photorheology measurements were performed for SR531 with varying amounts of the crosslinker Bomar and chain transfer agents C12VS or DVS (Table 3).

Table 3: Results of RT-NIR-photorheology measurements of SR531 polymers containing varying amounts of crosslinker Bomar and chain transfer agents C12VS and DVS.

Formulation name	C12VS (db%)	DVS (db%)	Bomar XR (db%)	Gel point (s)	DBC _{gel} (%)	Max G' (kPa)	DBC _{final} (%)
SR531	/	/	/	4.1±0.1	90.3±1.7	491±10	100 ¹
10B	/	/	10	2.0±0.2	87.4±0.4	480±15	99.2
2.5C12VS	2.5	/	/	4.8±0.1	95.6±0.5	498±8	99.9
2.5DVS	/	2.5	/	5.0±0.1	95.1±1.0	488±4	100 ¹
10B2.5C12VS	2.5	/	10	2.8±0.1	86.9±0.4	488±2	99.2
10B2.5DVS	/	2.5	10	2.8±0.1	88.2±0.1	487±5	99.9
10B10C12VS	10	/	10	3.3±0.1	88.6±2.4	486±12	100 ¹
10B10DVS	/	10	10	3.3±0.1	90.1±1.0	461±17	100 ¹

¹double bond conversion calculated as more than 100%



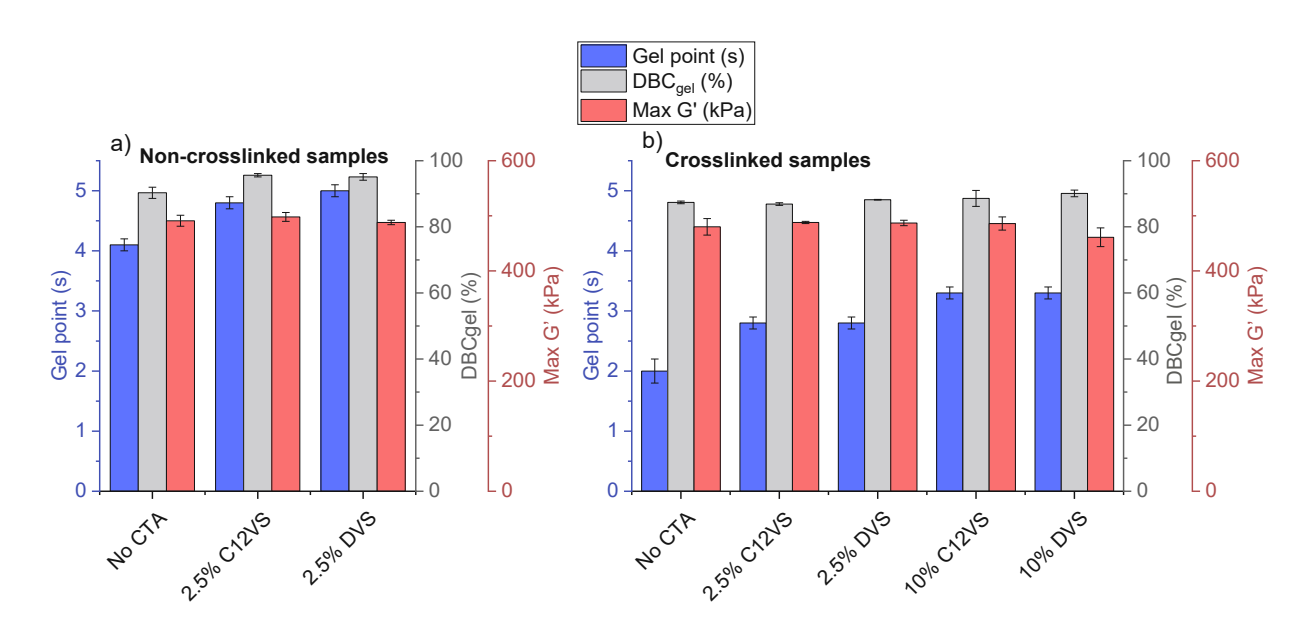


Figure 26: RT-NIR-photorheology results: gel point, double bond conversion at the gel point (DBCqel) and maximum storage modulus (G') of formulations containing mesogen-containing chain transfer agent C12VS and reference chain transfer agent DVS. a) Non-crosslinked samples. b) Crosslinked samples. Percentages of chain transfer agent content are given in double bond percent.

Gel points measured by RT-NIR-photorheology varied significantly across sample compositions, with the crosslinker Bomar reducing the gel point through quicker network formation, and chain transfer agents delaying the gel point by locally reducing the crosslinking density. Between the two chain transfer agents C12VS and DVS, no significant differences were found. At the gel point, double bond conversions were generally higher when chain transfer agents were part of the formulations. This is explained by a more homogeneously distributed growth of polymer chains, signifying the efficacy of the CTAs.

Double bond conversions at the gel point were slightly higher when the reference CTA DVS was used compared to the mesogenic C12VS. However, these results were not statistically significant across all samples. The maximum storage modulus was slightly higher when C12VS was used instead of DVS. Final double bond conversions were all measured as close to 100% or even over 100%. An adjustment of the integration method for these samples would therefore be necessary to achieve an exact result.

1.4 Thermomechanical behavior

To obtain an initial overview of the mechanical properties of the formulations over a wide temperature range, dynamic-mechanical thermal analysis (DMTA) measurements were conducted for crosslinked and non-crosslinked samples containing chain transfer agents C12VS and DVS (Table 4, Figure 27).

The measurements of linear samples that did not contain the crosslinker Bomar were intentionally stopped around 70 °C, as there was a risk of the samples melting inside the instrument, severely contaminating the measurement chamber.

Table 4: Dynamic-mechanical thermal analysis (DMTA) results of SR531 with and without crosslinker Bomar XR-741 and chain transfer agents C12VS and DVS. T_g is the glass transition temperature, tan δ_{max} is the maximum of the loss factor, which is obtained by dividing the loss modulus G" by the storage modulus G'.

Formulation name	C12VS (db-%)	DVS (db-%)	Bomar (db-%)	T _g (°C)	tan δ _{max}
SR531	/	/	/	42	2.43
10B	/	/	10	58	1.75
2.5C12VS	2.5	/	/	39	2.70
2.5DVS	/	2.5	/	41	2.78
10B2.5C12VS	2.5	/	10	56	1.93
10B2.5DVS	/	2.5	10	54	1.91
10B10C12VS	10	/	10	48	2.45
10B10DVS	/	10	10	44	2.30

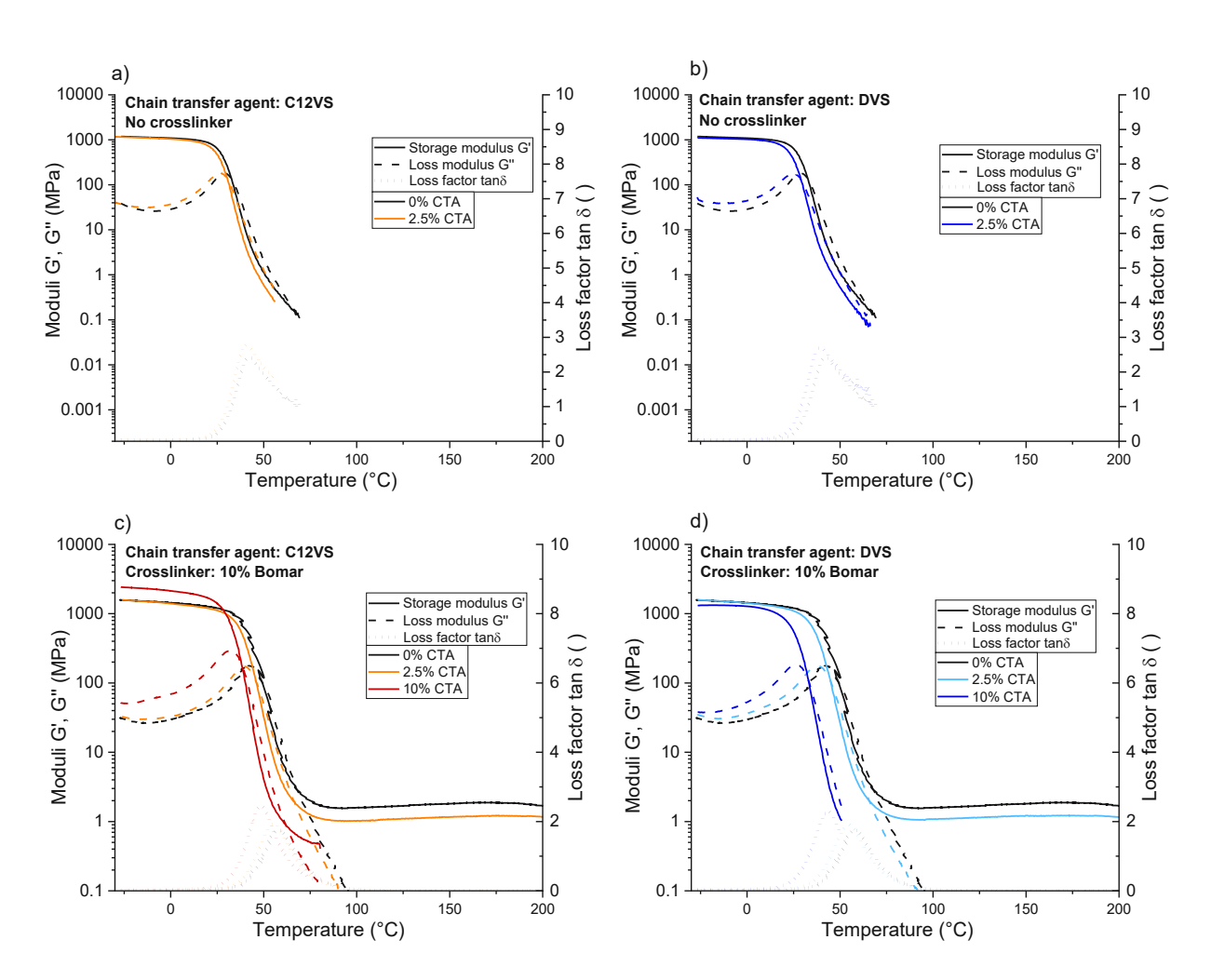


Figure 27: DMTA curves depicting storage modulus, loss modulus and loss factor comparing the impact of mesogen-containing chain transfer agent C12VS and reference chain transfer agent DVS on crosslinked and non-crosslinked samples. a) Non-crosslinked polymer containing 0 and 2.5% C12VS. b) Non-crosslinked polymer containing 0 and 2.5% DVS. c) Crosslinked polymer containing 0, 2.5 and 10% C12VS. d) Crosslinked polymer containing 0, 2.5 and 10% DVS. Percentages of chain transfer agents are given in double bond percent.

Across samples, glass transitions (T_g) were relatively sharp with maximum tan δ values around or above two, except for the sample that included the crosslinker Bomar without chain transfer agents. Herein, the highest glass transition temperature of 58 °C and lowest maximum tanδ value of 1.75 was observed. As Bomar is a relatively large oligomeric molecule, it caused only an increase in T_q by around 15 °C at 10 db%, as the network was still relatively loosely crosslinked.

In non-crosslinked samples, the storage modulus and glass transition temperature were slightly reduced by the presence of chain transfer agents, while the maximum loss factor increased. This indicates shorter chains and a more homogeneous chain length distribution. The use of C12VS provided slightly more homogeneous chain length distributions compared to DVS, while the glass transition temperature decrease was less compared to the DVS-containing sample.

Crosslinked samples exhibited a lower glass transition temperature and higher maximum $\tan \delta$ values when chain transfer agents were used. The differences between DVS and C12VS were marginal at 2.5 db% CTA content. At 10 db% chain transfer agent concentration, a noticeable difference was observed as the glass transition temperature of the C12VS-containing sample was measured at 4 °C higher than the DVS-containing sample, while simultaneously C12VS had a more beneficial effect on the network architecture than DVS, as demonstrated by a higher maximum tan δ value.

Across the samples, no crystallinity was found as the only transition during DMTA measurements was the glass transition. This was further confirmed using a polarized optical microscope, which showed complete optical isotropy under crossed polarizers.

1.5 Mechanical tests

To determine the differences in mechanical behaviour depending on CTA content, dogbone-shaped specimens of the formulations incorporating SR531, crosslinker Bomar and chain transfer agents C12VS or DVS were subjected to tensile tests (Table 5).

Table 5: Results of tensile tests of SR531 polymers containing varying amounts of crosslinker Bomar and chain transfer agents C12VS and DVS.

Formulation name	C12VS (db%)	DVS (db%)	Bomar XR (db%)	Tensile strength (MPa)	Elongation at break (%)	Tensile toughness (MJ m ⁻³)
SR531	/	/	/	17.3±0.7	365±10	49.3±2.2
10B	/	/	10	44.5±0.5	23±17	6.6±4.4
2.5C12VS	2.5	/	/	14.8±1.4	166±140	15.7±12.7

2.5DVS	/	2.5	/	9.5±1.2	288±151	19.4±10.1
10B2.5C12VS	2.5	/	10	38.3±2.0	80±33	19.1±7.6
10B2.5DVS	/	2.5	10	29.3±2.6	109±22	23.7±5.7
10B10C12VS	10	/	10	23.8±2.8	83±100	13.1±15.1
10B10DVS	/	10	10	16.3±1.2	242±18	25.8±2.8

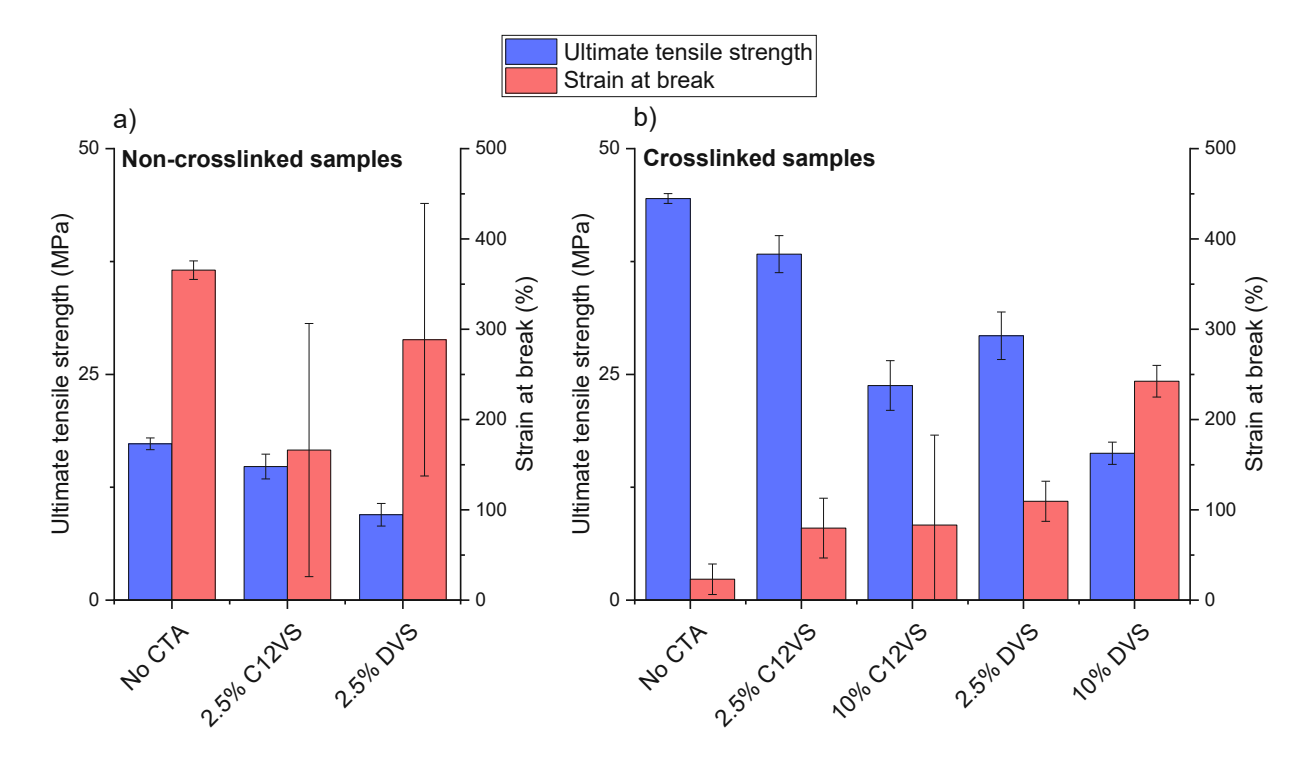


Figure 28: Ultimate tensile strength and strain at break of polymers containing mesogen-based chain transfer agent C12VS or reference chain transfer agent DVS in a) non-crosslinked samples and b) crosslinked samples. Percentages of chain transfer agent content are given in double bond percent.

Large deviations in measured elongations at break were caused by some samples exhibiting a relatively brittle fracture, and other samples exhibiting creep. This creeping behavior was especially pronounced for the linear polymer samples, and in case of C12VS, for the sample containing 10 db% chain transfer agent and crosslinker. For the base formulation containing purely the monofunctional acrylate monomer and for the sample containing 10 db% Bomar as crosslinker and 10 db% of the reference CTA DVS, no brittle fracture occurred during tensile tests, but the samples did exhibit brittle fracture upon sudden impacts, e.g., by quickly bending the specimens by hand. This behavior was

caused by the linear or very lightly crosslinked structure of the polymer combined with its glass transition temperature, which is situated 20-30 °C above room temperature. At the measurement temperature of the tensile tests (room temperature), the samples were in their glass transition range. The use of chain transfer agents generally decreased the tensile strength of the samples, while improving the elongation at break. Comparatively, DVS lowered the tensile strength more than C12VS while improving the elongation at break slightly more.

Most notably, the sample containing 10% Bomar and 2.5% C12VS exhibited a massive increase in toughness with only a small loss of tensile strength compared to the purely crosslinked sample incorporating 10% Bomar. The tensile strength saw a decrease of less than 15%, while there was a more than 300% increase in elongation at break. Though these positive results proved that the synthesized CTA C12VS is effective at regulating polymer network formation, the further synthesis and study of AFCT agents was not continued due to the lack of crystallinity in all polymers.

2 Synthesis and characterization of monomers

A variety of liquid crystalline monomers and thiol comonomers were synthesized in this work. In this chapter, their structural design and synthesis is explained. Before synthesizing each monomer presented in this thesis, a literature search and evaluation of synthesis options was performed. In the selection of monomers, the focus was set on having no more than three main synthesis steps and a satisfactory commercial availability of the reactants.

2.1 Synthesis of liquid crystalline monomers

Before this project, an iterative process was employed to identify a suitable monomer for the preparation of linear semicrystalline photopolymers. The most promising monomer LCM4 included a 3-ring phenylester mesogenic core with an 11-carbon (C₁₁) alkeneterminated chain (Figure 29). The melting point of the monomer was determined at 111 °C, where a transition into a colorless liquid crystalline phase, likely a smectic phase, took place. At 140 °C, a nematic phase with colorful strand patterns formed, which persisted until 177 °C, above which an isotropic molten phase was observed.

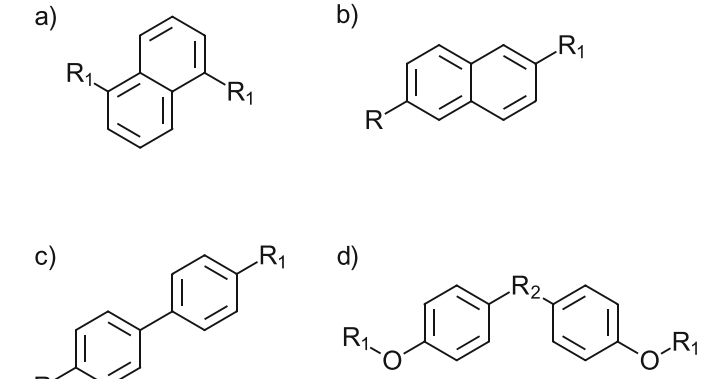
Figure 29: Liquid crystalline terminal alkene monomer LCM4.

Several potential points for improvement were found. The melting point of the monomer was manageable, but could be improved to be even lower for easier processability. Additionally, the long chains caused very loose polymer networks to form. Shorter chains were not an option as they would significantly increase the melting point of the monomer. Furthermore, the synthesis of the precursor often caused a byproduct to form, which, if not carefully removed, would lead to persistent impurities of the final monomer.

2.1.1 LCM5

The initial aim for the follow-up monomer of LCM4 was to lower the melting point of the monomer to better function with the existing high-temperature polymerization setup. Additionally, a more straightforward synthesis approach was desired. With our knowledge at the time of monomer selection, the only further possible modification for a 3-ring phenylester mesogen was the addition of a methyl group on the central aromatic ring, from which only a minor decrease in melting point (around 10 °C) could be expected.

Therefore, additional mesogens were investigated (Figure 30). Naphthalene central groups (Figure 30a, b) have previously been used in liquid crystalline molecules. However, they likely require further rigidity using aromatic structures linked to the naphthalene motif to form a liquid crystalline phase, which would increase the melting point significantly. 121,122 Biphenyl-based liquid crystals (Figure 30c) are well known in literature, and the ability of biphenyl groups to form liquid crystalline phases is widely reported for many different molecular architectures. 123-126 Bisphenols (Figure 30d) can also result in liquid crystallinity in some cases. 127



R₁: Spacer chain and terminal alkene group

R₂: CH₂, CH₂CH₃, C=O, other bisphenol central groups

Figure 30: Additional central groups that could be used to achieve liquid crystallinity in a monomer.

Due to the high amount of molecular order that they can provide in combination with relatively good commercial availability, the biphenyl mesogenic group was chosen as the central group for the first mesogenic monomer synthesized in this work. Combined with an alkene-terminated C₁₁ chain connected by an ester, this literature-known compound was reported to have a melting point below 80 °C, above which a highly ordered Smectic X liquid crystalline phase is present up to 111 °C (LCM5, Figure 31).

Figure 31: Biphenyl-based monomer LCM5.

The synthesis of the first liquid crystalline monomer in this work was performed in a single-step synthesis from commercially available reactants. The enumeration was continued from previous work with the number 5.

4'-(9-Decenylcarbonyloxy)-4-biphenylyl 10-undecenoate (LCM5) was prepared according to Imae et al. 128 using 4,4'-dihydroxybiphenyl and 10-undecenoyl chloride catalyzed by triethyl amine (TEA, Scheme 9). After purification by recrystallization, 34.05 g (92%) of the product were isolated. HPLC analysis confirmed purity of the product.

Scheme 9: Synthesis of liquid crystalline monomer 4'-(9-decenylcarbonyloxy)-4-biphenylyl 10-undecenoate (LCM5).

Melting point analysis on a polarized optical microscope showed a viscous liquid crystalline phase (~2000 mPa s by melt rheology), which was described in literature as a highly organized smectic X phase. 129 The liquid crystalline phase persisted from temperatures of 78 to 111 °C (Figure 32a), above which the compound turned into an isotropic melt (Figure 32c). Upon cooling, formation of liquid crystalline phase and

crystallization took place at the same temperatures as when heating. Appearance of the liquid crystalline phase upon cooling resembled a spherulitic texture.

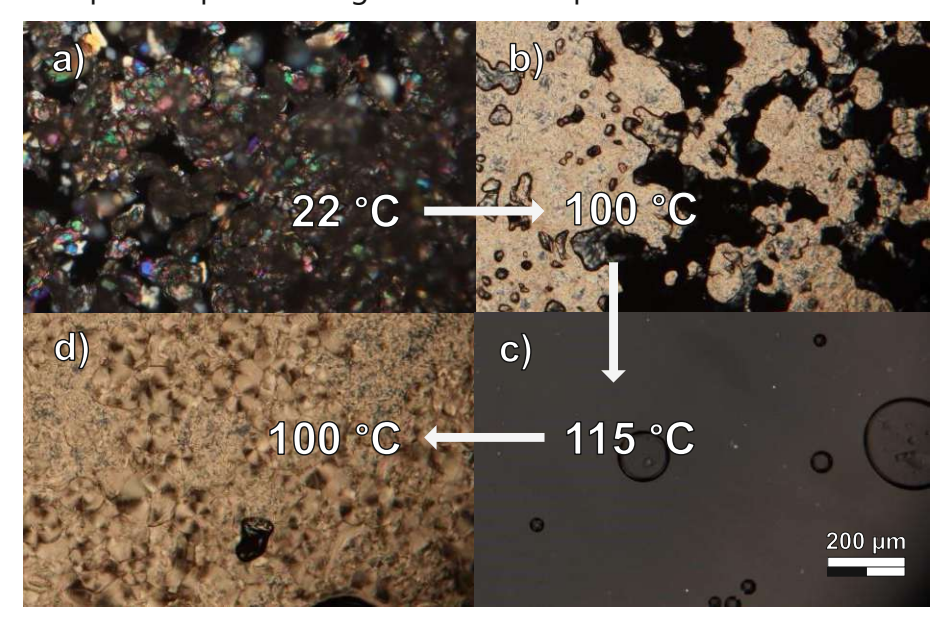


Figure 32: Heating and cooling cycle of LCM5 displaying liquid crystalline behavior. a) Crystalline LCM5 at room temperature (22 °C). b) Liquid crystalline phase of LCM5 upon heating (100 °C). c) Isotropic melt of LCM5 (115 °C). d) Liquid crystalline phase of LCM5 upon cooling (100 °C).

The melting behavior was further confirmed by differential scanning calorimetry analysis (Table 6, Figure 33).

Table 6: Comparison of phase transition temperatures of LCM5 measured via polarized optical microscopy (POM) and DSC (second heating cycle).

Measurement step	Phase transitions (POM)	Phase transitions (DSC)
Heating	Cr 78 SmX 111 I	Cr 76.6 SmX 111.3 I
Cooling	I 111 SmX 78 Cr	I 109.8 SmX 72.7 Cr

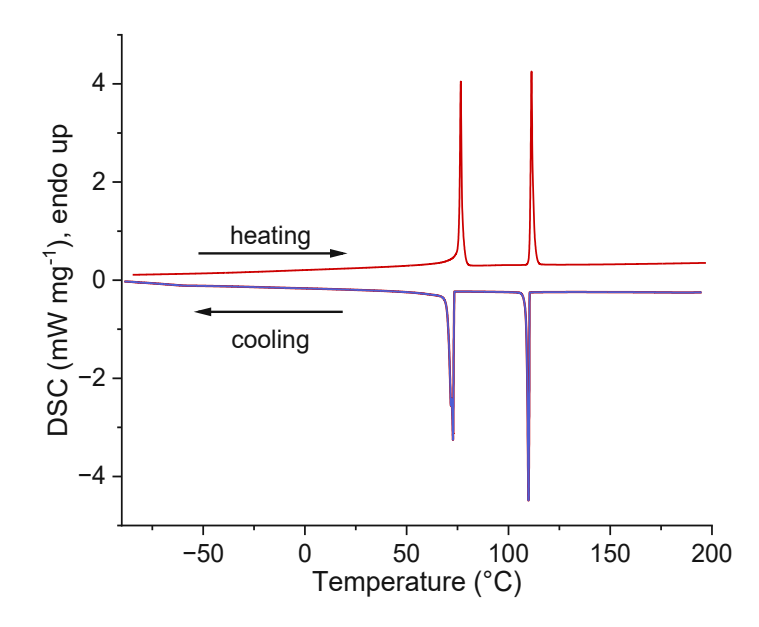


Figure 33: Differential scanning calorimetry results of liquid crystalline monomer LCM5 (endothermal up).

Two sharp phase transitions were observed in both directions with the first and second heating cycle matching well while cooling transition temperatures were shifted to slightly lower values compared to the heating cycles as supercooling of the substance took place.

2.1.2 LCM6

To further improve polymer mechanical properties, literature search led to the following requirements for the next generation of liquid crystalline monomer:

- Broad liquid crystalline phase (>25°C between melting point and LC→isotropic phase transition). This is necessary because the liquid crystalline phase always becomes narrower when a mixture of monomer and comonomer is present. Additionally, some variations in the formulation temperature are unavoidable, which necessitates a broader LC range.
- Difunctional terminal alkene
- Melting point <100 °C, ideally <80 °C

Higher crosslinking density of the resulting polymer network, therefore a short spacer chain relative to the size of the mesogenic group: for a two-ring system < 5, for a three-ring system < 8 carbon atoms. This change could not only increase polymer network density, but also simultaneously improve crystallinity, as a larger number of mesogenic groups is present due to the lower monomer molecular weight.

The initial search identified a two-ring phenylester system with a double bond terminated four-carbon spacer chain (C₄) as promising (Figure 34 a). While liquid-crystalline molecules with alkene-terminated aliphatic chain ends are more uncommon in literature, analogous compounds containing purely aliphatic chain ends have often been synthesized and analyzed (Figure 34 b).

Figure 34: Two-ring phenylester system with a) a C₄ aliphatic chain and b) an aliphatic chain with terminal alkene group.

In this case, the aliphatic C₄-terminated 2-ring LC molecule has a melting point of 69 °C and a nematic liquid crystalline phase that spans over 24 °C. However, after further review it was found that the alkene-terminated analog has a melting point of 52 °C that directly leads to an isotropic melt. Upon cooling, a narrow liquid crystalline phase is observed between 52 and 48 °C (monotropic liquid crystal). 115 An alkene-terminated chain of six carbon atoms (C₆) did show an enantiotropic liquid crystalline phase (observed when heating and cooling), but only over a range of 13 °C, which would likely not lead to liquid crystallinity in combination with a comonomer. The presence of a thiol comonomer lowers the liquid crystalline range as it effectively acts as an impurity, which disrupts the liquid

crystalline structure. From the systematic studies on LC-motifs presented in the state of the art, it has become apparent that the use of three-ring instead of two-ring mesogens broadens the LC range of the resulting molecule. Therefore, it is desirable herein to utilize three-ring LC-motifs despite their higher melting points. Thus, the two-ring phenylester mesogenic core was deemed unsuitable.

Therefore, a different strategy was employed: The ether bridge as an attachment point for the spacer chain was identified to increase the melting point of liquid crystalline molecules significantly compared to a direct C-C-bond attachment, while it does not impact the stability of the liquid crystalline phase negatively. Thus, it was concluded that the ether bridge must be avoided to have a low enough melting point for a three-ring system with a spacer length significantly below 10 carbon atoms to maintain comparably high crosslinking densities. With these considerations in mind, a new three-ring phenylester LC monomer was designed, which can be obtained from an ene-terminated alkyl-substituted phenylester and subsequent esterification with an aromatic diol (Figure 35).

Figure 35: New proposed liquid crystalline terminal alkene monomer.

Due to the potential broad liquid crystalline phase and an expected manageable melting point at low spacer length, a monomer of this type with a C₆ spacer chain was chosen for synthesis (LCM6, Figure 36).

Figure 36: Liquid crystalline monomer LCM6.

For the synthesis of this monomer, a more intricate synthesis pathway involving a crosscoupling reaction was necessary to avoid the aryl ether group. Subsequently, standard hydrolysis of the ester and esterification with hydroquinone were performed (Scheme 10).

Scheme 10: Synthesis of LCM6.

2.1.2.1 Synthesis of precursor HBE

The first step toward the LCM6-precursor methyl 4-(5-hexen-1-yl)benzoate (HBE) was performed according to Fürstner et al., using a Grignard reagent in conjunction with an iron catalyst (Scheme 11). 130 This pathway was necessary to directly couple the alkyl chain to the aromatic ring and avoid an aryl ether group, which exhibits lower melting points according to literature as analyzed previously.

Scheme 11: Synthesis of intermediate compound methyl 4-(5-hexen-1-yl)benzoate (HBE) according to Fürstner et al. 130

This synthesis route led to successful product formation, which was confirmed by NMR and mass spectroscopy analysis (experimental part chapter 2.1.2.1).

Separation of HBE from the starting material methyl 4-chlorobenzoate was initially achieved by splitting the ester group under alkaline conditions and subsequent column chromatography. In the final, simplified procedure, the esters were separated using fine vacuum distillation and hydrolyzed subsequently. After distillation, 14.55 g (35%) of HBE were isolated.

2.1.2.2 Synthesis of intermediate HBA

The methyl ester group of HBE was hydrolized under alkaline conditions in analogy to a procedure described by Fürstner (Scheme 12).131

Scheme 12: Ester hydrolysis of HBE to form the free carboxylic acid HBA.

The carboxylic acid HBA was isolated in near-quantitative yield (19.8 g, 94%) after liquidliquid extraction.

2.1.2.3 Synthesis of monomer LCM6

Synthesis of p-[p-(5-hexenyl)benzoyloxy]phenyl p-(5-hexenyl)benzoate (LCM6) was performed according to Zhang et al. 132 utilizing improvements reported by Jordan et al. (Scheme 13).133

Scheme 13: Steglich esterification to obtain the liquid crystalline monomer p-[p-(5-hexenyl)benzoyloxy]phenyl p-(5-hexenyl)benzoate (LCM6) using the reagents 1-ethyl-3-(3-dimethylaminopropyl)carbodiimide hydrochloride (EDC.HCl) and 4-dimethylaminopyridine (DMAP). 132,133

After recrystallization from methanol, 2.86 g (58%) of the pure product were obtained. Purity was confirmed via HPLC analysis, where some fractions were identified to contain a minor remaining impurity. This impurity was successfully removed with another recrystallization step (Figure 37).

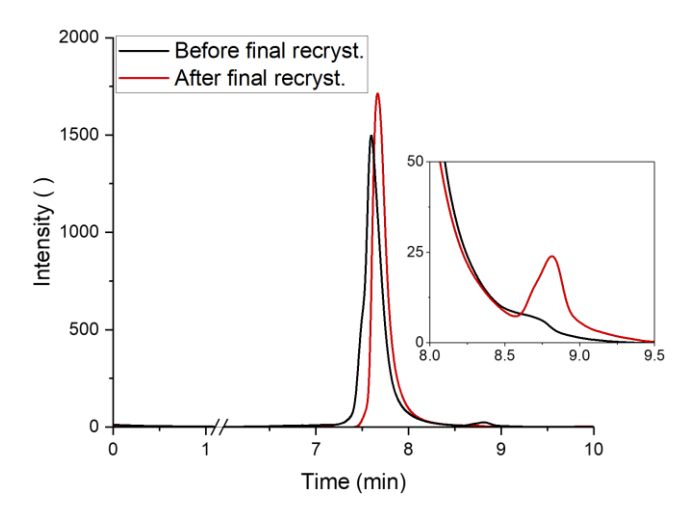


Figure 37: HPLC chromatogram of a batch of LCM6 before (black) and after (red) the final recrystallization step.

LCM6 was analyzed under the polarized optical microscope, where it exhibited a nearcolorless liquid LC phase upon heating to 100 °C, which persisted up to a temperature of 175 °C, where it turned into an isotropic melt. Upon cooling, formation of the liquid crystalline phase and crystallization took place at the same temperatures as they did while heating.

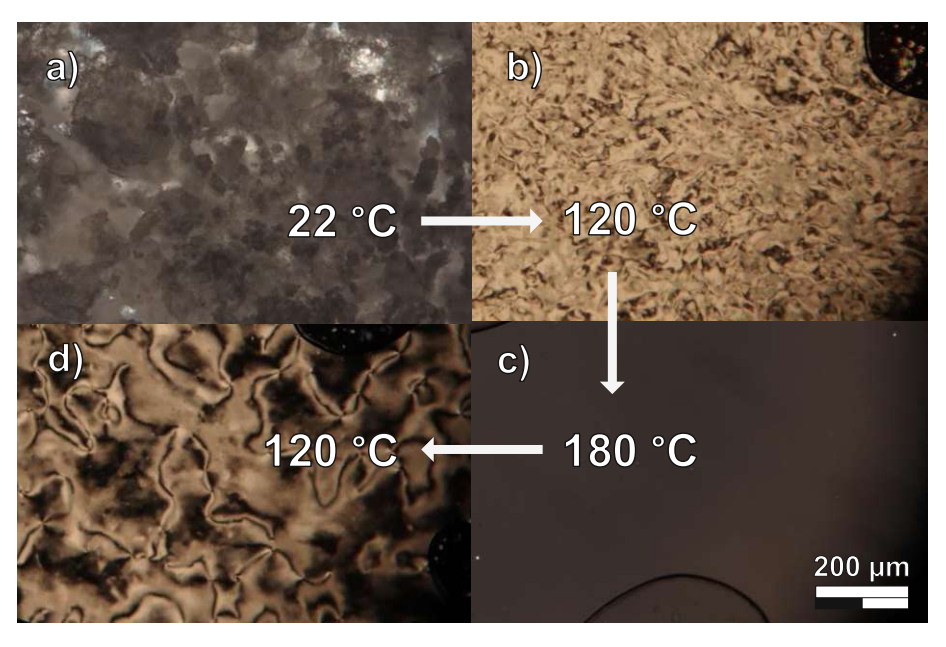


Figure 38: a) Crystalline LCM6 at room temperature (22 °C). b) Liquid crystalline phase of LCM6 upon heating (120 °C). c) Isotropic melt of LCM6 (180 °C). d) Liquid crystalline phase of LCM6 upon cooling (120 °C).

The melting behavior was further confirmed by differential scanning calorimetry analysis (Table 7, Figure 39).

Table 7: Comparison of phase transition temperatures of LCM6 measured via polarized optical microscopy (POM) and DSC (second heating cycle).

Measurement step	Phase transitions (POM)	Phase transitions (DSC)
Heating	Cr 100 LC 175 I	Cr 104.5 LC 173.0 I
Cooling	I 175 LC 100 Cr	l 171.9 LC 100.0 Cr

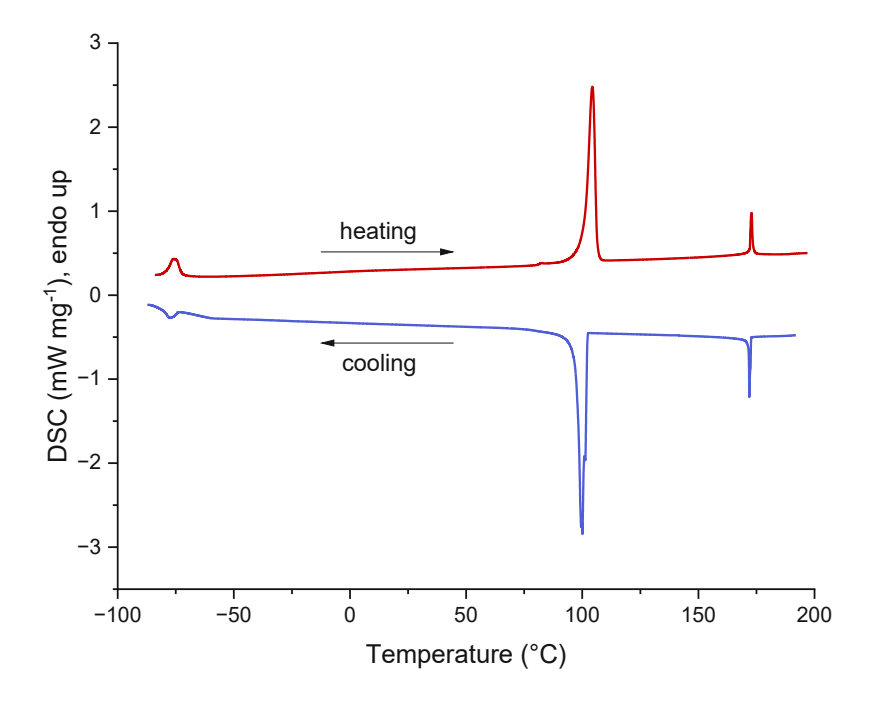


Figure 39: Differential scanning calorimetry results of liquid crystalline monomer LCM6 (endothermal up).

Two sharp phase transitions were observed in both directions with the first and second heating cycle matching well while cooling transition temperatures were shifted to lower values compared to heating transition temperatures as slight supercooling took place.

2.1.3 LCM7

The reactive end group was found to contain a potential improvement over the aliphatic terminal alkene-functionalized LCM6. Generally, higher ring strains and higher electron densities of the double bond are beneficial to the reaction rate of the thiol-ene click reaction (Figure 40).³⁷

Figure 40: Reactivity of various alkene monomers in the thiol-ene click reaction.

Therefore, a modification of the LCM6 monomer was proposed that could improve the reactivity. One methyl group in the aliphatic chain is substituted by an oxygen atom, resulting in an allyl ether end group (Figure 41). A side effect of this is a more flexible spacer chain, which could result in a lower melting point, facilitating the processing of the monomer into formulations, but also potentially reducing polymer crystallinity.

Figure 41: Allyl ether functionalized liquid crystalline monomer LCM7.

This adjustment of the monomer structure started with a hydrolysis of the nitrile group followed by the allylation of the aliphatic alcohol. Finally, the monomer was completed using a Steglich esterification (Scheme 14).

Scheme 14: Synthesis of LCM7.

In this case, the synthesis pathway did not involve an aromatic coupling reaction due to the commercial availability of a suitable precursor. After synthesis, the identity and purity of the monomer were confirmed with standard analytical methods and the monomer's liquid crystalline behavior was studied.

2.1.3.1 Synthesis of precursor HOEBA

In the first step, 4-(2-hydroxyethyl)benzoic acid (HOEBA) was prepared by hydrolysis of the commercially more widely available 4-(2-hydroxyethyl)benzonitrile as reported by Liverton et al (Scheme 15).¹³⁴

Scheme 15: Hydrolysis of 4-(2-hydroxyethyl)benzonitrile to 4-(2-hydroxyethyl)benzoic acid. 134

After liquid-liquid extraction, 10.7 g (95%) of the product were obtained as an off-white crystalline solid.

2.1.3.2 Synthesis of intermediate AEBA

Afterwards, a Williamson ether synthesis was employed to obtain the intermediate (2allyloxyethyl)benzoic acid (AEBA) according to Lee et al. (Scheme 16). 135

Scheme 16: Williamson ether synthesis using NaH according to Lee et al. 135

After an initially poor yield of only trace amounts of product, the reaction conditions were adjusted toward a long reaction time coupled with a higher temperature and further addition of allyl bromide and sodium hydride. This resulted in a satisfactory yield of 8.4 g (84%) after purification by column chromatography.

2.1.3.3 Synthesis of monomer LCM7

The synthesis of p-[p-[2-(allyloxy)ethyl]benzoyloxy]phenyl p-[2-(allyloxy)ethyl]benzoate (LCM7) was performed analogous to the synthesis of LCM6, according to Zhang et al. 132 utilizing improvements reported by Jordan et al. (Scheme 17). 133

Scheme Steglich obtain 17: esterification the liquid crystalline monomer p-[p-[2-(allyloxy)ethyl]benzoyloxy]phenyl p-[2-(allyloxy)ethyl]benzoate (LCM7). 132,133

7.9 g (83%) of the product were obtained as transparent crystalline needles after purification by recrystallization.

After full purification, the melting point of the product was observed at 98 °C using a polarized optical microscope, above which a colorful liquid crystalline phase, likely a nematic phase, was formed, which persisted up to a temperature of 108 °C, where it turned into an isotropic melt. Upon cooling, the liquid crystalline phase was formed at 108 °C and persisted to a temperature of 90 °C.

Initially, impurities in the product resulted in a broader liquid crystalline phase, which had a lower melting point at 80 °C as well as a higher LC->1 phase transition at 118 °C. This points to the impurities also having mesogenic properties, as nonmesogenic impurities typically lower the melting point and the LC→I phase transition temperature. 136

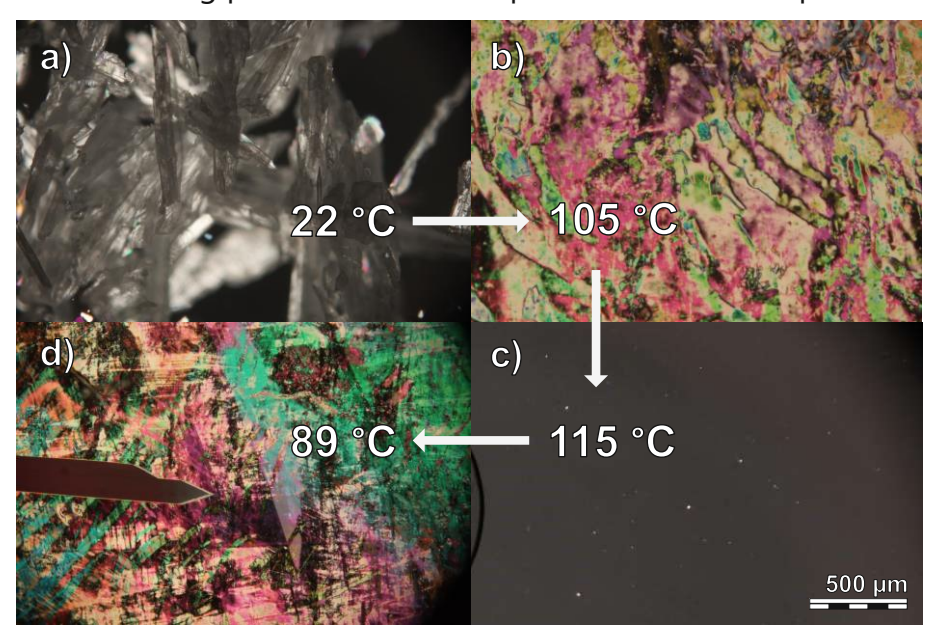


Figure 42: a) Crystalline LCM7 at room temperature (22 °C). b) Liquid crystalline phase of LCM7 upon heating (105 °C). c) Isotropic melt of LCM7 (115 °C). d) LCM7 at the liquid crystalline-crystalline phase transition with a needle-shaped crystal growing from the left-hand side of the picture. (89 °C).

Differential scanning calorimetry (DSC) was performed to confirm the phase transitions of the monomer, which revealed a complex phase behavior (Figure 43, Table 8). The heating cycle of the measurement matched the transitions recorded via polarized optical microscopy (POM) fairly well, with a slightly lower melting point (98 °C via POM, 97 °C via DSC) and a moderately lower LC-isotropic transition (108 °C via POM, 104 °C via DSC). Upon cooling, the isotropic-LC transition again shifted to a lower temperature (108 °C via POM, 102 °C via DSC), and crystallization took place at a significantly lower temperature (89 °C via POM, 81.5 °C via DSC). This could be explained by the higher likelihood of supercooling due to the small sample amount and the smooth surface of the DSC crucible.

Upon further cooling, a trimodal peak indicates potentially multiple solid-solid phase transitions between 74 °C and 65 °C.

Table 8: Comparison of phase transition temperatures of LCM7 measured via polarized optical microscopy (POM) and DSC (second heating cycle).

Measurement step	Phase transitions (POM)	Phase transitions (DSC)
Heating	Cr 98 LC 108 I	Cr 97 LC 104 I
Cooling	I 108 LC 89 Cr	l 102 LC 81.5 Cr

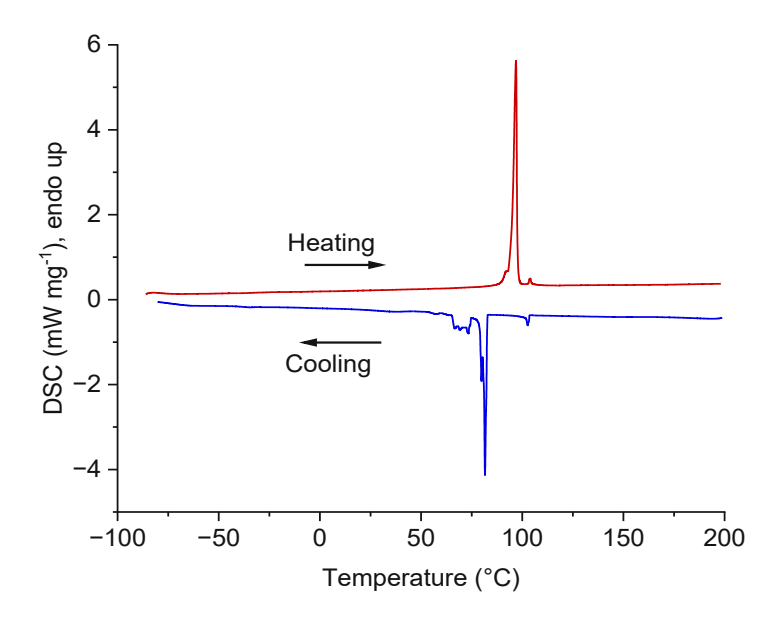


Figure 43: DSC analysis (second heating cycle and second cooling cycle) of LCM7 revealing a melting transition at 97 °C and a minor LC-isotropic transition at 104 °C. Upon cooling, the isotropic-LC transition took place at 102 °C and the monomer crystallized at 81.5 °C. This was followed by three minor solid-solid transition peaks.

2.1.4 Liquid crystalline dithiol LCDT

As commercial dithiol and trithiol monomer availability is limited, especially at low molecular weights, a liquid crystalline dithiol monomer was designed (Figure 44), which would significantly increase the number of options for low molecular weight ene-comonomers and combination with the synthesized ene-LCMs.

Figure 44: Liquid crystalline dithiol monomer structure achievable by combining LCM6-type monomers with ethanedithiol.

To achieve the LC dithiol, a simple one-step synthesis employing the radical-mediated thiol-ene click reaction could be performed starting from liquid crystalline ene monomers.

The initial synthesis was attempted from the existing LCM6 monomer with the aim of adjusting the spacer chain length depending on the melting point of the resulting product. A large excess of difunctional ethanedithiol was used to prevent oligomerization of the reactants and to obtain a near-quantitative yield of the proposed dithiol monomer p-[p-[6-(2-mercaptoethylthio)hexyl] benzoyloxy]phenyl p-[6-(2-mercaptoethylthio)hexyl] benzoate (LCDT).

Scheme 18: Synthesis of liquid crystalline dithiol monomer p-[p-[6-(2-mercaptoethylthio)hexyl]benzoyloxy]phenyl p-[6-(2-mercaptoethylthio)hexyl]benzoate (LCDT).

After purification by fine vacuum drying at elevated temperature and washing with hot methanol, 0.8 g (92%) of the product were afforded as a white solid with a strong, unpleasant odor. By polarized optical microscopy, the melting point was determined at 104 °C followed by a liquid crystalline phase that turned into an isotropic melt at 130 °C.

Investigation of successful thiol end-capping and purity by NMR proved difficult, as residues of ethanedithiol could be wrongly identified as end groups. Additionally, the chemical shifts overlap with the methylene spacer chains, which further hindered full characterization. Oligomerization was investigated by GPC (Figure 45).

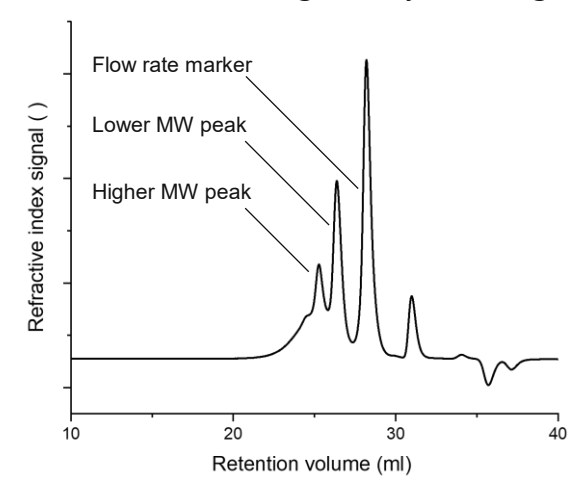


Figure 45: GPC elugram of LCDT monomer.

GPC analysis identified a higher and a lower molecular weight signal, signifying that oligomerization could not be prevented completely. This poses an issue when designing monomer formulations that include this monomer as the exact weight by weight ratio to achieve a balanced ratio of thiol to ene end groups is unknown.

A preliminary polymerization trial in combination with 1,2,4-trivinylcyclohexane (Figure 46) did not result in any success as the formulation remained liquid after irradiation and did not appear significantly different from the crystallized monomer formulation after cooling to room temperature.

Figure 46: Triene monomer 1,2,4-trivinylcyclohexane.

Due to the multitude of difficulties, this synthesis route for liquid crystalline dithiol monomers was not investigated further.

2.2 Synthesis of thiol crosslinkers

A variety of di- and multifunctional thiol monomers are commercially available (Figure 47).

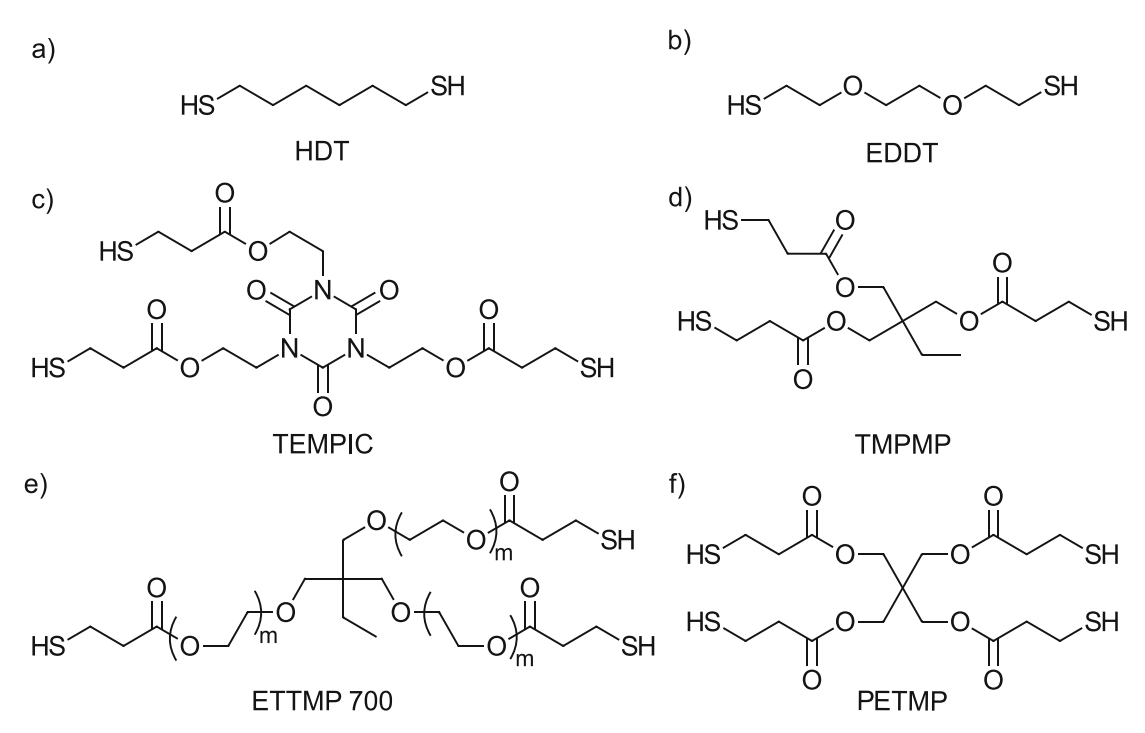


Figure 47: Commercially available thiol monomers. a) 1,6-Hexanedithiol (HDT), b) 2,2-(ethylenedioxy)diethanethiol, c) tris[(3-mercaptopropionyloxy)-ethyl]-isocyanurate, d) trimethylolpropane mercaptopropionate) (TMPMP), e) ethoxylated trimethylolpropane tris(3-mercaptopropionate) with an average molecular weight of 700 g mol⁻¹ (ETTMP 700), f) pentaerythritol tetrakis(3-mercaptopropionate) (PETMP).

A selection of these commercially available thiols was chosen for a screening experiment with every synthesized liquid crystalline alkene monomer. However, most of the commercial tri- and tetrafunctional monomers are of relatively high molecular weight, which may lead to a disruption of the liquid crystalline phase and a less densely crosslinked network. Therefore, two thiol crosslinkers with a low molecular weight and a rigid core structure were chosen to be synthesized, as these properties were predicted to lead to simultaneous improvements in mechanical strength and crystallinity.

2.2.1 Trithiol crosslinker CHTT

In addition to commercially available thiol monomers, the trithiol crosslinker 1,2,4-cyclohexanetriethanethiol (CHTT) was chosen for synthesis for polymerization experiments with liquid crystalline monomers. 137

Figure 48: Cyclohexane based trithiol comonomer 1,2,4-cyclohexanetriethanethiol (CHTT, mixture of isomers).

The monomer was chosen for its cyclic core, which could promote crystallization of the resulting polymers, and for its very low molecular weight per thiol group (88 g·mol⁻¹ FG), which results in a lower comonomer weight fraction. This results in a higher liquid crystalline phase stability, as less comonomer impurity is introduced. A potential downside is that the precursor, and thus also the monomer, is a mixture of isomers, which could hinder crystallization.¹³⁷

Synthesis of the cyclohexane-based trithiol crosslinker CHTT was performed based on a procedure by van Damme et al with some modifications. 137

2.2.1.1 Synthesis of precursor

The first step was performed using a solventless thiol-ene click reaction. After a spontaneous initial reaction, full conversion was ensured by the addition of a photoinitiator and irradiation by UV light. The reaction was monitored by ¹H-NMR analysis and stopped after the double bond signal had fully disappeared.

Scheme 19: Synthesis of precursor ethanethioic acid, $S^1, S^1', S^1'' - (1,2,4-cyclohexanetriyltri-2,1-ethanediyl)$ ester.

2.2.1.2 Synthesis of CHTT

Hydrolysis of the unpurified mixture under alkaline conditions led to the final product. After purification by distillation, 47.1 g (77.5%) of the product were isolated.

Scheme 20: Alkaline hydrolysis leading to the final product CHTT.

2.2.2 Trithiol crosslinker MTSH

After successful initial screening of the cyclohexane-based trithiol monomer CHTT, a mesitylene-derived trithiol crosslinker 1,3,5-benzenetrimethanethiol (MTSH, Figure 49) was chosen for synthesis due to multiple possible beneficial properties compared to the previously synthesized monomer CHTT. 138,139

Figure 49: Trithiol crosslinker MTSH.

The thus far lowest molecular weight per thiol group (72 g mol⁻¹ FG) could enhance the liquid crystalline phase stability of the ene-monomer due to a lower disturbance of the molecular order through the comonomer. Unlike CHTT, MTSH is achiral, which eliminates one molecular property that could additionally impair polymer crystallinity. Additionally, the aromatic structure of MTSH could have a positive effect on the liquid crystalline phase. However, depending on what position the aromatic rings occupies relative to the mesogenic groups, MTSH could also decrease LC phase stability by hindering the relative arrangement of the liquid crystals. Furthermore, synthesis of larger amounts could prove problematic due to the high price of the starting material. Nevertheless, the synthesis was attempted due to the potential benefits.

Synthesis of the mesitylene-derived trithiol crosslinker MTSH was performed according to a procedure outlined by Li et al. and modified according to Han et al. (Scheme 21). 138,139

$$CH_3COSH$$
 K_2CO_3
 CH_3COSH
 CH_3COSH

Scheme 21: Synthesis of trithiol crosslinker 1,3,5-benzenetrimethanethiol (MTSH).

0.62 g (51%) of the product were obtained as a colorless oil. The NMR spectrum contained some discrepancies from the expected integrals corresponding to the molecular structure

of the monomer, as the integral observed at a chemical shift of 3.75 ppm was 10% higher than expected. Additionally, minor unexpected peaks at slightly lower shifts of all main peaks signified some impurities. By NMR analysis, the purity of the monomer was estimated above 90%. (Figure 50).

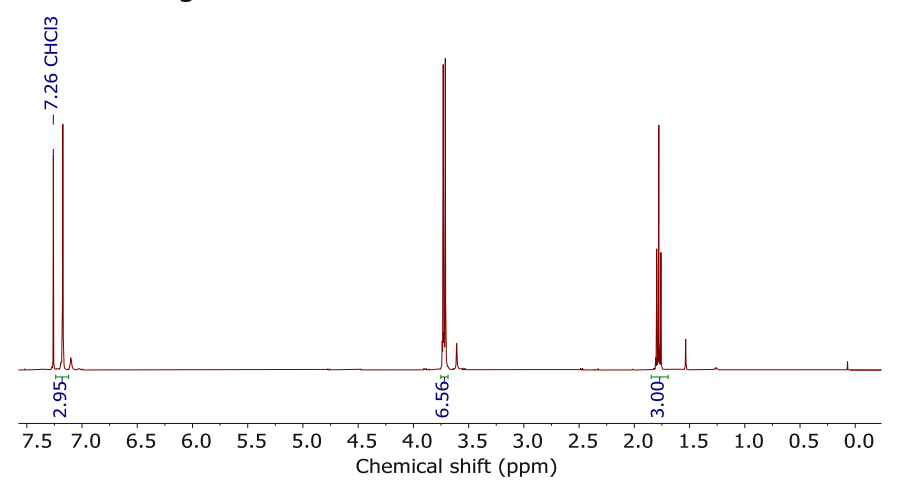


Figure 50: NMR spectrum of MTSH.

However, significantly higher amounts of impurities were detected by HPLC analysis (Figure 51). Therefore, it was concluded that the split into multiple peaks in the HPLC chromatogram likely occurred due to some oligomerization of the product. Before attempted optimization of the synthesis and purification, initial tests with the unpurified product were performed to evaluate the performance of the monomer in conjunction with a liquid crystalline monomer.



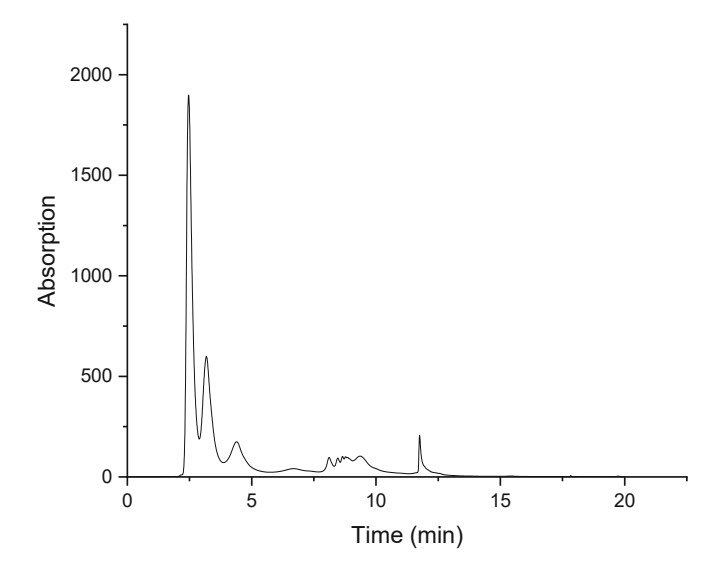


Figure 51: HPLC chromatogram of the synthesized trithiol crosslinker MTSH in a CN-functionalized normal phase column with a chloroform-methanol gradient (UV detection at 253 nm).

3 Synthesis and characterization of LCM-based polymers

3.1 LCM5-based polymers

Using the previously synthesized liquid crystalline monomer LCM4 (Figure 52a), preliminary bulk tests in combination with trithiol crosslinkers were performed, as thus far only linear polymers had been manufactured. The combination resulted in turbid, semicrystalline polymers with promising mechanical strength and toughness. The experiments were continued with LCM5 (Figure 52b) because the high melting point of LCM4 had proven to cause difficulties when processing the formulations.

Figure 52: Liquid crystalline monomers: a) previously synthesized monomer LCM4 with a melting point of 111 °C and b) newly synthesized monomer LCM5 with a melting point of 78 °C.

3.1.1 Pre-screening experiment

LCM5 was selected for a polymerization screening experiment with two commercially available dithiol monomers, HDT and EDDT (Figure 53a, b), which were the most promising thiol candidates in previous polymerization experiments concerning mechanical strength and polymer chain length. Additionally, the commercially available trithiol monomers TEMPIC, TMPMP and ETTMP 700 (Figure 53c, d, e) were used, as well as the trifunctional crosslinker CHTT (Figure 53f), which was synthesized from trivinylcyclohexane.

Figure 53: Difunctional and trifunctional thiol crosslinkers used in polymerization experiments with LCM5.

The selection of HDT and EDDT resulted from an earlier screening experiment of a larger number of dithiol monomers, in which reactivity, solubility and molecular weight of resulting polymers using an LCM-type monomer were measured. The various multifunctional thiols were chosen due to their differences in molecular weight, rigidity, and functionality, so that a wide variety of characteristics could be tested. Molecular weight per thiol group (grams per mole of functional group, g mol⁻¹ FG) is lowest for CHTT (88 g mol⁻¹ FG), followed by the intermediate molecular weights of TMPMP (133 g mol⁻¹ FG), TEMPIC (175 g mol⁻¹ FG) and the high molecular weight of ETTMP 700 (233 g mol⁻¹ FG). Lower molecular weights per thiol group can, among other factors, result in a higher liquid crystalline phase stability due to less disturbance of the LC-phase by the impurity of a comonomer. ETTMP 700 is the least rigid comonomer due to its long, flexible oligoethylene glycol chains, followed by TMPMP, which also contains the flexible trimethylolpropane core. TEMPIC and CHTT are much more rigid due to their cyclic structure. Rigidity of the comonomer may influence the glass transition temperature and stiffness of resulting polymers.

In all formulations, the number of thiol end groups was matched stoichiometrically with the number of terminal alkene groups. The formulations were stabilized with 0.1 wt% of pyrogallol, and 1 mol% of Ivocerin was added as photoinitiator. Curing was performed at a temperature of approximately 100 °C using a using a simple heated plate, on top of which a silicone mold was placed. The samples were cured in a UV chamber.

The combination of LCM5 with HDT and EDDT yielded highly crystalline polymers that suffered from the same brittleness issues that had been observed with linear thiol-ene polymers using LCM4. The samples could, in most cases, not be removed from the silicone molds in which they had been cured without breaking.

Of the trithiol crosslinker-containing formulations, use of TEMPIC and TMPMP led to inhomogeneous crystallization over some areas of the sample after irradiation (Figure 54).



Figure 54: Polymer resulting from combination of LCM5 and TMPMP. Crystallization occurred in the thicker sections of the sample, whereas in the thinner portions of the sample, the polymer remained transparent.

When the experiment was repeated, both materials remained fully transparent. This highlighted the issue of inhomogeneous heat distribution throughout the samples before curing. Additionally, the transparent part of the TEMPIC-containing polymer had a sticky, unreacted portion of the monomer mixture remaining at the bottom after irradiation. This monomer mixture was therefore disregarded for future experiments with LCM5.

The combination of LCM5 and ETTMP resulted in a semicrystalline polymer. The material appeared homogeneously crystalline throughout. When heating to 88 °C, the material turned transparent, and upon cooling, the semicrystallinity was restored.

All crosslinked samples were relatively soft, which is a common property of nonsemicrystalline thiol-ene polymers. Using a mix of di- and trifunctional thiol monomers was considered as a future option to enhance crystallinity.

3.1.1.1 Thermomechanical evaluation

Dynamic-mechanical thermal analysis (DMTA) measurements were attempted for four samples of thiols in combination with equimolar amounts of LCM5. Measuring the combination of LCM5 and difunctional thiols HDT and EDDT was unsuccessful, as the sample was too brittle to be fixed into the measurement device, even when applying a lower torque than recommended.

The other samples were measured successfully, and their storage (G') and loss moduli (G''), as well as their loss factors (tan δ , G'/G'') were analyzed as a function of temperature (Figure 55). The ETTMP-containing sample was stretched to around twice its original size by the device holding tension during the measurement, but the measurement could be completed. Additionally, the sample slipped slightly within the measurement clamps, which resulted in an irregularity in the measurement curve around -10 °C. The CHTTcontaining sample fractured at 125 °C.

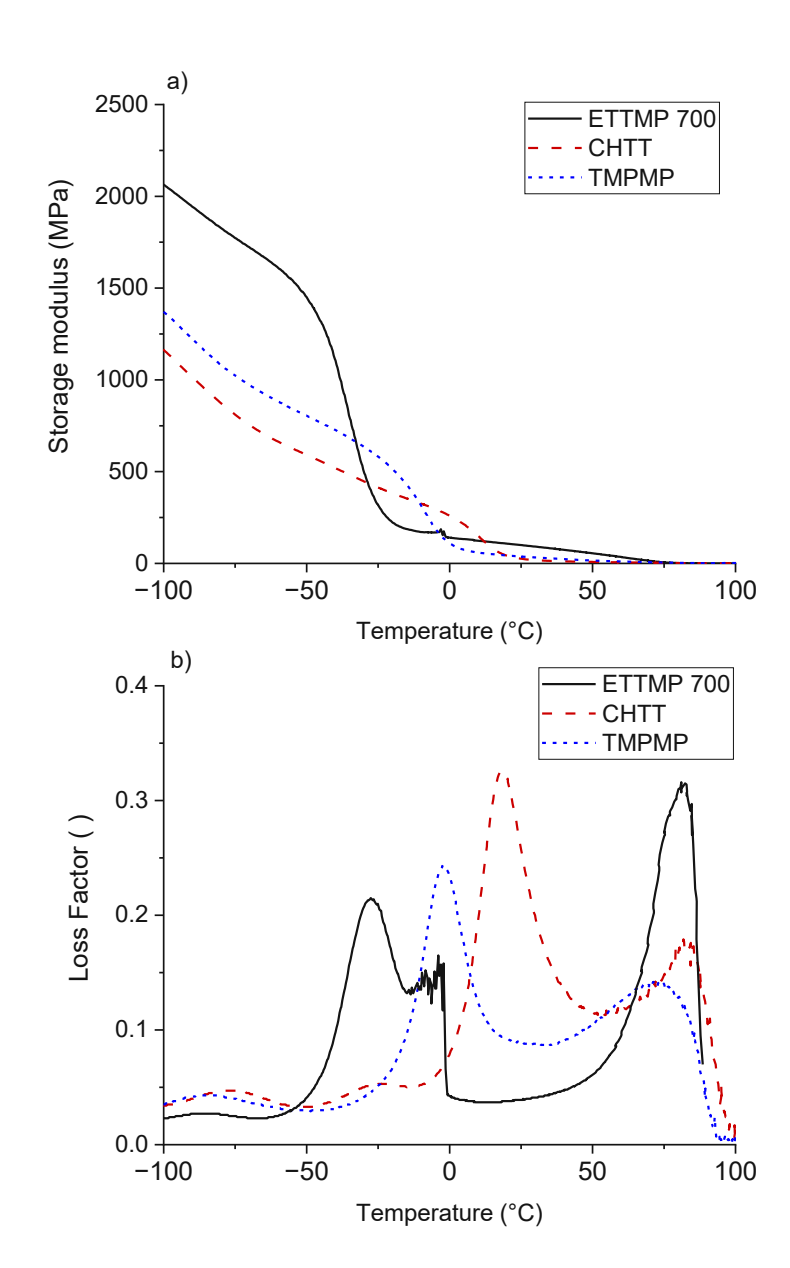


Figure 55: a) Storage modulus (G') and b) loss factor (tan δ) of LCM5 in combination with TMPMP, CHTT, and ETTMP 700. The displayed data was cut off above 100 °C in case of CHTT and TMPMP, and above 90 °C for ETTMP 700, as the signals of all samples showed a low signal/noise ratio when storage and loss moduli both decreased to near-zero.

The glass transition temperature was identified clearly for all polymers as the peak of the loss factor curve (Table 9). The values correlate inversely with the molecular weight of the trithiol crosslinker. This is explained by the flexibility of the network, which increases when fewer crosslinks are present. Even in the presence of pronounced semicrystallinity of the network, the ETTMP-containing polymer exhibited the lowest T_g. A second peak maximum is visible in all measured tan δ curves, signifying a melting point of crystalline domains. This is most significant for the ETTMP-containing network, where the semicrystallinity was also visible macroscopically as the sample appeared opaque. The progression of the storage modulus reflects this with a slower decline above the glass transition when ETTMP is employed. The crystallinity in the network acts against the softening that occurs during the glass transition.

Table 9: Peak maxima depicting the glass transition (T_a) and melting point temperature (T_m) in loss factor curves for polymers cured from LCM5 together with equimolar amounts of trifunctional thiol crosslinkers.

Formulation	T _g (°C)	T _m (°C)
LCM5 + TMPMP	-2	71
LCM5 + ETTMP 700	-26	82
LCM5 + CHTT	19	84

3.1.1.2 Phase analysis

To analyze the liquid crystalline behavior before curing in depth, the formulations were investigated using a polarized light microscope. The homogeneity of the solidified formulations at room temperature was observed to hold up well after cooling below their melting points as no large crystals had formed.

The temperature range, within which a liquid crystalline phase was observed, was noticeably narrower for the formulations in comparison to the pure LCM5 monomer. A viscous liquid crystalline phase was observed for most formulations in a temperature range of approximately 10 °C, starting around 80 °C. Pinpointing an exact temperature of start and finish for the phase transitions proved to be difficult, as the changes were gradual. Additionally, a liquid crystalline phase was often not present throughout the entire samples, as along the edges, an isotropic phase would often occur directly after the sample had molten. Longer isothermal periods may be necessary for the molecular arrangement to take place. This proved that in order to polymerize the studied formulations from the liquid crystalline phase, very accurate temperature control is necessary, prompting the need for more controlled bulk curing conditions.

3.1.2 Design of heated polymerization chamber

With the heated polymerization setup utilized up to this point, which consisted of a simple heating plate with a diameter of around 10 cm, it was not possible to accurately measure and control the temperature of monomer mixtures before and during irradiation. Additionally, an inhomogeneous heat distribution across the surface resulting from the small diameter of the heating plate prevented the formation of a homogeneous liquid crystalline phase across a tensile test or DMTA specimen. The problem was exacerbated by the bottom of the silicone mold expanding more than the top upon heating, which caused it to bend upwards at the corners and losing further contact with the heating plate.

To overcome these issues, a new polymerization chamber was planned utilizing a customized heat-conductive aluminium chamber manufactured using a CNC milling machine. A Heidolph MR Hei-Standard heated magnetic stirrer was deemed suitable as the heating element, as heat would be dispersed quickly throughout a thick aluminium base plate. The requirements for the new chamber are listed in Table 10, the final design is presented in Figure 56, and the finalized setup is displayed in Figure 57.

Table 10: Requirements for the newly designed polymerization chamber.

Reasons for loss over LC phase control	Proposed solution	
Inaccurate temperature control of heating	Large aluminium base for better heat	
element	distribution, temperature control through	
elefficit	heated stirrer thermocouple	
Inaccurate temperature monitoring of	Inlet for additional thermometer elements	
formulation	into silicone mold and formulation	
Cooling of ton layer of formulation by ambient	Fully sealable chamber with UV-	
Cooling of top layer of formulation by ambient air	transparent quartz glass lid and simple	
dii	opening and closing mechanism	
No option for inert atmosphere/vacuum	Gas inlet and outlet	
Only usable with UV curing chamber, which	Compatibility with LED UV light source by	
heats the formulation irregularly	placing the light source directly on top	
Silicone mold bends upward at the corners through thermal expansion	Mechanism to pin down silicone mold	

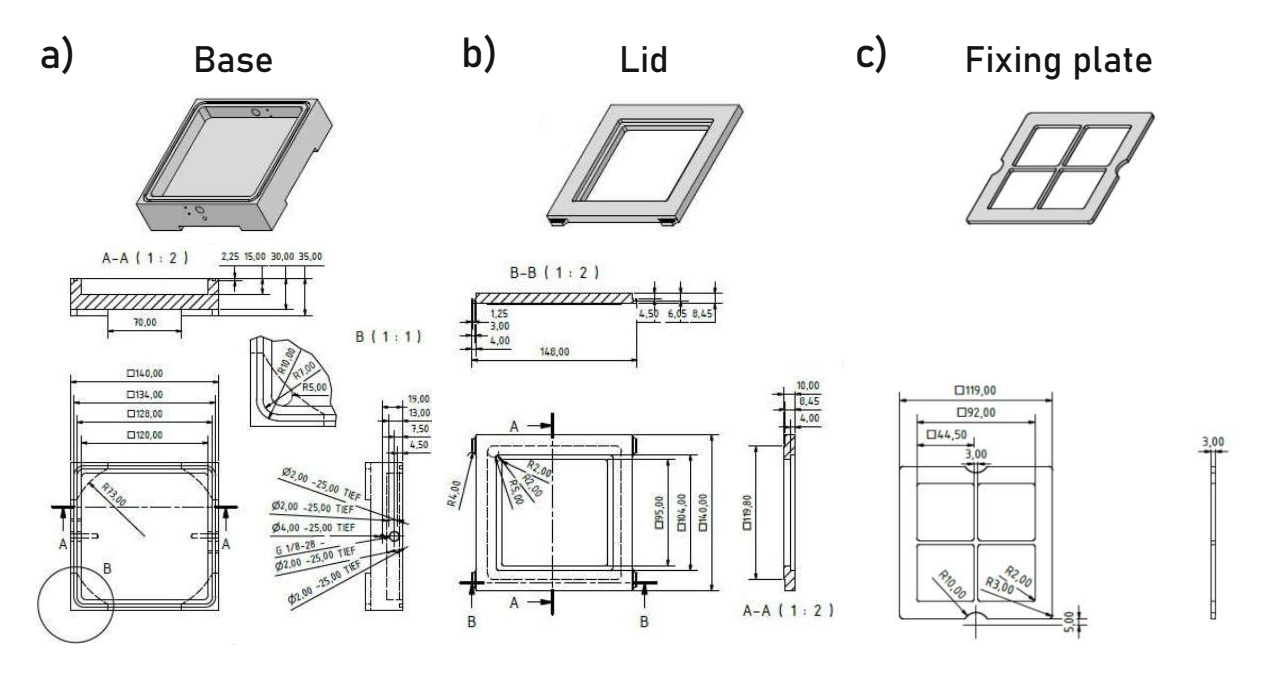


Figure 56: Design of the new polymerization chamber consisting of a) a base plate, b) a lid with inset for a quartz glass window, and c) a fixing plate.

The polymerization chamber's base and lid were CNC machined out of two aluminium blocks and joined by an X-ring seal, for which a groove was machined. Latch fasteners were used as a closing mechanism. An inlet for a quartz glass window was fashioned into the top block, on top of which the light source is placed. A thinner aluminium fixing plate with four cutouts to enable irradiation is inserted below the lid and the base to put pressure on the silicone mold with the help of four conical springs, preventing the silicone mold from contorting through thermal expansion. The silicone mold itself was modified by adding 20 wt% aluminium powder to provide better heat conduction, lower thermal expansion and increased stiffness. The chamber is designed for use with two light sources: a Hönle LEDCube LED array with a 405 and 465 nm wavelength setting and a UVET UV-LED LED array capable of high intensity irradiation with a fixed wavelength of 365 nm.

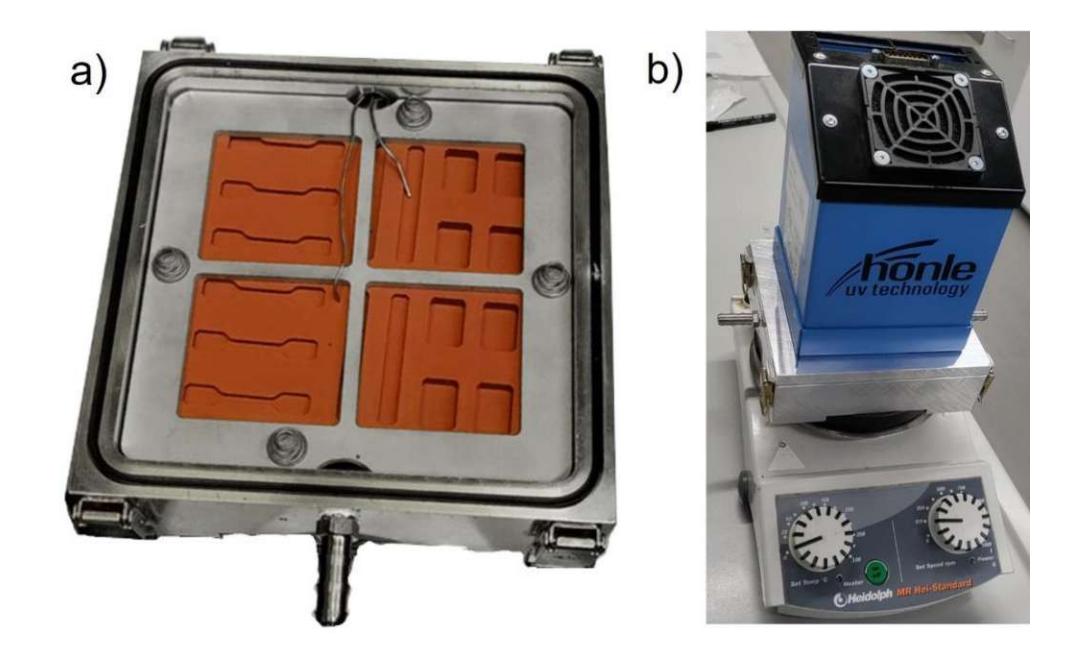


Figure 57: a) The open polymerization chamber with conical springs, two thermometer units and an aluminium-filled silicone mold with fixing plate and conical springs. b) The polymerization chamber on a Heidolph heated stirrer with the Hönle LED array.

Initial experiments with the polymerization chamber confirmed that all previously determined requirements for exact temperature control were fulfilled. Heating and temperature stabilization could be achieved in approximately 15 min, after which the heat distribution across the silicone mold varied by less than 1 °C, which was measured by applying three thermocouples in separate locations of the silicone mold.

3.1.3 Optimization of polymerization parameters

With the newly operational heated polymerization chamber, exact temperature control during polymerization was possible. However, the heat of polymerization is another significant influence on the polymer's crystallinity. In preliminary experiments with the formulation combining equimolar amounts of LCM5 and CHTT (Figure 58), it was determined that even if the formulation was initially in a liquid crystalline phase, highenergy irradiation would cause the formulation to heat up significantly through the enthalpy of polymerization and the heat transfer from the irradiation itself, before crosslinking could be completed. This caused the formulation to exceed the liquid

crystalline temperature range and the crosslinking of the polymer occurred from an isotropic molten phase, which produced a transparent, soft and non-crystalline material. To prevent this, the temperature had to be kept constant long enough to polymerize from the liquid crystalline state and thereby achieve solid phase crystallinity. In the following study (chapters 3.1.3.1 and 3.1.3.2), multiple methods to minimize the initial dose of irradiation were tested to keep the system from exceeding the liquid crystalline temperature range before crosslinking.

Figure 58: Equimolar monomer mixture used in polymer curing optimization experiments for the new heated polymerization chamber.

3.1.3.1 Single light source

The UVET UV-LED curing device has a spectral maximum of 365 nm and can be operated at 10-100% intensity. At 100% intensity, the device can output light at 2500 mW cm⁻². Even at the lowest intensity setting of 10% a relatively quick increase in temperature of a previously polymerized, and thus unreactive sample was observed (10 °C in roughly one minute, starting from 85 °C).

Therefore, the only option to effectively dissipate the heat that reaches the sample from the light source and the heat produced during polymerization was pulsing the light in short intervals. In a preliminary experiment, this had led to higher crystallinity of the sample in comparison to continuous exposure. However, achieving crystallization in a stoichiometrically balanced formulation of LCM5 and CHTT was still problematic. Therefore, an additional monomer mixture was tested with a lower amount of CHTT. In addition to a balanced 50/50 (eq./eq.) ratio of the monomers, a 56/44 (eq./eq.) ratio of LCM5/CHTT was investigated to facilitate crystallization through more liquid crystalline groups at the cost of reduced conversion of end groups. The end result could be a less

densely crosslinked, more crystalline network due to the enhanced freedom of movement of monoreacted LCM5 liquid crystalline groups, causing the LC motifs to align with each other.

Each of these two formulations was polymerized under three different curing modes with the UVET light source at the lowest intensity (Table 11). At low light dose liquid crystalline mode (LC-LD) the samples were heated to 85 °C, where the monomer mixtures were in their liquid crystalline state, and pulsed irradiation was employed, resulting in a low total light dose, which aimed to keep the temperature as low as possible during irradiation. With the **LC-MD** mode, the sample was continuously irradiated for 60 seconds (medium light dose), again starting from the liquid crystalline temperature range (85 °C). In the **Iso-LD** mode, the formulation was purposefully heated above its liquid crystalline state, to 120 °C, where it exists in an isotropic molten phase. This condition was intended to obtain a reference material not polymerized from the liquid crystalline phase. The initial irradiation step was performed with a low light dose to prevent the sample from reaching excessively high temperatures. After the initial curing stage, during which crystallinity was established, all samples underwent a final curing step at high intensity on both sides to reach full conversion.

Table 11: Formulations tested with different irradiation modes for the liquid crystalline phase curing optimization study. LD (low light dose) irradiation mode is a one-second irradiation that is repeated three times. With MD (medium dose) irradiation, the sample is irradiated for 60 seconds.

Formulation name	Reactive groups LCM5 (%)	Reactive groups CHTT (%)	Formulation temperature (°C)	Irradiation mode	Final curing step
50/50 LC-LD ¹	50	50	85 (LC phase)	LD^1	High light dose ³
50/50 LC-MD ²	50	50	85 (LC phase)	MD^2	High light dose ³
50/50 Iso-LD ³	50	50	120 (Isotropic melt)	LD^1	High light dose ³
56/44 LC-LD ¹	56	44	85 (LC phase)	LD^1	High light dose ³
56/44 LC-MD ²	56	44	85 (LC phase)	MD^2	High light dose ³
56/44 Iso-LD ³	56	44	120 (Isotropic melt)	LD ¹	High light dose ³

¹ low light dose of approximately 0.870 J cm⁻² (Hönle light source at 5%)

To compare the material properties, tensile tests of the samples polymerized under different conditions were performed (Table 12, Figure 59).

Table 12: Tensile test results of the samples polymerized under different conditions.

Formulation	Ultimate tensile strength (UTS) (MPa)	Tensile strength at yield point (MPa)	Elongation at break (%)
50/50 LC-LD	11.54±0.58	11.54±0.58 ¹	46 ± 16
50/50 LC-MD	8.61±1.40	5.99 ± 0.08^2	129 ± 18
50/50 Iso-LD	11.01±1.07	5.17±0.65	198 ± 12
56/44 LC-LD	8.16±2.83	3	2.9 ± 1.1
56/44 LC-MD	11.25±0.52	11.25±0.52 ¹	22.9 ± 4.3
56/44 Iso-LD	12.08±1.09	10.52±0.13	150 ± 86

¹ Equals ultimate tensile strength

² medium light dose of approximately 17.4 J cm⁻² (UVET light source at 10%)

³ high light dose of approximately 52.2 J cm⁻²

² Transition from elastic to plastic deformation, no pronounced yield point

³ No yield point

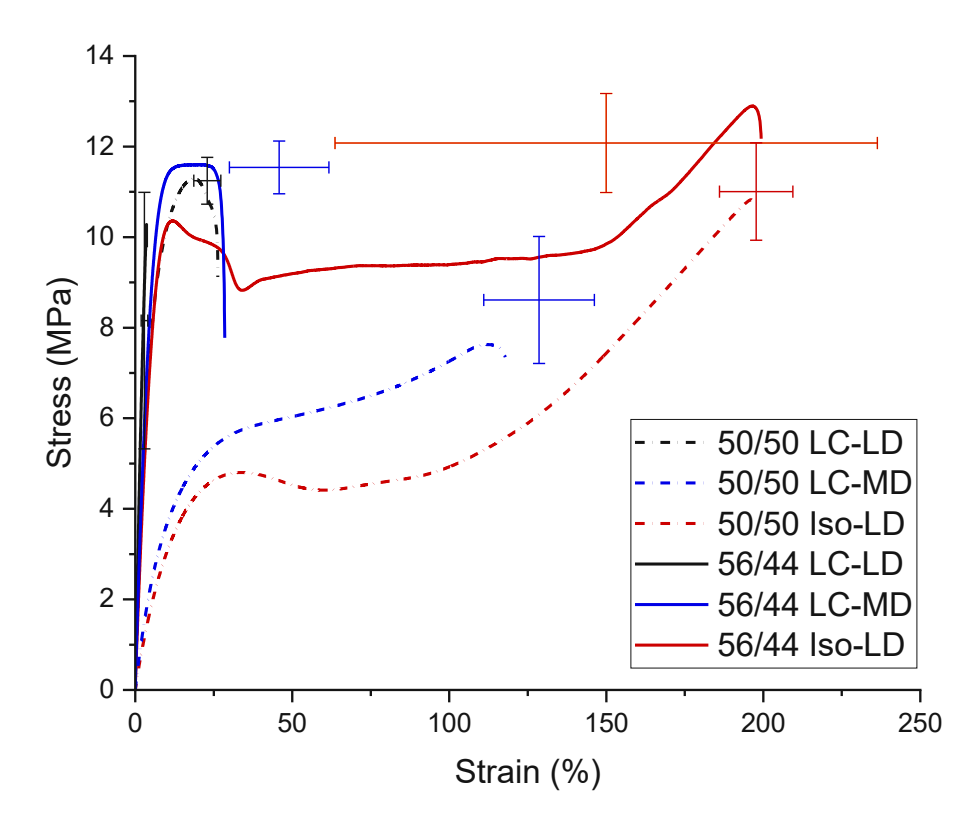


Figure 59: Representative stress-strain curves of LCM5-CHTT samples cured under different conditions. 50/50 (eq./eq) samples have equal stoichiometry, 56/44 (eq./eq.) samples contain an excess of LCM5. LC-LD and LC-MD samples were polymerized from the liquid crystalline phase (85°C) with low or medium intensity initial light doses, respectively. Iso-LD samples are polymerized from the isotropic melt (120 °C) with a low intensity initial light dose. Curing was completed for all samples with a second high intensity curing phase.

Lower irradiation doses directly correlated with higher stiffness of the samples, which, together with the increased sample opacity (Figure 60), leads to the conclusion that this enhanced curing technique can be used to induce higher sample crystallinity.

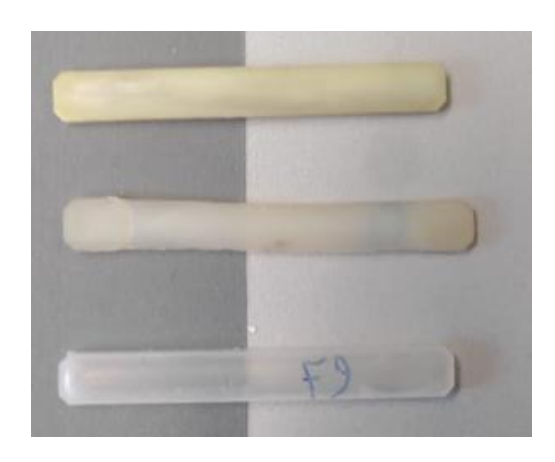


Figure 60: Opacities of different samples: top: 56/44 LC-LD, middle: 56/44 Iso-LD, bottom: 50/50 Iso.

All of the 50/50 samples exhibited some elasticity. The stiffest among them (50/50 LD) still exhibited a respectable elongation at break of around 45%. The two other 50/50 samples had a low strength at yield point, followed by a long elongation phase with significant necking of the sample. Since the 50/50 Iso sample was the reference for the least amount of crystallinity achievable, it can be concluded that the medium irradiation dose already caused the 50/50 sample to largely polymerize beyond the liquid crystalline temperature range from an isotropic melt, with only a low level of crystallinity remaining in the final polymer sample.

The 56/44 samples exhibited consistently higher stiffnesses than the 50/50 samples as indicated by the steep slope of the stress-strain curve. At low and medium irradiation dose starting in the liquid crystalline region, the 56/44 samples exhibit brittle fracture. The 56/44 Iso samples had a pronounced yield point followed by a long period of necking and strain hardening, finally resulting in the highest tensile strength after significant elongation of the specimens. The crystallinity in this sample was likely not induced by a liquid crystalline phase, as the temperature was very high before the irradiation took place. Instead, the stoichiometric excess of LCM5 likely caused the samples to crystallize after the polymerization through a fraction of the monomer which could only react on one side.

This experiment led to the conclusion that the heat of polymerization must not increase the sample temperature above the LC-temperature range before crosslinking takes place. Most importantly, significant crystallinity could be induced in the 50/50 LD sample with carefully chosen conditions.

3.1.3.2 Combination of two light sources

As the 50/50 LD (chapter 3.1.3.1) sample was deemed a success in translating liquid crystallinity into solid phase crystallinity in a polymer, the conditions were further optimized with regard to user-friendliness and reproducibility of sample preparation. Furthermore, this optimization could possibly further increase crystallinity in the samples. The main issue around ease of use and reproducibility was the one-second pulse of light that had to be repeated three times for the "LD" samples. To avoid this, the second available light source, a Hönle LEDCube light source was used in addition to the UVET light source, as it provides the option to irradiate at very low-intensity. Thus, the total light dose of the "LD" curing step can then be spread out over a longer time period, which leads to a milder and more reproducible curing procedure. The previous low irradiation dose (870 mJ cm⁻²) delivered over a total of three one-second light pulses was substituted by a light dose of 450 mJ cm⁻² delivered over a continuous 300-second irradiation.

With the help of thermometer elements, the LCM5-CHTT formulation's temperature increase during irradiation was monitored and analyzed along with the appearance of the sample. The sample was tested for 300 s initial irradiation periods using the Hönle light source on four different settings: 405 nm and 465 nm maximum wavelengths, each at 2% and 5% intensity. After this, an irradiation cycle with the UVET light source was applied to fully crosslink the samples. During each irradiation period, the temperature increase of the sample was monitored in comparison with the temperature of the silicone mold, and the initial 300 s irradiation was studied in detail (Figure 61).

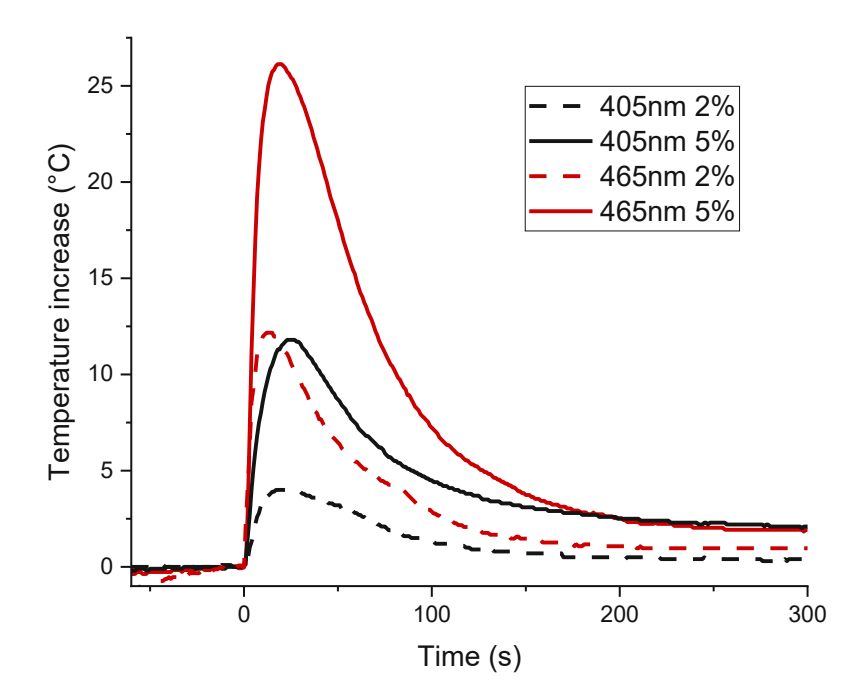


Figure 61: Temperature increases of the LCM5-CHTT 50/50 formulation relative to the silicone mold. Temperature of the silicone mold was measured separately and the difference of the temperatures is depicted in the graph.

As seen in the graphs, the temperature response to irradiation at 465 nm is much higher than at 405 nm. This is likely because the photoinitiator Ivocerin is more sensitive to higher wavelengths, as demonstrated by Barner-Kowollik et al. in a study, which showed the highest reactivity for different photoinitiators in the high-wavelength flank of their absorption spectrum. 140

Ideally, very mild irradiation is applied over a long period for the crystallization to take place before the polymer network forms fully. However, at 2% intensity at 405 nm, crystallization of the upper layer of the formulation blocked the light off almost completely. Therefore, light penetration deeper into the sample did not occur, which resulted in a very low total temperature increase (< 5 °C). The second, stronger irradiation period then caused the sample to produce significant heat of polymerization, causing the middle layer of the formulation to leave the LC temperature range and crosslink at this elevated temperature. The bottom layer of the sample remained in the LC temperature range throughout curing and was able to form a semicrystalline bottom layer. This led to

an inhomogeneous sandwich structure with a crystalline upper and lower layer and a transparent non-crystalline middle layer (Figure 62 a). A significantly longer initial irradiation period could solve this problem by allowing enough light to penetrate deeper into the sample to cause the initial crystallization. However, this is impractical due to time reasons and possible damage to the lamp resulting from prolonged close contact to the high temperature of the polymerization chamber. Irradiation at 405 nm at 5% intensity (Figure 62 b) and 465 nm at 2% intensity (Figure 62 c) caused the temperature to increase by around 12 °C for both samples during the initial irradiation period. In both cases, this led to satisfactory homogeneous crystallinity throughout the cross-section of the sample. This signifies that the temperature increase is low enough to allow the formulation to remain in the LC phase during the irradiation process. Between these two samples, curing with 465 nm light at 2% intensity led to a slightly faster temperature increase than curing with 405 nm light at 5% intensity. However, this deviation could have resulted from a slight difference in the position of the thermometer.

At 465 nm and 5% irradiation intensity, the sample's temperature increased rapidly, forming a transparent, non-crystalline layer, which resulted in crystallinity only in the lower layer of the polymer (Figure 62 d). A yellow coloration appeared in all the samples, likely resulting from the cleavage products of the photoinitiator. This discoloration is most apparent in the amorphous sections, as the crystalline areas appear whiter due to less transmission of light through the sample.

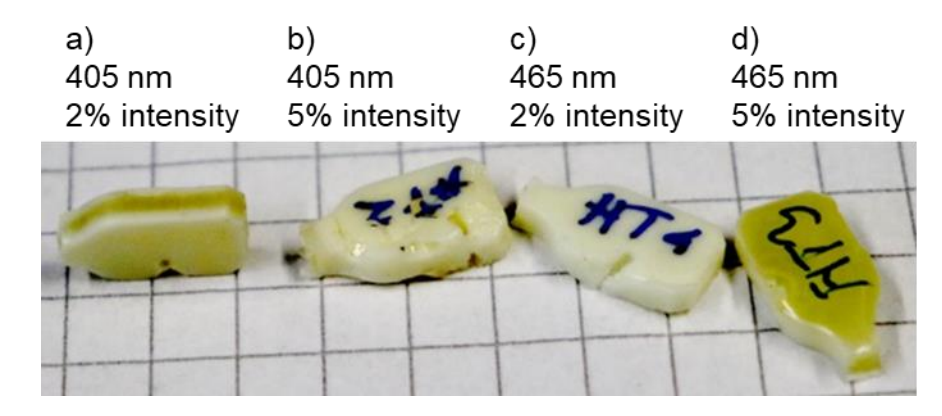


Figure 62: a) Sample irradiated at 405 nm at 2% intensity with sandwich-structure from incomplete initial curing, causing final curing to increase the sample temperature beyond the liquid crystalline range. b) Sample irradiated at 405 nm at 5% intensity with desired homogeneous crystallinity throughout the sample. c) Sample irradiated at 465 nm at 2% intensity with desired homogeneous crystallinity. d) Sample irradiated at 465 nm at 5% intensity with most parts of the sample turning into non-crystalline phases due to an excessive temperature increase during the initial irradiation phase. The contrast of the picture was increased to enhance the visibility of the transparent non-crystalline and opaque crystalline layers, which caused the slight yellow color of the samples to appear more distinct. The shapes of the samples result from them being polymerized in the wider part of a tensile test specimen mold.

With these observations, an initial curing step of 300 seconds at 405 nm at 5% intensity and 465 nm at 2% intensity were both identified as desirable. For future experiments, 405 nm with 5% intensity was chosen because the light source operates more stably at these conditions. These irradiation conditions will be referred to as LC-Opt (curing from liquid crystalline phase, optimized) from this point on.

Attenuated total reflection infrared spectroscopy (ATR-IR) was employed to investigate reactive group conversion for the samples irradiated using various conditions (Figure 63). The carbonyl group of LCM5 was used as a reference, since it does not change during polymerization, and the polymers' terminal double bond integral was compared to that of the unreacted formulation. The primary aim was to investigate whether crystallization exhibits a negative influence on the reactive group conversion. This could occur due to crystallization immobilizing growing polymer chains before complete conversion is reached. Additionally, the 56/44 monomer combination with an excess of LCM5 was

analyzed to identify how significant the detrimental effect of the imbalanced stoichiometry would be on reactive group conversion.

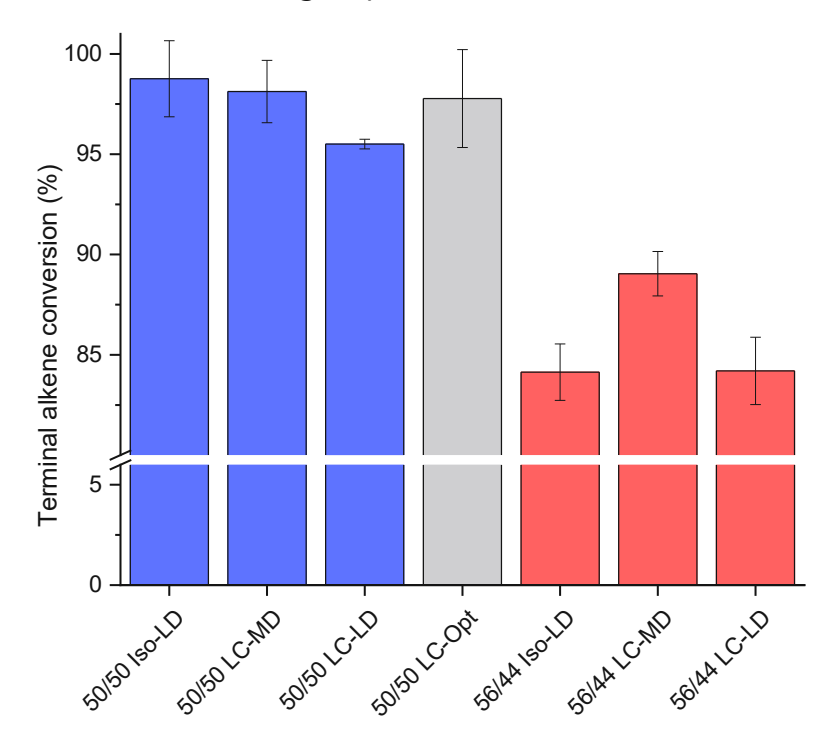


Figure 63: Results of ATR-IR conversion study for all polymers prepared from a combination of LCM5 and CHTT.

All stoichiometrically balanced samples exhibited conversions above 95%. Since crystallization may limit the mobility of reactive radical sites in the polymerizing formulation, slightly lower conversions were expected for the more crystalline polymers prepared by the LC-MD and LC-LD curing techniques. The initially measured samples suggested this expectation to be true, with samples polymerized from the isotropic phase exhibiting the highest conversions and subsequently milder initial irradiation modes leading to progressively lower conversion. However, measuring the sample optimized for crystallinity (50/50 LC-Opt), higher conversions were again observed, which were around the conversions observed after applying the LC-MD curing mode. Additionally, they were situated within the standard deviation range of the samples polymerized from the

isotropic phase. Therefore, it is likely that crystallization does not lead to a significant negative effect on the reactive group conversion.

Using the newly optimized curing conditions, a DMTA specimen was cured and measured (Figure 64). For comparison, the graph includes the sample previously identified as the most crystalline (56/44 LD, chapter 3.1.3.1) as well as the stoichiometrically balanced composition cured in its isotropic state, which resulted in a non-crystalline sample.

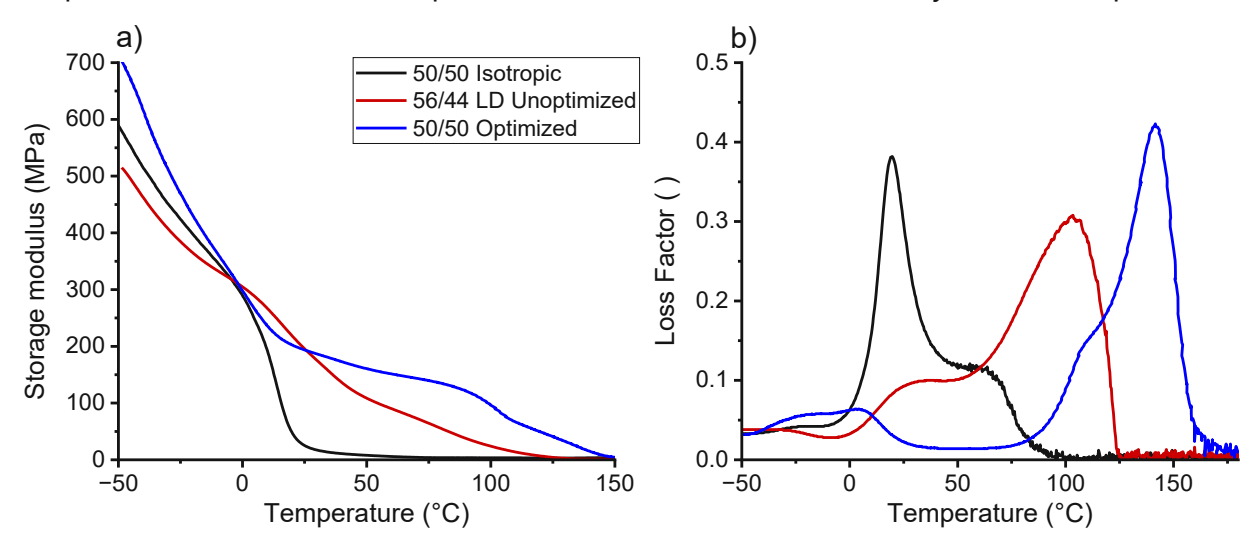


Figure 64: DMTA measurements of LCM5-CHTT monomer composition polymerized from isotropic melt (50/50 Isotropic), from its liquid crystalline phase with excess LCM5 (previously highest achieved crystallinity, 56/44 LC Unoptimized), and with stoichiometric monomer composition and optimized curing conditions (50/50 Optimized). a) Storage modulus G', b) loss factor tan δ .

With the optimized conditions the decline of mechanical properties above temperatures of 0 °C was reduced significantly, causing a plateau-like behavior of the storage modulus up to 100 °C, where the melting of crystalline domains starts. At 100 °C, the optimized sample still had a storage modulus comparable to the previously most crystalline sample at 50 °C. This is also highlighted in the loss factor graph, where a small peak around 0 °C represents the glass transition, which is overshadowed by a much larger second peak around 140 °C, which represents the crystallite melting point. Notably, this tan δ peak already exhibits a shoulder at 100 °C, which indicates the start of melting for smaller and/or less homogeneous crystalline domains and explains why the storage modulus

already decreases from 100 °C on. These observations led to the conclusion that the optimized curing procedure leads to higher and more stable liquid crystallinity, which directly impacts the thermomechanical properties of cured specimens, especially at higher temperatures.

In addition to the curing optimization, variation of the amount of photoinitiator was investigated for control over polymerization temperature (Table 13, Figure 65). 50/50 LC-Opt 1% PI thereby signifies the LCM5-CHTT 50/50 formulation previously subjected to optimized curing conditions and 50/50 LC-Opt 0.5% PI is a variant of the previously used formulation, utilizing 0.5 mol% photoinitiator instead of 1 mol%. Investigation of reactive group conversion via ATR-IR revealed a nearly identical double bond conversion to the sample in which 1% PI was used. Both optimized samples (1% PI and 0.5% PI) were subjected to tensile testing and exhibited the highest tensile strengths at their yield points measured thus far, with the 0.5% PI sample performing slightly better. This is probably caused by the slower polymerization leading to less heat development during irradiation.

Table 13: Tensile test results of previously measured samples in comparison with the samples optimized for crystallinity. σ_M is the ultimate tensile strength, σ_Y is the strength at the yield point, and ε_B is the elongation at break.

Formulation	σ_{M} (MPa)	σ _Y (MPa)	ε _B (%)
50/50 LC-LD	11.54±0.58	11.54±0.58 ¹	46±16
50/50 LC-MD	8.61±1.40	5.99 ± 0.08^2	129±18
50/50 Iso-LD	11.01±1.07	5.17±0.65	198±12
50/50 LC-Opt 1% PI	12.09±0.12	12.09±0.12 ¹	24±3
50/50 LC-Opt 0.5% PI	12.60±0.24	12.60±0.24 ¹	23±3

¹ equals ultimate tensile strength

² transition from elastic to plastic deformation, no pronounced yield point

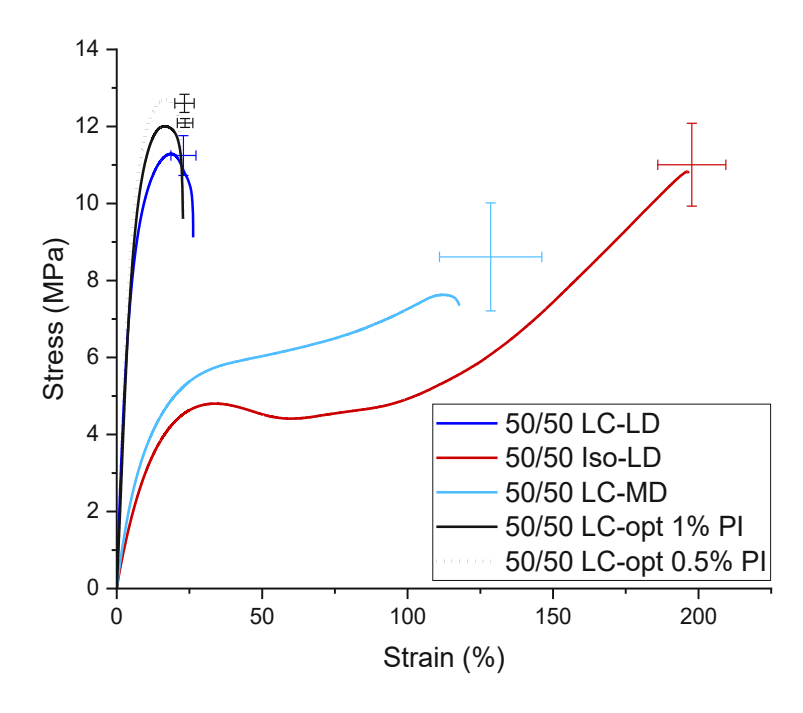


Figure 65: Representative stress-strain curves of the 50/50 LCM5-CHTT formulation including a sample subjected to the optimized curing program with 1 mol% photoinitiator (previously used, LC-Opt) and 0.5 mol% photoinitiator (LC-Opt halfPI).

The two most promising samples 50/50 LC-Opt 1% PI and 50/50 LC-Opt 0.5% PI were additionally subjected to differential scanning calorimetry (DSC) measurements to characterize sample crystallinity qualitatively and quantitatively and understand implications for mechanical properties (Table 14, Figure 66).

Table 14: Phase transition temperatures of LCM5-CHTT measured via DSC. The values were taken from the second heating cycle.

Measurement step 50/50 LC-Opt 1% F		50/50 LC-Opt 0.5% PI (°C)
T _m (heating)	142.1	141.3
T _m (cooling)	136.8	134.4

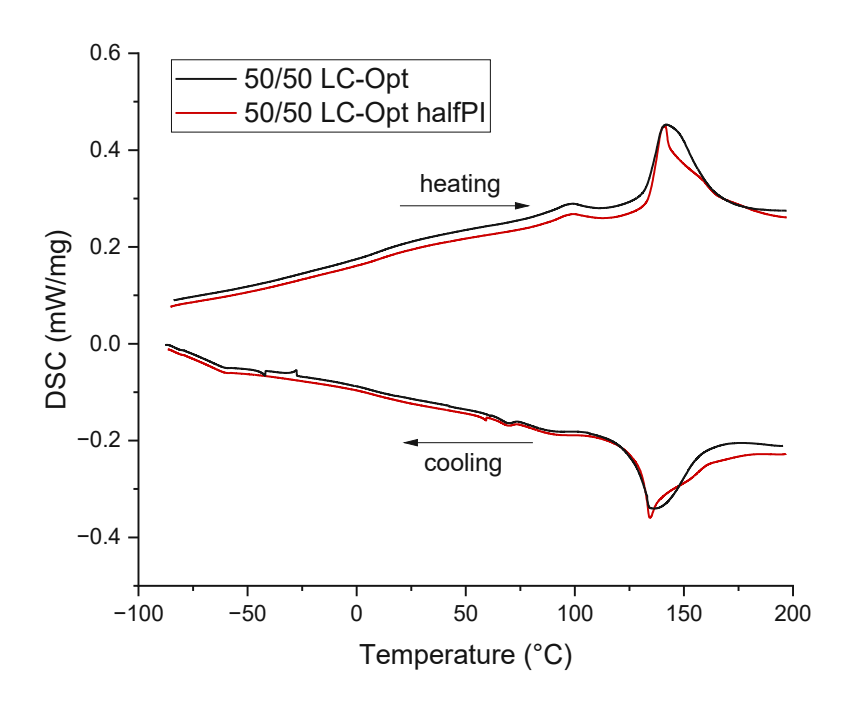


Figure 66: DSC measurements of LCM5-CHTT polymer with optimized curing procedure for a) 1% p and b) 0.5% photoinitiator Ivocerin (endothermal up). The second heating cycle is depicted.

Since the first cycle includes previous thermal history of the sample, the second heating cycle was used for comparison as it is generally considered to reflect a standard thermal history imprinted onto the sample. 141 Since crystallinity is fixed by covalent crosslinks, reformation of crystalline domains is additionally expected to be efficient. The polymer network that contained 1% photoinitiator exhibited a more diffuse melting point, while a smaller amount of photoinitiator led to a sharp onset but a longer tailout of the peak. The sharper peak in the sample containing a lower amount of photoinitiator could signify a more regular crystalline network, which could be formed due to slower polymerization.

A minor peak over a relatively broad temperature range centering around 100 °C was observed for both samples while heating. Since the onset of this peak coincides roughly with the melting point of the LCM5 monomer, it could be a remnant of this transition, which is widened by the immobilized LCM5 molecules in the network, making them unable to melt within a narrow transition temperature range.

The 56/44 ratio of LCM5 to CHTT were originally introduced as a workaround to induce crystallinity in the LCM5-CHTT monomer combination while the curing steps had not sufficiently been optimized. Expectedly, the excess of terminal alkene groups led to incomplete reactive group conversion, which would most likely cause problems with applications like 3D printing, since during the washing step of the printed part, the unreacted monomers could be leached out. As crystallization was successfully induced in the stoichiometrically balanced samples through optimization of irradiation conditions, and their reactive group conversion was found to reach close to 100%, the 56/44 (eq./eq.) composition was not investigated further.

3.1.3.3 Polymerization experiment with aromatic crosslinker

As the cyclic structure and low molecular weight of CHTT had led to the highest stiffness and melting point of any polymer synthesized thus far, an aromatic trithiol crosslinker, 1,3,5-benzenetrimethanethiol (MTSH, Figure 67), was envisioned to exploit the idea of using a stiff trithiol further. Upon synthesis, complete purification was not achieved. Due to potential oligomerization, the purity could not be determined exactly, but was estimated to be around 70%. Nonetheless, a polymerization experiment was attempted. A stoichiometrically balanced formulation of LCM5 with MTSH was subjected to optimized curing conditions (chapter 3.1.3.2), which involve a 300-second initial irradiation at low intensity followed by a final curing step at high intensity for 180 s.

Figure 67: Aromatic trithiol monomer MTSH.

A DMTA measurement of the polymer was performed to compare the thermomechanical properties to the LCM5-CHTT polymers (Figure 68).

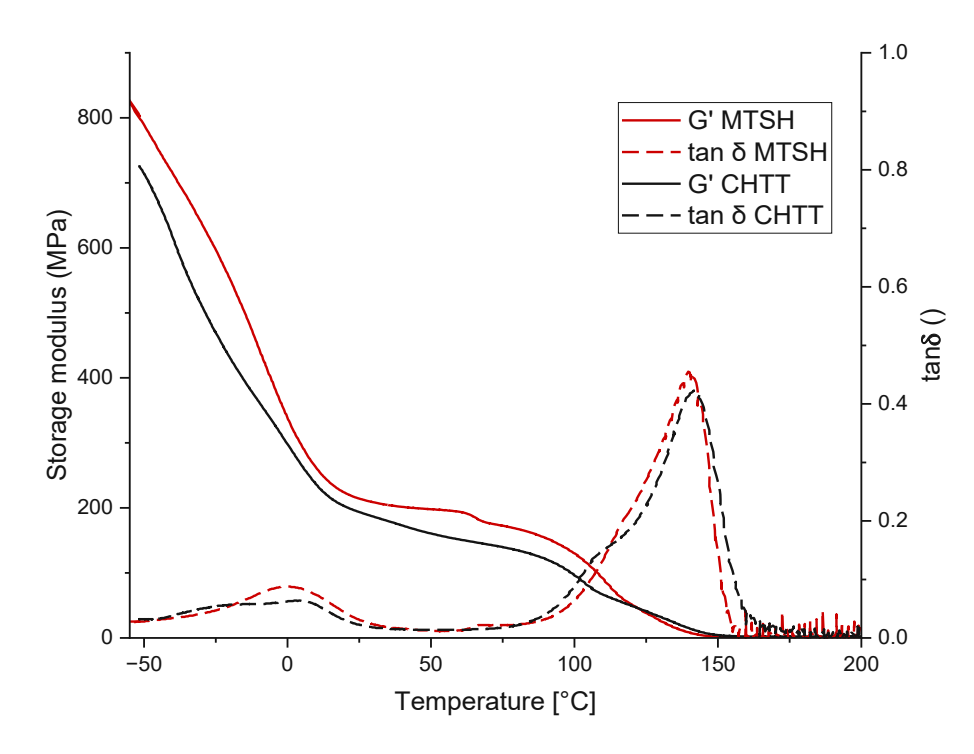
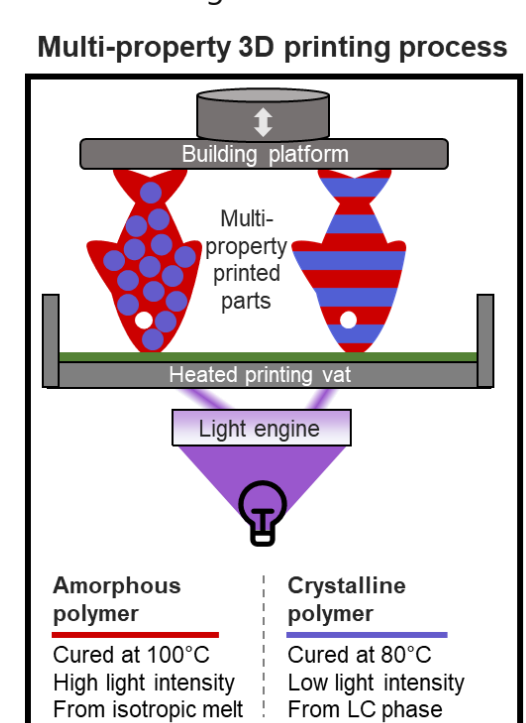


Figure 68: DMTA measurements of the LCM5-MTSH polymer in comparison with the LCM5-CHTT sample, curing conditions optimized for crystallinity according to chapter 3.1.3.2.

The measurement revealed nearly identical thermal behavior of the two polymers, with LCM5-MTSH exhibiting a slightly higher storage modulus throughout the entire temperature range. However, due to the undesirable atom efficiency of the synthesis, the high cost of the reactant and the difficulties with purification, the marginal improvement in stiffness was not deemed sufficient to outweigh the downsides of MTSH synthesis.

3.1.4 3D printing experiments

Bulk tests had revealed that careful tuning of temperature and irradiation conditions during curing could drastically influence the properties of the LCM5-CHTT polymer between those of a soft, transparent material and a hard, crystalline material (Figure 64, Figure 65). To expand upon these promising results, initial tests were conducted that should reveal if this behavior could be reproduced using a Hot Lithography DLP 3D printer. In case of success, it would be possible to not just manufacture various materials from one formulation by varying the conditions, but also to combine these different properties within one printed part (Figure 69). This would enable the fabrication of composite materials such as multilayer or fiber composites for mechanical strengthening. Additionally, specialized optical and shape memory applications could be explored as described in the following.



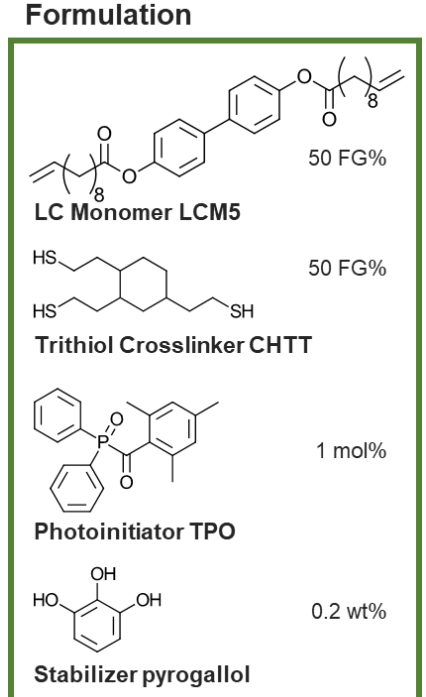


Figure 69: Concept of multi-property 3D printing from one formulation. The formulation is irradiated at varying temperature and irradiation conditions, which induces crystallization at any desired location in the polymer network. The formulation consists of equimolar end groups (50 functional group-%, FG%) of the liquid crystalline monomer LCM5 and the crosslinker CHTT with 1 mol% photoinitiator diphenyl(2,4,6trimethylbenzoyl)phosphine oxide (TPO) and 0.2 wt% of the stabilizer pyrogallol.

3.1.4.1 Initial crystalline and amorphous print test

Initially, the formulation was subjected to preliminary irradiation and stability tests, which were performed directly on the printer. During these experiments, some adjustments to the formulation composition were made, which led to the use of 1 mol% of the initiator diphenyl(2,4,6-trimethylbenzoyl)phosphine oxide (TPO), and four times concentration of the stabilizer pyrogallol compared to bulk formulations. The photoinitiator was changed to potentially enhance crystallinity through a slightly less

reactive initiating system. The higher stabilizer concentration was necessary to ensure stability against spontaneous polymerization due to the high vat temperature over a long period of time during the printing process. Additionally, the light engine of the used printer does not exhibit a perfect contrast between light and dark sections, which causes approximately 1% of the light intensity to reach the sections of the formulations not intended to be irradiated, further harming stability.

To assess which conditions on the printing platform would lead to amorphous and crystalline properties, a temperature gradient was applied to the printing process by changing the vat temperature by 1 °C every five layers, and irradiating two areas in each layer (left half and right half of the vat) at two different intensities (Figure 70). The printed part was cut using a cryo-microtome and analyzed using polarized optical microscopy using a λ -plate. The experiment revealed that crystallites in the printed parts took different shapes on the border between layers compared to within the bulk of one printed layer. Within the bulk of the layer, larger crystallites formed. As expected, crystalline and noncrystalline polymer networks could be generated depending on the printing temperature. Through the variation of irradiation intensity, it was further possible to induce a significant difference in crystallinity with a minor temperature difference as low as 5 °C, for example between 84 and 89 °C. In this case, one part of the sample could be irradiated at 89 °C at high intensity to cure the material in its amorphous network structure, and the other part of the sample could be irradiated at 84 °C to cure the material in its semicrystalline state.

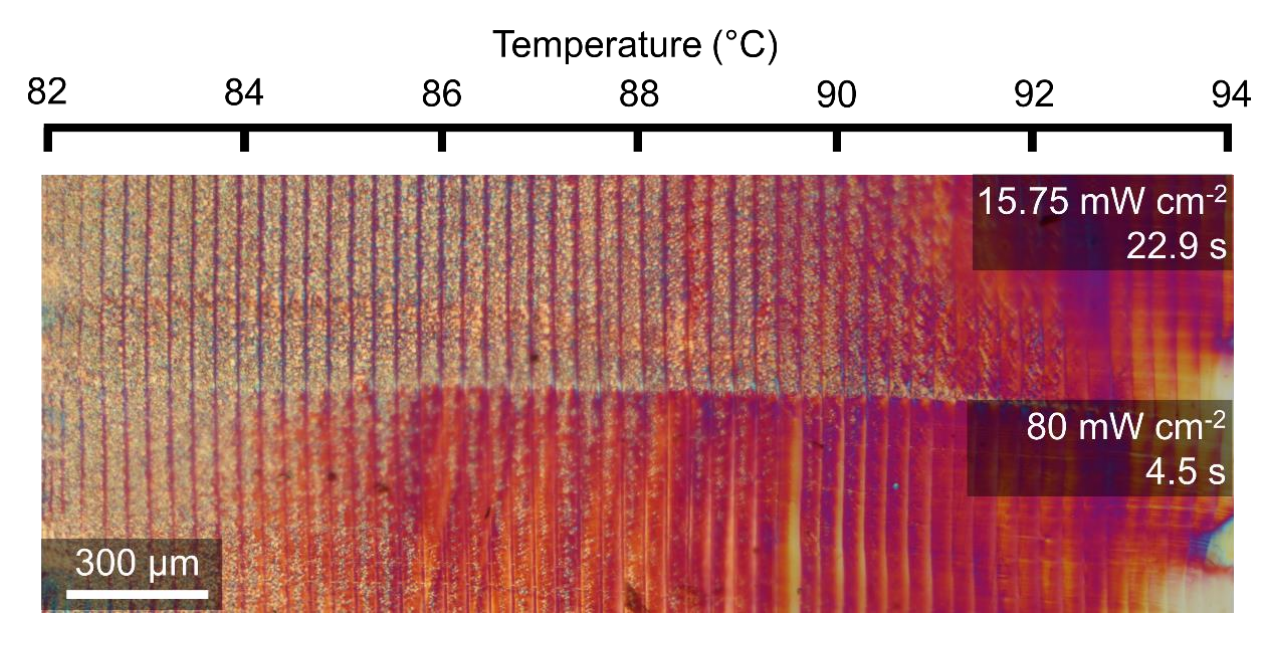


Figure 70: Temperature gradient throughout a printing process with the application of two different irradiation conditions (above: milder irradiation, below: harsher irradiation) and a temperature gradient from 82 °C to 94 °C throughout the process. The image was recorded under crossed polarizers using a polarized optical microscope. To enhance the contrast between crystalline and amorphous areas, a λ -plate was used, which causes the red color of the amorphous parts.

In the following experiment, a large temperature difference between crystalline and amorphous parts was chosen to ensure successful crystallization and amorphization when desired. 1x1 cm resolution test chips with highly tunable transparency were successfully printed (Figure 71). The transparent samples were printed at 110 °C at an irradiation intensity of approximately 80 mW cm⁻² with an irradiation time of 4.5 s. 110 °C was chosen to more closely match the temperature used to cure bulk specimens. The crystalline samples were printed at 80 °C at an irradiation intensity of 15.75 mW cm⁻² applied over a time of 22.9 s, which gives both settings the same irradiation dose.

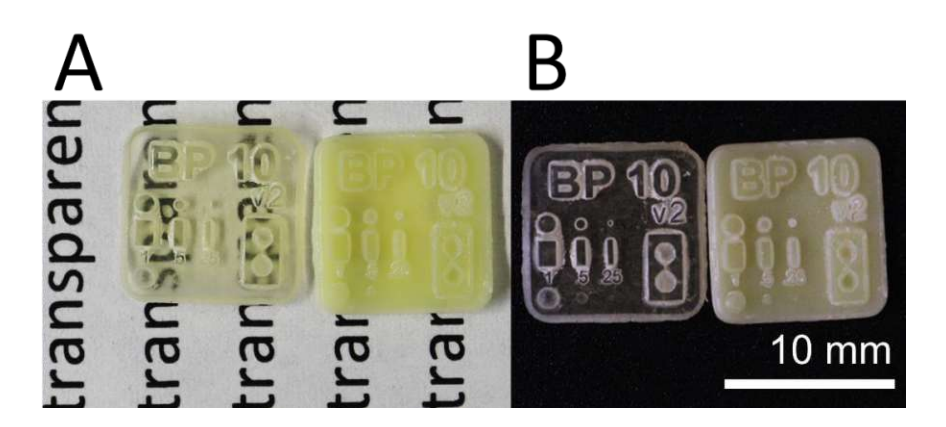


Figure 71: Printed resolution test chips with varying crystallinity cured from the same formulation. In both subfigures A and B, the transparent specimen is on the left and the crystalline specimen is on the right. A) on white paper background with letters "transparent" showcasing sample transparency; B) on black background showcasing print details.

After removal of excess formulation by sonication in toluene, excellent print resolution of the samples was revealed. Minor overpolymerization in the form of oligomers was observed around the letters in the form of white areas, which arises from light scattering and incomplete thermal stability. More aggressive treatment of the samples by longer sonication at higher temperature removed large parts of these white areas, but also caused the samples to swell and deform. Notably, the amorphous specimens had a much lower tolerance to the solvent treatment than the crystalline samples as they started swelling at lower temperatures (approximately 35 °C for the amorphous specimens and approximately 45 °C for the crystalline specimens when sonicated for 4 min). This indicates an enhanced solvent resistance caused by crystallinity, which is likely due to the solvent having to penetrate both the crystallized chains and the polymer network before swelling takes place.

3.1.4.2 Thermomechanical tests of multi-material printed parts

With the successful multi-property printing proof of concept (chapter 3.1.4.1), a test was laid out to determine if a printed composite structure could have a positive impact on the mechanical strength of the printed parts. Therefore, amorphous and crystalline tensile test specimens were printed at 110 °C and 80 °C, respectively, with the precise irradiation

conditions as described in chapter 3.1.4.1 (Figure 72 A). The amorphous specimens exhibited cracks after removal from the building platform and appeared fragile. Therefore, another series of amorphous specimens was printed at 100 °C to test if the lower temperature would have a positive impact on the samples. Subsequently, a five-layer composite structure was manufactured from three crystalline layers printed at 80 °C, and two amorphous layers printed at 100 °C by adjusting the temperature and irradiation conditions during the printing process (Figure 72 B). Of each of these variations, three tensile test specimens were manufactured and tested (Figure 72 C) and their melting points were investigated via differential scanning calorimetry (DSC, Figure 72 D).

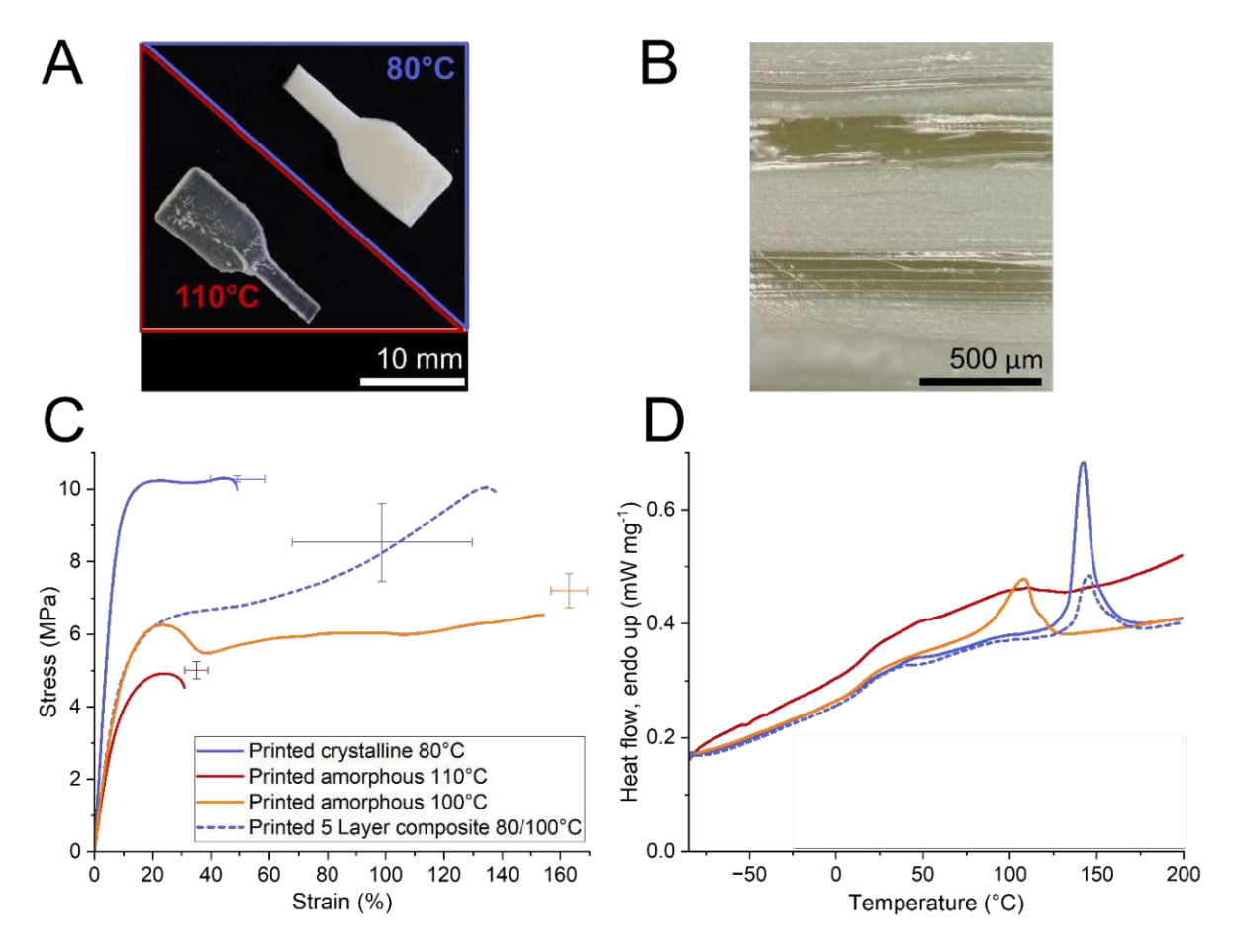


Figure 72: A) Difference in transparency between crystalline (marked blue) and amorphous specimen (marked red). B) Crystalline and amorphous five-layer composite structure achieved by varying the temperature and irradiation intensity within one printing process of a tensile test specimen. C) Representative stress-strain curves of various printed specimens including averages and standard deviations. D) Differential scanning calorimetry of various printed tensile test specimens.

A sharp transition between crystalline and amorphous was achieved in the layered specimen (Figure 72 B). The tensile tests of all printed specimens (Figure 72 C) except the amorphous ones printed at 110 °C performed well compared to the bulk specimens (Figure 65). A relatively tough tensile behavior was observed in all samples with elongations at break above 50% even for the crystalline sample, which is a doubling in elongation at break compared to the bulk specimen at around 15% lower tensile strength. The amorphous samples printed at 100 °C exhibited a pronounced yield point with significant necking before breaking at around 160% elongation. In this case, the printed

and bulk tensile curves closely resemble each other, with the printed samples breaking at slightly lower elongation. The amorphous samples printed at 110 °C performed badly in terms of strength and elongation at break. Potentially, the higher curing temperature led to an incomplete polymerization due to radical recombination and termination reactions occurring quickly after the start of the irradiation. However, as higher temperatures had not led to problems when curing bulk specimens, the exact reason for this behavior is unclear. The five-layer composite successfully combined the mechanical properties of the crystalline and amorphous specimens by exhibiting a less pronounced yield point and a further elongation at higher stresses than the amorphous specimen, which continued until the samples broke at around 100% elongation. The mechanical strength of the printed specimens combined with the tunability of their mechanical properties through composite structures significantly enhances the functionality of this polymer system and proves that complete curing is achieved on the printer without the need for a post-curing process.

Differential scanning calorimetry (Figure 72 D) was used to elucidate the effect of crystallinity on the tensile properties of the samples. A shift in the baseline, which indicates the glass transition temperature, was observed for all samples around 25 °C. A flat melting peak around 100 °C was observed for the amorphous specimen printed at 110 °C, while the amorphous specimen printed at 100 °C displayed a much more pronounced melting point around the same temperature. This indicates that a certain degree of crystallinity is still present even in the amorphous samples, possibly represented by very small crystallites formed post-printing that do not have a significant effect on the transparency of the material. For the samples containing highly crystalline domains (fully crystalline and five-layer composite specimens), a sharp melting point around 145 °C occurred. As expected, the melting peak area of the fully crystalline material was approximately twice as large the melting peak area of the composite. A minor peak around 90 °C in the composite sample could signify the melting point of the crystalline domains present in the amorphous part of the sample.

In addition to the five-layer composite structure, printing of more challenging composite structures was attempted, in which the curing conditions were adjusted between amorphous and crystalline within the same layer. However, the parameters could not be modified successfully to print full tensile test specimens due to lack of formulation stability. Some success was achieved when attempting to print fiber-composite structures. These structures were intended to have amorphous fiber layers in a crystalline matrix to improve toughness. In one attempt, in which a thin fiber structure was printed, every second fiber layer inadvertently turned out to be fully amorphous (Figure 73 A). Potentially, a lack of crystallite nucleation sites could be responsible. However, this still does not explain the occurrence of the phenomenon precisely every second layer. Another composite structure was printed with thicker amorphous fiber sections, which initially did not develop well (Figure 73 B) as during the first half of the printing process, the material was fully crystalline (bottom half of the sample depicted). Afterwards, the cross-section of the sample appears as intended, with rectangular amorphous channels formed throughout the sample. One theory for this phenomenon is that the building platform acted as a heat sink, which lowered the temperature of the formulation significantly enough for crystallites to develop. During the second half of the printing process, the structure developed as intended.

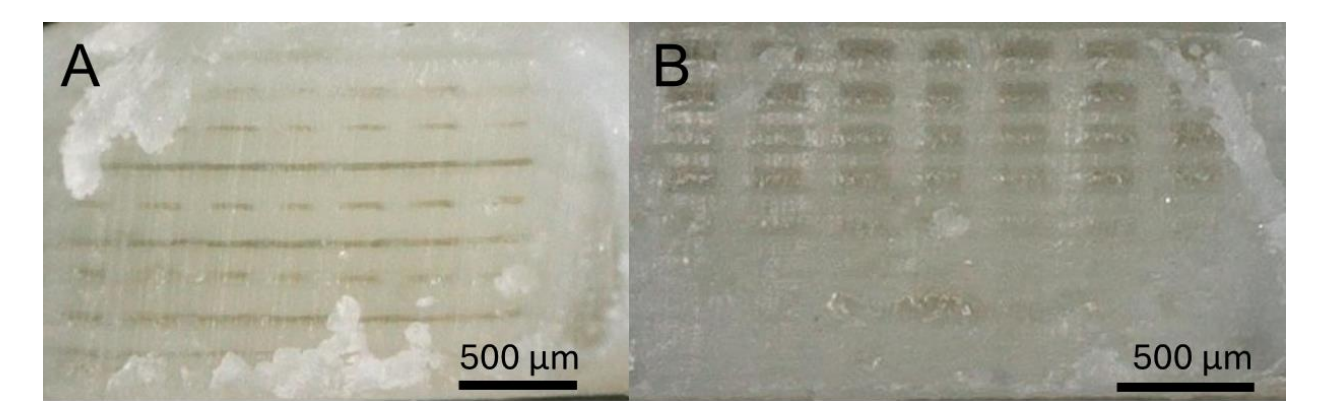


Figure 73: Digital microscopy images of cross-sections of complex composite structures. A) Thin fiber composite structure, in which two layers exhibit an alternating amorphous and crystalline structure followed by eight layers of fully crystalline material. Every second "fiber" layer turned fully amorphous, which was not intended. B) Thick fiber composite structure, in which 50% of the layers are printed with an alternating amorphous and crystalline fiber structure, and the remaining layers are fully crystalline. Initially (bottom half of the picture), the structure did not develop well and only became clearly visible as the printing process progressed.

3.1.4.3 3D printing of functional multi-material parts

Further applications in the optical and cryptography field were explored by varying the temperature and curing conditions within print layers to achieve tunable transparency of the sample. Initial tests involved the printing of a QR code and a "human body with skeleton" specimen (Figure 74). Excellent resolution and contrast between crystalline and amorphous sections were achieved in these tests.

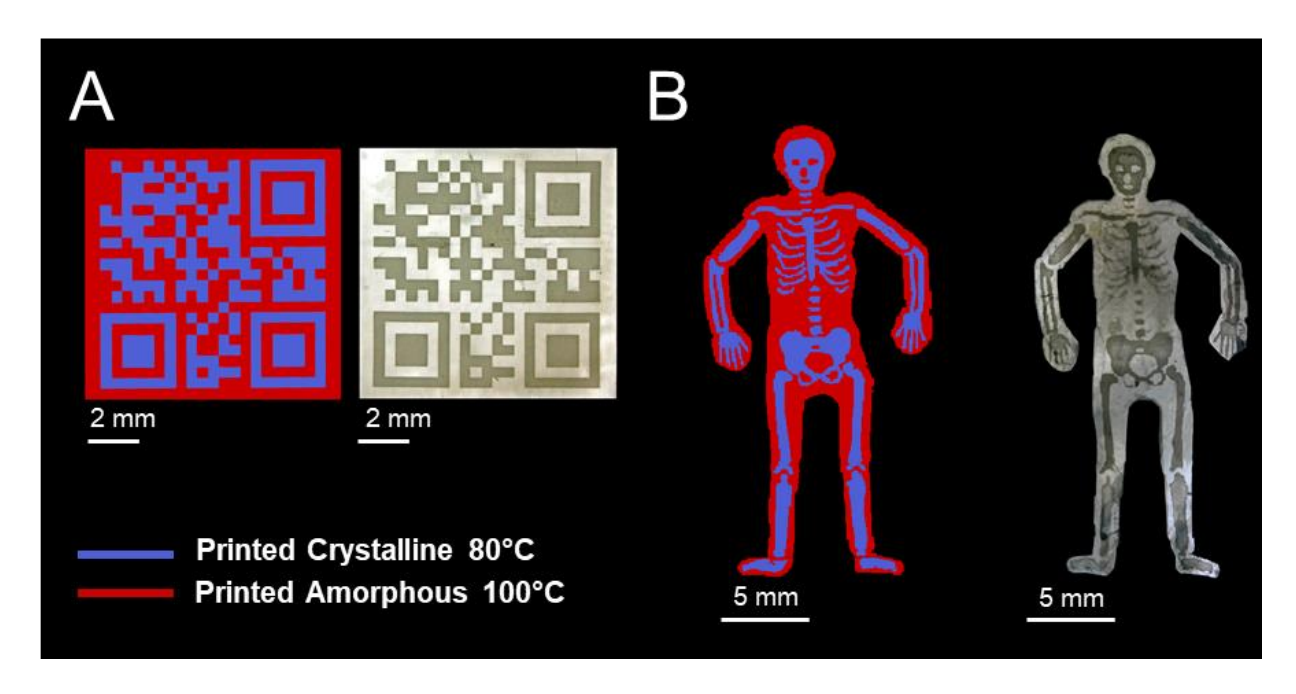


Figure 74: Printing of images by variation of crystallinity. In blue and red color, the digital models are displayed. The images of the printed specimens were recorded on a digital microscope in transmitted light mode. Therefore, the crystalline parts appear darker as they absorb more light than the amorphous parts. A) QR code spelling "3D-Encoding", B) Human body + skeleton model.

An advanced application of this system could be concealing sensitive information. As a proof-of-concept experiment, a 0.5 mm thick QR code was printed on an amorphous base layer. Thereafter, an amorphous buffer layer was printed, and finally, a crystalline layer was again printed to conceal the QR code. Under the right conditions, the QR code is revealed by carefully and evenly heating the crystalline top layer, which causes the crystalline domains to melt. Uniform heating is achieved by placing a glass plate on top of the printed part and heating it from above with a powerful heat source. If done incorrectly by heating the part unevenly or too high, the concealing layer does not melt completely or the QR code melts partially and is not readable.

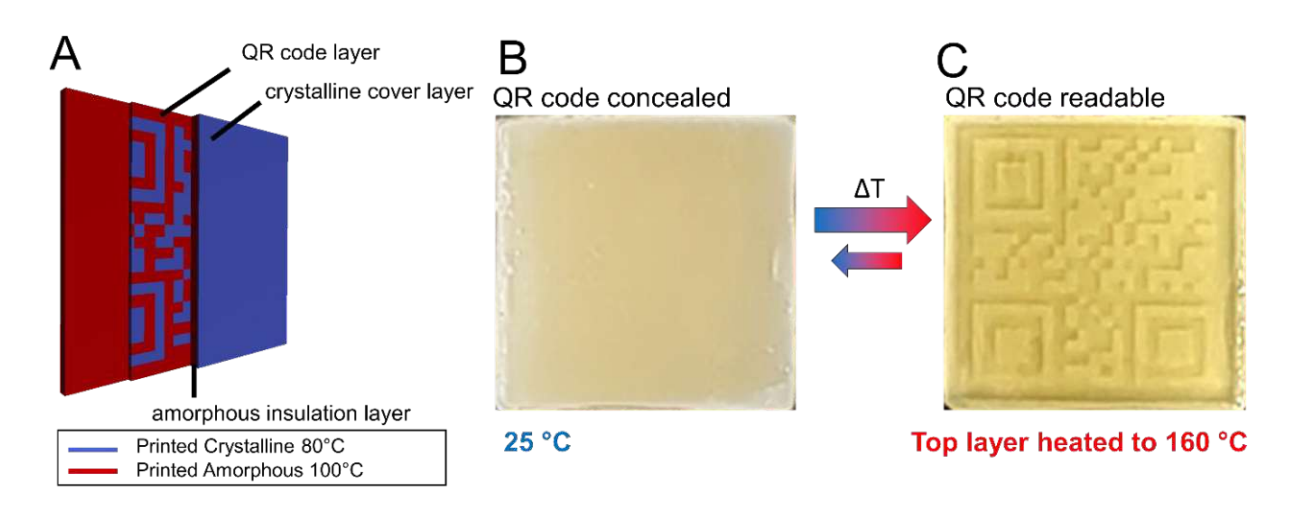


Figure 75: Printing and revealing process of a concealed QR code. A) printed layers of the concealed QR code. B) The QR code in concealed form at room temperature. C) The QR code is revealed by evenly heating the top layer using a heated glass plate placed on top.

Thus far, manufacturing thicker samples with more printed layers using this approach has proven challenging, as the long duration and frequent temperature changes during curing negatively impact the formulation's stability. Further stabilizing the formulation was not an option as accurate control of crystalline and amorphous properties was not possible.

3.1.4.4 Printing of complex structure

To test the conventional 3D printing capabilities of the formulation, a complex shape only achievable through additive manufacturing was printed. For this printing test, crystallinity control was not a priority. Instead, a formulation with a larger amount of the stabilizer pyrogallol was used (0.5 wt%, 2.5 times the usual amount for printing). The reduced reactivity was compensated for with the addition of a larger amount of the photoinitiator TPO (1.5 mol%, 50% higher than the usual amount used for printing). The same irradiation settings used in previous tests to print amorphous specimens were used (chapter 3.1.4.1). With the enhanced stability, a hollow 7x7 mm pyramid was printed at a temperature of 90 °C (Figure 76).

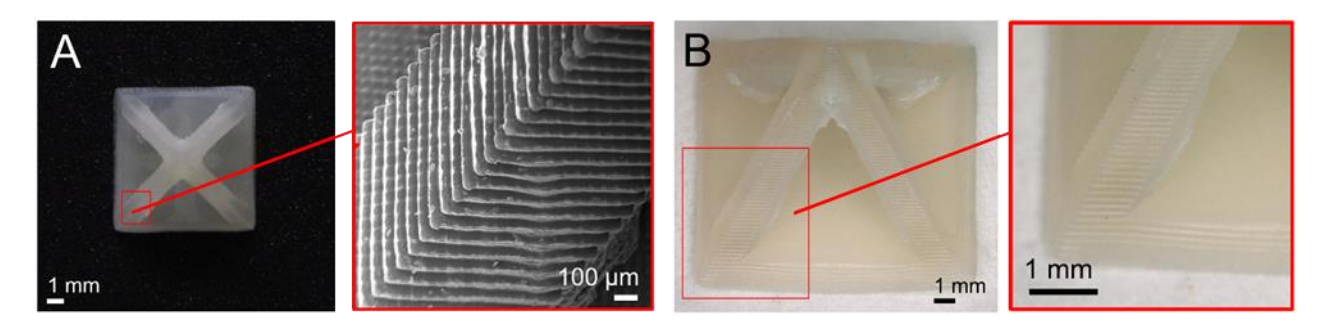


Figure 76: 3D printed pyramid specimen. A) Left: Camera photograph. Right: Scanning electron microscope image. B) Left: Depth-of-field digital microscope picture of the full pyramid specimen. Right: Larger magnification of the base plate and pillar.

The enhanced stabilization of the formulation proved successful, as a much smaller amounts of oligomerized residues were found to be attached to the specimen after printing. After cleaning the pyramid in an ultrasonic bath using toluene, the specimen was investigated using scanning electron microscopy (Figure 76 A, zoom-in), which revealed an even layer formation and pixel-accurate (pixel size 50 µm) curing of the formulation. Some oligomerized residues on the inside of the hollow space were revealed by depthof-field imaging using a digital microscope. Nevertheless, the specimen displayed excellent form stability and layering quality, which proves the capability of the system to be used to create complex three-dimensional objects.

3.2 LCM6-based polymers

The newly developed monomer LCM6, in which the aromatic ether bond was avoided, was combined with various di- and trithiol monomers to test the mechanical properties of the resulting materials (Figure 77).

Figure 77: Thiol comonomers used in equimolar combination with LCM6 to test polymer properties. Two linear difunctional comonomers (HDT, EDDT), two trimethylolpropane-derived trifunctional monomers (TMPMP, ETTMP) and two cyclic trifunctional comonomers (TEMPIC, CHTT) were tested.

Before the screening experiment, a further optimization step was employed to test the impact of a change in photoinitiator on thermomechanical properties, which is the focus of the next chapter.

3.2.1 Photoinitiator study

A previous optimization study (chapter 3.1.3.2) led to the conclusion that an initial lowintensity irradiation followed by a final high-intensity curing step (Table 15) can lead to higher stiffness and tensile strength, which is a result of higher crystallinity.

Table 15: Irradiation parameters for optimized crystallinity of polymer samples from liquid crystalline monomers (lamp intensity relative to maximum performance I%, approximate maximum irradiation intensity I_{abs} , maximum of the wavelength distribution λ_{max} , irradiation duration t).

Irradiation step	Light source	I _% (%)	I _{abs} (mW cm ⁻²)	λ _{max} (nm)	t (s)
Mild initial curing for crystallinity	Hönle LEDcube	5	1.5 ¹	405	300
Final curing step	UVET UV-LED	10	290 ²	365	180

¹ Measured using an EIT Uvicure Plus

This behavior was attributed to reaction exothermicity through rapid generation of radicals as well as energy transferred to the sample through high-intensity irradiation, which can cause the temperature of the formulation to increase beyond the liquid crystalline regime. This hinders the formation of crystallinity in the polymer, resulting in a non-crystalline, transparent and flexible polymer. In contrast, slower curing due to mild irradiation causes polymer crystallinity that develops during the polymerization from the liquid crystalline phase. Through the second high-intensity step, the network is then cured to its final end group conversion.

Over the course of these experiments, lowering the concentration of the photoinitiator concentration (Ivocerin, Figure 78 a) from 1 mol% to 0.5 mol% led to an increase in tensile strength. Therefore, a further attempt to slow down the generation of radicals led to the consideration of utilizing diphenyl (2,4,6-trimethylbenzoyl)-phosphine oxide (TPO, Figure 78 b) as photoinitiator. TPO is another relatively red-shifted initiator that is still considered highly reactive, but less reactive than Ivocerin.

² Measured using a Coherent FieldMax II-TO Laser Power Meter

Figure 78: Photoinitiators Ivocerin and diphenyl (2,4,6-trimethylbenzoyl)-phosphine oxide (TPO).

Since CHTT was the best-performing thiol monomer with previously synthesized LCM5, it was chosen for a preliminary study to test the effect of using TPO instead of Ivocerin. The formulations, each consisting of 50 end group-% terminal alkene and 50 end group-% thiol functional groups with 0.5 mol% photoinitiator, were irradiated under the conditions identified as optimal for crystallinity (Table 15). The samples were then subjected to DMTA measurements (Figure 79).

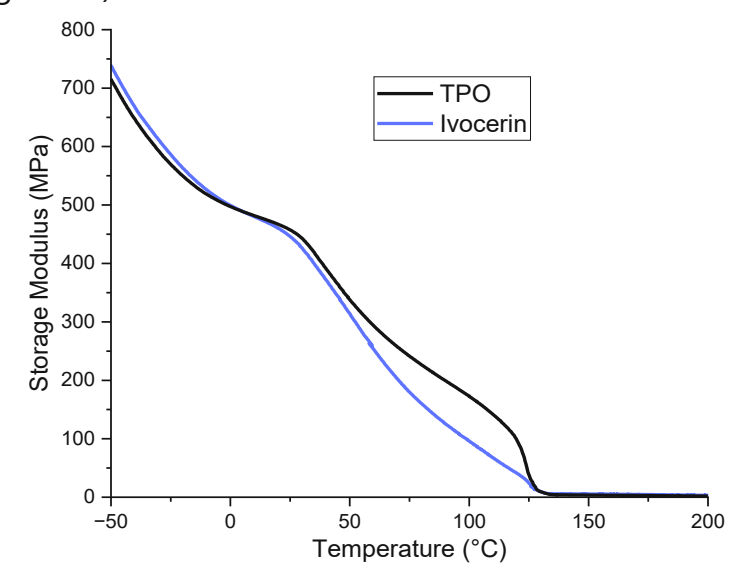


Figure 79: Storage modulus of an equimolar combination of LCM6 and CHTT using photoinitiators TPO and Ivocerin.

The analysis revealed that TPO led to equal or higher storage modulus values within a large temperature range (0-130 °C). The increase in storage modulus is especially pronounced at temperatures above 50 °C, indicating well-formed crystalline domains and identifying TPO as the superior initiator for the purpose of obtaining highly crystalline

polymers. The storage modulus was slightly higher for Ivocerin below 0 °C and above 130 °C. This could be explained by a slightly higher degree of crosslinking, which occurs due to a larger temperature increase during polymerization. This observation also reinforces the theory that crystallization and crosslinking are competing mechanisms.

Since relevant application temperatures for polymers are typically between 0 and 100 °C, the decision was made to utilize TPO for future experiments.

3.2.2 Qualitative evaluation

An initial overview of polymers resulting from the combination of LCM6 with various thiol comonomers was compiled, assessing bulk optical and mechanical properties (Table 16). The molecular weight per functional group (MW per FG) is also listed, which largely determines if liquid crystalline phase formation is disturbed in the formulation. Thereby, less disturbance is expected if MW per FG is lower.

The initial assessment of bulk properties identified CHTT as a promising comonomer as the resulting sample showed respectable strength and stiffness. However, the sample appeared more brittle than other samples that incorporated trithiol monomers, which is why the softer comonomer ETTMP was employed in additional formulation, in which it was used as a in concentrations of 10 and 20 end group-% (which led to CHTT making up 90% and 80% of the thiol end groups, respectively).

Table 16: Overview of qualitative polymer properties for various thiol comonomers in stoichiometrically equivalent combination with LCM6 (by reactive end groups). The molecular weight per reactive thiol end group is listed for correlation with the polymer properties.

Comonomer	MW per FG (g mol ⁻¹ FG)	Bulk optical properties	Bulk mechanical properties
HDT	75	White, fully opaque	Very weak and brittle
EDDT	91	White, fully opaque	Very weak and brittle
TMPMP	133	White, fully opaque	Relatively stiff, weak
ETTMP	350	Almost fully transparent	Soft, elastic
TEMPIC	175	Semitransparent	Semiflexible, weak
CHTT	88	White, fully opaque	Strong, hard, stiff
90% CHTT 10% ETTMP	114	White, fully opaque	Semiflexible, strong
80% CHTT 20% ETTMP	141	White, fully opaque	Semiflexible, strong, tough

Linear polymers resulting from the combination of LCM6 with dithiol monomers HDT or EDDT exhibit the same highly crystalline, but weak and brittle properties that had been observed with the use of LCM5. All trithiol crosslinkers resulted in some crystallinity, which was apparent by the opacity of the resulting polymers, with crystalline properties increasing as molecular weight per reactive group decreases.

3.2.3 Reactive group conversion investigation

Attenuated total reflection infrared (ATR-IR) spectroscopy was employed to gain an overview over the effectiveness of the polymerization reaction of LCM6 in conjunction with various comonomers (Figure 80). For the formation of mechanically strong linear polymers, a near-perfect double bond conversion (DBC) is necessary as in an idealized step-growth polymerization, the chain length increases tenfold between 99% and 99.9% end group conversion. The DBC of the polymer containing TEMPIC as a comonomer could not be measured, since the isocyanurate group exhibits a large signal over the region where the double bond is situated, preventing an accurate calculation.

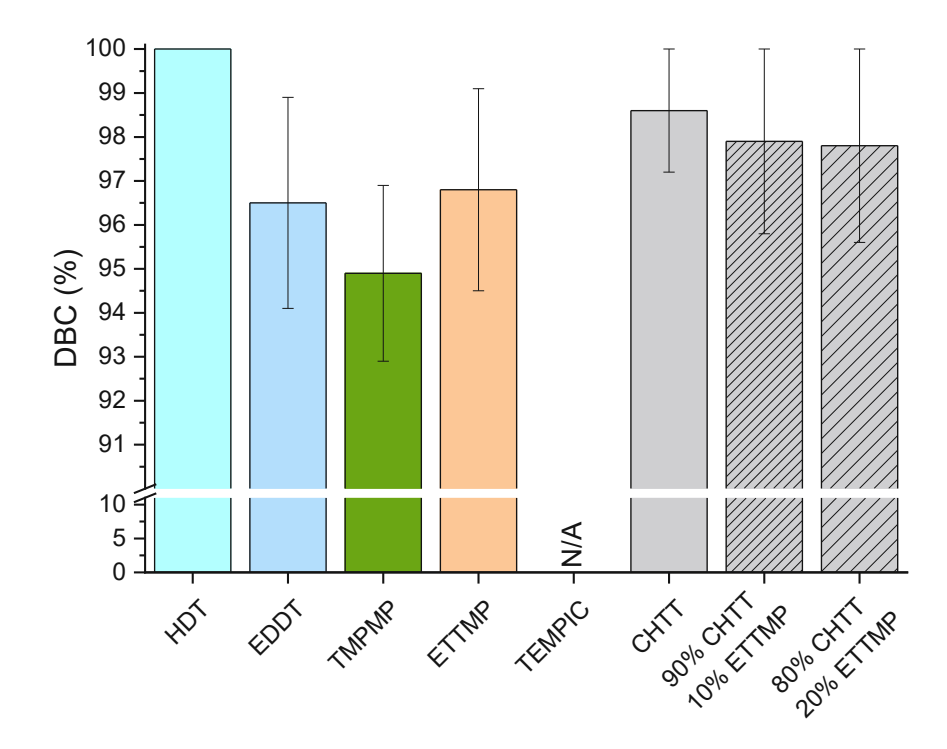


Figure 80: Investigation of double bond conversion in various samples containing LCM6 as the ene component. The DBC of the polymer prepared by combining LCM7 and TEMPIC could not be assessed due to the strong signal of the isocyanurate groups present in TEMPIC.

Across all samples, high conversions above 94% were reached. For the linear polymer obtained from HDT, complete conversion was measured, while EDDT resulted in lower conversion around 96%. However, the brittleness of the linear polymers did not allow for them to be pressed onto the diamond surface as firmly as the other specimens, which reduced the general signal intensity. This, along with a relatively low base sensitivity of the measurement method, likely led to some inaccuracy. As the LCM6-HDT polymer exhibited brittle and weak material properties, it is unlikely that 100% conversion was reached.

The crosslinked polymers exhibited satisfactory conversions. Contrary to linear polymers, a 1-2% change in conversion does not have an as severe negative impact on the mechanical properties, and around 95% conversion can be sufficient to form a strong material. The highest conversion was achieved for the sample containing purely CHTT as

a comonomer. This confirms that high crystallinity did not negatively affect the reactive group conversion by immobilizing the polymer chains during polymerization.

3.2.4 Thermomechanical evaluation

For an initial determination of the thermomechanical properties of the polymers attained from combining LCM6 with different thiol monomers, dynamic mechanical thermal analysis (DMTA) was utilized. This provides insight into the suitability of the polymers as structural materials without performing tensile tests, which consume a much larger amount of monomer. Additionally, DMTA reveals information about the crystallinity of the samples. When crystalline domains are present, two peak maxima are found in the tan δ graph, the first representing the glass transition temperature (T_q) and the second representing the crystallite melting point (T_m). The desired properties are a high storage modulus at room and body temperature (25 °C and 37 °C), and ideally also at higher temperatures.

Measurements were performed for all crosslinked polymer samples (Table 17, Figure 81). Linear specimens from HDT and EDDT could not be clamped into the measurement device without breaking.

Table 17: Key values from DMTA measurements of polymers cured from various thiol comonomers in stoichiometrically equivalent combination with LCM6 (by reactive end groups).

	Tg	T _m	G' at 25 °C	G' at 37 °C
Comonomer	(°C)	(°C)	(MPa)	(MPa)
HDT	1	1	1	1
EDDT	1	1	1	1
TMPMP	12	80	90	54
ETTMP	-27	38	8.6	0.46
TEMPIC	31	87	356	50
CHTT	52 ²	125 ²	458	407
90% CHTT, 10% ETTMP	46 ²	117 ²	279	222
80% CHTT, 20% ETTMP	49 ²	107 ²	164	125

¹Measurement not possible due to the specimens being too brittle to clamp in

²Minor transition

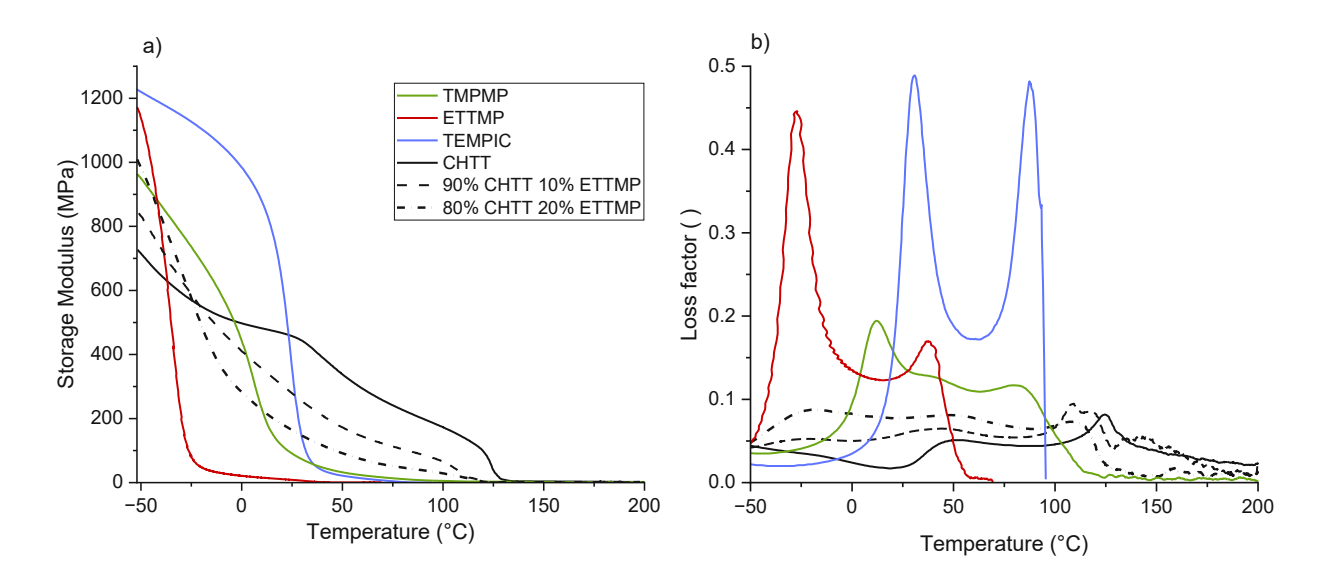


Figure 81: a) Storage modulus (G') and b) loss factor (tan δ) of polymer samples containing LCM6 as the ene component in combination with different thiol comonomers. A smoothing algorithm (adjacent averaging over 10 data points) was applied to the loss factor curves as they displayed significant amount of noise during and after the melting transition.

The samples, in which the crosslinkers TMPMP, ETTMP and TEMPIC were used as the sole thiol component experienced a rapid and extensive decline in storage modulus at their glass transition temperature. A crystallite melting point was only identifiable as a distinct second peak maximum in the loss factor graph, which occurred after the storage modulus had already declined to near zero. Therefore, it can be concluded that the mechanical properties were mostly influenced by the glass transition of the polymer network, and not significantly by the samples' crystallinity. At body temperature (i.e. 37 °C), all three samples exhibited less than 10% of their initial storage modulus.

ETTMP-containing samples showed expectedly low stiffness with a very low glass transition temperature and crystallite melting point. These elastomeric properties were utilized to toughen samples in combination with CHTT.

The polymer networks containing CHTT led to the best results out of all LCM-thiol combinations so far, displaying a relatively high storage modulus at room temperature and body temperature. Their crystallinity led to different DMTA curve shapes compared to most other samples, with a steady decline in mechanical strength up to the crystallite melting point, which was above 100 °C even when the toughener ETTMP was used to substitute the more rigid monomer CHTT partially. The only sharp drop in storage modulus of CHTT-containing materials was observed above the melting point. This mechanical behavior dominated by crystallinity further confirms that the rigidity and low molecular weight of CHTT (causing a high weight fraction of LCM6) is beneficial when trying to achieve a stiff and crystalline polymer system.

When the toughener ETTMP was employed in thiol end group concentrations of 10 and 20 mol% to partially substitute CHTT, it led to a decrease in storage modulus of ~47% and ~67%. This is caused by the long ethylene glycol chains contributing to more elastomeric properties in the polymer.

3.2.5 Evaluation of crystallinity

To identify the number, temperature, and intensity of their phase transitions, differential scanning calorimetry (DSC) was performed for all polymer samples containing LCM6 as well as the pure monomer (Table 18). This elucidates the influence of crystallinity on the

mechanical properties probed by DMTA, which can then inform monomer and formulation design. The measurement graphs of all samples can be found in the Appendix (Figure S 1). For all samples, the second heating cycle was analyzed since a standardized thermal history is imprinted on each sample during the first cycle. Generally, the differences between the first and second heating cycle were minor, which also confirms that the crystalline domains are locked into the network and reform after melting.

Table 18: DSC results of polymers cured from various thiol comonomers in stoichiometrically equivalent combination with LCM6 (by reactive end groups), and of the LC monomer itself: phase transition temperatures (T_{PT}) and corresponding transition enthalpies (ΔH).

Ene-monomer	Thiol comonomer (s)	T _{PT} (°C)	ΔH (J g ⁻¹)
LCM6	/	104, 173	52.3, 5.1 ³
LCM6	HDT	140, 158	14.3, 3.3 ³
LCM6	EDDT	110, 144	26.1, 2.5 ³
LCM6	TMPMP	$(12)^2$, 100^1	1
LCM6	ETTMP	$(-34)^2$, 70.6	11.0
LCM6	TEMPIC	$(37)^2$, 80^1	1
LCM6	CHTT	120	13.2
LCM6	90% CHTT, 10% ETTMP	117	10.6
LCM6	80% CHTT, 20% ETTMP	116	5.5

¹broad and very low peak, no meaningful baseline correction possible

Linear polymer samples using HDT and EDDT as the comonomer exhibited a melting point and a liquid-liquid phase transition from liquid crystalline to isotropic, confirming the presence of a liquid crystalline phase for polymer melts. In the case of the combination of LCM6 and HDT, the polymer melting point was significantly above the monomer melting point, which could point to higher chain lengths. Use of EDDT led to a melting point very close to the monomer itself, and the overall appearance of the DSC graph also closely resembles the monomer. This led to the assumption that only short polymer chains had been formed.

²Glass transition temperature signified by a baseline shift

³LC→I transition

For all crosslinked samples, crystallinity was observed via DSC in the form of a melting point peak. This peak appeared at a lower temperature than the pure monomer in the case of polymers derived from TMPMP, ETTMP and TEMPIC. The peak shifted to higher temperatures than the monomer melting temperature in the case of comonomer CHTT and mixtures of CHTT and ETTMP. The temperatures of the transitions align well with the DMTA results.

A glass transition, indicated by a shift in the baseline, was observed for polymers containing comonomers TMPMP, ETTMP and TEMPIC, matching the transition temperatures measured via DMTA. An analogous transition was not found in samples that contained CHTT as the main comonomer. This correlates with DMTA results, where the glass transition exhibited a much more significant impact on the mechanical properties compared to the melting points for TMPMP-, ETTMP- and TEMPIC-containing polymers.

To obtain the degree of crystallinity in the polymer (D) as a percentage, the assumption was made that the thiol comonomer would not contribute to the polymer crystallinity. Therefore, the weight percentage of LCM6 in the formulation was introduced as an additional factor. The exact calculations are described in the experimental part (chapter 3.2.5).

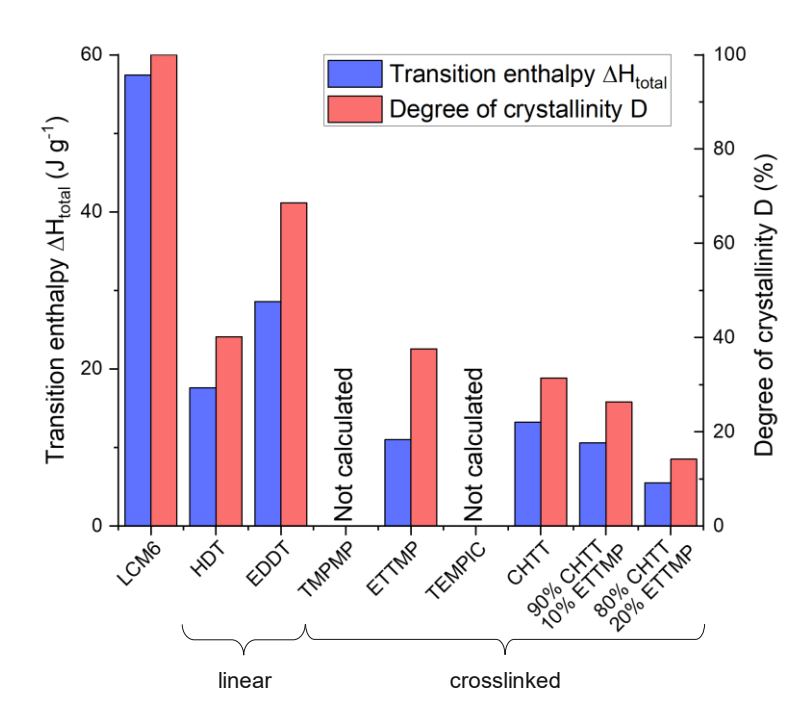


Figure 82: Transition enthalpy and degree of crystallinity of various polymer samples containing LCM6 as an ene monomer. No transition enthalpy and crystallinity could be calculated for samples containing TMPMP and TEMPIC as comonomers as the DSC peaks were broad and flat and did not allow for baseline correction.

The linear polymers created by using HDT and EDDT as comonomers gave the highest measured crystallinity, which can be explained by the higher mobility of non-crosslinked polymer chains, allowing for crystallization to occur. LCM6-HDT exhibited a lower degree of crystallinity while having a much higher melting point than the monomer itself, which could be attributed to a higher chain length. In contrast, polymerization of LCM6 with EDDT resulted in a very high degree of crystallinity at a lower melting point, likely due to the low chain length suspected earlier.

For the networks obtained by employing the trifunctional thiols TMPMP and TEMPIC, a baseline correction and thus degree of crystallinity calculation was not possible due to a broad and flat transition peak.

A high degree of crystallinity was calculated for the polymer containing purely ETTMP as the comonomer. It exhibited an initially broad phase transition with a sharp peak at the end of the transition. This high crystallinity in conjunction with the sample's low stiffness

points to the presence of a structure of localized crystalline centers surrounded by a soft matrix, akin to raisins in a cake. Hence, the crystalline centers do not provide a significant increase in mechanical strength and stiffness, yet still result in a high transition enthalpy. Furthermore, a large fraction of the polymer-incorporated LCM6 is allowed to crystallize because it is embedded in a soft, mobile matrix. The melting point determined via DSC (71 °C) was much higher than the melting point measured via DMTA (38 °C). Since the DSC melting point signal is very broad with an incline in the curve starting around 37 °C, it is possible that the lowest temperature at which crystalline regions start melting could lead to a significant increase in the samples' flexibility, explaining the decline of sample stiffness already at low temperatures. The bulk of the crystalline regions melts after this decline in flexibility, explaining the discrepancy.

LCM6-CHTT exhibited the highest transition enthalpy of all the polymer networks, which matches its behavior in DMTA measurements, where crystallinity influenced the thermomechanical behavior, causing a significant level of stiffness to remain above the glass transition temperature. When ETTMP was used as a toughener, substituting CHTT in end group concentrations of 10 and 20 mol%, the transition enthalpies and degrees of crystallinity decreased. 10 FG% ETTMP saw a minor decrease in crystallinity of about 10% compared to pure CHTT as comonomer. 20 FG% decreased the crystallinity by more than 50%.

3.2.6 Mechanical tests

Tensile tests were performed for a selection of samples that exhibited the best results during the initial DMTA study due to the effort and cost of LCM6's synthesis. CHTTcontaining polymers were identified as most promising candidates for tough photopolymers (Table 19).

Table 19: Tensile test results of formulations containing LCM6 as the ene component, and various combinations of CHTT and ETTMP as the thiol component.

Co-monomer	Tensile strength (MPa)	Elongation at break (%)
100% CHTT	18.7±1.7	4.1±0.4
90% CHTT, 10% ETTMP	12.9±0.4	13.0±1.7
80% CHTT, 20% ETTMP	12.8±0.9 (9.8±0.2 ¹)	$204.9 \pm 10.9 (10.9 \pm 0.3^{1})$
100% ETTMP	4.6±0.4	45.2±9.3

¹at yield point

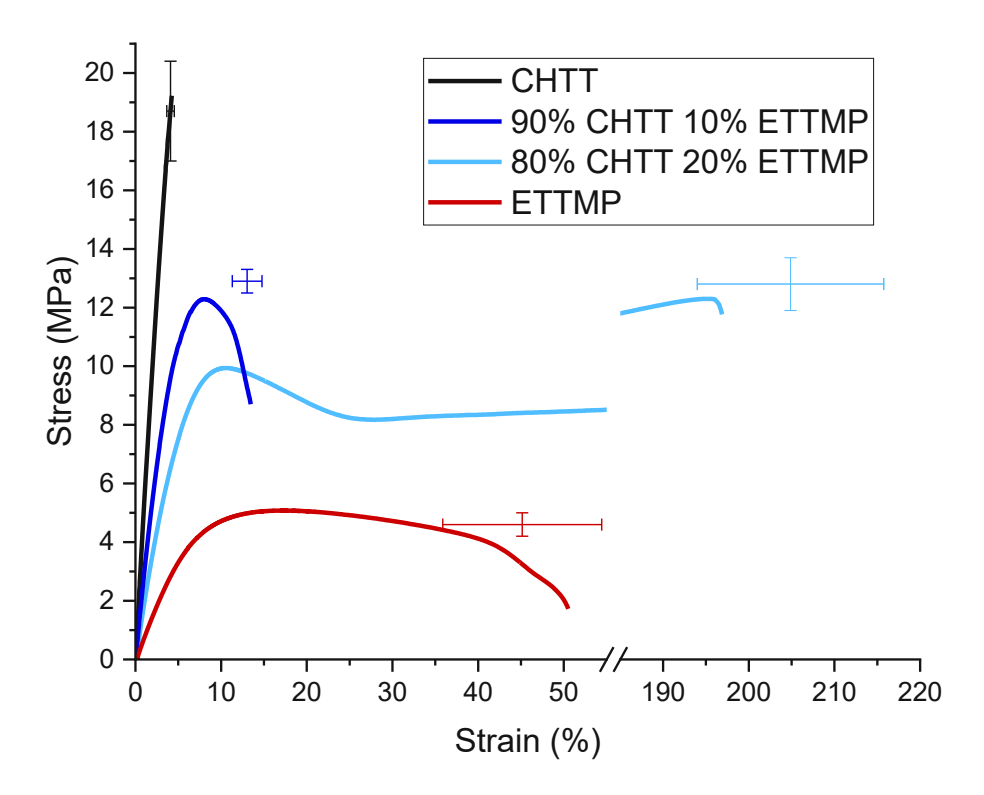


Figure 83: Tensile test curves of polymer samples comprising LCM6 as the sole ene component with different combinations of CHTT and ETTMP as comonomers.

Using LCM6, the highest tensile strength of any sample using a liquid crystalline enemonomer was achieved. This came at the cost of some toughness. To compensate for this, ETTMP was successfully employed as a toughening agent. At a thiol group concentration of 10%, it led to a tripling in elongation at break at the cost of ~30% of tensile strength. Upon further addition of ETTMP at a thiol group concentration of 20%,

the brittle fracture behavior changed into tensile properties akin to semicrystalline thermoplastics, with a pronounced yield point and a necking elongation that ends in a maximum of the tensile strength at the point of fracture. The sample using ETTMP as the only thiol component showed much worse tensile behavior than the other samples for both stress and strain. It is possible that a strong phase separation of soft, amorphous phases and hard, crystalline phases had a negative effect on these properties. Through DSC, a high degree of crystallinity was observed, which contrasted with the elastomer-like mechanical behavior but matched the opaque appearance of the polymer. Therefore, it was assumed that the crystalline domains in the polymer did not form a continuous matrix but rather large isolated domains, which did not have a positive effect on the mechanical strength of the polymer.

3.2.7 Micro- and nanostructural evaluation

Atomic force microscopy (AFM) was employed to elucidate the nanostructure of the tensile test samples tested in chapter 3.2.6. Due to a preliminary measurement showing a strong directional texture (Figure 84), pieces of a tensile test sample were embedded in a transparent epoxy resin in three different orientations for sample preparation to further investigate for signs of anisotropy in the samples (Figure 85).

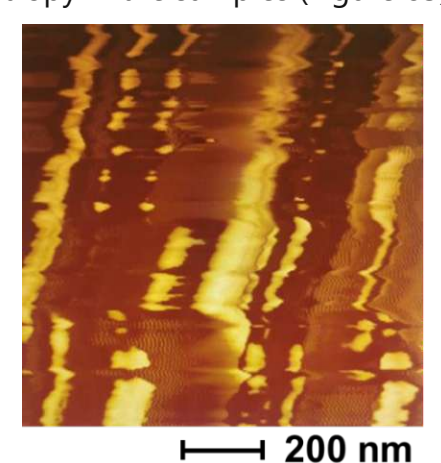


Figure 84: Preliminary AFM experiment of polymer cured from LCM6 and CHTT, which shows signs of phase separation (bright and dark areas) and directional texture.

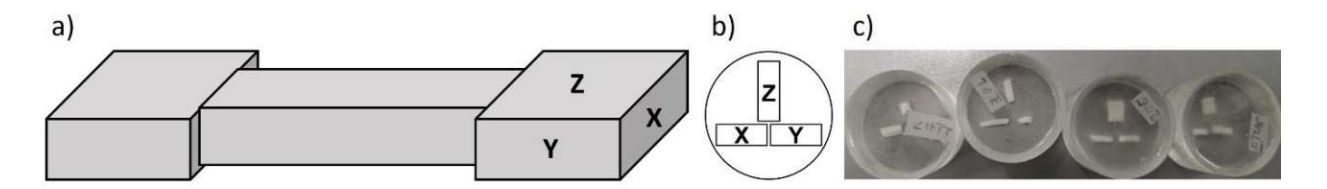


Figure 85: Sample preparation of AFM samples. a) Orientation of tensile test specimens measured by AFM. b) Orientation of test specimen pieces in resin. C) Resin-encased pieces of tensile test specimens.

Reflected-light microscopy images were taken after the grinding and polishing procedure to ensure that the sample preparation had been successful (Figure 86). Satisfactory surface flatness was achieved for all samples. LCM6-CHTT showed a generally smooth surface while the samples with 10 and 20% ETTMP contained a number of small cavities, which could either be microscopic gas bubbles, or, potentially, weakly integrated regions of the network that were removed during sonication. For LCM6-ETTMP, a larger-scale texture was identified (Figure 86 d). Brighter features above 1 µm in diameter were found scattered across the sample. This texture supports the suspicion derived from DSC measurement and tensile test results that a "raisins-in-cake" type structure of larger crystalline areas in a soft matrix could be present.

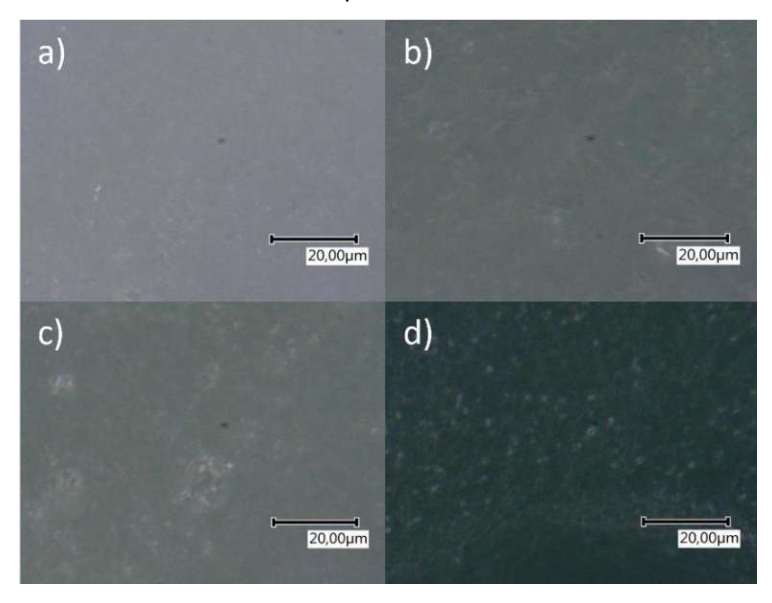


Figure 86: Sample surfaces after grinding and polishing to produce a smooth surface for AFM measurement. a) LCM6-CHTT, b) LCM6-CHTT with 10 mol% ETTMP end groups substituting CHTT, c) LCM6-CHTT with 20 mol% ETTMP end groups substituting CHTT, d) LCM6-ETTMP.

Tapping mode AFM was used to analyze the tensile test specimens tested in the previous chapter. Phase imaging was used to analyze the sample microstructure in conjunction with topography imaging. Phase imaging reveals differences in modulus of the surface while topography imaging is employed as a comparison to ensure that topographical features visible in phase imaging are not overinterpreted as phase features (Figure 87). Across the samples, no x/y/z-directional differences were found. Therefore, the anisotropic texture found during the initial measurement was likely an effect of an unoptimized surface preparation.

The darker areas of the images are most likely the harder segments of the sample, while the lighter areas are softer segments. Therefore, judging from the AFM measurements, a hard matrix encasing softer segments appears to be the prevalent microstructure for all samples except LCM6-ETTMP.

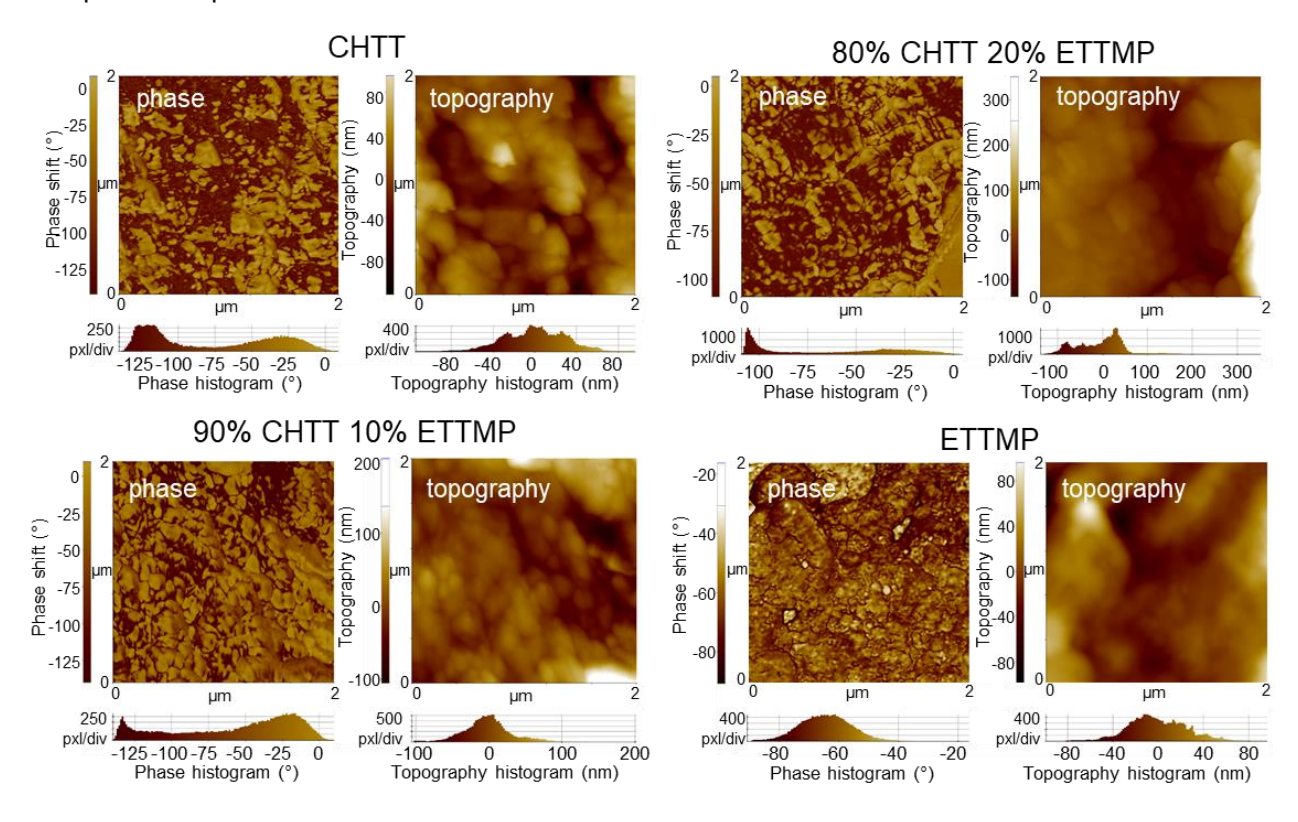


Figure 87: AFM phase and topography micrographs of polymers cured from combinations of the thiol comonomers CHTT and ETTMP in stoichiometrically equivalent formulations with LCM6 (by reactive end groups).

By applying a particle model to the images, an approximate calculation of the fraction of hard and soft segments in the images could be made. Due to a lack of phase separation in the pure ETTMP specimens, this type of calculation was not possible for this sample. In case of LCM6-CHTT, around 44% of the area of the image was found to be made of the lighter-colored soft segments. Upon substituting CHTT with ETTMP, amounting to 10 mol% thiol end groups, the soft segment area was calculated to make up around 63% of the image area, and for 20 mol% ETTMP end groups, around 50% of the image area was found to be made of soft segments. No steady decrease of hard segments was found across these three samples with an increase of ETTMP-content. This is partially due to the measurement conditions being adjusted for each sample. Therefore, it is possible that the harder segments in case of 20 mol% ETTMP were much softer than the ones in the pure CHTT sample. An absolute value could be determined in the future by punctual forcedistance spectroscopy of multiple points of each image.

The histograms of phase angles of the images are compared in Figure 88. In the highly phase separated LCM6-CHTT, the dark-colored harder features form a much bigger peak than in the other samples. Therefore, a strong phase separation with predominantly hard phases can be assumed, which is in line with the fact that this sample contains the highest weight fraction of LCM6. In the 10 mol% ETTMP-containing sample, a higher interface and a larger light-colored soft phase peak is visible, while with 20 mol% ETTMP, the hard phase peak is considerably closer to the soft phase peak on the right side. No phase separation was found for the 100% ETTMP sample. Potentially, much larger-scale separation between crystalline and non-crystalline areas occurs in this sample, as suggested earlier by the reflected light microscopy image (Figure 86). These soft and hard areas would be too large to measure via AFM.

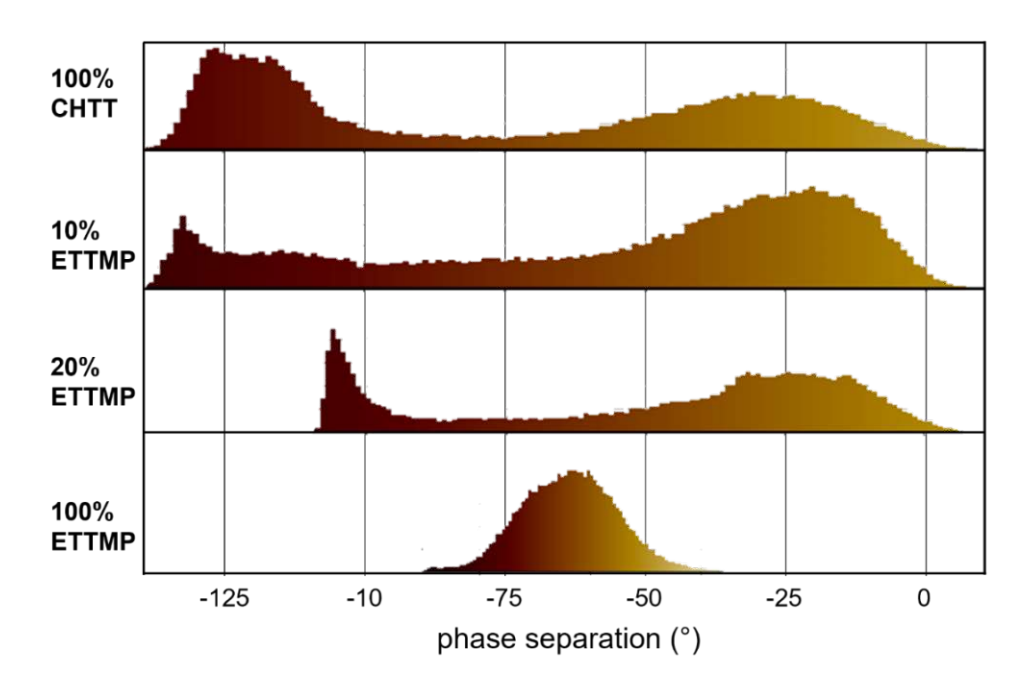


Figure 88: Comparison of phase separation of four AFM images.

Some caution is necessary when analyzing these results, as the degrees of phase separation must not be taken as absolute values due to individually changing measurement conditions for each sample to allow for detection of phase separation at varying scales of modulus-differences between hard and soft domains.

3.2.8 Shape memory evaluation

The formulation employing 100% CHTT as a comonomer was investigated for shapememory properties, as it is a trait that is often found in crystalline networks like liquid crystalline elastomers. 142 In an initial experiment, it was determined that after deformation at high temperature and subsequent cooling of a tensile test specimen, the material did indeed return to its original shape after reheating. Therefore, a quantitative test of shape memory properties was laid out (Figure 89). A tensile test specimen was clamped into a DMTA device and heated to 140 °C (i). The sample was elongated until the parallel section of the sample reached 50% elongation (ii). Then, the sample was cooled to room temperature while the elongation was held (iii). The tension was released, which caused the sample to contract slightly. The percentage of elongation that stays persistent in this

step is known as the shape fixity ratio. 143 Then, the sample is heated once again to 140 °C (v), which causes the specimen to assume its initial shape. The percentage in shape recovery in this step is known as the shape recovery ratio. 143 After this process, the cycle is repeated multiple times. Usually, the so-called training phenomenon causes the first two or three cycles to have worse recovery, after which the final shape recovery capabilities are reached. 144 A total of five shape memory measurement cycles were performed on two different samples.

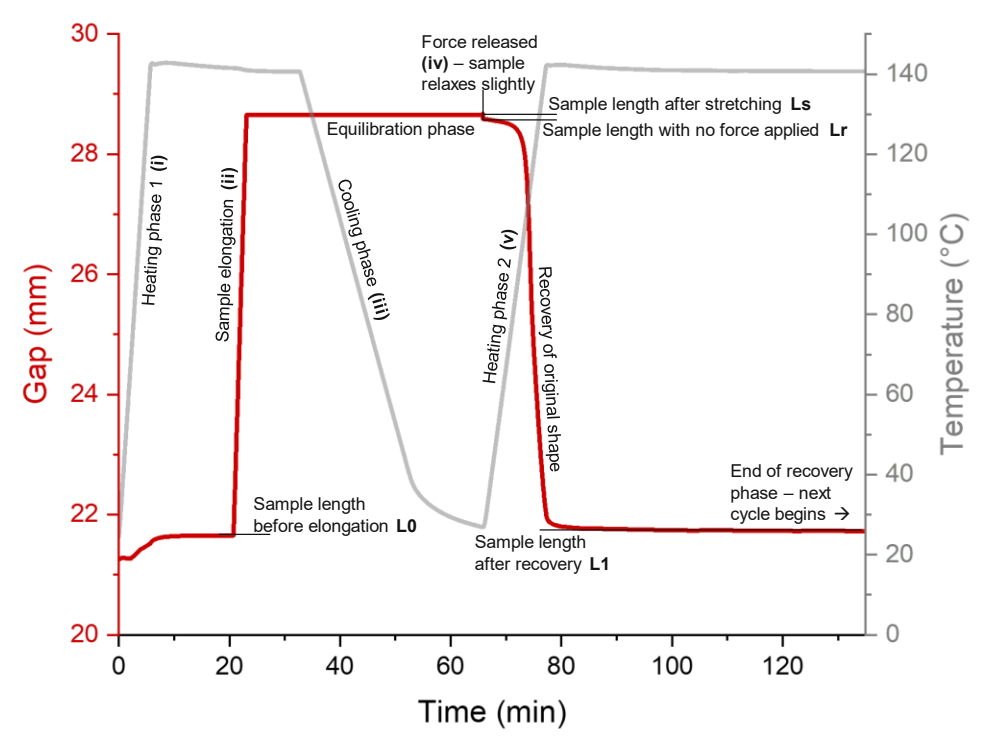


Figure 89: Details of one cycle of shape memory testing.

The shape memory tests resulted in excellent shape memory and recovery capabilities. One experiment with seven cycles is depicted in Figure 90. The rest of the cyclic measurements are depicted in the appendix (chapter 2). In the measurement depicted herein, the training effect is distinctly visible, with a sharp increase in the quality of shape recovery throughout the first three cycles. The shape fixity ratio was high throughout the entire measurement. These results confirm the capability of the polymer to be deformed into arbitrary shapes with the capability of recovery into its original shape through a

temperature stimulus. Throughout all measurements, the average shape fixity ratio was 99%, which signifies a near-perfect capability of deformation into any shape, as 99% of the applied deformation is persistent after cooling. The average shape recovery rate was measured at 97%, which means that the original shape was nearly fully recovered upon a thermal stimulus, confirming the material's suitability for shape memory applications.

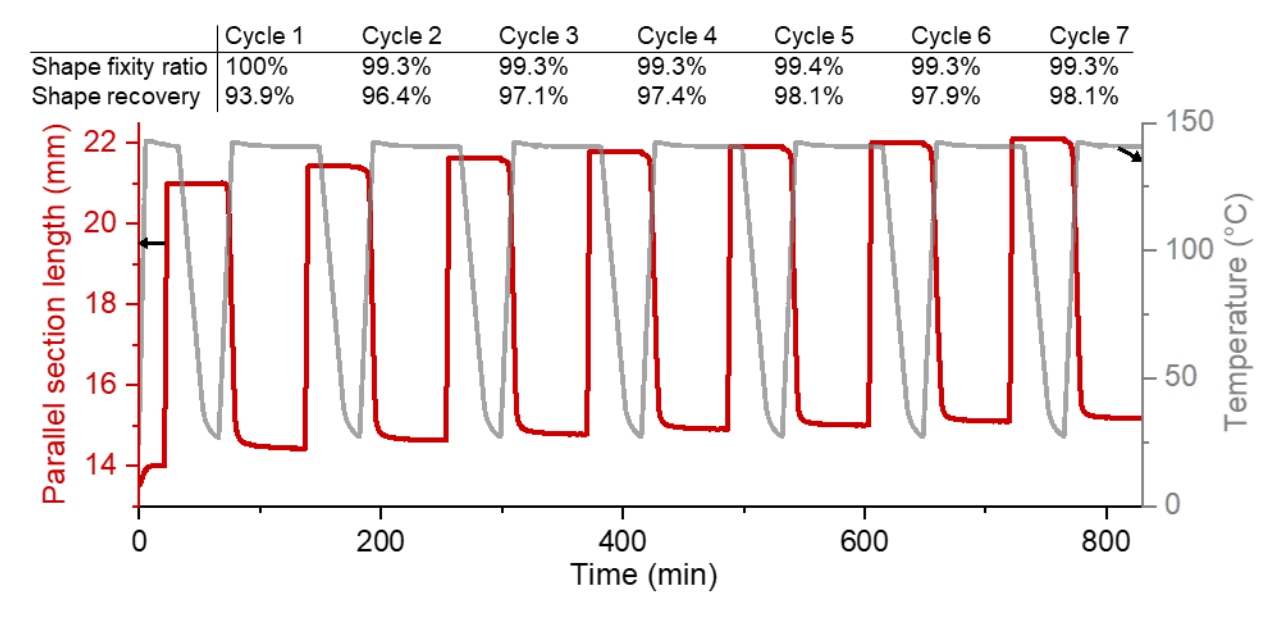


Figure 90: First shape memory test of the second sample tested. Seven cycles were performed. The shape fixity ratio and shape recovery ratio are listed in the table above each cycle.

3.2.9 3D printing experiments

Since the combination of LCM6 and CHTT had already been proven to exhibit great mechanical strength as well as shape memory capabilities, a further step towards smart material applications would be successful additive manufacturing of the material. To test this, several pyramid specimens and a resolution test chip were printed (Figure 91).

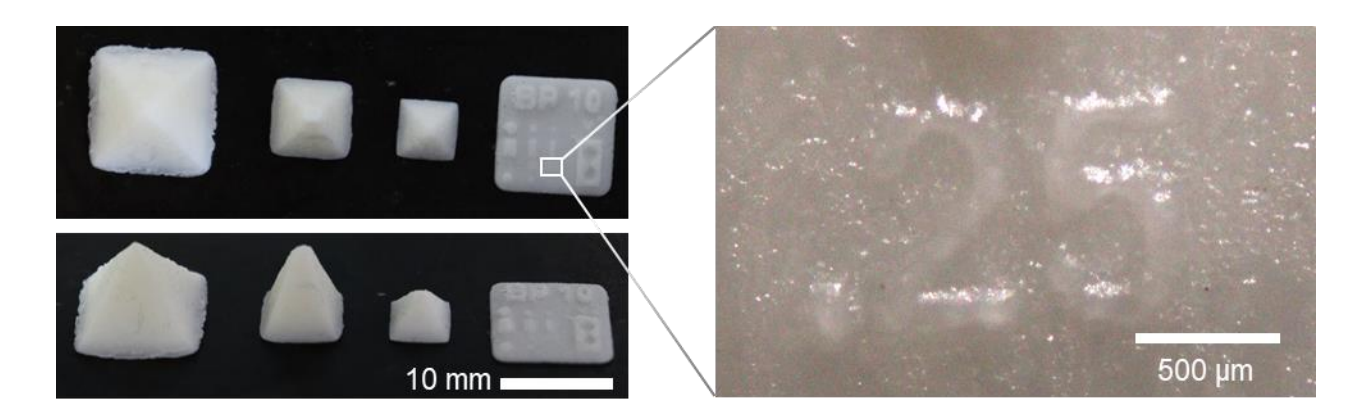


Figure 91: 3D printing of formulation from LCM6 and CHTT.

Generally, good layer formation and resolution were achieved. The text depicting ".25" on the zoomed image has a font thickness of 125 µm, which is resolved in good detail. To remove excess partially oligomerized formulation, a relatively aggressive cleaning procedure had to be employed, in which the specimens were submerged in toluene and sonicated for 5 min at 45 °C. This caused some of the finer details of the pyramid specimens, like the tips, to become rounded.

To combine the advanced applications of shape memory and 3D printing, a spiral-shaped specimen was printed, which was tested for its shape memory capabilities (Figure 92). The specimen was heated to 140 °C. Upon softening of the material, it was stretched into a straight shape and held in this shape until it cooled. Upon reheating, the spiral shape was restored successfully. The experiment was repeated 20+ times. Typically, after 3-4 cycles, the force of the tweezers would break a piece off the specimen, but this did not negatively impact the shape memory capabilities.



Figure 92: Shape memory test of a 3D printed specimen.

3.2.10 Linear polymer conversion study

Thus far, linear polymers made from LC monomers did not exhibit satisfactory mechanical strength. Typically, they would be relatively hard and crystalline but break and crumble at very low mechanical strain. The likely reason for this is a low polymer chain length, which is insufficient to achieve the typical desired properties of strong linear polymers. Additionally, very high crystallinity with strong LC-LC-group interaction likely contributes to this brittleness. Bowman et al. have achieved high chain lengths and good mechanical properties in a semicrystalline polymer by combining the monomers 1,6-hexanedithiol and diallyl terephthalate. Their proposed explanation for the development of long chains an initial fast thiol-ene step growth followed by a slower, continued homopolymerization of the remaining allyl ester end groups.⁵³

To test for potential improvements of the molecular weights of LCM-containing polymers, a study was designed, which should investigate a variety of parameters such as photoinitiator type and concentration, curing temperature, and irradiation time and intensity, which could all potentially affect polymer chain length. The chain length should be analyzed by using gel permeation chromatography (GPC).

3.2.10.1 Variation of photoinitiator and curing temperature

The first test of parameters saw five different formulations comprising an equimolar combination of freshly purified monomers LCM6 and 1,6-hexanedithiol (HDT), in which the photoinitiator type and concentration was varied (Figure 93) and irradiated at three different curing temperatures. The previously optimized irradiation parameters described in chapter 3.1.3.2 were used for the first set of tested conditions, which consist of a 300second low intensity irradiation (1.5 mW cm⁻²) followed by a 180-second final curing step at higher intensity (290 mW cm⁻²).

2,4,6-Trimethylbenzoyldiphenyl phosphine oxide (TPO), which is a monoacyl phosphine oxide photoinitiator commonly used in industry, was used in concentrations of 1 mol% and 0.5 mol%. The photoinitiator Ivocerin, a very reactive high-wavelength initiator developed for dental applications, was used in concentrations of 1 mol%, 0.5 mol% and 0.25 mol%. When testing the phase behavior of the formulations on a polarized optical microscope, the solid-LC transition temperature was identified at ~85 °C, and the LCisotropic transition at ~120 °C. Hence, 90 °C was chosen as the lowest possible temperature at which the formulation would reliably be present in a molten liquid crystalline state. 100 °C, which is close to the melting point of the pure LCM6 monomer and the standard temperature used in previous studies, was selected as the second temperature. The highest tested temperature was 130 °C, at which the formulations are in an isotropic molten phase. This temperature was chosen to rule out the possibility of liquid crystallinity immobilizing the polymer structure and thus impairing chain growth.

Figure 93: Monomer system LCM6 and HDT used for linear polymer conversion experiments in conjunction with photoinitiators Ivocerin or TPO.

After irradiating the samples, gel permeation chromatography was performed to assess the molecular weight of the obtained polymers. The typical step-growth shape of elugrams showed incomplete polymerization in all cases, with oligomer and even some monomer units still present. To test which of the peaks represented the pure LCM6 monomer, or potentially LCM6 in conjunction with one or two connected HDT monomers, a spiked GPC sample was measured, which contained the polymer as well as the unreacted

monomer (Figure 94b). This revealed the monomer peak, thus allowing the identification of the dimer, trimer, tetramer etc. peaks. Above about seven repeating units, the oligomer peaks overlap completely, preventing a differentiation of individual chains.

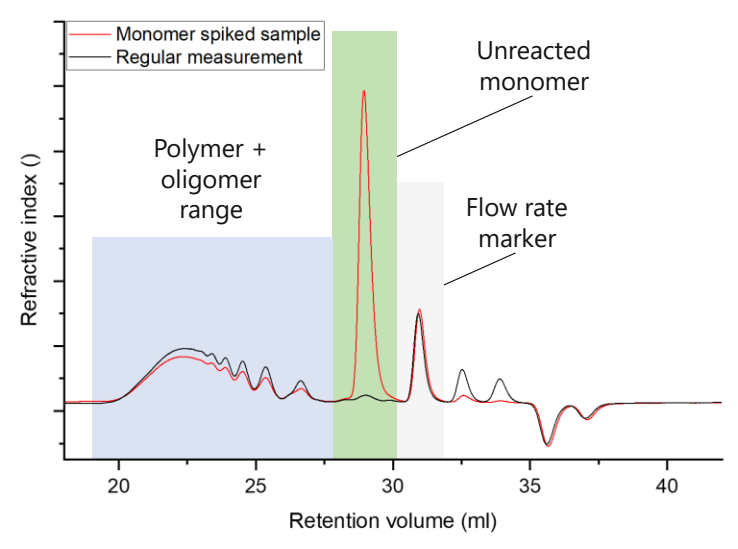


Figure 94: GPC measurement of LCM6-HDT formulation without (black) and with (red) added unreacted monomer. In addition to the monomer-spiking, BHT was utilized as spiking agent in the GPC solvent as the flow rate marker to obtain reproducible elution times across different samples.

Molecular weights were compared between the different polymers (Figure 95).

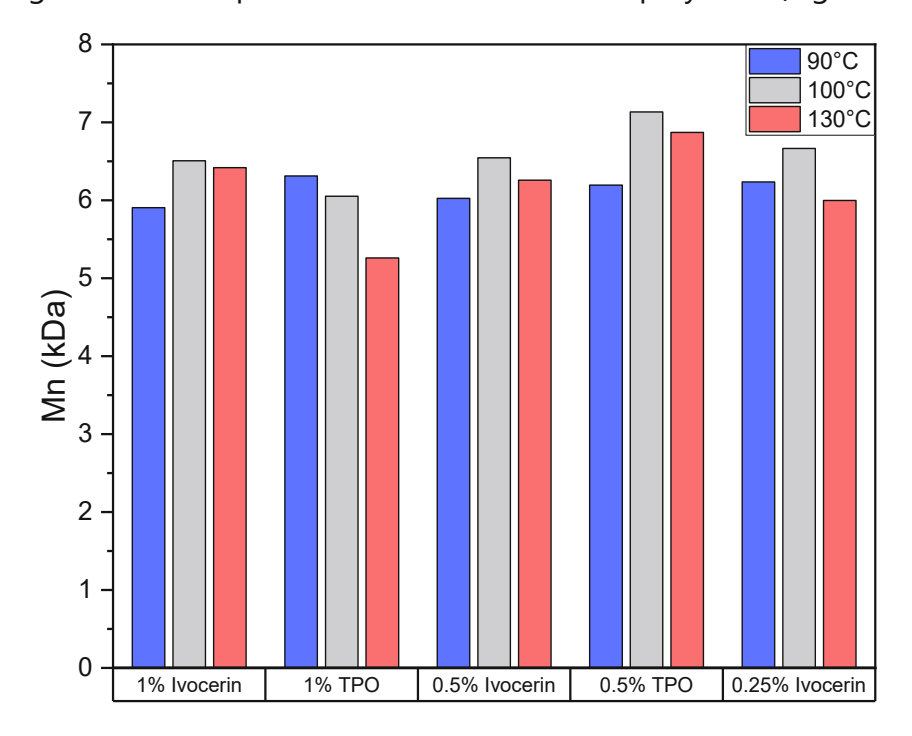


Figure 95: Results of varying type and concentration of photoinitiator and curing temperature: Number average molecular weight of the GPC elugram using conventional calibration using a polystyrene standard.

Across samples, relatively similar molecular weights were achieved, with 90 °C curing temperature causing a general trend toward lower molecular weights. The highest chain length was achieved using 0.5% TPO while curing the polymer at 130 °C. However, at 130 °C curing temperature, a significant variation of molecular weights was observed, with the lowest measured molecular weight sample also having been cured at this temperature. Therefore, this curing temperature was deemed unreliable for general measurements, which is exacerbated by longer preheating times, higher temperature gradients within the samples, and poor comparability with many hot lithography 3D printer models, which have a maximum operating temperature of 120 °C. 100 °C curing temperature led to consistently high molecular weights with the best performance using 0.5 mol% TPO as a photoinitiator. Concluding from this study, using 0.5 mol% TPO and curing at 100 °C will be used in future experiments, as these conditions were previously

used successfully for networks and were now proven to lead to satisfactory results with linear polymers.

3.2.10.2 Variation of irradiation parameters and stoichiometry

Thus far, irradiation parameters had been optimized for networks obtained through the use of tri- or tetrafunctional (crosslinking) thiol monomers. The main criterion was achieving high crystallinity by curing from the LC phase and mechanical stiffness of the resulting specimens, which depends on crystallinity and monomer structure. The result of the optimization study was a combination of a weak initial irradiation step, which allows for crystallization, followed by a stronger final curing step, which increases reactive group conversion to above 95%. For linear polymers, a separate parameter study was performed with the primary aim of maximizing polymer chain length, which should lead to an increase in mechanical strength. Higher crystallinity was not a primary point of focus as crystallization of linear polymers occurs readily post-curing in presence of liquid crystalline monomers.

Three different irradiation programs were tested along the previously optimized irradiation procedure, which consists of a 300-second low intensity irradiation (1.5 mW cm⁻²) followed by a 180-second final curing step at higher intensity (290 mW cm⁻²). The first new irradiation program (Program 1) consisted of a short 18-second, highintensity irradiation step (2660 mW cm⁻²) with the same total light dose of the usual irradiation procedure. In the second variation (Program 2), the 300-second first step of the optimized program was replaced by three one-second pulses at higher intensity (290 mW cm⁻²), followed by the usual 180-second irradiation at 290 mW cm⁻². The final variation (Program 3) consisted of three 300-second irradiation steps with a progressive increase in intensity (1.5, 9, 36 mW cm⁻²). All low intensity (≤36 mW cm⁻²) irradiation steps use the Hönle light source with an emission profile centered around 405 nm, while all higher intensity (≥290 mW cm⁻²) irradiation steps use the stronger UVET light source with

an emission profile centered around 365 nm. The exact parameters are listed in the experimental part (Table 41).

Additionally, an experiment was carried out to rule out two potential factors that could affect the formulation stoichiometry and thus chain length negatively: homopolymerization of the ene-monomer and evaporation of the thiol monomer. In the former case, a slight excess of LCM6 would be necessary to reach higher chain lengths; in the latter case, an excess of thiol would be required. Therefore, two formulations were tested, in one of which a 5% excess of thiol, and in one of which a 5% deficit of thiol was employed.

The different irradiation modes and the stoichiometric variations were tested in a formulation with 0.5 mol% TPO and cured at 100 °C, which was proven optimal during the experiments described in chapter 3.2.10.1, and compared to the previously optimized formulation (Figure 96).

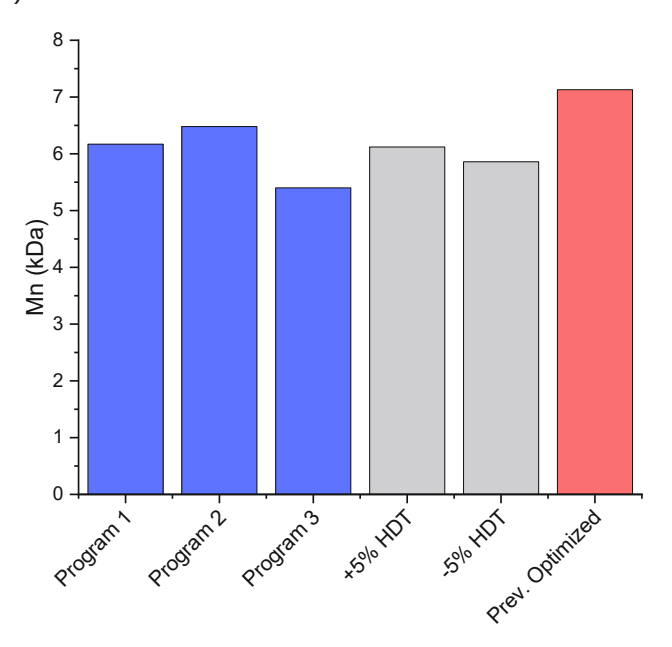


Figure 96: GPC results of polymers cured with different irradiation programs and variations of stoichiometric monomer ratios.

None of the changed irradiation conditions led to higher molecular weights than the previously optimized reference. Irradiation programs 1 and 2 led to the highest molecular weights of the newly tested methods, which leads to the conclusion that the strong irradiation step of the UVET UV-Cure device is necessary to obtain full conversion. Having an excess or a deficit of one of the two monomers in the formulation led to a negative effect on the molecular weight of the obtained polymers in both cases. This confirms that the stoichiometry of the formulations is sufficiently balanced and that neither homopolymerization of the ene-monomer nor evaporation of the thiol monomer play a significant role.

The mechanical properties of the obtained polymers did not differ significantly from each other. All of the obtained samples were brittle and weak, and often broke while being removed from the silicone mold. Therefore, no mechanical testing was performed. A much higher degree of polymerization would likely be necessary to achieve an improvement in strength and toughness. One option for improvement would be modifying the LC monomer to contain a more reactive end group, such as an allyl ether.

3.3 LCM7-based polymers

The newly synthesized allyl ether functionalized liquid crystalline monomer LCM7 (Figure 97) was polymerized in bulk in conjunction with a variety of thiol comonomers.

Figure 97: New liquid crystalline terminal alkene monomer LCM7.

The allyl ether built into the spacer is known to be more reactive in the thiol-ene click reaction.³⁷ Therefore, an experiment was performed to test the performance of LCM7 in conjunction with a difunctional thiol comonomer, which would result in a linear polymer. Afterwards, the performance of the monomer in the formation of polymer networks was tested with tri- and tetrafunctional thiol comonomers.

3.3.1 Linear polymerization test

To attempt an improvement in molecular weight of linear polymers due to the more reactive allyl ether end groups, the newly synthesized LCM7 was tested in a linear polymerization experiment in conjunction with HDT (Figure 98) with the same conditions that had previously led to the highest molecular weights in linear polymers (chapter 3.2.10).

Figure 98: Formulation tested to assess the performance of LCM7 in the formation of linear polymers consisting of LCM7 and the difunctional thiol comonomer HDT. In analogy to previous experiments, 0.5 mol% of the photoinitiator diphenyl(2,4,6-trimethyl benzoyl)phosphine oxide (TPO) and 0.05 wt% of the stabilizer pyrogallol were used added to the formulation.

The previously optimized irradiation parameters described in chapter 3.1.3.2 were used to cure the specimens. Although the monomer was not confirmed to be purified fully via methods like HPLC or GC-MS, an initial evaluation of polymerization performance was required to estimate usability of the monomer for further tests (Figure 99).

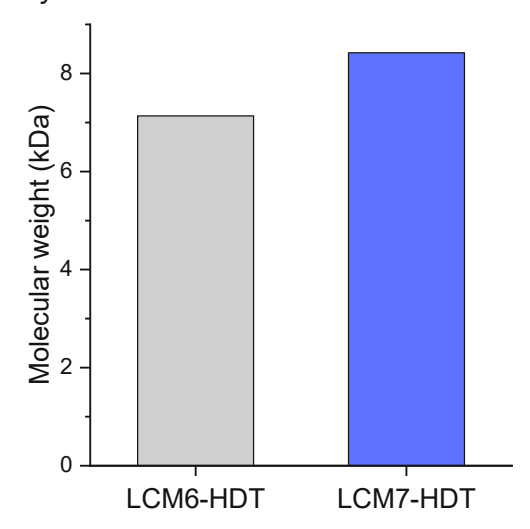


Figure 99: Molecular weight of linear polymers from LCM6 and LCM7.

The molecular weight of the obtained LCM7 polymer was higher than any of the polymers obtained in the previous LCM6 optimization study, confirming the reactivity increase of allyl ethers over aliphatic terminal alkenes reported in literature. In direct comparison, longer maximum chain lengths and smaller amounts of short oligomers were found in the LCM7 GPC elugram (Figure 100). However, this molecular weight increase was not sufficient for enhanced mechanical strength, as the material was still brittle. Therefore, the synthesis of linear polymers was not continued and LCM7 was tested in conjunction with tri- and tetrafunctional thiols to form polymer networks.

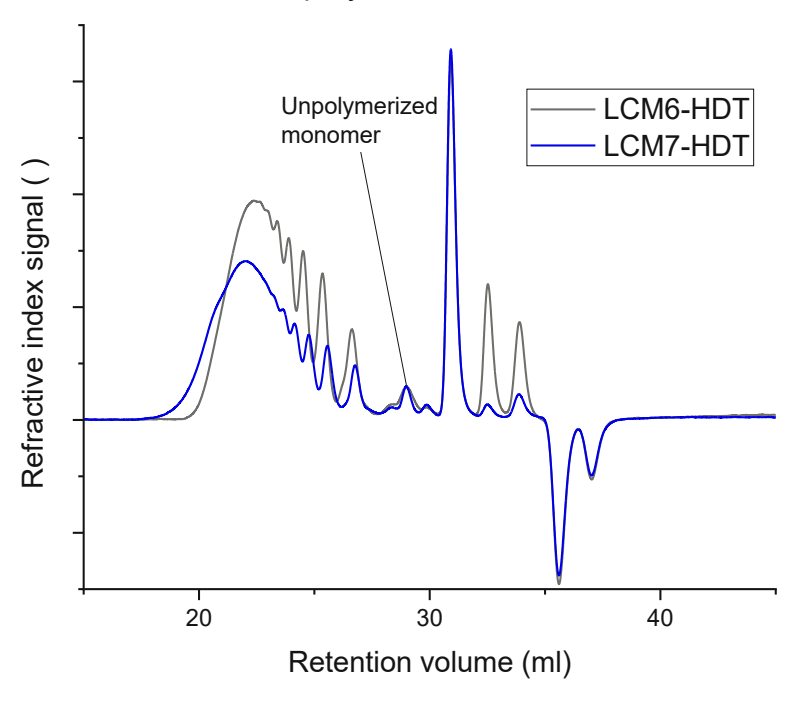


Figure 100: Direct comparison of GPC elugrams of polymers LCM6-HDT and LCM7-HDT.

3.3.2 LCM7-based polymer networks

To test the performance of LCM7 in polymer networks, it was combined with the trithiol comonomers TMPMP, TEMPIC, ETTMP, CHTT, and the tetrathiol monomer PETMP (Figure 101) in formulations with equimolar thiol and terminal alkene reactive groups. Prior to polymerization, the formulations were investigated under a polarized optical microscope, which revealed that none of them exhibit liquid crystalline properties.

Figure 101: Comonomers used in conjunction with LCM7.

Curing of the formulations was performed using the heated polymerization chamber with conditions optimized for crystallinity, which involves an initial 300-second irradiation at low intensity (1.5 mW cm⁻², 405 nm LED light source) followed by a 180-second highintensity (290 mW cm⁻², 365 nm LED light source) final curing step.

The combination with ETTMP resulted in a very soft and sticky material that could not be removed from the silicone mold without stretching significantly. Therefore, this comonomer was not further investigated in conjunction with LCM7. The specimens resulting from the other comonomers were nearly fully transparent and relatively soft, especially after handling them for a brief time, leading to the assumption of very low or no present crystallinity, which is in line with the lack of a liquid crystalline phase of the formulation. The softening indicates a glass transition temperature around room temperature.

To enhance crystallinity in the polymers, the trifunctional thiol comonomers were combined with the difunctional chain extenders HDT and EDDT (Figure 102). The goal of the resulting looser network architecture should allow the mesogenic groups to align, leading to a more crystalline polymer.

$$HS$$
 SH
 HS
 O
 O
 SH
 $EDDT$

Figure 102: Difunctional thiol chain extenders HDT and EDDT.

The initial test, in which HDT and EDDT were compared by polymerizing them in bulk in conjunction with TMPMP, gave a promising indication of crystallinity as the test specimens now exhibited increased stiffness and had turned opaque after curing. A DMTA measurement identified HDT as more suitable in causing crystallinity compared to EDDT. Therefore, two more formulations utilizing HDT as a chain extender were created. In one, the previously well-performing crosslinker CHTT was used, while in the other, a higher concentration of the chain extender HDT (64% of thiol end groups) was used in conjunction with TMPMP. A complete overview of the tested LCM7-containing formulations is given in Table 20.

Table 20: Overview of all formulations containing the liquid crystalline terminal alkene monomer LCM7. The ratio of monomers (r_{LCM7}, r_{Comonomers}) is given in reactive end group percentage (FG%).

Formulation name	r _{LCM7} (FG%)	Comonomer(s)		r _{Comonomers} (FG%)	
100% TMPMP	50	TMPMP		50	
100% TEMPIC	50	TEMPIC		50	
100% ETTMP	50	ETTMP		50	
100% CHTT	50	CHTT		50	
100% PETMP	50	PETMP		50	
50% TMPMP 50% HDT	50	TMPMP	HDT	25	25
36% TMPMP 64% HDT	50	TMPMP	HDT	18	32
50% TMPMP 50% EDDT	50	TMPMP	EDDT	25	25
50% CHTT 50% HDT	50	CHTT	HDT	25	25

3.3.3 Reactive group conversion investigation

Attenuated total reflection infrared (ATR-IR) spectroscopy was employed to gain an overview over the effectiveness of the polymerization reaction of LCM7 in conjunction

with various comonomers (Figure 103). The desired conversion for crosslinked polymers would be around or above 97%. The DBC of the polymer containing TEMPIC as a comonomer could not be measured, since the isocyanurate group exhibits a large signal over the region where the double bond is situated, preventing an accurate calculation.

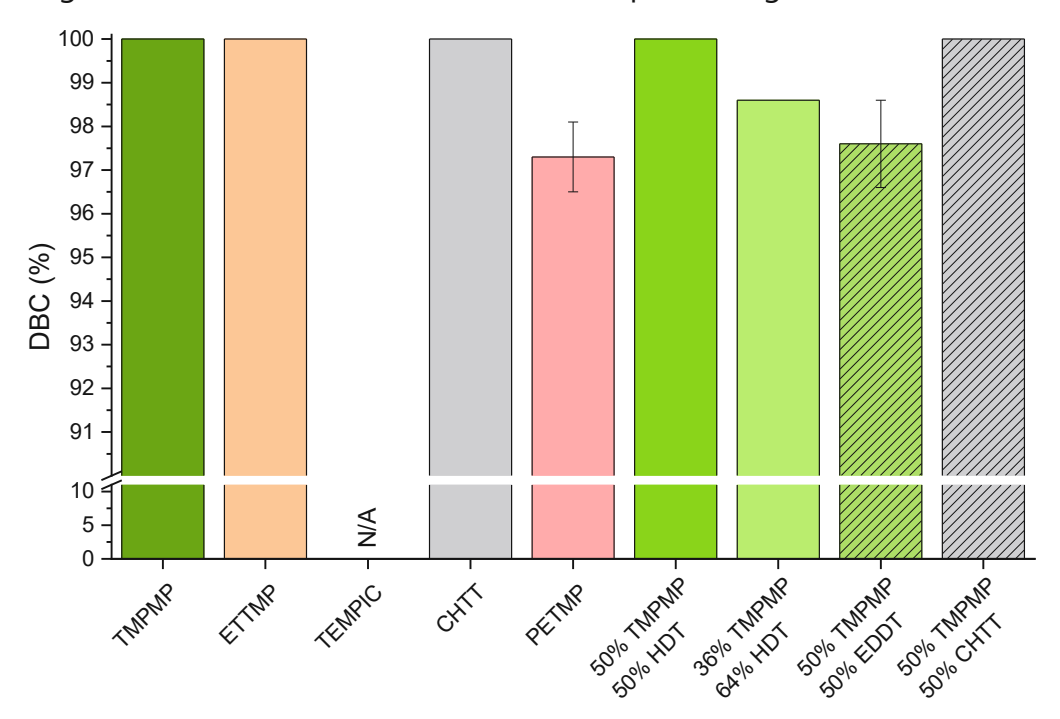


Figure 103: Investigation of double bond conversion (DBC) in various polymer networks containing LCM7 as the ene component. The DBC of the polymer prepared by combining LCM7 and TEMPIC could not be assessed due to the strong signal of the isocyanurate groups present in TEMPIC.

The allyl ether end group of LCM7, which is known to react more strongly in the thiol-ene click reaction than an aliphatic terminal alkene, exhibited a noticeable positive effect on the DBC of resulting polymers. 100% DBC was calculated for five out of the eight polymers for which a calculation could be performed. With the previously synthesized LCM6, none of the crosslinked polymers reached 100% DBC (chapter 3.2.3). Due to inaccuracy of the measurement method, it is unlikely that 100% DBC was truly achieved, but a conversion around or above 99% is likely. The chain extender EDDT performed worse than HDT in LCM7-containing polymers, which also occurred in linear polymers when used in combination with LCM6. Generally, satisfactory conversions were achieved. As di- and

trifunctional monomers were used, it is likely that nearly all monomer molecules were incorporated into the network, which is important to prevent leeching of unreacted monomers.

3.3.4 Thermomechanical evaluation

Dynamic mechanical thermal analysis (DMTA) was conducted for all LCM7-based test specimens to gain an overview of their mechanical properties over a large temperature range. Figure 104 displays all samples that only employed crosslinkers as comonomers with no chain extenders.

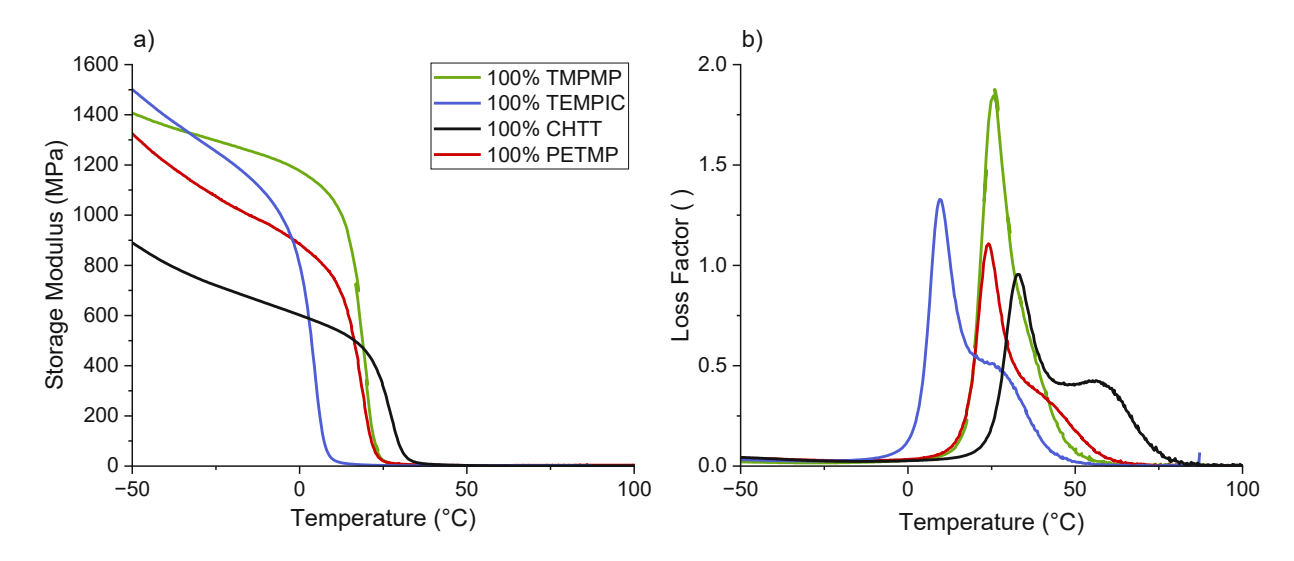


Figure 104: DMTA measurements of polymers obtained by combining LCM7 with thiol crosslinkers. a) Storage modulus G', b) loss factor tan δ .

DMTA curves of the samples without an incorporated chain extender are in alignment with the initial assumption of low crystallinity due to sample transparency. Storage moduli of all measured specimens rapidly dropped to near zero during the glass transition. As this transition occurs around room temperature, this softening was easily noticeable when touching then samples by hand and thereby warming them up slightly. A minor melting transition is visible in the loss factor graphs as a shoulder of the T_q peaks, which points to the presence of a minimal amount of crystallinity, likely from a small fraction of the LCM7 molecules aligning into minor crystalline domains in the polymer. This feature is most

prominent in the CHTT-containing sample and nearly invisible in the TMPMP-containing sample. As the utilization of CHTT has previously led to the most crystalline polymers, this is in line with previous experimental results.

The glass transition temperatures inversely correlate with the comonomer molecular weight per reactive group (Table 21). At body temperature (i.e., 37 °C), this trend is also clearly visible as storage moduli decrease with increasing comonomer molecular weight per reactive group.

Table 21: DMTA measurement results obtained by polymerizing formulations of LCM7 with thiol crosslinkers. Molecular weights per reactive group of comonomer inversely correlate with the glass transition temperatures and storage moduli at 37 °C.

Co-monomer	Molecular weight per reactive group (g·mol ⁻¹ FG)	Glass transition temperature (°C)	Storage modulus at 37 °C (MPa)
TEMPIC	175	10	1.5
TMPMP	132	26	2.3
PETMP	122	24	4.7
CHTT	88	33	9.6

After polymerizing these formulations, their appearance immediately illustrated that the crystallinity enhancement was successful, as all samples were now opaque and much stiffer at room temperature. DMTA results confirmed this assessment (Figure 105).

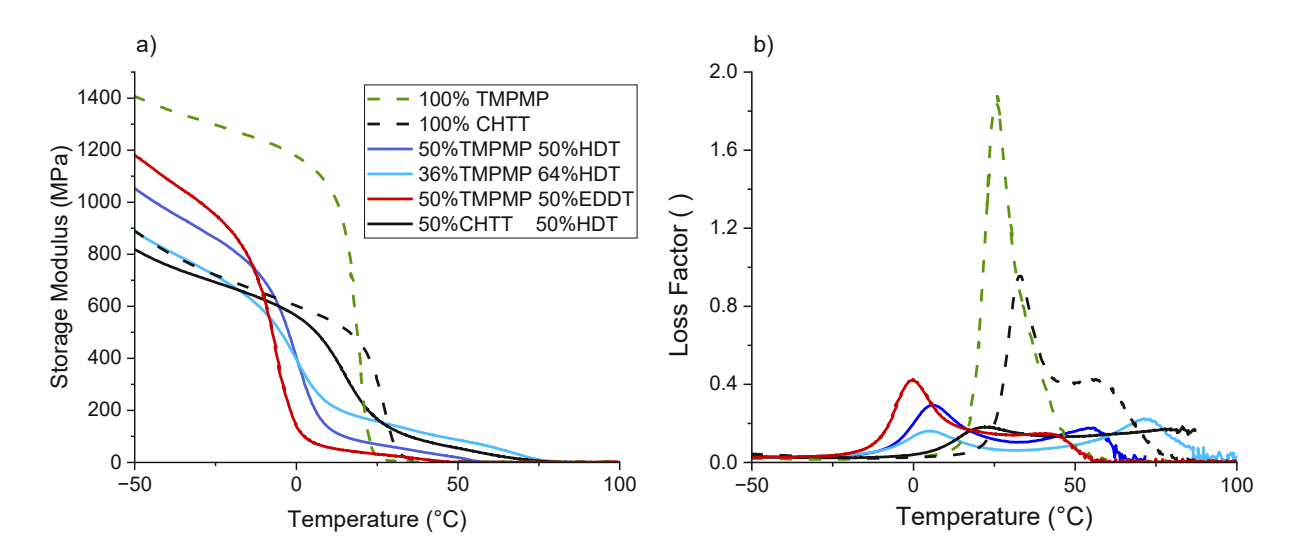


Figure 105: DMTA measurements of polymers obtained by combining LCM7 with thiol crosslinkers TMPMP and CHTT in combination with the difunctional chain extenders HDT and EDDT. a) Storage modulus G', b) loss factors $\tan \delta$. Comonomer percentages are given in functional group percentages of the thiol component in the formulation. For comparison, the polymers resulting from 100% CHTT and TMPMP as comonomers are displayed in dashed lines.

In direct comparison, EDDT led to a much less beneficial effect on crystallinity, as identified by a very low storage modulus throughout the measurement. When chain extenders were incorporated into polymers, the glass transition temperatures decreased by 20-25% in case of TMPMP, and by 10 °C in case of CHTT compared to the polymers in which only thiol crosslinkers had been used (Table 22). This highlights the glass transition temperature as a network density-dependent property. Nevertheless, the negative impact of the glass transition on the stiffness was successfully reduced due to crystallinity in the sample. As a result, the storage modulus at 37 °C increased nearly tenfold in case of CHTT compared to the non-crystalline sample that did not incorporate a chain extender. In case of TMPMP, the increase was even more significant, with an increase of the storage modulus by a factor around 20 at the lower ratio of the chain extender HDT (50 FG% dithiol), and a factor of 50 at the higher fraction of HDT (64 FG% dithiol), which was also the highest of all tested samples. The latter sample also exhibited the highest storage modulus above 26 °C.

A crystallite melting point is visible in the loss factor graph for all polymers in which a chain extender had been used. Use of CHTT led to the highest melting point, followed by the TMPMP-containing formulation that incorporated a higher fraction of the chain extender.

Table 22: DMTA results of formulations combining LCM7 with trithiol crosslinkers TMPMP and CHTT, and dithiol chain extender HDT.

Formulation	Glass transition Crystallite mulation temperature (°C) point		Storage modulus at 37°C (MPa)
50% TMPMP 50% HDT	5	55	45
36% TMPMP 64% HDT	6	72	120
50% TMPMP 50% EDDT	0	40	15
50% CHTT 50% HDT	22	78	91

3.3.5 Mechanical tests

In this chapter, polymers are referred to by the abbreviation and functional group fraction of the comonomers. E.g., the sample obtained by polymerizing LCM7 with a 36/64% FG ratio of TMPMP and HDT will be referred to as 36% TMPMP.

A selection of polymers was chosen for tensile tests. Of the polymers without a chain extender, the two exhibiting the highest glass transition temperatures (100% TMPMP and 100% CHTT) were tested. All polymers in which HDT was employed as a chain extender were analyzed using tensile testing (Figure 106).

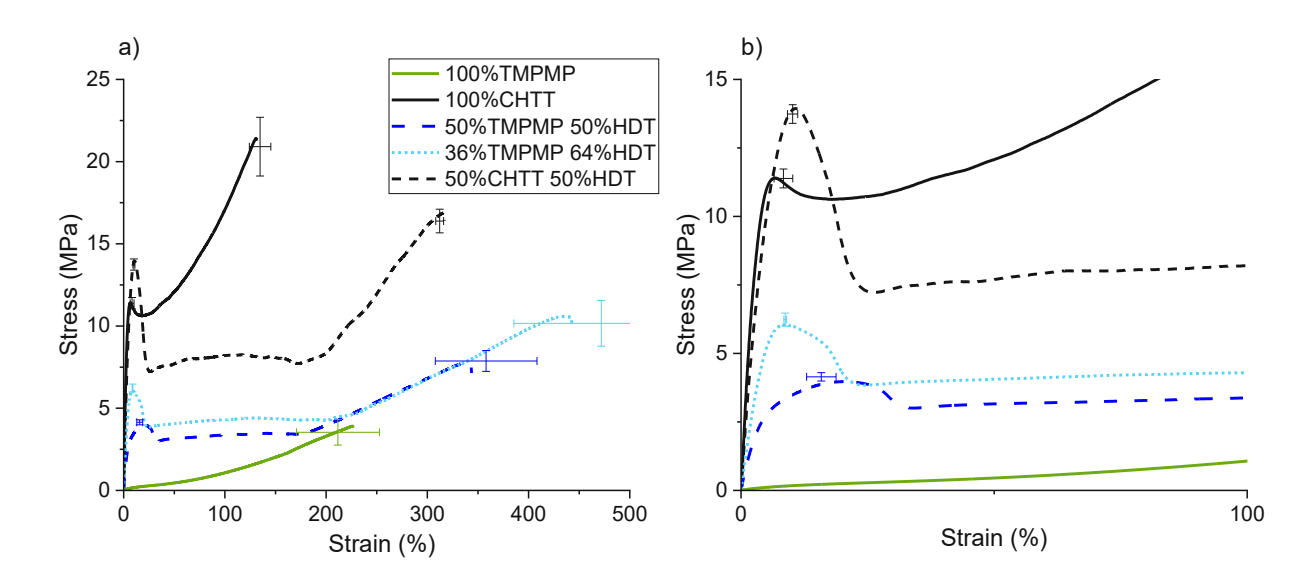


Figure 106: Tensile testing curves of polymers from LCM7 in combination with crosslinkers TMPMP and CHTT with various concentrations of chain extender substituting the crosslinkers. a) Full overview of the tensile tests including averages and standard deviations of yield strength, elongation at yield, ultimate tensile strength and elongation at break. b) Magnification of the initial 100% of elongation of the tensile tests, highlighting yield strength and elongation at yield of the samples. Comonomer percentages are given in functional group percentages of the thiol.

A distinct yield point is visible in the tensile test graphs of all polymers except 100% TMPMP. In this sample, the absence of a yield point and the elastomeric behavior is explained by the missing sample crystallinity and a glass transition close to room temperature (26 °C, measurement conducted at 21.5 °C). Additionally, the sample exhibited the lowest strength and the second lowest elongation at break. Conversely, the other sample containing no chain extender, 100% CHTT, performed very well during tensile tests with the second highest yield strength and the highest ultimate tensile strength of all measured samples. Since the glass transition of 100% CHTT is also close to room temperature (33 °C), it is likely that a more elastomeric tensile behavior akin to 100% TMPMP would have been displayed, had the measurement been conducted at a slightly higher temperature. At a slightly lower temperature, another change of tensile properties is likely as the polymer transitions into a glassy, brittle state.

The tested polymers containing the chain extender HDT all exhibited similar behavior, albeit at differing absolute tensile strengths. An initial elastic deformation was followed by a distinct yield point between 8 and 16% elongation. After this, the samples underwent a long period of over 150% of plastic deformation without a significant increase in stress. One or multiple necking sections appeared at this point, which increased in length until they encompassed the entire specimen (Figure 107). The plastic deformation was accompanied by an increase in transparency of the sample, likely by polymer chains aligning within the samples by being stretched. After this, a strain hardening deformation took place that finally caused an increase in stress above the yield strength and finally led to failure of the specimen.



Figure 107: Necking of a tensile test specimen of 36% TMPMP with transparency change in the elongated sections.

The highest yield strength of all measured samples along with the second highest ultimate tensile strength was measured for 50% CHTT. The behavior of 50% TMPMP and 36% TMPMP was relatively similar, with 36% TMPMP displaying a higher yield strength and the highest measured elongation at break. During part of the strain hardening elongation, the representative curves of these two samples align nearly perfectly.

Generally, good tensile test results were obtained by the samples polymerized from LCM7 with the highest strain at break and the highest elongation at break of any LCMcontaining polymer achieved by 100% CHTT and 50% CHTT, respectively. However, the narrow operational range of 100% CHTT and the need for a chain extender, which causes the polymer to have a thiol odor even after polymerization, causes these strong materials to have a slight drawback compared to the ones incorporating LCM6.

3.3.6 Evaluation of crystallinity

In this chapter, polymers are referred to by the abbreviation and reactive group fraction of the crosslinker. E.g., the sample obtained by polymerizing LCM7 with a 36/64 FG% fraction of TMPMP and HDT will be referred to as 36% TMPMP.

Crystallinity of the polymer samples was evaluated using differential scanning calorimetry (DSC, Figure 108).

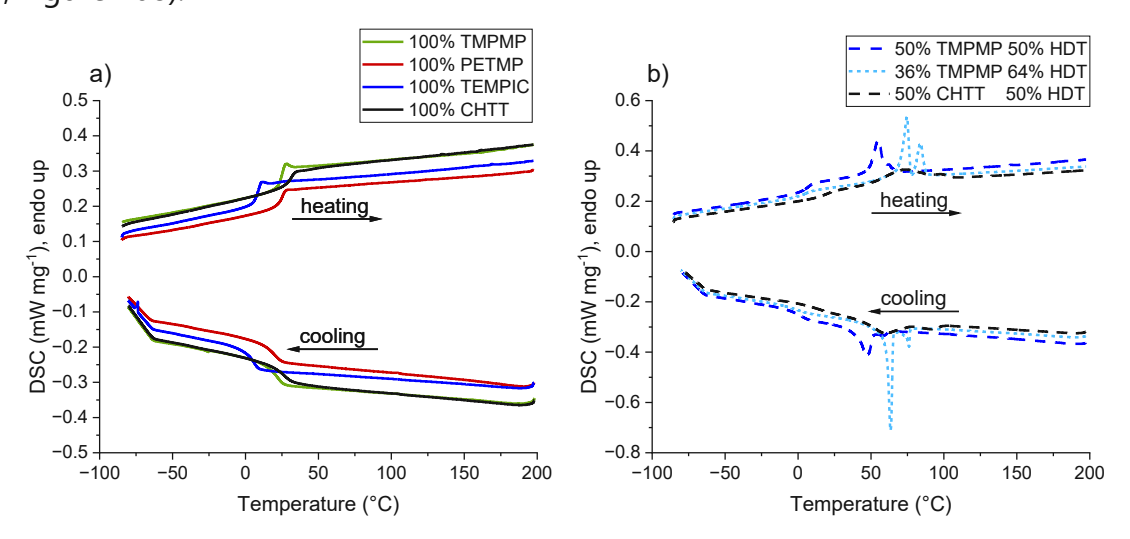


Figure 108: Cooling cycle and second heating cycle DSC measurements of samples containing LCM7 as the ene-component. a) Polymers without a chain extender, which exhibit a glass transition and no visible melting point. b) Polymers with chain extender HDT in various molar ratios, which exhibit a glass transition and a crystallite melting point. Percentages are given in reactive group percent.

DSC results were in line with results obtained by measuring DMTA. The samples, in which LCM7 was combined with crosslinkers and no chain extender was used, did not exhibit a

crystallite melting point. Instead, a baseline shift is clearly recognizable in the DSC graph, which is a sign of the glass transition occurring. The temperature of this shift aligns well with the results obtained via DMTA with less than 5 °C difference (Table 23). The most distinct glass transition peak was measured for 100% TMPMP, which also matches the DMTA results, where this sample exhibited the highest loss factor peak during the glass transition.

Table 23: DSC results of samples obtained by polymerizing LCM7 in conjunction with crosslinkers TEMPIC, TMPMP, PETMP and CHTT. Glass transitions via DSC are compared to results obtained via DMTA. MW/FG is the molecular weight per functional group, T_q is the glass transition temperature.

Formulation	MW/FG (g·mol ⁻¹ FG)	T _g (DSC, °C)	T _g (DMTA, °C)
100% TEMPIC	175	12	10
100% TMPMP	132	29	26
100% PETMP	122	29	24
100% CHTT	88	36	33

Samples containing the chain extender HDT in addition to the crosslinkers CHTT and TMPMP still had a distinctly visible glass transition with a matching transition temperature measured via DMTA relatively well with less than 10 °C difference (Table 24). The glass transition was less distinct than for the samples without a chain extender, which is likely caused by the samples' crystallinity. Additionally, all samples containing HDT exhibited two melting peaks in the DSC graph, a larger peak occurring at a lower temperature and a smaller one at a higher temperature. For 36% TMPMP, the second peak was distinctly separated from the first one, while for 50% TMPMP, the second peak was only visible as a small shoulder of the melting point peak. In the case of CHTT, both peaks were broad and flat. The two melting peaks point to the presence of distinct crystalline phases in the polymers, likely the HDT chain extended sections and the more highly crosslinked sections. The melting transitions were integrated over time, which resulted in the polymers' melting enthalpies (Figure 109). 50% TMPMP exhibited the lowest melting enthalpy, followed by 50% CHTT. The highest melting enthalpy was measured for

36% TMPMP, which is likely due to its loose network structure, which allows for crystallization of a large fraction of the LCM7 mesogenic groups and likely also leads to crystallization of a portion of the HDT chains.

Table 24: DSC results of formulations combining LCM7 with trithiol crosslinkers TMPMP and CHTT, and dithiol chain extender HDT. Glass transitions (T_a) and crystallite melting points (T_m) are compared with the results obtained via DMTA, and melt enthalpies (ΔH) were calculated by integrating the melting peaks measured via DSC. AH values may be imprecise as automatic baseline correction was not possible. Instead, the baseline points were marked manually. Separate ΔH calculation for the first and second peak was only possible for 36% TMPMP.

Formulation	T _g <i>via</i> DSC (°C)	T _g <i>via</i> DMTA (°C)	T _m via DSC (°C)	T _m via DMTA (°C)	ΔΗ (J·g ⁻¹)
50% TMPMP 50% HDT	13		56, 63 ¹	55	
30% TMPIMP 30% HDT	15	5	50, 05	22	7.5
36% TMPMP 64% HDT	11	6	75, 84	72	8.6, 4.0
50% CHTT 50% HDT	24	22	75, 98 ¹	78	9.9
¹ Broad and low peak	•				

14 12 Melt enthalpy $\Delta H (J g^{-1})$ 10 8 2 -50% CHIT

Figure 109: Total melt enthalpies of samples polymerized from LCM7, which contain the chain extender HDT and crosslinkers TMPMP or CHTT.

3.3.7 Shape memory evaluation

Crystalline networks that have remaining elasticity above their crystallite melting point typically exhibit shape memory behavior. With this ability, a certain shape can be imprinted onto a polymeric material. After deformation into a stable altered shape, the specimen can then return to its original imprinted shape. If a second imprinting step is possible, and the material can switch its shape between the two shapes with certain stimuli, the material is a so-called two-way shape memory material.^{52,145,146}

Since only one imprinting step can be conducted with the present material, one-way shape memory behavior is possible for the crystalline LCM7-containing polymers. After deformation, their shape would return to the original shape that they were cured in. The formulation containing LCM7 as the ene component with 50 FG% CHTT and 50 FG% HDT as the thiol component was chosen for a shape memory experiment. As an initial test, one of the plastically elongated tensile test specimens was heated above 100 °C, which resulted in a return to the initial shape in approximately 60 s.

After this initial success, an S-shaped silicone mold was prepared in which the formulation was polymerized (Figure 110 a). As the polymer's crystallite melting point is at approximately 80 °C, a convenient way to access a temperature above this is to submerge the polymer in near-boiling water. The specimen was stretched to a straight shape at this temperature, upon which a small part of it broke off. Nevertheless, a relatively well straightened stable shape could be obtained after cooling the specimen (Figure 110b). When the shape was plunged into a heated water bath, a rapid transition back to the originally imprinted shape took place within approximately three seconds. Complete shape recovery was confirmed by measuring the dimensions of the sample (Figure 110c).

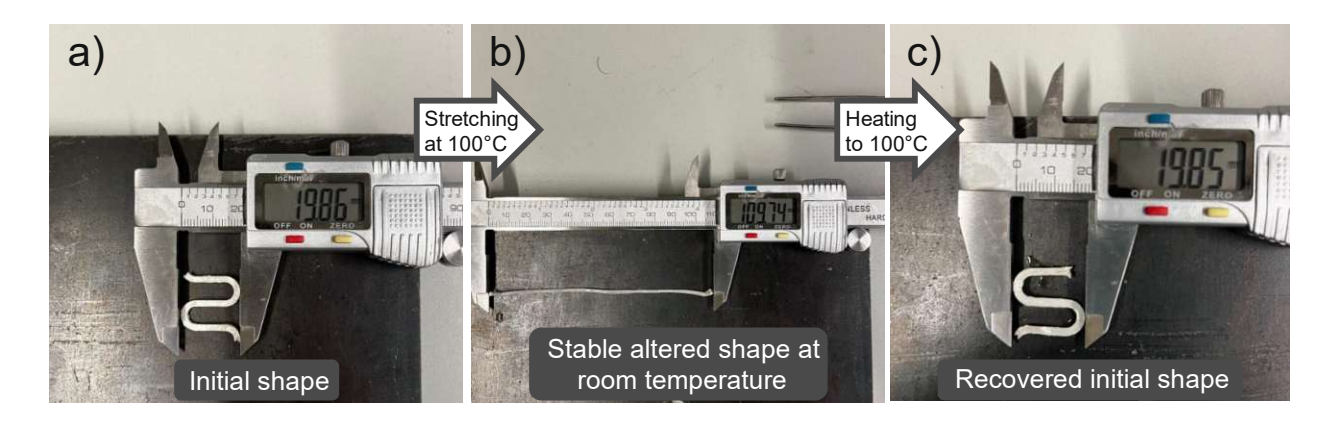


Figure 110: Demonstration of shape memory behavior of curved specimen of the polymer obtained by polymerizing LCM7 with the crosslinker CHTT and the chain extender HDT.

3.3.8 3D printing experiments

LCM7 The mechanically best-performing crystalline polymer obtained from (50/50 CHTT/HDT, FG%/FG% as comonomers) was tested in a DLP hot lithography printer. Prior to the printing test, a rheology stability study was conducted, which confirmed that the formulation was stable at 110 °C for 24 h.

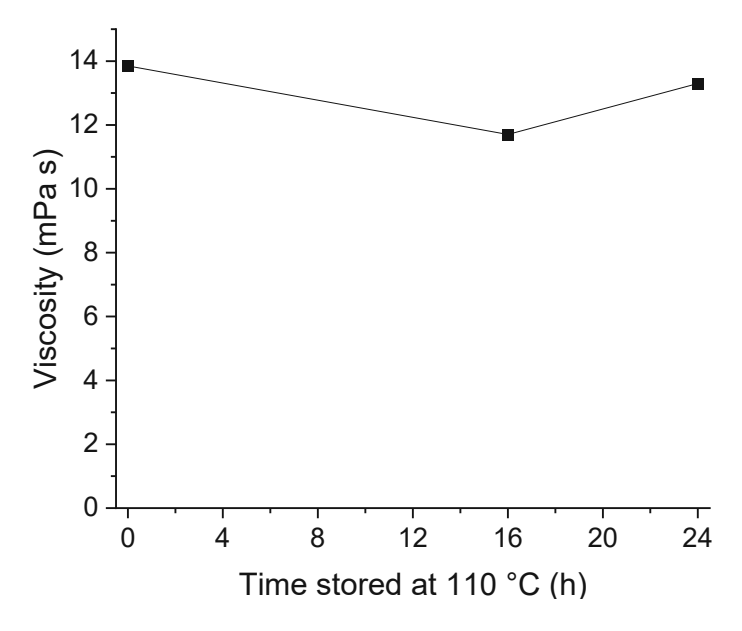


Figure 111: Viscosity of formulation tested in a printing experiment directly after mixing and when stored for 16 and 24 h.

After initial optimization, a 1x1 cm chip was printed and displayed good resolution before cleaning (Figure 112a). However, some oligomerization of the surrounding formulation was also apparent, which hindered the success of the washing step using isopropanol in an ultrasonic bath, and necessitated the use of acetone as a washing solvent, which then caused the polymer to swell and deform slightly (Figure 112b). In a further optimization step, isopropanol at around 50 °C was discovered to work as well as acetone without swelling the polymer as much. A small pyramid specimen was subsequently printed successfully (Figure 112c). Generally, the relatively loose network structure coupled with imperfect stability of the formulation made the printing of small details difficult. Possible optimizations include the modification of the type and concentration of photoinitiator and stabilizer.

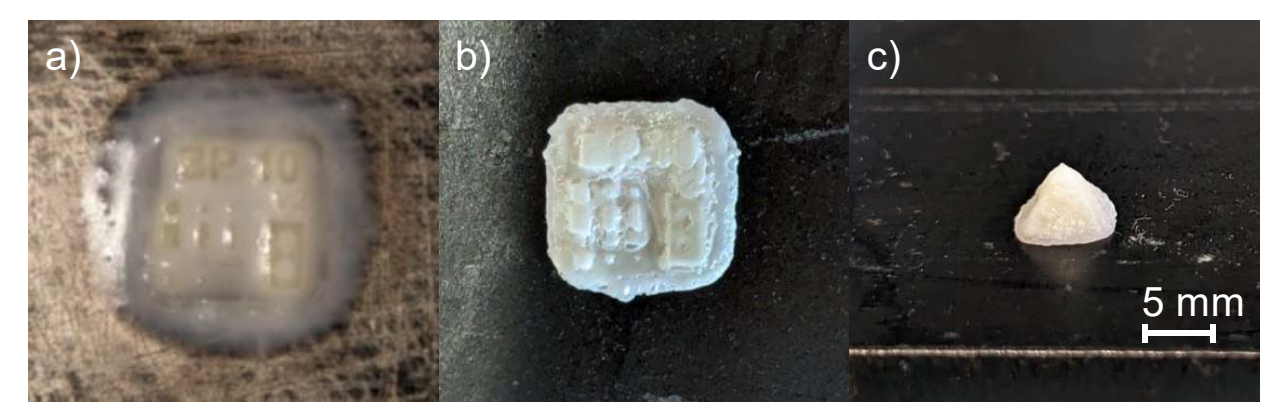


Figure 112: DLP printing tests of LCM7 with comonomers CHTT and HDT (50/50, FG/FG%%). a) Chip specimen on building platform before cleaning. b) Chip specimen after washing with isopropanol and acetone highlighting good resolution but issues from acetone partially swelling the polymer network. c) Printed pyramid specimen washed by sonicating with isopropanol at elevated temperature.

Summary

Thiol-ene photopolymerization has proven to be a rapid and versatile method for preparation of linear and network polymers with a wide range of properties. Their relatively good biocompatibility makes them a desirable alternative to acrylate and methacrylate systems in medical applications. However, their glass transition temperature tends to be below or around room temperature, and thus, their stiffness and hardness is typically not sufficient for many applications. 32,37

Liquid crystalline structures have become increasingly popular in polymer research since their discovery in the 19th century. 147 Even after their discovery and ubiquitous implementation in LCD screens, scientific interest has continued with a recent focus on their optical and electrical properties and applicability in 3D printing applications and soft robotics due to their shape memory capabilities.^{8,148-150} Liquid crystals lead to a preordered structure, which can be used to synthesize a semicrystalline polymer in bulk from building blocks that would typically not lead to crystallinity. This crystallinity can circumvent the issue of low glass transition temperatures in thiol-ene systems and cause mechanical stability beyond the glass transition, which typically still occurs around room temperature.

In this project, three liquid crystalline terminal alkene monomers were synthesized for thiol-ene copolymerization (Figure 113). Molecular structures were adjusted in an iterative process, which was interspersed by periodic literature review.

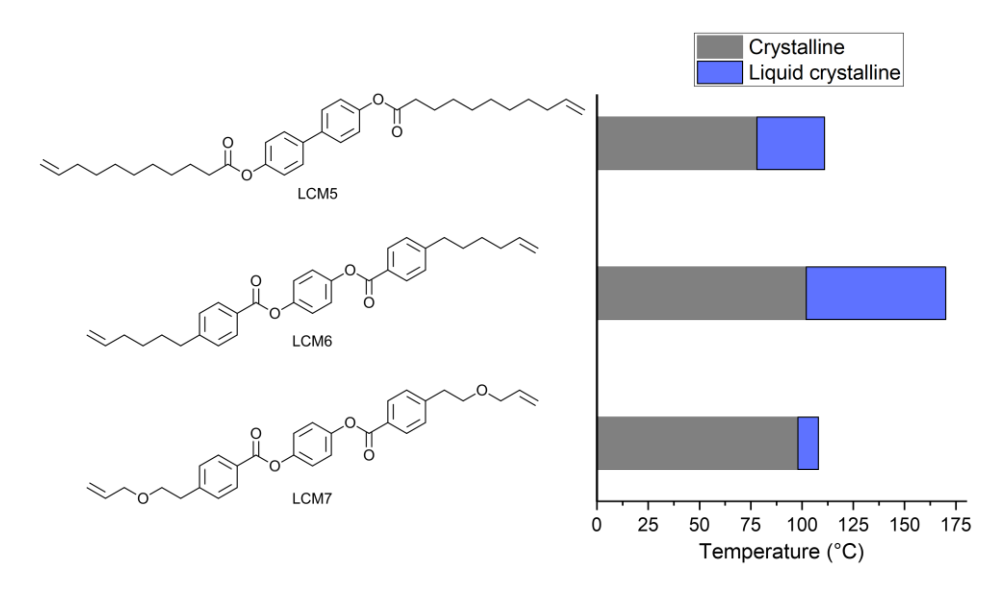


Figure 113: Liquid crystalline monomers synthesized in this work and visualization of their melting points and liquid crystalline ranges.

In addition to liquid crystalline monomers, a mesogenic moiety was also introduced to an addition fragmentation chain transfer agent. The aim was to introduce crystallinity into linear and crosslinked (meth)acrylate formulations while creating a homogeneous network. The attempt to introduce liquid crystallinity was not successful as the chain transfer agent did not exhibit any mesogenic properties. Nevertheless, the chain transfer agent was tested in comparison with a reference system and proven to be highly effective at regulating polymer network formation.

Previous work on the topic of liquid crystalline thiol-ene formulations had been focused on linear polymers using the previous generation of liquid crystalline monomer LCM4. In this project, both linear polymers and crosslinked networks were synthesized and characterized via various methods of thermomechanical analysis. The first networks created using the monomer LCM5 resulted in slightly crystalline, soft specimens. Nevertheless, the result was deemed promising, as the unoptimized conditions still resulted in significant crystallinity in a relatively tightly crosslinked polymer.

The preordered structure of a liquid crystalline phase can be translated into polymer crystallinity if the polymerization process takes place within the appropriate temperature range where liquid crystallinity of the monomer occurs. For this purpose, heat distribution is required to be homogeneous across the bulk of the formulation so that a liquid crystalline phase is present across the sample. Additionally, the heat of polymerization must not cause the sample temperature to exceed the liquid crystalline temperature range.

To effectively control the polymerization conditions, a novel polymerization setup was designed in form of a heated polymerization chamber. This chamber enables accurate temperature control and allows for use of different LED light sources, which led to massive improvements regarding the crystallinity of polymer networks cured from LCM enemonomers and thiol crosslinkers. An optimization study of curing conditions, which included temperature, irradiation conditions, and photoinitiator type and concentration was performed, resulting in successful integration of high degrees of crystallinity in the networks.

As all experiments to synthesize linear polymers using LCM-type monomers had previously resulted in very weak and brittle polymers, an in-depth study of polymerization conditions for linear polymers was conducted. A combination of LCM6 and the dithiol comonomer HDT (Figure 114 a) was subjected to a variety of different curing temperatures, irradiation parameters and adjustments to the photoinitiator as well as formulation stoichiometry. Compared to the curing procedure found by the optimization study and exact stoichiometric reactant use, no significant improvement of polymer chain length or mechanical properties could be achieved with these modified polymerization conditions.

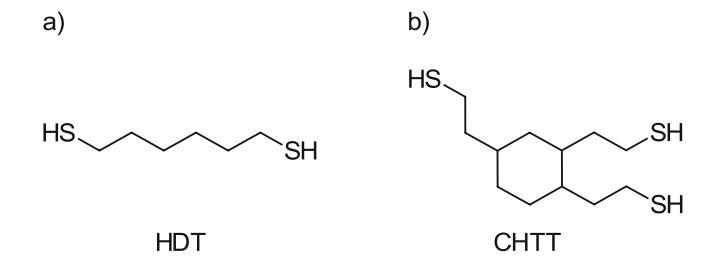


Figure 114: a) Dithiol chain extender HDT, b) trithiol crosslinker CHTT.

The crosslinker CHTT (Figure 114 b) has consistently exhibited promising material properties in combination with the liquid crystalline monomers synthesized in this work. In conjunction with LCM5, a remarkable range of tensile strengths and elongations at break was achieved purely determined by variation of the curing temperature, ranging from a nearly elastomeric material to a stiff, crystalline polymer with high tensile strength (Figure 115).

The highest crystallinity of networks along with the highest tensile strengths before yielding were achieved by combining LCM6 with CHTT. A detailed study of the materials' micro- and nanostructure was performed for the polymers obtained from LCM6, which revealed a significant influence of the thiol comonomer on phase separation between a harder and a softer phase, the likely cause of the high strength of polymers containing LCM6 and CHTT.

With LCM7, polymerization from the liquid crystalline phase was not possible as the addition of thiol comonomers caused a disruption of the LC phase. The samples obtained by polymerizing LCM7 with tri- and tetrafunctional comonomers resulted in minimal crystallinity. Therefore, the difunctional thiol chain extender HDT (Figure 114 a) was introduced into polymer networks, and polymers were synthesized from mixtures of chain extender and crosslinker. This resulted in much higher crystallinities and therefore, stiffer, tough polymers that resulted in the highest elongation and strength at break for separate samples. Figure 115 showcases the versatility of polymers synthesized from liquid crystalline monomers, as a formidable range of material properties is achieved from very similar chemistries.

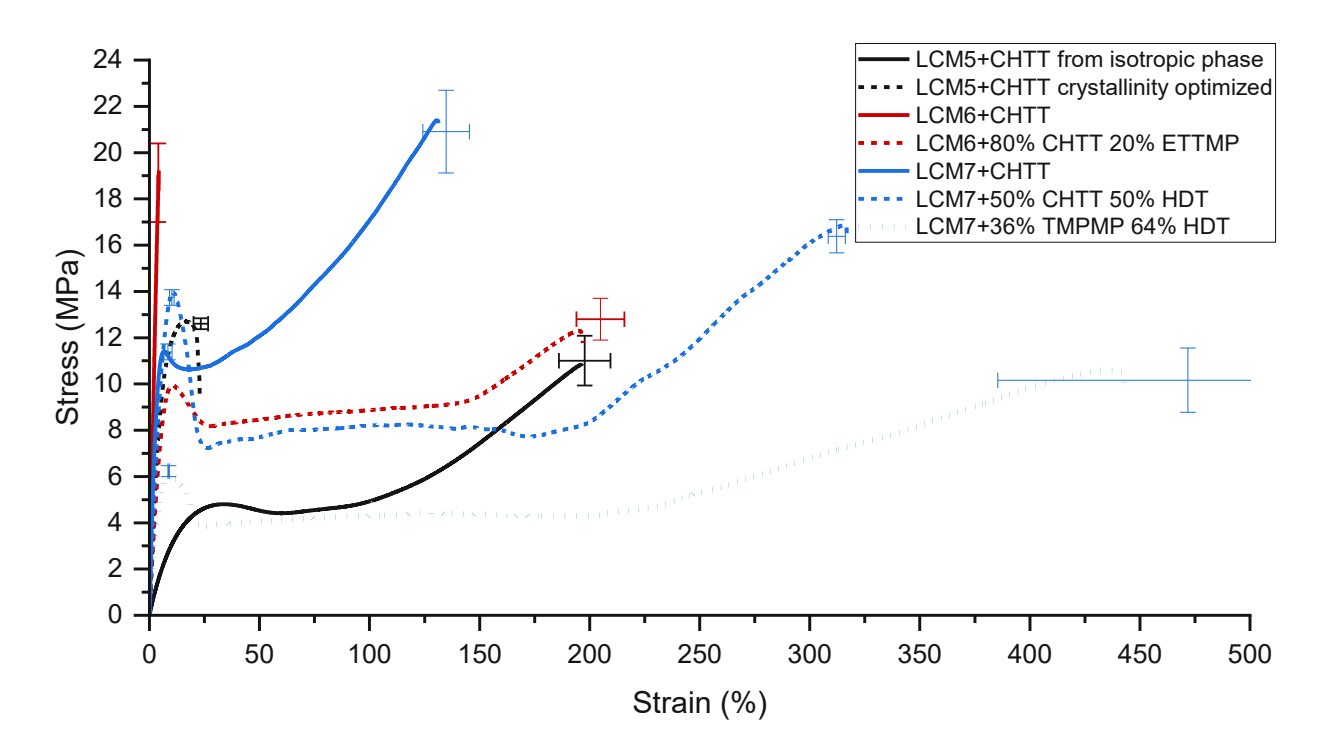


Figure 115: Selection of tensile tests of network polymers from liquid crystalline monomers LCM5, LCM6 and LCM7. Comonomer percentages are given in functional group percentages of the thiol.

The tunability of crystallinity using a variation of curing parameters for the LCM5+CHTT monomer system was demonstrated successfully in 3D printing tests. Herein, variation of the temperature during the curing process allowed for manufacture of multilayered composite parts and even the modulation of crystallinity within a single printed layer (Figure 116).

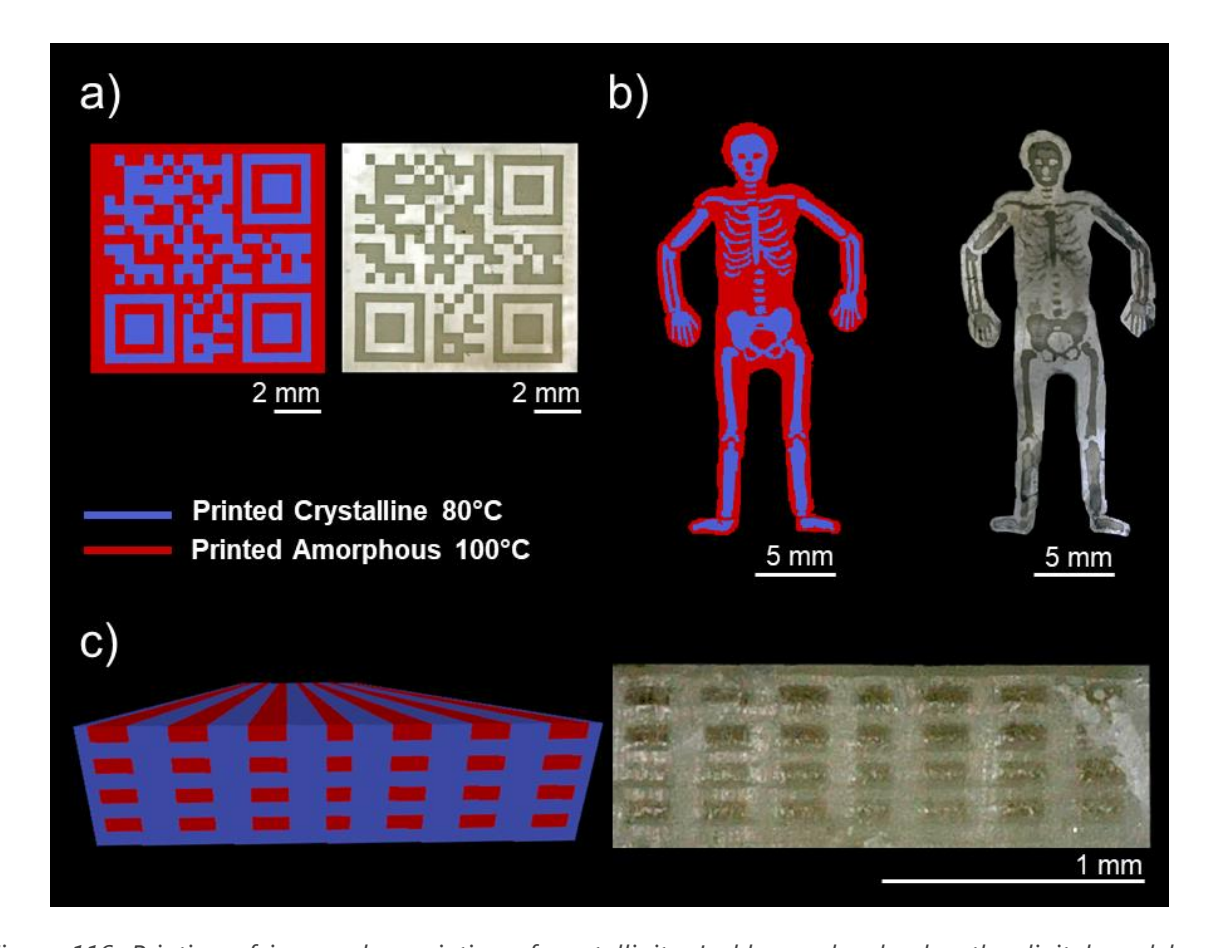


Figure 116: Printing of images by variation of crystallinity. In blue and red color, the digital models are displayed. The images of the printed specimens were recorded on a digital microscope in transmitted light mode. Therefore, the crystalline parts appear darker as they absorb more light than the amorphous parts. a) QR code spelling "3D-Encoding", b) human body + crystalline skeleton model, c) fiber composite structure with amorphous channels for toughening.

printing experiments were also performed for the LCM6+CHTT monomer combination. While a less detailed print result was achieved, the parts were very hard and stiff, indicating a successful formation of high crystallinity in the printed parts. Attempts to print LCM7-containing formulations did achieve high curing resolutions, but the networks containing chain extenders exhibited a much lower tolerance to solvents due to their loosely crosslinked structure, causing the printed parts to swell when removal of excess formulation was performed.

After elongation or deformation either though tensile tests at room temperature, or at a temperature above their crystallite melting point, the polymers demonstrated shape-

memory capabilities (Figure 117), returning to the original shape that they were cured in. For the LCM6+CHTT monomer combination, cyclic shape memory tests proved a nearperfect shape imprintability and recovery (>97%). With an LCM7-containing polymer, shape memory was also observed, and in this case, a rapid recovery of the original shape in less than three seconds was achieved.

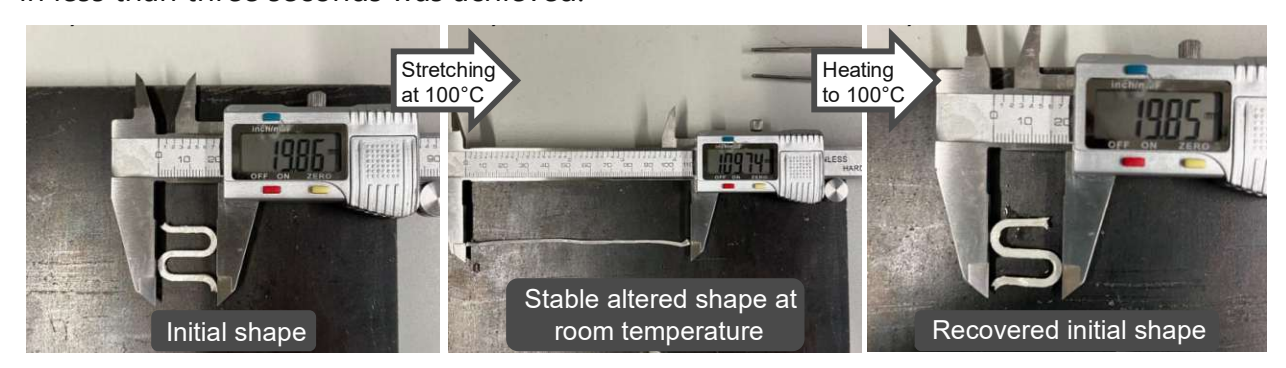


Figure 117: Demonstration of shape memory behavior of curved specimen of the polymer obtained by polymerizing LCM7 with the crosslinker CHTT and the chain extender HDT.

Experimental part

1 Studies with AFCT agents

1.1 Synthesis of AFCT agents

1.1.1 Mesogen-containing chain transfer agent BPVS

1.1.1.1 Synthesis of precursor TDP

((Oxybis(ethane-2,1-diyl))bis(oxy))bis(ethane-2,1-diyl) bis(2-oxopropanoate) (TDP) was synthesized in a Steglich esterification according to Gorsche et al. (Scheme 22).³⁵

Scheme 22: Synthesis of pyruvate ester intermediate.

A solution of freshly distilled pyruvic acid (21 g, 238.5 mmol, 2.1 eq), tetraethylene glycol (22.058 g, 113.57 mmol, 1 eq) and dimethylaminopyridine (DMAP, 1.39 g, 11.357 mmol, 0.1 eq) in 200 mL anhydrous CH₂Cl₂ was stirred at -10 °C. Then dicyclohexylcarbodiimide (DCC, 51.55 g, 249.85 mmol, 2.2 eq, dissolved in 250 mL anhydrous CH₂Cl₂) was added dropwise to the reaction mixture over a time span of 45 min. Afterwards, the reaction was stirred for another 2 h at -10 °C and then slowly allowed to warm up to room temperature. After 24 h, the mixture was filtered through silica and the solvent was removed using a rotary evaporator. The crude product was purified via column chromatography (petroleum ether/ethyl acetate 1/10) to give 13.12 g (35%) of TDP as a clear oil.

¹H-NMR (400 MHz, CDCl₃): δ (ppm) = 4.40 (m, 4H), 3.78 (m, 4H), 3.65 (m, 8H), 2.48 (s, 6H).

¹³C NMR-APT (101 MHz, CDCl₃) δ (ppm) = 191.62, 160.75, 70.76, 70.60, 68.52, 65.35, 26.77

 R_f -value (petroleum ether/ethyl acetate 1/9) = 0.5

1.1.1.2 Synthesis of BPVS

synthesis (11-[1-(biphenyl-4-ylsulfonyloxy)ethenylcarbonyloxy]-3,6,9-The of trioxaundecyl 2-(biphenyl-4-ylsulfonyloxy)prop-2-enoate) (BPVS) performed according to Gorsche et al. (Scheme 23).35

Scheme 23: Synthesis of mesogen-containing AFCT chain transfer agent BPVS.

80 mL dry CH₂CL₂, TDP (5.98 g, 17.9 mmol, 1 eq), 1,4-diazabicyclo[2.2.2]octane (DABCO, 4.77 g, 42.5 mmol, 2.4 eq) and a minimal amount of butylhydroxytoluene (BHT) were transferred to a 250 mL three necked round bottom flask under counter current of dry synthetic air and cooled to 0 °C. Biphenylsulfonyl chloride (9.81 g, 38.8 mmol, 2.2 eg, dissolved in 80 mL CH₂Cl₂) was added dropwise to the reaction mixture. The temperature of the reaction mixture was kept below 7 °C during the addition. After 2 h of stirring at 0 °C, the mixture was allowed to warm up to room temperature and stirring was continued for 72 h. The mixture was filtered through a thin layer of silica and the filtrate was washed twice with 50 mL portions of 1N HCl, once with 50 mL H₂O and twice with 50 mL portions of brine. The aqueous solutions were combined and extracted three times with 50 mL CH₂Cl₂ each. The organic phases were collected and dried over anhydrous Na₂SO₄. The solution was stabilized with BHT and concentrated using a rotary evaporator. The crude mixture was purified using medium pressure column chromatography (petroleum ether/ethyl acetate; the ethyl acetate concentration was raised from 0 to 100% over the course of 60 min). The fractions containing the product were stabilized with a small amount of BHT and concentrated using a rotary evaporator. 8.9 g BPVS (32%) were

obtained as a clear oil. Full purification of the product could not be achieved as oligomerization likely occurred during synthesis or purification.

¹H-NMR (400 MHz, CDCl₃): δ (ppm) = 8.00 (m, 4H), 7.76 (m, 4H), 7.60 (m, 4H), 7.49 (t, 4H), 7.43 (m, 2H), 6.19 (d, 2H), 5.69 (d, 2H), 4.26 (m, 4H), 3.69 (m, 4H), 3.59 (m, 8H).

¹³C NMR-APT (101 MHz, CDCl₃) δ (ppm) = 164.30, 161.01, 148.41, 147.44, 146.85, 143.08, 138.68, 134.62, 132.83, 129.27, 129.00, 128.85, 128.60, 128.19, 127.93, 127.83, 127.57, 127.48, 70.73, 69.62, 68.60, 65.89.

 R_f -value (petroleum ether/ethyl acetate 1/3) = 0.55

1.1.2 Mesogen-containing chain transfer agent C12VS

1.1.2.1 Synthesis of precursor C12DP

(12-(Acetylcarbonyloxy)dodecyl pyruvate) (C12DP) was synthesized according to a procedure published by Gorsche et al. (Scheme 24).³⁵

Scheme 24: Synthesis of chain transfer agent precursor C12DP.

A solution of freshly distilled pyruvic acid (28.6 g, 325.2 mmol, 3 eq), 1,12-dodecanediol (14.33 g, 108.4 mmol, 1 eq) and dimethylaminopyridine (DMAP, 0.87 g, 7.1 mmol, 0.1 eq), 0.1 eq) in 200 mL anhydrous CH₂Cl₂ was stirred at -10 °C. Then dicyclohexylcarbodiimide (DCC, 43.1 g, 208.9 mmol, 3 eq, dissolved in 250 mL anhydrous CH₂Cl₂) was added dropwise to the reaction mixture over a time span of 45 min. Afterwards, the reaction was stirred for another 2 h at -10 °C and then slowly allowed to warm up to room temperature. After 24 h of continued stirring, the mixture was filtered through silica and the solvent was removed using a rotary evaporator. The crude product was purified via column chromatography (petroleum ether/ethyl acetate 2/10) to give 13.33 g (36%) of C12DP as a white solid.

¹H-NMR (400 MHz, CDCl₃): δ (ppm) = 4.24 (t, 4H), 2.46 (s, 6H), 1.72 (m, 4H), 1.26 (m, 16H). ¹³C NMR-APT (101 MHz, CDCl₃) δ (ppm) = 192.17 (C=O), 161.07 (C=O), 66.76 (COOCH₂), 29.60 (CH₂), 29.55 (CH₂), 29.28 (CH₂), 28.47 (CH₂), 26.88 (CH₃), 25.88 (CH₂)

 R_f -value (petroleum ether/ethyl acetate 9/1) = 0.25

HR-MS: (Acetonitrile, ESI+, m/z): calculated: 343.2116 [M+H]+; found: 343.2115 [M+H]+

1.1.2.2 Synthesis of C12VS

The synthesis of 12-[1-(biphenyl-4-ylsulfonyloxy)ethenylcarbonyloxy] dodecyl 2-(biphenyl-4-ylsulfonyloxy)prop-2-enoate (C12VS) was performed based on a procedure described by Gorsche et al (Scheme 25).35

Scheme 25: Synthesis of mesogen-containing AFCT chain transfer agent C12VS.

70 mL dry CH₂CL₂, C12DP (3.65 g, 10.7 mmol, 1 eq), 1,4-diazabicyclo[2.2.2]octane (DABCO, 2.86 g, 25.5 mmol, 2.4 eg) and a minimal amount of butylhydroxytoluene (BHT) were transferred to a 250 mL three-necked round bottom flask under counter current of dry synthetic air and cooled to 0 °C. Biphenylsulfonyl chloride (5.81 g, 23.0 mmol, 2.2 eg) dissolved in 70 mL CH₂Cl₂ was added dropwise to the reaction mixture. The temperature of the reaction mixture was kept below 7 °C during the addition. After 2 h of stirring at 0 °C, the mixture was allowed to warm up to room temperature and stirred for 72 h. The mixture was filtered through a thin layer of silica and the filtrate was washed twice with 50 mL portions of 1 N HCl, once with 50 mL H₂O and twice with 50 mL portions of brine. The aqueous solutions were combined and extracted three times with 50 mL CH₂Cl₂ each. The organic phases were collected and dried over anhydrous Na₂SO₄. The solution was

stabilized with around 5 mg butylhydroxytoluene (BHT) and concentrated using a rotary evaporator. The crude mixture was purified using medium pressure column chromatography (petroleum ether/ethyl acetate) using gradient elution. The ethyl acetate concentration of 0% (v/v) at the start was raised to 10% over the course of 30 min. After 30 min, the concentration was raised to 20% over the course of 25 min and then to 100% over the course of 65 min. The fractions containing the product were stabilized with around 5 mg BHT and concentrated using a rotary evaporator. 6.0 g (72.6%) of C12VS were obtained as a white powder.

¹H-NMR (400 MHz, CDCl₃): δ (ppm) = 8.03 (d, 4H, Ar-H), 7.76 (d, 4H, Ar-H), 7.61 (d, 4H, Ar-H), 7.49 (t, 4H, Ar-H), 7.44 (t, 2H, Ar-H), 6.18 (d, 2H, C=CH₂), 5.69 (d, 2H, C=CH₂), 4.09 (t, 4H, O-CH₂-CH₂), 1.56 (m, 4H, CH₂-CH₂-CH₂), 1.26 (m, 16H, CH₂-CH₂-CH₂).

¹³C NMR-APT (101 MHz, CDCl3) δ (ppm) = 161.15 (- \underline{C} =O), 147.46 (- \underline{C} =CH₂), 143.44, 139.00, 134.32, 129.29 (-Car), 129.21 (-Car), 129.01 (-Car), 127.81 (-Car), 127.51 (-Car), 117.18 $(-C=CH_2)$, 66.36 $(O-CH_2-CH_2-)$, 29.58 $(CH_2-CH_2-CH_2-)$, 29.30 $(CH_2-CH_2-CH_2-)$, 28.50 $(CH_2-\underline{C}H_2-CH_2-)$, 25.87 $(CH_2-\underline{C}H_2-CH_2-)$.

 R_f -value (petroleum ether/ethyl acetate 9/1) = 0.58

HR-MS: (Acetonitrile, ESI+, m/z): calculated: 797.2424 [M+Na]+; found: 797.2433 [M+H]+

1.1.3 Reference chain transfer agent DVS

The literature-known reference chain transfer agent (11-[1-(4-methyl-phenylsulfonyloxy)ethenyl carbonyloxy]-3,6,9-trioxaundecyl 2-(4-methylphenylsulfonyloxy) prop-2-enoate) (DVS) was synthesized according to Gorsche et al. (Scheme 26).³⁵

Scheme 26: Synthesis of reference AFCT chain transfer agent DVS.

80 mL dry CH₂CL₂, TDP (5.35 g, 16.0 mmol, 1 eq, for synthesis see chapter 1.1.1.1), 1,4diazabicyclo[2.2.2]octane (DABCO, 4.33 g, 38.6 mmol, 2.4 eq) and around 5 mg of butylhydroxytoluene (BHT) were transferred to a reaction flask under counter current of dry synthetic air and cooled to 0 °C. p-Tosylsulfonyl chloride (6.75 g, 35.4 mmol, 2.2 eq, dissolved in 70 mL CH₂Cl₂) was added dropwise to the reaction mixture. The reaction mixture was kept below a temperature of 7 °C during the addition. After 2 h of stirring at 0 °C, the mixture was allowed to warm up to room temperature and stirred for 72 h. The mixture was filtered through a thin layer of silica and the filtrate was washed twice with 50 mL portions of 1N HCl, once with 50 mL H₂O and twice with 50 mL portions of brine. The aqueous solutions were combined and extracted three times with 50 mL CH₂Cl₂ each. The organic phases were collected and dried over anhydrous Na₂SO₄. The solution was stabilized with around 5 mg BHT and concentrated using a rotary evaporator. The crude mixture was purified using medium pressure column chromatography (petroleum ether/ethyl acetate; the ethyl acetate concentration was raised from 30 to 100% over the course of 90 min). The fractions containing the product were stabilized with around 5 mg BHT and concentrated using a rotary evaporator. 3.54 g (34.4%) of DVS were obtained as a clear oil.

¹H-NMR (400 MHz, CDCl₃): δ (ppm) = 7.84 (d, 4H), 7.34 (d, 4H), 6.15 (d, 2H), 5.62 (d, 2H), 4.25 (t, 4H), 3.64 (m, 12H), 2.45 (s, 6H)

¹³C NMR-APT (101 MHz, CDCl₃) δ (ppm) = 161.02, 145.68, 143,12, 132.60, 129.94, 128.67, 117.33, 70.76, 68.64, 65.10, 21.85

 R_f -value (petroleum ether/ethyl acetate 1/1) = 0.25

1.2 Selection of crosslinker

To prepare the formulations, the components were weighed into a brown glass vial starting with the compound making up the smallest part (in weight) of the final formulation. 0.5 mol% Ivocerin was used as photoinitiator in all formulations after determining it as the optimal concentration in a preliminary experiment. Homogeneity was ensured by mixing the formulations on a vortex mixer. This process was done in an orange light laboratory and the brown glass vials containing the formulations were covered with aluminium foil before they were taken outside the orange light laboratory. Formulations containing 10 db% Bomar were additionally warmed to 45 °C using a water bath before mixing with the vortex mixer multiple times to facilitate the homogenization process.

Table 25: Formulations used in the preliminary study to determine which crosslinker should be used in future experiment. The monomer trimethylolpropane formal acrylate (SR531) was combined with varying concentrations of the crosslinkers Bomar XR-741MS (Bomar) and 1,10-decanediol dimethacrylate (D3MA). Amounts are given in monomer ratio (r) and in mass (m) for one gram of formulation, which was the most commonly prepared amount of formulation. Every formulation also contains 0.5 mol% Ivocerin as a photoinitiator, which was added on top of the one-gram quantity.

Formulation	SR531		Воі	mar	D3MA	
name	r (db%)	m (mg)	r (db%)	m (mg)	r (db%)	m (mg)
SR531	100	1000	0	0	0	0
5% B	95	884	5	116	0	0
10% B	90	783	10	217	0	0
5% D	95	961	0	0	5	39
10% D	90	921	0	0	10	79

The cuboid samples (DIN EN ISO 6721) for the DMTA measurements were cured in a silicone mold using an Uvitron IntelliRay 600 Shuttered UV Floodlight at 50% intensity (approximately 90 mW·cm⁻², emission spectrum in Figure 118) for 300 s. The samples were turned around and irradiated a second time from the other side to ensure complete curing.

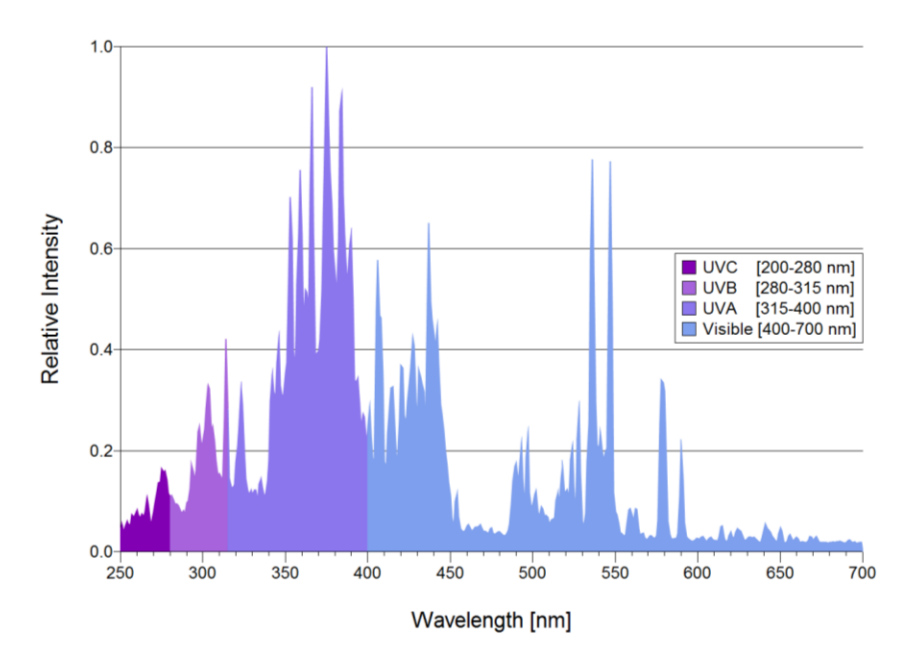


Figure 118: Emission spectrum of the Uvitron IntelliRay 600 Shuttered UV Floodlight.

DMTA measurements were performed according to the procedure in chapter 6 of the Methods section in a temperature range of -25 to 200 °C.

For the sample not containing any crosslinker, the measurements were aborted early as there were concerns about the samples melting inside the measurement clamps. In these cases, the measurements were aborted soon after the loss factor peak had been reached.

1.3 Photoreactivity study

Photoreactivity was tested for the formulations listed in Table 26.

Table 26: Formulations used to test AFCT agents: the monomer trimethylolpropane formal acrylate (SR531) was combined with varying concentrations of the crosslinker Bomar XR-741MS (Bomar) and chain transfer agents C12VS and DVS. Amounts are given in monomer ratio (r) and in mass (m) for one gram of formulation, which was the most commonly prepared amount of formulation. Every formulation also contains 0.5 mol% Ivocerin (in relation to reactive double bonds) as a photoinitiator, which was added on top of the one-gram quantity.

Formulation	SR	531	Воі	mar	C12VS		DVS	
name	r (db%)	m (mg)						
SR531	100	1000	0	0	0	0	0	0
10B	90	783	10	217	0	0	0	0
2.5C12VS	97.5	953	0	0	2.5	47	0	0
2.5DVS	97.5	960	0	0	0	0	2.5	40
10B2.5C12VS	87.5	746	10	213	2.5	41	0	0
10B2.5DVS	87.5	751	10	214	0	0	2.5	34
10B10C12VS	80	643	10	201	10	156	0	0
10B10DVS	80	661	10	206	0	0	10	133

Photo-DSC measurements were performed according to the procedure in chapter 4 of the Methods section.

RT-NIR-photorheology measurements were performed according to the procedure in chapter 5 of the Methods section.

1.4 Thermomechanical behavior

The cuboid samples (DIN EN ISO 6721) for the DMTA measurements were cured in a silicone mold using an Uvitron IntelliRay 600 Shuttered UV Floodlight at 50% intensity (approximately 90 mW·cm⁻², emission spectrum in Figure 118) for 300 s. The samples were turned around and irradiated a second time from the other side to ensure complete curing.

DMTA measurements were performed for polymers cured from all formulations listed in Table 26 according to the procedure in chapter 6 of the Methods section in a temperature range of -25 to 200 °C.

For the samples not containing any crosslinker, the measurements were aborted early as there were concerns about the samples melting inside the measurement clamps. In these cases, the measurements were aborted soon after the loss factor peak had been reached.

1.5 Mechanical tests

The samples (DIN EN ISO 527 test specimen 5b) for tensile tests were produced in analogy to the DMTA specimens mentioned above in chapter 1.4.

Tensile tests were performed of polymers cured from all formulations listed in Table 26 according to the procedure in chapter 7 of the Methods section. The resulting stressstrain curve was integrated numerically using the trapezoidal rule using the software OriginPro to obtain the toughness of each sample.

2 Synthesis and characterization of monomers

2.1 Synthesis of liquid crystalline monomers

2.1.1 LCM5

LCM5 was synthesized according to Imae et al. 128

4,4'-Dihydroxybiphenyl (1 eq, 0.0705 mol, 13.13 g) and triethylamine (2.2 eq, 0.1551 mol, 15.69 g) were dissolved in 300 mL THF and stirred under argon atmosphere. After cooling to 0 °C, 10-undecenoyl chloride (2.1 eq, 0.1445 mol, 30.02 g) was added slowly, and the reaction was allowed to warm up to room temperature slowly, after which it was stirred for another 48 h. The mixture was filtered through a thin layer of silica, which was washed with CH₂Cl₂. Then, the solvent was removed from the filtrate using a rotational evaporator. After recrystallization from a small amount of ethanol and drying under vacuum, 34.05 g (92%) of the product were isolated as white flakes.

Scheme 27: Synthesis of LCM5.

Melting point analysis on the polarized optical microscope (POM) showed a viscous liquid crystalline phase (~2000 MPa s by melt rheology) from 78 to 111 °C. HPLC analysis of the product showed no impurities (Figure 119).

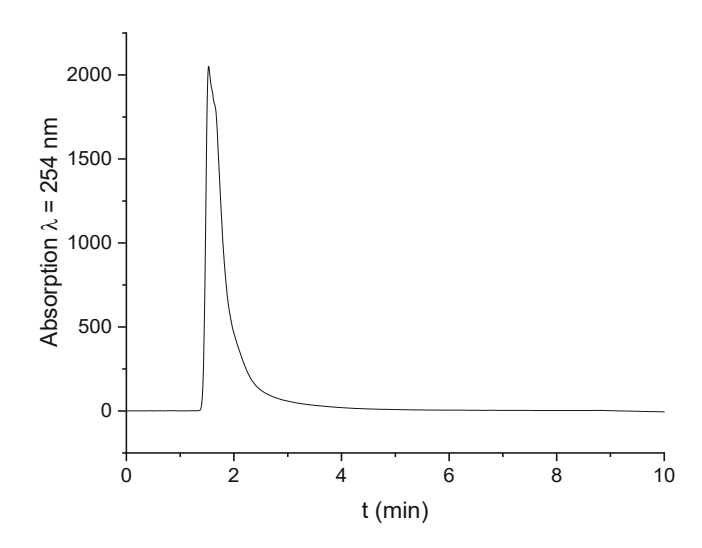


Figure 119: HPLC chromatogram of LCM5 in a CN-functionalized normal phase column with a heptanechloroform gradient (UV detection at 254 nm).

 R_f -value (petroleum ether/ethyl acetate 10/1) = 0.48

¹H NMR (400 MHz, CDCl₃) $\delta = 7.57 - 7.52$ (m, 4H, Ar-<u>H</u>), 7.18 - 7.08 (m, 4H, Ar-<u>H</u>), 5.89 -5.70 (m, 2H, $=C\underline{H}_2$), 5.03 - 4.91 (m, 4H, $-C\underline{H}_2$), 2.58 (t, J = 7.5 Hz, 4H, $-C\underline{H}_2$ -), 2.06 (tdd, J =6.6, 5.3, 1.4 Hz, 4H, -C<u>H</u>₂-), 1.83 – 1.71 (m, 4H, -C<u>H</u>₂-), 1.37 (m, 16H, -C<u>H</u>₂-).

¹³C NMR-APT (101 MHz, CDCl₃) δ = 172.51 (-C=O), 150.37 (C_{Ar}-C=O), 139.32 (-CH=), 138.21 (\underline{C}_{Ar} -H), 128.27 (\underline{C}_{Ar}), 122.05 (\underline{C}_{Ar}), 114.32 ($=\underline{C}_{H_2}$), 34.58 ($O-\underline{C}_{H_2}$ -CH), 33.94 ($-\underline{C}_{H_2}$ -), 29.44 (-<u>C</u>H₂-), 29.36 (-<u>C</u>H₂-), 29.24 (-<u>C</u>H₂-), 29.20 (-<u>C</u>H₂-), 29.05 (-<u>C</u>H₂-), 25.10 (-<u>C</u>H₂-).

HR-MS: (Acetonitrile, ESI+, m/z): calculated: 519.3470 [M+H]⁺; found: 519.3472 [M+H]⁺

DSC analysis of the product was performed with a heating and cooling ramp of 10 °C·min⁻¹.

Heating (DSC): Cr 76.6 SmX 111.3 I

Cooling (DSC): I 109.8 SmX 72.7 Cr

2.1.2 LCM6

2.1.2.1 Synthesis of precursor HBE

4-(5-Hexen-1-yl)benzoic acid methyl ester (HBE) was synthesized according to Fürstner et al (Scheme 28). 130

Scheme 28: Synthesis of HBE according to Fürstner et al. 130

First, magnesium turnings (1.25 eq, 7.35 g, 302.5 mmol) were transferred into a 1 L argonflushed round bottom flask. The flask was flame-dried under vacuum while stirring the magnesium turnings. After cooling to ambient temperature and flushing with argon, the magnesium turnings were covered with approximately 40 mL dry THF. A solution of 6bromo-1-hexene (1 eq. 39.54 g, 242.5 mmol) in 250 mL dry THF was then added using a dropping funnel. Initially, a larger amount was added to start the reaction. After a noticeable increase in temperature, the dropping frequency was reduced to maintain controlled reflux of the mixture. Upon complete addition, the mixture was refluxed for another 30 min. The resulting solution of hexenylmagnesium bromide with a concentration of approximately 1 mol L⁻¹ was cooled to room temperature and prepared to be transferred via cannula by equipping the flask with a rubber septum.

Next to the first apparatus, a 2 L argon-flushed round bottom flask was prepared. THF (500 mL), 4-chlorobenzoic acid methyl ester (1 eq. 32.50 g. 190.5 mmol), Fe(acac)₃ (0.05 eq, 3.37 g, 9.6 mmol) and N-methylpyrrolidone (NMP, 65 mL) were transferred to the flask under argon countercurrent. The freshly prepared solution of hexenylmagnesium bromide (1.27 eq, 242.5 mmol, 1 mol L⁻¹ in THF) was added to the red solution via transfer cannula while stirring vigorously, causing a rapid color change to dark brown and then finally to dark violet. After stirring for around 20 min at room temperature, the mixture was diluted with around 300 mL of diethyl ether and slowly quenched using 1.5M aq. HCl until a pH of ~2-3 was reached while cooling with an ice bath. ~100 mL H₂O were added and the mixture was extracted three times with Et₂O. The combined organic phases were dried over Na₂SO₄ followed by evaporation of the solvent. The crude product was dissolved in petroleum ether/ethyl acetate 30/1 and filtered through silica, which afforded a clear oil identified as a mixture of HBE and 4-chlorobenzoic acid by GC-MS and NMR analysis.

Fine vacuum distillation (2·10⁻² mbar, 100 °C) was used to purify the product. Residual impurities of the chloride reactant in one fraction were removed by fine-vacuum drying of the product at around 80 °C.

14.55 g (35%) of the product were obtained as a clear oil.

¹H NMR (400 MHz, CDCl₃): δ (ppm) = 7.94 (d, 2H), 7.24 (d, 2H), 5.79 (m, 1H), 4.97 (m, 2H), 3.90 (s, 3H), 2.66(t, 2H), 2.08 (m, 2H), 1.65 (m, 2H), 1.42 (m, 2H)

¹³C NMR-APT (101 MHz, DMSO) δ (ppm) = 165.65 (COOCH₃), 148.60 (C_{Ar}), 139.08 $(CH=CH_2)$, 129.84 $(C_{Ar}-H)$, 128.80 $(C_{Ar}-H)$, 128.23 (C_{Ar}) , 115.26 $(CH=CH_2)$, 52.08 $(COOCH_3)$ 35.36 (CH₂-CH₂), 33.39 (CH₂-CH₂), 30.52 (CH₂-CH₂), 28.24 (CH₂-CH₂)

 R_f -value (petroleum ether/ethyl acetate 30/1) = 0.5.

2.1.2.2 Synthesis of intermediate HBA

The methyl ester was split under alkaline conditions according to Fürstner to obtain 4-(5hexen-1-yl)benzoic acid (HBA, Scheme 29). 131

Scheme 29: Ester splitting of HBE to form the free carboxylic acid HBA.

250 mL of methanol, 250 mL of 1M aqueous NaOH and HBE (22.5 g, 103.1 mmol) were transferred to a 1 L round bottom flask equipped with a reflux condenser. The mixture was heated at reflux for 18 h. After cooling to room temperature approximately 400 mL of 1.5 M aqueous HCl were used to acidify the mixture. The solution was transferred to a separatory funnel and extracted four times with 250 mL portions of ethyl acetate. The combined organic layers were dried over sodium sulphate, filtered, and concentrated using a rotary evaporator. After recrystallization from approximately 150 ml hexanes, 19.8 g (94%) HBA were obtained as an off-white solid.

¹H NMR (400 MHz, DMSO) δ = 12.76 (s, 1H), 7.92 – 7.81 (m, 2H), 7.36 – 7.26 (m, 2H), 5.78 (ddt, J = 16.9, 10.2, 6.7 Hz, 1H), 5.06 - 4.89 (m, 2H), 2.64 (t, J = 7.6 Hz, 2H), 2.12 - 1.98 (m, 2H), 2.12 - 1.2H), 1.69 – 1.50 (m, 2H), 1.44 – 1.30 (m, 2H).

¹³C NMR-APT (101 MHz, DMSO) δ (ppm) = 167.80 (COOH), 148.08 (C_{Ar}), 139.05 (CH=CH₂), 129.84 (\underline{C}_{Ar} -H), 128.80 (\underline{C}_{Ar} -H), 128.66 (\underline{C}_{Ar}), 115.25 (\underline{C}_{H2} - \underline{C}_{H2}), 35.34 (\underline{C}_{H2} - \underline{C}_{H2}), 33.41 (\underline{C}_{H2} -CH₂), 30.54 (<u>C</u>H₂-CH₂), 28.27 (<u>C</u>H₂-CH₂).

 R_f -value (petroleum ether/ethyl acetate 1/1) = 0.35

The melting behavior was analyzed using a polarized optical microscope (POM).

Phase transitions (POM): Cr 85 N 105 I (Lit. Cr 84 N 114 I)

2.1.2.3 Synthesis of monomer LCM6

The final step was performed according to Zhang et al.¹³² with improvements by Jordan et al (Scheme 30). 133

Scheme 30: Synthesis of liquid crystalline monomer LCM6 using the reagents 1-ethyl-3-(3dimethylaminopropyl)carbodiimide hydrochloride (EDC.HCl), dimethylaminopyridine (DMAP) and the solvent dichloromethane (CH₂Cl₂).

4-(5-Hexen-1-yl)benzoic acid (4.43 g, 22.5 mmol, 2.12 eq) hydroquinone (1,126 g, 10.2 mmol, 1 eg), and dimethylaminopyridine (DMAP, 0.568 g, 4.6 mmol, 0.45 eg) were stirred in 140 mL of anhydrous dichloromethane in an oven-dried, argon-flushed flask. After cooling the mixture below -10 °C using an NaCl/ice bath, 1-ethyl-3-(3dimethylaminopropyl)carbodiimide hydrochloride (EDC.HCl, 4.31 g, 22.5 mmol, 2.20 eg) dissolved in 160 mL of dichloromethane was slowly dripped into the reaction mixture using a dropping funnel while keeping the temperature below -5 °C. The mixture was stirred for 48 h after slowly being allowed to warm up to room temperature. The mixture was extracted three times with 100 mL portions of water and dried over sodium sulphate. The combined organic phases were filtered through a small amount of silica, after which the solvent was removed under reduced pressure. After purification by recrystallization from around 250 mL methanol, 2.86 g of LCM6 (58%) were obtained as a white powder.

¹H NMR (400 MHz, CDCl₃): $\delta = 8.12$ (d, 4H, Ar- \underline{H}), 7.33 (d, 4H, Ar- \underline{H}), 7.27 (s, 4H, Ar- \underline{H}), 5.81 (m, 2H, =C \underline{H} -), 4.99 (m, 4H, =C \underline{H} ₂), 2.72 (t, 4H, -C \underline{H} ₂-), 2.11 (m, 4H, -C \underline{H} ₂-), 1.69 (m, 4H, -C<u>H</u>₂-), 1.46 (m, 4H, -C<u>H</u>₂-)

¹³C NMR-APT (101 MHz, CDCl₃) δ = 165.14 (-C=O), 149.22 (-C_{Ar}-O), 148.43 (-C_{Ar}-C=O), 138.63 (= \underline{C} H-), 130.32 (\underline{C}_{Ar} -H), 128.70 (\underline{C}_{Ar} -H), 126.91 (- \underline{C}_{Ar} -CH₂), 122.66 (\underline{C}_{Ar} -H), 114.63 $(=CH_2)$, 35.93 $(-CH_2-)$, 33.56 $(-CH_2-)$, 30.55 $(-CH_2-)$, 28.46 $(-CH_2-)$.

 R_f -value (petroleum ether/ethyl acetate 30/1) = 0.42

HR-MS: (Acetonitrile, ESI+, m/z): calculated: 505.2349 [M+Na]⁺; found: 505.2357 [M+Na]⁺ DSC analysis of the product was performed with a heating and cooling ramp of 10 °C·min⁻¹.

Heating (DSC): Cr 104.5 LC 173.0 I

Cooling (DSC): I 172.0 LC 100.0 Cr

2.1.3 LCM7

2.1.3.1 Synthesis of precursor HOEBA

4-(2-Hydroxyethyl)benzoic acid (HOEBA) was synthesized by hydrolysis of 4-(2-hydroxyethyl)benzonitrile as reported by Liverton et al. (Scheme 31). 134

Scheme 31: Hydrolysis of 4-(2-hydroxyethyl)benzonitrile to 4-(2-hydroxyethyl)benzoic acid. 134

4-(2-hydroxyethyl)benzonitrile (10 g, 680 mmol) was added to 400 mL ethanol. After adding 140 mL of 2M NaOH, the solution was heated to 100 °C and stirred for 24 h at this temperature. The solvents were evaporated using a rotary evaporator. The remaining white solid was dissolved in 200 mL ethyl acetate and 500 mL saturated agueous sodium bicarbonate. The two phases were separated and the organic layer was discarded. The

aqueous layer was acidified using 6 N HCl until pH 2 was reached. Afterwards, three portions of 250 mL ethyl acetate each were used to extract the product. The organic phases were collected, dried over Na₂SO₄, filtered and evaporated. 10.7 g (94%) of the product were obtained as an off-white crystalline solid.

¹H-NMR (400 MHz, DMSO) δ = 12.74 (s, 1H), 7.85 (d, J = 8.3 Hz, 2H), 7.37 – 7.30 (d, J = 8.3 Hz, 2H), 4.67 (t, J = 5.1 Hz, 1H), 3.63 (dt, J = 10.6, 5.0 Hz, 2H), 2.78 (t, J = 6.9 Hz, 2H).

Rf-value (ethyl acetate) = 0.20-0.35 (significant tailing is observed, R_f-value is higher with higher sample concentration)

The melting point of the substance was evaluated using polarized optical microscopy.

Melting point (POM): 127 °C (Lit. 127-128 °C)

2.1.3.2 Synthesis of intermediate AEBA

Afterwards, a Williamson ether synthesis was employed to obtain the intermediate (2allyloxyethyl)benzoic acid (AEBA) from HOEBA according to a modified procedure derived from a publication by Lee et al. (Scheme 16). 135

Scheme 32: Williamson ether synthesis using NaH according to Lee et al. 135

A solution of HOEBA (8.07 g, 48.5 mmol, 1 eq) in anhydrous THF (350 mL) was prepared under argon atmosphere and cooled to 0 °C. NaH (7.43 g, 60% dispersion in mineral oil, 185.8 mmol, 3.83 eg) was added. Upon stirring for 20 min at 0 °C, allyl bromide (13.49 g, 111.5 mmol, 2.3 eq) was added. After 4 h, the reaction mixture was allowed to warm to room temperature and subsequently heated to 60 °C. After stirring for 48 h at 60 °C, additional NaH (1.94 g, 48.5 mmol, 1 eg) and allyl bromide (5.86 g 48.5 mmol, 1 eg) were added and stirring was continued for another five days at 60 °C. Thereafter, the mixture was cooled to room temperature, diluted by adding approximately 250 mL CH₂Cl₂ and quenched using approximately 250 mL saturated aqueous ammonium chloride. After separation of the layers, the aqueous layer was extracted another three times with CH₂Cl₂. The combined organic phases were dried over anhydrous Na₂SO₄ and concentrated using a rotary evaporator. The residue was purified using medium pressure column chromatography (silica gel, petroleum ether/ethyl acetate, 3/1 isocratic) to afford AEBA as a yellow solid that crystallized slowly at room temperature (8.41 g, 84%).

¹H-NMR (400 MHz, DMSO) δ = 12.77 (s, 1H), 7.89 – 7.82 (m, 2H), 7.39 – 7.32 (m, 2H), 5.85 (ddt, J = 17.3, 10.5, 5.3 Hz, 1H), 5.20 (dq, J = 17.3, 1.8 Hz, 1H), 5.11 (dq, J = 10.4, 1.5 Hz, 1.51H), 3.93 (dt, J = 5.3, 1.6 Hz, 2H), 3.62 (t, J = 6.7 Hz, 2H), 2.89 (t, J = 6.7 Hz, 2H).

¹³C NMR-APT (101 MHz, DMSO) δ 167.32 (-COOH), 144.63 (C_{Ar}), 135.21 (-CH=CH₂), 129.25 $(C_{Ar}-H)$, 129.09 $(C_{Ar}-H)$, 128.65 (C_{Ar}) , 116.28 $(-CH=CH_2)$, 70.78 $(-CH_2-)$, 69.90 $(-CH_2-)$, 35.49 $(-CH_2-).$

 R_f -value (ethyl acetate) = 0.78

HR-MS: (Acetonitrile, ESI+, m/z): calculated: 207.1016 [M+H]+; found: 207.1015 [M+H]+ Melting point: 24-27 °C

2.1.3.3 Synthesis of monomer LCM7

The final step was performed according to Zhang et al. 132 with improvements by Jordan et al. (Scheme 33).¹³³

Scheme 33: Synthesis of liquid crystalline monomer LCM7.

AEBA (8.56 g, 41.5 mmol, 2.12 eq) hydroquinone (2.16 g, 19.6 mmol, 1 eq), and dimethylaminopyridine (1.09 g, 8.9 mmol, 0.45 eq) were stirred in 200 mL anhydrous dichloromethane in an oven-dried, argon-flushed flask. After cooling the mixture to -10 °C using an NaCl/ice bath, 1-ethyl-3-(3-dimethylaminopropyl)carbodiimide hydrochloride (EDC.HCl 8.24 g, 43.0 mmol, 2.20 eq) dissolved in 250 mL dichloromethane was added dropwise while keeping the temperature below -5 °C. The mixture was allowed to slowly warm up to room temperature and continued to be stirred for 48 h. The mixture was extracted three times with 100 mL portions of water and dried over sodium sulphate. The mixture was filtered through a small amount of silica, after which the solvent was removed under reduced pressure. After purification by recrystallization from around 200 mL methanol, 7.90 g of LCM7 (83%) were obtained as white needle-shaped crystals.

¹H NMR (400 MHz, DMSO) δ = 8.07 (d, J = 8.29 Hz, 4H, Ar- \underline{H}), 7.50 (d, J = 8.30 Hz, 4H, Ar-H), 7.38 (s, 4H, Ar-H), 5.86 (m, 2H, =CH-), 5.30 - 5.06 (m, 4H, $=CH_2$), 3.95 (m, 4H, $-CH_2-$), 3.66 (t, J = 6.6 Hz, 4H, $-C\underline{H}_2$ -), 2.96 (t, J = 6.6 Hz, 4H, $-C\underline{H}_2$ -).

¹³C NMR-APT (101 MHz, CDCl₃) $\delta = 165.20 (-C=0)$, 148.56 (-C=0), 145.80 (C=0), 134.78 (= $\underline{C}H$ -), 130.45 (- \underline{C}_{Ar}), 129.36 (- \underline{C}_{Ar}), 127.54, (- \underline{C}_{Ar}) 122.79 (- \underline{C}_{Ar} - $\underline{C}H_2$), 117.17 (= $\underline{C}H_2$), 72.10 ($-CH_2$ -), 70.62 ($-CH_2$ -), 36.62 ($-CH_2$ -)

 R_f -value (petroleum ether/ethyl acetate 2/1) = 0.56

HR-MS: (Acetonitrile, ESI+, m/z): calculated: 509.1934 [M+Na]⁺; found: 509.1936 [M+Na]⁺ DSC analysis of the product was performed with a heating and cooling ramp of 10 °C·min⁻¹.

Heating (DSC): Cr 97.0 LC 104.0 I

Cooling (DSC): I 102.0 LC 81.5 Cr (Cr-Cr phase transitions at 73.5, 69.0, 66.5 °C)

2.1.4 Liquid crystalline dithiol LCDT

The synthesis of LCDT was performed using a bulk thiol-ene click reaction (Scheme 35).

LCM6 (0.63 g, 1.3 mmol, 1 eq) and ethanedithiol (2.45 g, 26 mmol, 20 eq) were stirred at room temperature in a three-necked flask. The mixture was heated to 75 °C over the course of 2 h, throughout which 0.21 g (1.3 mmol) azobisisobutyronitrile (AIBN) were added in four equal portions. Afterwards, the mixture was stirred at 75 °C overnight. Next, the dithiol and the degradation products of AIBN were distilled off at 20 mbar and 42 °C. After most of the reaction mixture had been distilled off, the flask was kept under fine vacuum (2.1·10⁻² mbar) at 80 °C. The remainder of the contents of the flask was suspended in 100 mL methanol, heated to 60 °C, and filtered hot. The filter cake was investigated via NMR, which confirmed full conversion of the double bonds.

Scheme 34: Synthesis of liquid crystalline dithiol monomer LCDT.

After purification by fine vacuum drying at elevated temperature and washing with hot methanol, 0.8 g (92%) of the product were afforded as a white solid with a strong, unpleasant odor.

Investigation of successful thiol end-capping and purity by NMR proved difficult, as residues of ethanedithiol could be wrongly identified as end groups. Additionally, the chemical shifts overlap with the methylene spacer chains, further hindering full characterization. Oligomerization was investigated via gel permeation chromatography according to the procedure in chapter 1 of the Methods section.

¹H-NMR (600 MHz, CDCl₃) δ = 8.12 (d, 4H), 7.32 (d, 4H), 7.25 (s, 4H), 2.92 – 2.80 (m, 4H), 2.77 – 2.66 (m, 8H), 2.57-2.50 (m, 4H), 1.70 – 1.63 (m, 4H), 1.59 (m, 6H), 1.48 – 1.40 (m, 4H), 1.40-1.32 (m, 4H).

 R_f -value (petroleum ether/ethyl acetate 5/1) = 0.48

The melting point was determined by polarized optical microscopy (POM).

Phase transitions (POM): Cr 104 LC 130 I

HR-MS and ¹³C-APT-NMR spectra were not measured as the synthesis was not pursued further due to oligomerization of the product, which could not be avoided.

2.2 Synthesis of trithiol crosslinkers

2.2.1 Trithiol crosslinker CHTT

2-[2,4-Bis(2-mercaptoethyl)cyclohexyl]ethanethiol (CHTT) was synthesized according to a modified procedure reported by van Damme et al. 137

2.2.1.1 Synthesis of precursor

To synthesize the precursor ethanethioic acid, S1,S1,',S1,''-(1,2,4-cyclohexanetriyltri-2,1ethanediyl) ester, a bulk thiol-ene click reaction was employed (Scheme 35).

Scheme 35: Synthesis of precursor ethanethioic acid, $S^1, S^1', S^1'' - (1,2,4-cyclohexanetriyltri-2,1-ethanediyl)$ ester.

1,2,4-trivinylcyclohexane (mixture of isomers, 40 g, 246.52 mmol, 1 eq) was transferred into a 250 mL round bottom flask and cooled to -10 °C in an ice-NaCl bath under an argon atmosphere. While stirring and continuously cooling in the ice-NaCl bath, thioacetic acid (60.05 g, 788.86 mmol, 3.2 eg) was added slowly. After around 30 min, 2,2dimethoxy-2 phenylacetophenone (IRGACURE 651, 1.6 g, 4 wt%; 6.24 mmol) was added in three portions. After each portion, the reaction mixture was irradiated for 20 min with UV light (Omnicure S2000; 320-500 nm filter; 110 mW cm⁻² at the source, emission profile in Figure 120) through a Lumatec Series 300 liquid light guide, which was place onto a quartz glass window attached to one of the necks.

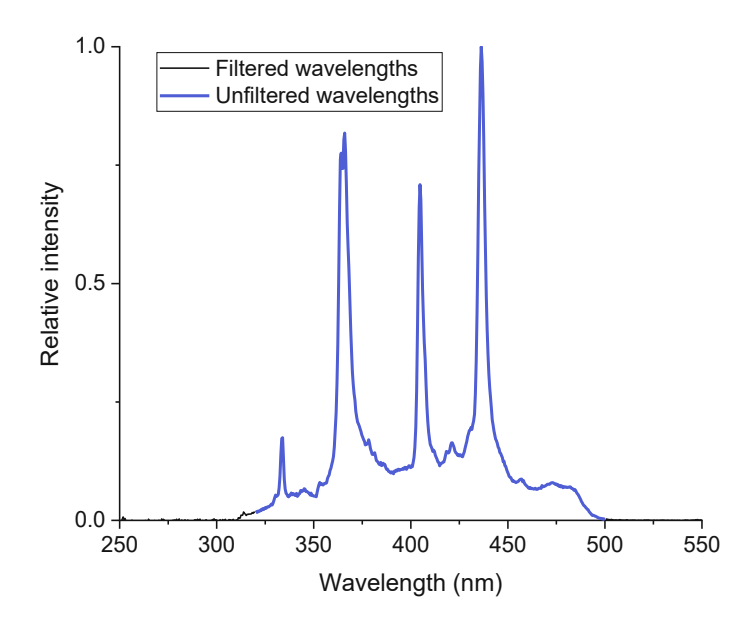


Figure 120: Emission spectrum of the light source used for photochemical synthesis. In blue, the unfiltered wavelengths are shown.

The reaction was stopped after ¹H NMR analysis showed full double bond conversion as the double bond peaks had fully disappeared (4.88-5.09 and 5.62-6.02 ppm). The obtained orange oil, which exhibited a strong thiol odor, was used without further purification. Due to the efficiency of the thiol-ene click reaction and the reaction control confirming full double bond conversion, the yield of the intermediate was assumed as 96.29 g (quantitative).

 1 H NMR (400 MHz, CDCl₃) δ 3.04 – 2.71 (m, 6H), 2.37 – 2.22 (m, 9H), 1.91 – 0.57 (m, 15H).

2.2.1.2 Synthesis of CHTT

The intermediate product was dissolved in THF (600 mL) in a round bottom flask, the solution was cooled to 0 °C and 2 M NaOH (560 mL) was added. After 30 min, the mixture was allowed to warm up to room temperature and stirring was continued for another 48 h before neutralization with approximately 300 mL 4 M HCl, during which the mixture was cooled. Next, the mixture was extracted three times with 200 mL portions of diethyl ether. The combined organic phases were washed with approximately 150 mL brine, dried over sodium sulfate, and concentrated using a rotary evaporator. ¹H-NMR of the crude product was performed and revealed that the acetate peak (2.22 to 2.37 ppm) had fully disappeared, and the crude product was obtained as an orange oil with a strong thiol odor.

Scheme 36: Alkaline hydrolysis to obtain CHTT.

The product was then distilled in two batches at 145 °C and a pressure of 0.022 mbar. 47.1 g (77.5%) of 1,2,4-Cyclohexanetriethanethiol (CHTT, mixture of isomers) were isolated as a clear liquid with a slight thiol odor.

¹H NMR (400 MHz, CDCl₃) δ = 2.69 – 2.36 (m, 6H), 1.90 – 0.57 (m, 18H).

 R_f -value (petroleum ether/ethyl acetate 10/1) = 0.6 (significant tailing)

2.2.2 Trithiol crosslinker MTSH

The synthesis of the mesitylene-derived trithiol crosslinker MTSH (mesitylene tri-SH) was performed according to a procedure outlined by Li et al. and modified according to Han et al. (Scheme 37). 138, 139

Scheme 37: Synthesis of mesitylene-based trithiol crosslinker MTSH.

1,3,5-tri(bromomethyl)benzene (2.00 g, 5.6 mmol, 1 eq), thioacetic acid (1.53 g, 1421 µL, 20.16 mmol, 3.6 eq) and K₂CO₃ (2.79 g, 20.16 mmol, 3.6 eq) were stirred in methanol

(24 mL) in a 100 mL round bottom flask at ambient temperature for 30 min under argon atmosphere. After adding another portion of K₂CO₃ (2.79 g, 20.16 mmol, 3.6 eg), the mixture was stirred for another 30 min before acidification to pH 4 using 6 M HCl. The reaction mixture was diluted with 50 mL deionized water and extracted with three 50 mL portions of CHCl₃. The combined organic phases were dried over Na₂SO₄ and filtered through Celite as an unidentified precipitate could not be removed using filter paper. Afterwards, the filtrate was concentrated under vacuum, yielding an oily, slightly yellow liquid (0.62 g, 51%).

¹H NMR (400 MHz, CDCl₃) δ 7.28 (s, 3H), 3.73 (d, J = 7.5 Hz, 5H), 1.75 (t, J = 7.5 Hz, 2H) ppm.

 R_f -value (petroleum ether/ethyl acetate 10/1) = 0.66 (significant tailing)

HR-MS and ¹³C-APT-NMR spectra were not measured as the synthesis was not pursued further due to persistent impurities of the product, the high cost of the reactant and the reaction's unfavorable atom efficiency.

3 Synthesis and characterization of LCM-based polymers

3.1 LCM5-based polymers

3.1.1 Pre-screening experiment

To prepare the monomer mixtures, the thiol-ene formulating procedure in chapter 3 of the Methods section was followed.

Table 27: Formulations used to test LCM5 in linear and crosslinked polymers. Amounts of monomers are given in monomer ratio (r in functional group-percent, FG%) and in mass (m) for one gram of formulation, which was the most commonly prepared amount of formulation. Every formulation also contains 1 mol% (in relation to double bonds) Ivocerin as a photoinitiator and 0.1 wt% (in relation to total formulation mass) pyrogallol as stabilizer, which were added on top of the one-gram quantity.

F	LC	M5	Thiol comonomer			
Formulation name	r (FG%)	m (mg)	Туре	r (FG%)	m (mg)	
LCM5-HDT	50	775	HDT	50	225	
LCM5-EDDT	50	740	EDDT	50	260	
LCM5-TEMPIC	50	597	TEMPIC	50	403	
LCM5-TMPMP	50	661	TMPMP	50	339	
LCM5-ETTMP	50	526	ETTMP	50	474	
LCM5-CHTT	50	746	CHTT	50	254	

To prepare test specimens for qualitative evaluation of properties, the formulations from Table 27 were heated to an isotropic molten state, and then poured into a silicone mold, which was placed on a heated plate with a temperature of approximately 100 °C. The specimens were cured using a Uvitron IntelliRay 600 broadband UV floodlight at 100% intensity (approximately 180 mW·cm⁻², emission spectrum in Figure 118) for 300 s on each side.

3.1.1.1 Thermomechanical evaluation

To prepare DMTA specimens, the formulations listed above in Table 27 were heated to an isotropic molten state, and then poured into a silicone mold, which was placed on a

heated plate with a temperature of approximately 100 °C. The specimens were cured using a Uvitron IntelliRay 600 broadband UV floodlight at 100% intensity (approximately 180 mW·cm⁻², emission spectrum in Figure 118) for 300 s on each side.

DMTA measurements were performed of polymers obtained from formulations LCM5-TMPMP, LCM5-ETTMP and LCM5-CHTT according to the procedure in chapter 6 of the Methods section in a temperature range of -100 to 200 °C.

3.1.1.2 Phase analysis

Phase analysis was performed of all the formulations listed above in Table 27 on a polarized optical microscope according to the procedure in chapter 2 of the Methods section.

3.1.2 Design of heated polymerization chamber

The experimental details pertaining to the design and construction of the heated polymerization chamber are part of the results and discussion section due to their relevance to further work in this thesis. Measurements of the heat distribution and exact temperature of the silicone mold were performed by inserting flexible wire thermometers into different areas of the silicone mold at a depth of approximately 2 mm. The thermometers were connected to a PC via a Pico Technology interface. PicoLog version 6.2.8 was used to evaluate the results.

3.1.3 Optimization of polymerization parameters

To gain an approximate overview of parameters influencing polymer crystallinity, multiple small quantities (two to three drops) of formulation LCM5-CHTT listed in Table 28 were irradiated with various intensities and durations of the UVET UV-LED light source, which emits light at intensities of 290 to 2650 mW cm⁻² around a wavelength of 365 nm.

Table 28: Formulation used in the initial test to screen for crystallinity. Amounts of monomers are given in monomer ratio (r in functional group-percent, FG%) and in mass (m) for one gram of formulation, which was the most commonly prepared amount of formulation. Every formulation also contains 1 mol% (in relation to double bonds) Ivocerin as a photoinitiator and 0.1 wt% (in relation to total formulation mass) pyrogallol as stabilizer, which were added on top of the one-gram quantity.

Formulation	LC	M5	СНТТ		
name	r (FG%) m (mg)		r (FG%)	m (mg)	
LCM5-CHTT	50	746	50	254	

To determine crystallinity of small bulk samples, a visual and manual assessment of the sample was performed. The highest sample stiffness and opacity indicated the highest obtained crystallinity.

3.1.3.1 Single light source

To prepare the monomer mixtures, the thiol-ene formulating procedure in chapter 3 of the Methods section was followed.

Table 29: Formulations used to screen for crystallinity with various conditions. Amounts of monomers are given in monomer ratio (r in functional group-percent, FG%) and in mass (m) for one gram of formulation, which was the most commonly prepared amount of formulation. Every formulation also contains 1 mol% (in relation to double bonds) Ivocerin as a photoinitiator and 0.1 wt% (in relation to total formulation mass) pyrogallol as stabilizer, which were added on top of the one-gram quantity.

Formulation	LC	M5	CH	ITT
name	r (FG%)	m (mg)	r (FG%)	m (mg)
50/50	50	746	50	254
56/44	55.6	786	44.4	214

Preparation of test specimens was performed by placing a silicone mold in the heated polymerization chamber and preheating the chamber to the desired temperature with the lid closed. The silicone mold, which was made more thermally conductive by adding 20 wt% aluminium powder to its formulation, was prepared in an aluminium positive mold. DMTA negatives were prepared as cuboids with the dimensions 2x5x40 mm. Tensile test specimen negatives were prepared according to ISO 527 test specimen 5b.

Temperature was measured by a thermometer directly inserted into the silicone, which was connected to a Pico Technology interface, which allowed the temperature to be monitored on a PC. The formulations were cast into the silicone mold by melting them inside the vial and carefully pouring them into the silicone mold, which was already in the preheated chamber, after which the lid was placed back on the chamber.

After an equilibration period of around 3 min, the irradiation was started. After irradiation, the specimens were removed from the silicone mold carefully, turned upside down, and irradiated using the same procedure after heating to the desired temperature and a subsequent equilibration period of around 3 min.

The exact irradiation intensities and times are listed in Table 30.

Table 30: Formulations tested with different irradiation modes for the liquid crystal phase curing optimization study. For the LD initial curing step, a 60 s break was implemented between the 1 s curing steps.

	React. groups			Irradiation mode	
Formulation name	LCM5/CHTT (%/%)	Curing step	T (°C)	Time	Intensity (mW·cm ⁻²)
50/50 LC-LD	50/50	Initial curing	85	1 s on, 60 s off 1 s on, 60 s off 1 s on, 60 s off	290
		Final curing	85	180 s on	290
50/50 LC-MD	50/50	Final curing	85	180 s on	290
50/50 Iso-LD	50/50	Initial curing	120	1 s on, 60 s off 1 s on, 60 s off 1 s on, 60 s off	290
	_	Final curing	120	180 s on	290
56/44 LC-LD	56/44	Initial curing	85	1 s on, 60 s off 1 s on, 60 s off 1 s on, 60 s off	290
		Final curing	85	180 s on	290
56/44 LC-MD	56/44	Final curing	85	180 s on	290
56/44 Iso-LD	56/44	Initial curing	120	1 s on, 60 s off 1 s on, 60 s off 1 s on, 60 s off	290
		Final curing	120	180 s on	290

Tensile tests were performed according to the procedure in chapter 7 of the Methods section.

3.1.3.2 Combination of two light sources

To prepare the monomer mixtures, the thiol-ene formulating procedure in chapter 3 of the Methods section was followed.

Table 31: Formulations used to screen for crystallinity with various conditions. Amounts of monomers are given in monomer ratio (r in functional group-percent, FG%) and in mass (m) for one gram of formulation, which was the most commonly prepared amount of formulation. Photoinitiator Ivocerin and stabilizer pyrogallol were added on top of the one-gram quantity.

Formulation	LC	M5	СНТТ		Ivocerin		Pyrogallol	
name	r (FG%)	m (mg)	r (FG%)	m (mg)	r (FG%)	m(mg)	r (wt%)	m(mg)
50/50 1% PI	50	746	50	254	1	10.1	0.1	1
50/50 0.5% PI	50	746	50	254	0.5	5.1	0.05	0.5

To measure the heat of polymerization from a small amount of formulation, smaller molds were created by blocking off the narrow part of tensile test specimen negatives using silicone. The molten formulations were then cast into the broader part of the tensile test molds, after which a thermometer was inserted directly into the formulation. Approximately 150 mg of the formulations were cast into the mold for each specimen.

The polymerization heat was measured by subtracting the temperature of the silicone mold during irradiation from the temperature of the polymer.

After 300 s irradiation with the Hönle light source (405 nm, 1.5 mW cm⁻², 450 mJ cm⁻²), the UVET light source was immediately placed on the heated polymerization chamber (less than 30 s after finishing the first irradiation cycle). A 180 s irradiation period at minimum intensity of the UVET light source (365 nm, 290 mW cm⁻², 52 J cm⁻²) was employed for all samples. This irradiation procedure will hereafter be referred to as the optimized curing procedure for LCM-containing formulations (Methods section, chapter 9).

Previously polymerized tensile test specimens were measured on a PerkinElmer Spectrum 65 FT-IR Spectrometer equipped with a Specac MKII Golden Gate Single Reflection ATR System. Evaluation of results was performed in Bruker OPUS 7.0. Double bonds were integrated over the range of 1658-1627 cm⁻¹, and the carbonyl bond used as a reference was integrated over the range of 1808-1691 cm⁻¹. Double bond conversion (DBC) was calculated using Equation 1.

Equation 1: Calculation of double bond conversion using ATR-IR-spectroscopy.

$$DBC = \left(1 - \frac{\left(\frac{DBI_{polymer}}{COI_{polymer}}\right)}{\left(\frac{DBI_{LCM5}}{COI_{LCM5}}\right)}\right) * 100$$

DBC double bond conversion (%)

..... double bond integral of the measured polymer sample DBI_{polymer}

..... carbonyl bond integral of the measured polymer sample *COI*_{polymer}

..... double bond integral of the monomer LCM5 DBI_{LCM5}

COI_{LCM5} carbonyl bond integral of the monomer LCM5

DMTA measurements were performed according to the procedure in chapter 6 of the Methods section in a temperature range of -50 to 200 °C.

Tensile tests were performed according to the procedure in chapter 7 of the Methods section.

3.1.3.3 Polymerization experiment with aromatic crosslinker

To prepare the formulations and to polymerize DMTA test specimens, the standard thiolene formulating and optimized curing procedures described in chapters 1 and 9 of the Methods section were followed.

Table 32: Formulations used to test the newly synthesized aromatic trithiol monomer 1,3,5benzenetrimethanethiol (MTSH). Amounts of monomers are given in monomer ratio (r in functional grouppercent, FG%) and in mass (m) for one gram of formulation, which was the most commonly prepared amount of formulation. The formulations also contain 0.5 mol% (in relation to double bonds) Ivocerin as a photoinitiator and 0.05 wt% (in relation to total formulation mass) pyrogallol as stabilizer, which were added on top of the one-gram quantity.

From Local Comment	LC	Thiol comonomer			
Formulation name	r (FG%)	m (mg)	Туре	r (FG%)	m (mg)
LCM5-CHTT	50	746	CHTT	50	254
LCM5-MTSH	50	782	MTSH	50	218

DMTA measurements were performed according to the procedure in chapter 6 of the Methods section in a temperature range of -50 to 200 °C.

3.1.4 3D printing experiments

To prepare the monomer mixtures, the thiol-ene formulating procedure in chapter 3 of the Methods section was followed.

Table 33: Formulation used for 3D printing of LCM5-containing polymers. Amounts of monomers are given in monomer ratio (r in functional group-percent, FG%) and in mass (m) for one gram of formulation, which was the most commonly prepared amount of formulation. The formulation also contains 1 mol% (in relation to double bonds) diphenyl(2,4,6-trimethylbenzoyl)phosphine oxide (TPO) as a photoinitiator and 0.2 wt% (in relation to total formulation mass) pyrogallol as stabilizer, which were added on top of the one-gram quantity.

Formulation	LCI	M5	СНТТ		
name	r (FG%)	m (mg)	r (FG%)	m (mg)	
LCM5-CHTT	50	746	50	254	

3.1.4.1 Initial crystalline and amorphous print test

The formulations were prepared as described in chapter 3.1.4.

The general printing process was performed according to the procedure in chapter 11 of the Methods section.

The gradient print was achieved by slowly increasing the temperature of the vat and the platform from 82 to 94 °C throughout the printing process. A cuboid with a 4x4 mm base was printed, with the left side irradiated at an intensity of 15.75 mW cm⁻² over a period of 22.9 s to achieve a mild irradiation, throughout which the irradiation heat and heat of polymerization would not cause the specimen to leave the liquid crystalline phase. Additionally, crystallinity has more time to develop. The right side was irradiated at an intensity of approximately 80 mW cm⁻² (maximum of the printer's light engine) over a period of 4.5 s to induce fast network formation without the formation of crystallites.

10 µm-thin sections of the gradient print were cut using a cryo-microtome equipped with a glass knife at -100 °C. The slices were placed on a glass slide and covered with silicone oil. Images of the gradient print were recorded using a Canon EOS 250D camera from a Zeiss Axio. Scope A1 polarized optical microscope equipped with a λ -plate under crossed polars.

The crystalline, opaque resolution test chip was printed at 80 °C with an irradiation intensity of 15.75 mW cm⁻² over a period of 22.9 s. The amorphous, transparent resolution test chip was printed at 110 °C with an irradiation intensity of 80 mW cm⁻² over a period of 4.5 s.

Pictures of the resolution test chips were taken using a Canon EOS 250D camera with a paper background, on which the word "transparent" was repeatedly printed, as well as on a black paper background.

3.1.4.2 Thermomechanical tests of multi-material printed parts

The formulations were prepared as described in chapter 3.1.4.

The general printing process was performed according to the procedure in chapter 11 of the Methods section.

Tensile test specimens were printed according to DIN EN ISO 527 test specimen 5b. The crystalline, opaque tensile test specimens were printed at 80 °C with an irradiation intensity of 15.75 mW cm⁻² over a period of 22.9 s. The amorphous, transparent tensile test specimens were printed at 100 °C and 110 °C (three specimens each) with an irradiation intensity of 80 mW cm⁻² over a period of 4.5 s.

Pictures of the printed tensile test specimens were taken using a DSLR camera with a paper background, on which the word "transparent" was printed repeatedly, as well as on a black paper background.

The five-layer composite specimens were printed by first setting the parameters to those used to induce crystallinity (temperature 80 °C, intensity 15.75 mW cm⁻², irradiation time 22.9 s) and printing seven layers, then switching the parameters to those used to prepare amorphous polymers (temperature 100 °C, intensity 80 mW cm⁻², irradiation time 4.5 s) and printing another seven layers. The process was repeated until three 0.35 mm thick crystalline layers had been printed in turns with two 0.35 mm thick amorphous layers, giving the specimen a total thickness of 1.75 mm.

DMTA measurements were performed according to the procedure in chapter 6 of the Methods section in a temperature range of -50 to 200 °C.

Tensile tests were performed according to the procedure in chapter 7 of the Methods section.

To achieve different crystallinities within one printed layer, the temperature and irradiation was first set to the parameters used to induce crystallinity (temperature 80 °C, intensity 15.75 mW cm⁻², irradiation time 22.9 s). Only the desired areas were irradiated, after which the conditions were changed to those used to prepare an amorphous polymer (temperature 100 °C, intensity 80 mW cm⁻², irradiation time 4.5 s). Only then was the platform lifted off the vat, and the process was repeated as often as desired. The programming for this process was achieved by first designing a voxel-based model for multi-material parts. These were then saved as a set of images, in which each pixel corresponds to one voxel. The printing software then sequentially reads out these images,

in which different colors represent either the curing of crystalline material, curing of amorphous material, or not irradiating the area. 151

3.1.4.3 3D printing of functional multi-material parts

The formulations were prepared as described in chapter 3.1.4. The process to achieve different crystallinities within one printed layer was performed according to chapter 3.1.4.2.

The general printing process was performed according to the procedure in chapter 11 of the Methods section.

The hidden QR code was revealed by placing a microscope glass slide on the opaque cover layer of the printed part and weighing it down using metal objects. The glass slide was heated to approximately 160 °C from above using a heat gun, which led to the melting of the crystallites of the opaque upper layer.

3.1.4.4 Printing of complex structure

The formulations were prepared as described in chapter 3.1.4. However, for the printing of the pyramid specimen, 0.5 wt% pyrogallol and 1.5 mol% TPO were used.

The general printing process was performed according to the procedure in chapter 11 of the Methods section.

The irradiation conditions used to print the pyramid were those used to prepare amorphous polymers, with the only exception that the temperature was kept slightly lower (temperature 90 °C, intensity 80 mW cm⁻², irradiation time 4.5 s).

3.2 LCM6-based polymers

3.2.1 Photoinitiator study

To prepare the formulations and to polymerize DMTA test specimens, the standard thiolene formulating and optimized curing procedures described in chapters 1 and 9 of the Methods section were followed.

Table 34: Formulations used to test which photoinitiator should be used for experiments with LCM6. Amounts of monomers are given in monomer ratio (r in functional group-percent, FG%) and in mass (m) for one gram of formulation, which was the most commonly prepared amount of formulation. The photoinitiators and the stabilizer pyrogallol were added on top of the one-gram quantity.

F	LC	M6	СН	ITT	Pł	notoinitiat	or
Formulation name	r (FG%)	m (mg)	r (FG%)	m (mg)	Туре	r (FG%)	m (mg)
LCM6-CHTT TPO	50	732	50	268	TPO	0.5	4.41
LCM6-CHTT Ivocerin	50	732	50	268	Ivocerin	0.5	5.1

DMTA measurements were performed according to the procedure in chapter 6 of the Methods section in a temperature range of -50 to 200 °C.

3.2.2 Qualitative evaluation

To prepare the formulations and to polymerize DMTA test specimens, the standard thiolene formulating and optimized curing procedures described in chapters 1 and 9 of the Methods section were followed.

Table 35: Formulations used to test LCM6 in linear and crosslinked polymers. Amounts of monomers are given in monomer ratio (r in functional group-percent, FG%) and in mass (m) for one gram of formulation, which was the most commonly prepared amount of formulation. Every formulation also contains 0.5 mol% (in relation to double bonds) TPO as a photoinitiator and 0.05 wt% (in relation to total formulation mass) pyrogallol as stabilizer, which were added on top of the one-gram quantity. The formulations were named after the thiol comonomers used in them.

From Letter const	LCM6		Thiol comonomer(s)			
Formulation name	r (FG%)	m (mg)	Туре	r (FG%)	m (mg)	
HDT	50	763	HDT	50	237	
EDDT	50	726	EDDT	50	274	
TEMPIC	50	579	TMPMP	50	421	
TMPMP	50	645	ETTMP	50	355	
ETTMP	50	508	TEMPIC	50	492	
CHTT	50	732	CHTT	50	268	
90% CHTT, 10% ETTMP	50	701	CHTT ETTMP	45 5	231 68	
80% CHTT, 20% ETTMP	50	673	CHTT ETTMP	40 10	197 130	

3.2.3 Reactive group conversion investigation

To prepare the formulations and to polymerize bulk test specimens, the standard thiolene formulating and optimized curing procedures described in chapters 1 and 9 of the Methods section were followed.

The ratio of monomers and curing conditions used are listed above in Table 35.

Test specimens were measured on a PerkinElmer Spectrum 65 FT-IR Spectrometer equipped with a Specac MKII Golden Gate Single Reflection ATR System. Evaluation of results was performed in Bruker OPUS 7.0. Double bonds were integrated over the range of 1650-1630 cm⁻¹, and the carbonyl bond used as a reference was integrated over the range of 1808-1691 cm⁻¹. Double bond conversion (DBC) was calculated using Equation 2.

Equation 2: Calculation of double bond conversion using ATR-IR-spectroscopy.

$$DBC = \left(1 - \frac{\left(\frac{DBI_{polymer}}{COI_{polymer}}\right)}{\left(\frac{DBI_{LCM6}}{COI_{LCM6}}\right)}\right) * 100$$

DBC double bond conversion (%)

..... double bond integral of the measured polymer sample DBI_{polymer}

COI_{polymer} carbonyl bond integral of the measured polymer sample

 DBI_{LCM5} double bond integral of the monomer LCM6 COI_{LCM5} carbonyl bond integral of the monomer LCM6

3.2.4 Thermomechanical evaluation

To prepare the formulations and to polymerize tensile test specimens, the standard thiolene formulating and optimized curing procedures described in chapters 1 and 9 of the Methods section were followed.

The ratio of monomers and curing conditions used are listed above in Table 35.

DMTA measurements were performed according to the procedure in chapter 6 of the Methods section in a temperature range of -50 to 200 °C.

3.2.5 Evaluation of crystallinity

To prepare the formulations and to polymerize tensile test specimens, the standard thiolene formulating and optimized curing procedures described in chapters 1 and 9 of the Methods section were followed.

The ratio of monomers and curing conditions used are listed above in Table 35.

Differential scanning calorimetry measurements were performed according to the procedure in chapter 8 of the Methods section.

To quantify the degree of crystallinity, the integrals of the phase transition enthalpy ΔH_{total} (polymer) observed in DSC for the respective sample were compared to the transition enthalpy of the monomer ΔH_{total} (LCM6). To obtain the degree of crystallinity in

the polymer (D), the assumption was made that the thiol comonomer would not contribute to the polymer crystallinity. Therefore, the percentage of LCM6 in the formulation was introduced as an additional factor (wt% LCM6). The calculation of the degree of crystallinity was performed according to Equation 3.

Equation 3: Calculation of the degree of crystallinity of polymers.

$$D = \frac{\Delta H_{total} (polymer)}{\Delta H_{total} (LCM6)} * \frac{100}{r_{LCM6}}$$

..... degree of crystallinity (%) D

..... phase transition enthalpy of all melting transitions ($J g^{-1}$) ΔH_{total}

wt% LCM6 weight fraction of monomer LCM6 in formulation (%)

Table 36: Steps for calculation of degree of crystallinity (phase transition temperature T_{PT} , melt enthalpy ΔH_{melt} , total phase transition enthalpy ΔH_{total} weight ratio of LCM6 r_{LCM6} , degree of crystallinity D). The first row displays the measured data for the pure monomer LCM6, while the other rows refer to polymers cured from LCM6 and the respective comonomer mentioned (e.g., HDT refers to the polymer cured from stoichiometrically equal end group ratios of LCM6 and HDT).

(Co-)					
monomer	T _{PT} (° C)	ΔH_{melt} (J g ⁻¹)	$\Delta H_{\text{total}} (J g^{-1})$	r _{LCM6} (%)	D (%)
LCM6 (monomer)	104, 173	52.3, 5.1 ³	57.4	100	100
HDT	140, 158	14.3, 3.3 ³	17.6	76.3	40.2
EDDT	110, 144	26.1, 2.5 ³	28.6	72.6	68.6
TMPMP	$(12)^2$, 100	4.75	4.75	64.5	12.8
ETTMP	$(-34)^2$, 70.6	11.0	11.0	50.9	37.6
TEMPIC	$(37)^2$, 80^1	4.84	4.84	57.9	12.9
CHTT	120	13.2	14.23	73.2	33.9
90% CHTT 10% ETTMP	117	10.6	10.6	70.1	26.4
80% CHTT 20% ETTMP	116	5.45	5.45	67.3	14.1

¹broad and low peak

3.2.6 Mechanical tests

To prepare the formulations and to polymerize tensile test specimens, the standard thiolene formulating and optimized curing procedures described in chapters 1 and 9 of the Methods section were followed. The ratio of monomers and curing conditions used are listed above in Table 35, out of which only the formulations containing CHTT and/or ETTMP were tested further.

Tensile tests were performed according to the procedure in chapter 7 of the Methods section.

²Glass transition temperature signified by a baseline shift

³LC→I transition

3.2.7 Micro- and nanostructural evaluation

To prepare the formulations and to polymerize the tensile test specimens, the standard thiol-ene formulating and optimized curing procedures described in chapters 1 and 9 of the Methods section were followed. The ratio of monomers and conditions used are listed above in Table 35, out of which only the formulations containing CHTT and/or ETTMP were tested further.

To prepare samples for AFM measurements, they were encased in Struers EpoFix clear epoxy resin (Figure 121) and grinded/polished using a Struers Tegramin-30 polishing machine (Table 37). Between steps, the samples were sonicated for about 5 min each time.

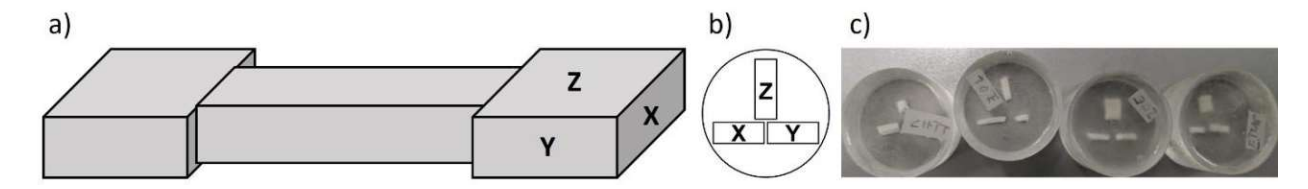


Figure 121: Sample preparation of AFM samples. a) Orientation of tensile test specimens measured by AFM. b) Orientation of test specimen pieces in resin. C) Resin-encased pieces of tensile test specimens.

Table 37: Grinding and polishing conditions for AFM sample preparation protocol.

Grinding/polishing	Time		Downward	Speed
medium	(min)	Lubricant	force (N)	(rpm)
Struers MD-Piano disc	0.5	Water	10	150
Diamond paste 15 µm	10	Struers DP-Lubricant blue	10	150
Diamond paste 6 µm	10	Struers DP-Lubricant blue	10	150
Diamond paste 1 µm	20	Struers DP-Lubricant blue	10	150

Imaging was performed in intermittent (tapping) mode at a scan rate of 0.7 Hz, using an AC160TS cantilever with a spring constant of 26 N m⁻¹, and a tip radius of 7 nm. The phase images were compared with topography images to verify that the observed features were not artifacts of surface unevenness.

The particle model was applied by using the "Grain" function in the AFM evaluation software Park Systems XEI. Here, the "Threshold" method was selected and the slider was moved to the minimum between the two peaks in the histogram. The detected grain area was recorded as a percentage of the total image area.

3.2.8 Shape memory evaluation

To prepare the formulations and to polymerize the tensile test specimens used for shape memory evaluation, the standard thiol-ene formulating and optimized curing procedures described in chapters 1 and 9 of the Methods section were followed.

The ratio of monomers and conditions used are listed above in Table 35, out of which only the formulation containing 100% CHTT as a comonomer was tested in this chapter.

Cyclic shape memory tests were performed according to the procedure in chapter 10 of the Methods section.

The results of all cyclic shape memory measurements are displayed in Table 38 and Table 39.

Table 38: Shape fixity ratio results of all cyclic shape memory measurement.

Shape fixity ratio (%)

Cycle	Sample 1,	Sample 1,	Sample 1,	Sample 2,	Sample 2,
	Measuremt. 1	Measuremt. 2	Measuremt. 3	Measuremt. 1	Measuremt. 2
1	99.2	99.0	98.9	98.7	100.0
2	99.1	99.0	99.1	98.8	99.3
3	99.1	99.0	99.1	98.8	99.3
4	98.9	98.9	99.1	98.7	99.3
5	99.1	99.1	99.2	98.8	99.4
6	-	-	-	98.7	99.3
7	-	-	-	98.8	99.3
8	-	-	-	98.7	-
9	-	-	-	98.7	-
10	-	-	-	99.0	-

Table 39: Shape recoveries of all cyclic shape memory measurements.

Shape recovery (%)

Cycle	Sample 1,	Sample 1,	Sample 1,	Sample 2,	Sample 2,
Сусте	Measuremt. 1	Measuremt. 2	Measuremt. 3	Measuremt. 1	Measuremt. 2
1	93.2	96.4	97.7	89.2	93.9
2	93.4	97.0	98.3	92.5	96.4
3	96.6	97.6	98.3	97.7	97.1
4	96.5	98.0	98.3	95.8	97.4
5	96.9	98.4	98.8	96.0	98.1
6	-	-	-	96.2	97.9
7	-	-	-	96.3	98.1
8	-	-	-	96.0	-
9	-	-	-	96.7	-
10	-	-	-	97.0	-

3.2.9 3D printing experiments

To prepare the formulation for 3D printing experiments, the standard thiol-ene formulating procedures described in chapter 3 of the Methods section was followed.

The ratio of monomers and conditions used are listed above in Table 35, out of which only the formulation containing 100% CHTT as a comonomer was tested in this chapter.

3D printing was performed according to the procedure described in chapter 11 of the Methods section at a temperature of 105 °C. Each 50-μm layer was irradiated for 11 s at 25 mW·cm⁻².

3.2.10 Linear polymer conversion study

3.2.10.1 Variation of photoinitiator and curing temperature

To prepare the formulations and to polymerize the test specimens, the standard thiol-ene formulating and optimized curing procedures described in chapters 1 and 9 of the Methods section were followed.

Photoinitiator concentration and type of an equimolar formulation consisting of the monomers LCM6 and HDT were varied along with curing temperature as listed in Table 40.

Table 40: Monomer system (LCM6 and CHTT in an equal functional group (FG%) ratio, photoinitiator (PI) type (Ivocerin vs. diphenyl(2,4,6-trimethylbenzoyl)phosphine oxide (TPO)), concentration (r_{Pl}), and curing temperatures (T_{cure}) used in the first part of the linear polymer conversion study. Pyrogallol was used as a stabilizer for all formulations in a weight percent ratio (r_{pyrogallol}) that was adjusted based on PI content. The monomers LCM6 and HDT were used in an equimolar ratio. The weights given in the table (m_{component}) were the amounts used to make one gram of formulation. Each formulation was cured at three different temperatures.

Formulation	1	2	3	4	5
r _{LCM6} (FG%)	50	50	50	50	50
m _{LCM6} (mg)	763	763	763	763	763
r _{HDT} (FG%)	50	50	50	50	50
m _{HDT} (mg)	237	237	237	237	237
PI type	Ivocerin	TPO	Ivocerin	TPO	Ivocerin
r _{Pl} (FG%)	1	1	0.5	0.5	0.25
m _{Pl} (mg)	12.67	11.0	6.34	5.5	3.17
r _{pyrogallol} (wt%)	0.1	0.1	0.05	0.05	0.025
m _{pyrogallol} (mg)	1	1	0.5	0.5	0.25
	90	90	90	90	90
T_{cure} (°C)	100	100	100	100	100
	130	130	130	130	130

To consume a smaller amount of formulation, small molds were created by blocking off the narrow part of tensile test specimen negatives using silicone. The molten formulations were then cast into the broader part of the tensile test molds, after which a thermometer was inserted directly into the formulation. Approximately 150 mg of the formulations were cast into the mold for each specimen.

The molecular weights of polymers in this chapter were analyzed using gel permeation chromatography (GPC). Measurements were performed as described in chapter 1 of the Methods section.

3.2.10.2 Variation of irradiation parameters and stoichiometry

To prepare the monomer mixtures, the thiol-ene formulating procedure in chapter 3 of the Methods section was followed.

To test various irradiation parameters, formulation 4 listed above in Table 40 was used at a curing temperature of 100 °C with various irradiation parameters.

For the three variations of irradiation parameters, values are listed in Table 41.

Table 41: Irradiation programs used to test a variety of conditions ranging from short, intense irradiation to mild, gradual increase of irradiation intensity. All irradiation steps were performed at a formulation temperature of 100 °C.

Irradiation program	Step	Light source	Intensity (%)	Wavelength (nm)	Approx. intensity (mW cm ⁻²)	Time (s)
Program 1	1	UVET UV-LED	100	365	2660	18
Program 2	1	UVET UV-LED	10	365	290	1
	2	UVET UV-LED	10	365	290	1
	3	UVET UV-LED	10	365	290	1
	4	UVET UV-LED	10	365	290	180
Program 3	1	Hönle LEDcube	5	405	1.5	300
	2	Hönle LEDcube	25	405	9	300
	3	Hönle LEDcube	100	405	36	300
Previously	1	Hönle LEDcube	5	405	1.5	300
optimized	2	UVET UV-LED	10	365	290	180

Table 42: Formulations used to test the influence of the variation of stoichiometry on the molecular weight of linear polymers. Amounts of monomers are given in monomer ratio (r in functional group-percent, FG%) and in mass (m) for one gram of formulation, which was the most commonly prepared amount of formulation. Every formulation also contains 0.5 mol% (in relation to double bonds) TPO as a photoinitiator and 0.05 wt% (in relation to total formulation mass) pyrogallol as stabilizer, which were added on top of the one-gram quantity.

F	LC	M6	Thiol comonomer		
Formulation name	r (FG%)	m (mg)	r (FG%)	m (mg)	
+5% HDT	48.8	754	51.2	246	
-5% HDT	51.3	772	48.7	228	

The molecular weights of polymers in this chapter were analyzed using gel permeation chromatography (GPC). Measurements were performed as described in chapter 1 of the Methods section.

3.3 LCM7-based polymers

3.3.1 Linear polymerization test

To prepare the formulation and to polymerize the test specimens, the standard thiol-ene formulating and optimized curing procedures described in chapters 1 and 9 of the Methods section were followed.

Table 43: Formulations used to assess the performance of LCM7 in linear polymers. Amounts of monomers are given in monomer ratio (r in functional group-percent, FG%) and in mass (m) for one gram of formulation, which was the most commonly prepared amount of formulation. Every formulation also contains 0.5 mol% (in relation to double bonds) TPO as a photoinitiator and 0.05 wt% (in relation to total formulation mass) pyrogallol as stabilizer, which were added on top of the one-gram quantity. The formulations were named after the thiol comonomers used in them.

Formulation	е	ne-monom	er	HE	T	Curing
name	Type	r (FG%)	m (mg)	r (FG%)	m (mg)	temperature (°C)
LCM6-HDT	LCM6	50	763	50	237	100
LCM7-HDT	LCM7	50	764	50	236	90

Due to the lower melting points of LCM7-containing formulations, curing of LCM7-HDT was performed at a lower temperature than LCM6-HDT to polymerize both formulations from slightly above their melting points.

The molecular weights of polymers in this chapter were analyzed using gel permeation chromatography (GPC). Measurements were performed as described in chapter 1 of the Methods section.

3.3.2 LCM7-based polymer networks

To prepare the formulations and to polymerize test specimens, the standard thiol-ene formulating and optimized curing procedures described in chapters 1 and 9 of the Methods section were followed. Curing was performed at a temperature of 90 °C.

Table 44: Formulations used to test LCM7 in polymer networks. Amounts of monomers are given in monomer ratio (r in functional group-percent, FG%) and in mass (m) for one gram of formulation, which was the most commonly prepared amount of formulation. Every formulation also contains 0.5 mol% (in relation to double bonds) TPO as a photoinitiator and 0.05 wt% (in relation to total formulation mass) pyrogallol as stabilizer, which were added on top of the one-gram quantity. The formulations were named after the thiol comonomers used in them.

F	LC	M7	Thiol comonomer(s)					
Formulation name	r (FG%)	m (mg)	Тур	e	r (FC	3 %)	m (r	ng)
100% TMPMP	50	647	TMPI	MP	5	0	35	53
100% TEMPIC	50	581	TEM	PIC	5	0	41	9
100% ETTMP	50	510	ETTN	ЛP	5	0	49	00
100% CHTT	50	734	CH1	ГΤ	5	0	26	66
100% PETMP	50	666	PETN	MΡ	5	0	33	34
50% TMPMP 50% HDT	50	701	TMPMP	HDT	25	25	191	108
36% TMPMP 64% HDT	50	717	TMPMP	HDT	18	32	141	142
50% TMPMP 50% EDDT	50	685	TMPMP	EDDT	25	25	187	128
50% CHTT 50% HDT	50	748	CHTT	HDT	25	25	136	116

3.3.3 Reactive group conversion investigation

To prepare the formulations and to polymerize test specimens, the standard thiol-ene formulating and optimized curing procedures described in chapters 1 and 9 of the Methods section were followed. Curing was performed at a temperature of 90 °C.

The ratio of monomers and additives used are listed above in Table 44.

Test specimens were measured on a PerkinElmer Spectrum 65 FT-IR Spectrometer equipped with a Specac MKII Golden Gate Single Reflection ATR System. Evaluation of results was performed in Bruker OPUS 7.0. Double bonds were integrated over the range of 1653-1640 cm⁻¹, and the carbonyl bond used as a reference was integrated over the range of 1825-1652 cm⁻¹. Double bond conversion (DBC) was calculated using Equation 2.

Equation 4: Calculation of double bond conversion using ATR-IR-spectroscopy.

$$DBC = \left(1 - \frac{\left(\frac{DBI_{polymer}}{COI_{polymer}}\right)}{\left(\frac{DBI_{LCM7}}{COI_{LCM7}}\right)}\right) * 100$$

DBC double bond conversion (%)

..... double bond integral of the measured polymer sample DBI_{polymer}

COI_{polymer} carbonyl bond integral of the measured polymer sample

 DBI_{LCM5} double bond integral of the monomer LCM7

COI_{LCM5} carbonyl bond integral of the monomer LCM7

3.3.4 Thermomechanical evaluation

To prepare the formulations and to polymerize test specimens, the standard thiol-ene formulating and optimized curing procedures described in chapters 1 and 9 of the Methods section were followed. Curing was performed at a temperature of 90 °C.

The ratio of monomers and additives used are listed above in Table 44.

DMTA measurements were performed according to the procedure in chapter 6 of the Methods section in a temperature range of -50 to 150 °C.

3.3.5 Mechanical tests

To prepare the formulations and to polymerize test specimens, the standard thiol-ene formulating and optimized curing procedures described in chapters 1 and 9 of the Methods section were followed. Curing was performed at a temperature of 90 °C.

The ratio of monomers and additives used are listed above in Table 44.

Tensile tests were performed according to the procedure in chapter 7 of the Methods section.

3.3.6 Evaluation of crystallinity

To prepare the formulations and to polymerize test specimens, the standard thiol-ene formulating and optimized curing procedures described in chapters 1 and 9 of the Methods section were followed. Curing was performed at a temperature of 90 °C.

The ratio of monomers and additives used are listed above in Table 44.

DSC samples were measured according to chapter 8 of the Methods section.

3.3.7 Shape memory evaluation

To prepare the formulations and to polymerize test specimens, the standard thiol-ene formulating and optimized curing procedures described in chapters 1 and 9 of the Methods section were followed. Curing was performed at a temperature of 90 °C.

The ratio of monomers and additives used are listed above in Table 44. The formulation used for shape memory evaluation was 50% CHTT 50% HDT.

An S-shaped mold was prepared by casting silicone around a 3D printed 2x2 mm cross section S-shaped positive specimen.

3.3.8 3D printing experiments

To prepare the formulation for 3D printing experiments, the standard thiol-ene formulating procedures described in chapter 3 of the Methods section was followed. The ratio of monomers and additives used are listed above in Table 44. The formulation used for 3D printing tests was 50% CHTT 50% HDT.

3D printing was performed according to the procedure described in chapter 11 of the Methods section at a temperature of 70 °C. Each 50-μm layer was irradiated for 5 s at 65 mW·cm⁻².

Methods

1 Gel permeation chromatography

Malvern VISCOTEK TDA system equipped with a VISCOTEK SEC-MALS 9 light scattering detector, a VISCOTEK TDA 305-021 RI+Visc detector, and a UV Detector Module 2550 for TDA 305.

The sample was dissolved at a concentration of 4 mg mL⁻¹ in a THF solution spiked with 0.5 mg mL⁻¹ butylhydroxytoluene, which was used as a flow rate marker. Before separation, the solution was filtered through a 0.2 µm PTFE syringe filter. Separation was conducted through three consecutive PSS SDV columns (100 Å, 1,000 Å, and 100,000 Å) using THF as solvent at a flow rate of 0.8 ml min⁻¹. Calibration was performed using polystyrene standards between 479 and 44 kDa.

2 Polarized optical microscopy procedure

Phase analysis was performed using a Zeiss Axio. Scope A1 optical microscope using crossed polarization filters combined with a Linkam LTS 350 heated stage. Images were recorded using a Canon EOS 250D attached to the microscope with a connective piece custom-made by RafCamera.

Prior to the analysis, the samples were transferred to a glass slide and covered with a glass cover slip. When analyzing solids, the glass slide was pressed onto the samples to ensure a homogeneous height of the sample. To determine melting points and phase transitions, the sample stage was heated at a rate of 5 °C per minute. Melting points were measured upon melting the sample for the second time after crystallization on the microscope.

3 Thiol-ene formulating procedure

To prepare the formulations, first, the radical inhibitor pyrogallol was weighed into a brown glass vial, followed by the photoinitiator and the thiol component(s). The mixture was briefly heated to about 70 °C and homogenized with a vortex mixer to disperse and dissolve the stabilizer and the photoinitiator. Afterwards, the alkene monomer was added, and the formulation was heated until an isotropic molten liquid was obtained, after which it was vortexed for at least 30 s. The mixture was allowed to cool to room temperature and the vial was wrapped in aluminium foil to protect it from light. If the formulation was not used immediately, it was stored at -19 °C. Typically, formulation batches of 1-3 g were prepared, as larger batches had to be heated for extended times, which impacted the formulation stability negatively.

4 Photo-DSC measurements

To measure photo-DSC, 9-15 mg of each formulation were weighed into an aluminium crucible and covered with a glass lid. Three samples of each formulation were analyzed. A mercury lamp (Lumen Dynamics Omnicure S2000 spot UV curing system) equipped with a filter that limited its spectral output from 400 to 500 nm was used as a light source, which was calibrated using an Omnicure R2000 radiometer.

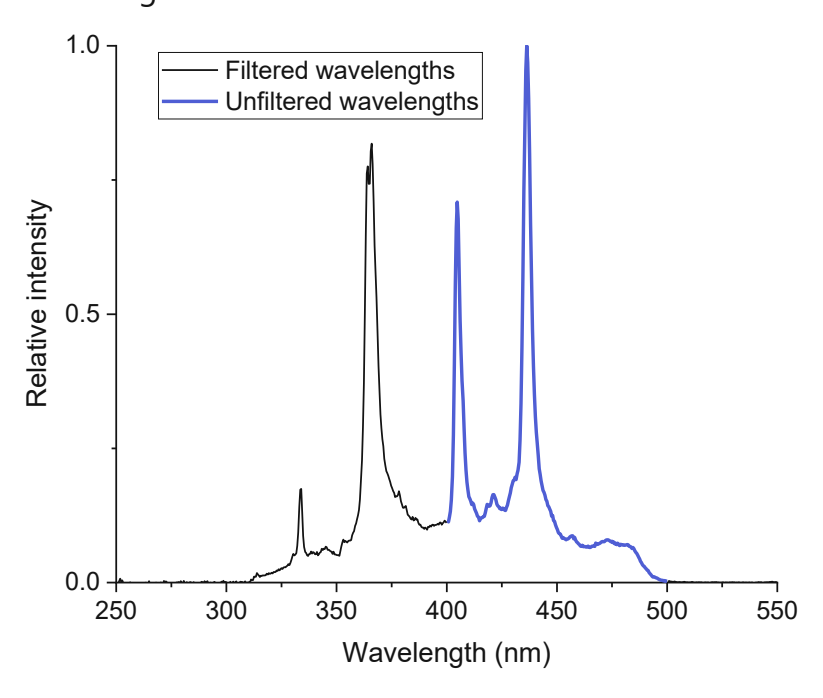


Figure 122: Emission spectrum of the light source used for photo-DSC and RT-NIR-photorheology. The graph shows the full emission spectrum of the light source, with the unfiltered wavelengths marked in blue.

The intensity was set to 50 mW·cm⁻² (at the sample surface). After an initial 60 s equilibration period the sample was irradiated for 360 s at 25 °C. Afterwards the sample was irradiated a second time to enable baseline correction. The resulting peak area given in J·g⁻¹ was converted to J·mol⁻¹, wherein the mol refer to reactive double bonds in the formulations. To do this, the given value in J·mol⁻¹ was divided by the amount of double bonds per gram formulation (mol·g⁻¹). Time at 95% conversion (t₉₅) was calculated by integration of the curve. The measurements were recorded and analyzed using the software Netzsch Proteus thermal analysis V8.0.1. 5 RT-NIR-photorheology measurements

RT-NIR-photorheology was measured using an AntonPaar MCR 302 rheometer coupled with a Bruker Vertex 80 IR spectrometer. The same light source and irradiation conditions as for photo-DSC (Methods section chapter 4) were used, with the only deviation that a 300 s irradiation period was used. The light source was calibrated using an OceanOptics USB 2000+ radiometer using the software SpectraSuite 1.6.0_11. To prepare the measurements, 140 µL of a formulation were transferred onto the measuring surface using a micropipette. Three samples of each formulation were analyzed. The measuring surface was kept at 25 °C and covered with polyethylene tape. The plate-plate geometry rheology stamp with a diameter of 25 mm was used at a gap size of 0.2 mm. After 65 s equilibration time, the sample was irradiated using light with wavelengths between 400 and 500 nm at an intensity of approximately 50 mW·cm⁻² for 300 s and an NIR-spectrum was recorded every 0.2 s. A baseline correction of the NIR data was performed using the concave rubber band method with 10 iterations. To determine the DBC the integral of the curve from around 6100 cm⁻¹ to around 6200 cm⁻¹ was calculated. The exact boundaries varied slightly from sample to sample. Each formulation was measured three times. AntonPaar Rheocompass was used to analyze rheological data and Bruker OPUS 7.0 was used to analyze IR data.

6 DMTA measurements

Prior to DMTA measurements, the cured samples were sanded using 800, 1600 and 3200 grit sandpaper until even thickness (variations ≤0.05 mm) and a flat surface were achieved.

DMTA was measured by clamping the specimens into DMTA sample holder brackets with a torque of 25-35 cN·m. Then, the sample was cooled to -50 °C unless stated otherwise and heated by 2 °C min⁻¹ up to 200 °C unless stated otherwise under oscillating torsional stress with a frequency of 1 Hz and a shear strain of 0.1%. During the measurement, various parameters were recorded, most importantly the storage and loss moduli G' and G" and the resulting loss factor, which is calculated by dividing the loss modulus by the storage modulus.

7 Tensile test procedure

Prior to tensile testing, the cured samples were sanded using 800, 1600 and 3200 grit sandpaper until even thickness (variations ≤0.05 mm) and a flat surface were achieved.

The dimensions of each sample were measured using calipers before the sample was fixed between the measurement clamps. At least three samples of each formulation were tested using a Zwick Z050 and recorded using the software Zwick textXpert. The traverse speed was set to 200 mm·min⁻¹.

8 DSC measurements

To measure differential scanning calorimetry (DSC), 3-5 mg of the polymers were weighed into aluminium DSC crucibles and heated to 200 °C from room temperature, after which the sample was cooled to -90 °C. With this uniformized thermal history, the samples were once again heated to 200 °C (Figure 123). All heating and cooling rates were constant at 10 °C min⁻¹. All measured transition temperatures and enthalpies were taken from the



second heating cycle. When a bimodal peak occurred (<10 °C difference between peak maxima), the higher temperature peak was taken as the phase transition temperature.

DSC measurements were performed using a TA Instruments DSC 2500 and recorded using the software TA Instruments TRIOS.

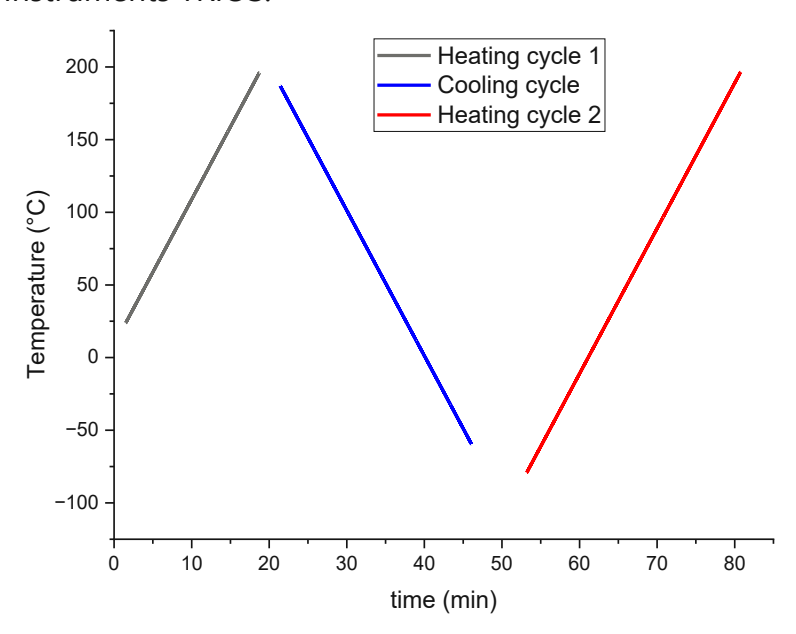


Figure 123: Exact heating and cooling cycles applied to samples during DSC measurements. The missing segments represent sections of the temperature cycle not recorded by the measurement device.

9 Optimized polymer curing

Preparation of test specimens was performed by placing a silicone mold in the heated polymerization chamber and preheating the chamber to the desired temperature with the lid closed. The silicone mold, which was made more thermally conductive by adding 20 wt% aluminium powder to its formulation, was prepared in an aluminium positive mold. DMTA negatives were prepared as cuboids with the dimensions 2x5x40 mm. Tensile test specimen negatives were prepared according to ISO 527 test specimen 5b.

Temperature was measured by a thermometer directly inserted into the silicone, which was connected to a Pico Technology interface, which allowed the temperature to be monitored on a PC. Formulations were cast into the silicone mold by melting them inside

the vial and carefully pouring them into the silicone mold, which was already in the preheated chamber, after which the lid was placed back on the chamber.

After an equilibration period of around 3 min, the irradiation was started. After irradiation, the specimens were removed from the silicone mold carefully, turned upside down, and irradiated using the same procedure after heating to the desired temperature and a subsequent equilibration period of around 3 min.

Unless described otherwise, the irradiation procedure followed the steps determined as optimal for crystallinity, which are listed in Table 45. The normalized emission spectra for the light sources used for curing are displayed in Figure 124.

Table 45: Irradiation parameters for optimized crystallinity of polymer samples from liquid crystalline monomers using the heated polymerization chamber (lamp intensity relative to maximum performance I% approximate irradiation intensity I_{abs} , maximum of the wavelength distribution λ_{max} , irradiation duration t, approximate total light dose d_L).

Irradiation step	Light source	I _% (%)	I _{abs} (mW cm ⁻²)	λ _{max} (nm)	t (s)	d _L (J cm ⁻²)
Mild initial curing for crystallinity	Hönle LEDcube	5	1.5 ¹	405	300	0.45
Final curing step	UVET UV-LED	10	290 ²	365	180	52

¹ Measured using an EIT Uvicure Plus

² Measured using a Coherent FieldMax II-TO Laser Power Meter

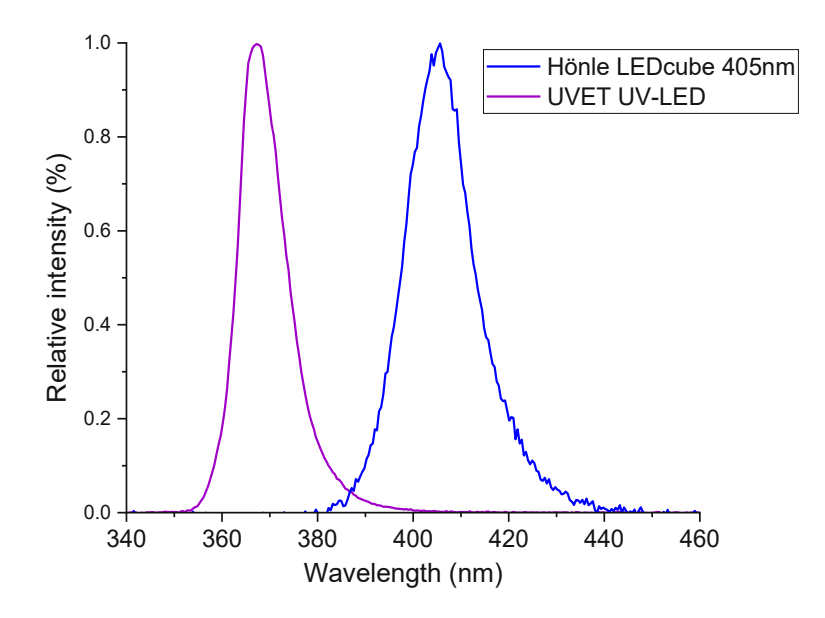


Figure 124: Normalized emission spectra of the LED light sources used in conjunction with the heated polymerization chamber measured using an OceanOptics USB 2000+ spectrometer.

Shape memory evaluation procedure 10

Cyclic shape memory tests were performed using a DMTA instrument (TA Instruments RSA-G2 DMA) equipped with a tensile test sample bracket and recorded using the software TA instruments TRIOS. A tensile test dogbone specimen (DIN EN ISO 527 test specimen 5b) was fastened into the bracket.

To evaluate shape memory properties, the sample was heated to 140 °C using a heating rate of 20 °C min⁻¹. After an equilibration period of 10 min, the sample was stretched until its parallel section had reached an elongation of 50%. Thereafter, the temperature was held for another 10 min. Next, the sample was cooled to room temperature after which the tension was released by the device. Subsequently, the temperature was increased again to 140 °C under no tension, which caused the sample to contract back to its original shape. The process was repeated 5-10 times, while the force and elongation were recorded.

The shape fixity ratio was calculated using Equation 5.

Equation 5: Calculation of the shape fixity ratio.

$$R_{sf} = \frac{L_r - L_0}{L_s - L_0} * 100$$

 R_{sf} shape fixity ratio (%)

 L_r parallel sample section length after elongation and cooling with no force applied (mm)

..... parallel sample section length before elongation (mm) L_0

..... parallel sample section length after elongation while force is still applied (mm) L_s

The shape recovery ratio was calculated using Equation 6.

Equation 6: Calculation of the shape recovery ratio.

$$R_{sr} = \frac{L_r - L_1}{L_s - L_0} * 100$$

 R_{sr} shape recovery ratio (%)

..... parallel sample section length after elongation and cooling with no force applied L_r

..... parallel sample section length after recovery L_1

..... parallel sample section length after elongation while force is still applied Ls

..... parallel sample section length before elongation L_0

3D printing procedure 11

3D printing was performed using a custom-built heated digital light processing (DLP) printer equipped with a DLP light engine, which emits light from an LED light source around a wavelength of 385 nm with a maximum intensity of 75 mW cm⁻² (Figure 125). Pixel sizes of 50 µm² are projected onto an area of 54 x 54 mm². 151

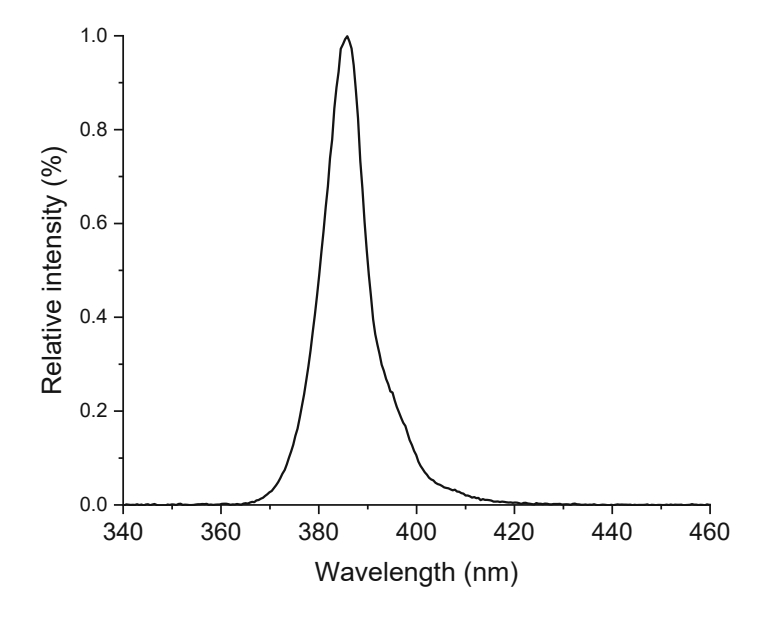


Figure 125: Normalized emission spectrum of the light source used in conjunction with the 3D printer.

For the printing experiments, the vat was preheated to around 15 °C higher than the initial printing temperature and the solid formulation was transferred to the vat, where it melted. After melting the formulation completely, the vat was cooled down to the desired printing temperature, to which the building platform was also preheated. To perform the printing steps, the building platform was lowered into the molten formulation, leaving a 50 µm gap. Next, the formulation layer was irradiated in the desired areas, and after complete irradiation, the building platform was lifted up to allow the formulation to flow under it. Then, the building platform was lowered into the molten formulation, again leaving a 50 µm gap, which was irradiated to form the next layer. The process was repeated until the part was printed. To clean any unpolymerized and oligomerized residues off the printed part, the part was placed in a screw-top vial along with a solvent (in most cases, toluene, unless mentioned otherwise) and cleaned in an ultrasonic bath for one to five minutes while frequently monitoring the progress and taking care that the process was stopped immediately if any sign of swelling of the printed part started to occur.

Materials

Compound	Purity	Manufacturer
1,12-Dodecanediol	99%	Sigma-Aldrich
1,2,4-Trivinylcyclohexane (mixture of isomers)	98%	Sigma-Aldrich
1,4-Diazabicyclo[2.2.2]octane (DABCO)	98%	TCI
1,6-Hexanedithiol (HDT)	>97%	TCI
10-Undecenoyl chloride	99%	BLDPharm
1-Ethyl-3-(3-dimethylaminopropyl)carbodiimide hydrochloride	98.00%	Szabo-Scandic
2,2-Dimethoxy-2 phenylacetophenone (IRGACURE 651)	98%	Fisher Chemical
4-(2-Hydroxyethyl)benzonitrile	98%	BLDPharm
4,4'-Dihydroxybiphenyl	99%	Fisher Scientific
4-Dimethylaminopyridine (DMAP)	99%	Sigma-Aldrich
6-Bromo-1-hexene	98%	ChemPUR
Allyl bromide	>98%	TCI
Biphenylsulfonyl chloride	97%	ABCR
Butylhydroxytoluene (BHT)	>99%	Sigma-Aldrich
Dicyclohexylcarbodiimide (DCC)	99%	Sigma-Aldrich
Diphenyl (2,4,6-trimethylbenzoyl)-phosphine oxide (TPO)	1	Lambson
EpoFix Kit	1	Struers
Ethoxylated trimethylolpropan tri-3-mercaptopropionate	95%	Bruno Bock
Hydroquinone	99%	Sigma-Aldrich
Iron(III) acetylacetonate	99%	ChemPUR
lvocerin	1	Ivoclar
M4470 silicone	1	Farben Wolf
Magnesium turnings acc. to Grignard	1	Sigma-Aldrich
Methyl 4-chlorobenzoate	99%	ChemPUR
N-methyl-2-pyrrolidone	99.5%, extra dry	Fisher Scientific
Pyrogallol	98%	Sigma-Aldrich
Pyruvic acid	>95%	TCI
Sodium hydride (suspended in mineral oil)	60%	TCI
T37 silicone crosslinker	1	Farben Wolf
Tetraethylene glycol	99%	Fisher Scientific
Thioacetic acid	95%	TCI
Triethylamine	99%	Sigma-Aldrich
Trimethylolpropane tris(3-mercaptopropionate) (TMPMP)	95%	Sigma-Aldrich
Tris[(3-mercaptopropionyloxy)-ethyl]-isocyanurate (TEMPIC)	95%	Bruno Bock

¹No purity given by manufacturer

Instruments

3D printing was performed on a custom-built heated digital light processing (DLP) printer equipped with a DLP light engine. An LED light source emits light at a wavelength maximum of 385 nm with a maximum intensity of 75 mW cm⁻² at the printing platform. Pixel sizes of 50 µm are projected onto an area of 96 x 54 mm². The vat and building platform can be heated separately up to 140 °C.

Atomic force microscopy was performed using a Park Systems XE7 instrument and evaluated using the software Park Systems XEI.

Attenuated total reflection infrared spectroscopy (ATR-IR) was performed using a PerkinElmer Spectrum 65 FT-IR Spectrometer equipped with a Specac MKII Golden Gate Single Reflection ATR System. Results were recorded and evaluated using the PerkinElmer Spectrum software.

Bulk polymerization was performed using three different light sources: a Hönle LEDcube LED array, a UVET UV-LED light source and, before the LED light sources and the heated polymerization chamber were available, a Uvitron IntelliRay 600 UV floodlight.

Data analysis and graphing was performed using the software Origin 2023b.

Differential scanning calorimetry (DSC) was performed using a TA Instruments DSC 2500 and recorded using the software TA Instruments TRIOS.

Dynamic mechanical thermal analysis (DMTA) was performed using an Anton Paar MCR 302 with a SRF12 clamp. Measurements were recorded using the software AntonPaar RheoPlus.

Emission spectra of light sources used to cure polymers were recorded using an OceanOptics 2000+ USB radiometer with the software SpectraSuite.

Gel permeation chromatography was performed using a Malvern VISCOTEK TDA system equipped with a VISCOTEK SEC-MALS 9 light scattering detector, a VISCOTEK TDA 305-021 RI+Visc detector, and a UV Detector Module 2550 for TDA 305.

Grinding and polishing of samples as preparation for atomic force microscopy was performed using a Struers Tegramin-30 polishing machine.

Microtome cuts were performed using a MICROM HM 360 rotational microtome equipped with a cryo system CN 30. Glass knives were used to cut the specimens.

NMR-spectroscopy was performed on a Bruker Avance DRX-400 FT-NMR spectrometer at 400 MHz for ¹H and 100 MHz for ¹³C. The spectra were referenced to the used NMR solvent (¹H, CDCl₃: 7.26 ppm; ¹³C, CDCl₃: 77.16 ppm; ¹H, DMSO-d₆: 2.5 ppm). The spectra were evaluated using the software MestreNova 15.0.1.

Photo-DSC was measured using a Netzsch Photo-DSC 204 F1. The measurements were recorded and analyzed using the software Netzsch Proteus thermal analysis V8.0.1. A Lumen Dynamics Omnicure S2000 spot UV curing system was used as a light source. The light source was calibrated using an Omnicure R2000 radiometer.

Photochemical synthesis of the trithiol comonomer CHTT was performed using an Omnicure S2000 UV curing system equipped with a 320-500 nm filter and a Lumatec Series 300 liquid light quide.

Polarized optical microscopy was performed using a Zeiss Axio. Scope A.1 microscope combined with a Linkam LTS 350 heated stage. Images were recorded using a Canon EOS 250D attached to the microscope with a connective piece custom-made by RafCamera.

Preparative column chromatography was performed using a Büchi Sepacore system (Büchi pump module C-605, Büchi control unit C-620, Büchi UV-Photometer C-635, Büchi fraction collector C-660). Glass columns packed with silica gel 60 (0.040-0.063 mm particle size) were used for separation.

RT-NIR-Photorheology was measured using an AntonPaar MCR 302 rheometer combined with a Bruker Vertex 80 IR spectrometer. A Lumen Dynamics Omnicure S2000 spot UV curing system was used as a light source. The light source was calibrated at the sample surface using an OceanOptics USB 2000+ radiometer using the software

SpectraSuite 1.6.0_11. The rheological data was evaluated using the software AntonPaar Rheocompass v1.24. IR spectra were evaluated using the software Bruker OPUS 7.0.

Shape memory tests were performed using a TA Instruments RSA-G2 DMA instrument equipped with a tensile test sample bracket and recorded using the software TA instruments TRIOS.

Tensile tests were performed using a Zwick Z050 and recorded using the software Zwick textXpert.

Abbreviations

AFCT addition fragmentation chain transfer

AIBN azobisisobutyronitrile

aqueous aq.

ATR attenuated total reflection

BPVS biphenyl-based vinyl sulfonate chain transfer agent C12VS dodecyl-based vinyl sulfonate chain transfer agent

CDCI₃ deuterated chloroform

dichloromethane CH₂Cl₂

CHCI₃ chloroform

CHTT 1,2,4-cyclohexanetriethanethiol

Cr crystalline phase (in liquid crystalline transition descriptions)

CTA chain transfer agent

D3MA 1,10-decanediol dimethacrylate

db% double bond percentage DBC double bond conversion DLP digital light processing

DMSO dimethylsulfoxide

DMSO-d6 deuterated dimethylsulfoxide

DMTA dynamic mechanical thermal analysis DSC differential scanning calorimetry

DVS difunctional vinyl sulfonate chain transfer agent

EΑ ethyl acetate

EDDT 2,2'-(ethylenedioxy)diethanethiol

Et2O diethyl ether **EtOH** ethanol

ETTMP ethoxylated trimethylolpropane-tris(3-mercaptopropionate)

FG% percentage of functional/reactive groups in a mixture

HCI hydrochloric acid HDT 1,6-hexanedithiol

HPLC high-performance liquid chromatography

I isotropic molten phase (in liquid crystalline transition descriptions)

infrared (spectroscopy) IR

LC liquid crystal/liquid crystalline

LCDT liquid crystalline dithiol LCE liquid crystalline elastomer LCM liquid crystalline monomer

LCN liquid crystalline polymer network

LD low light dose MD medium light dose MeOH methanol

mol% mole percentage

MPLC (preparative) medium-pressure liquid chromatography

MTSH 1,3,5-benzenetrimethanethiol

nematic phase (in liquid crystalline transition descriptions) Ν

NIR near infrared (spectroscopy)

NMR nuclear magnetic resonance (spectroscopy)

PΕ petroleum ether

Photo-DSC photo-differential scanning calorimetry

POM polarized optical microscopy SAXS small angle X-ray scattering

SLA stereolithography

Sm smectic phase (in liquid crystalline transition descriptions)

TEA triethyl amine

TEMPIC tris[(3-mercaptopropionyloxy)-ethyl]-isocyanurate **TMPMP** trimethylolpropane-tris(3-mercaptopropionate)

wt% weight percentage **XRD** X-ray diffraction

Appendix

1 DSC measurement graphs

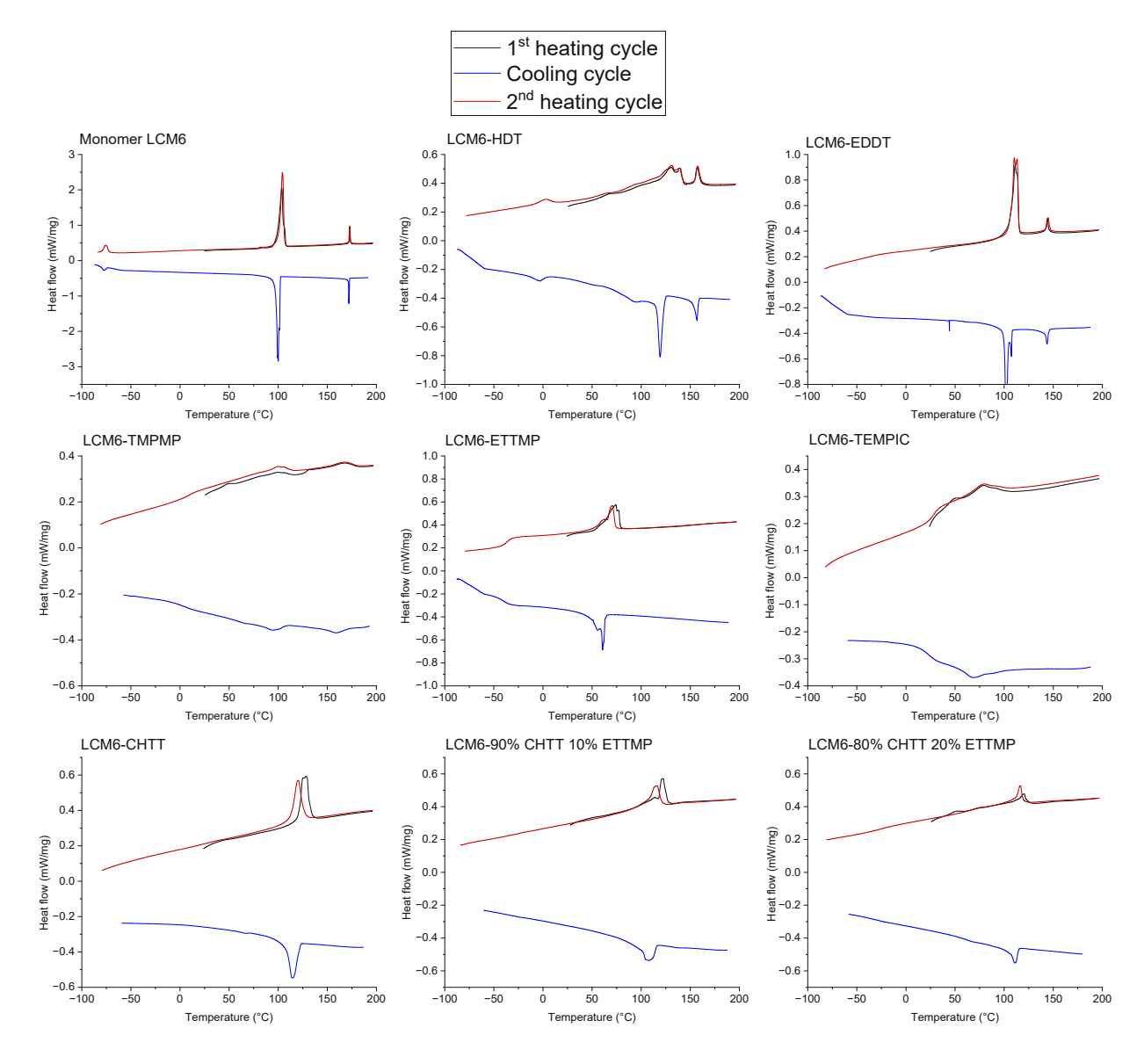


Figure S 1: DSC measurement graphs of LCM6 and all polymers obtained by combining thiol comonomers with LCM6.

2 Shape memory measurements

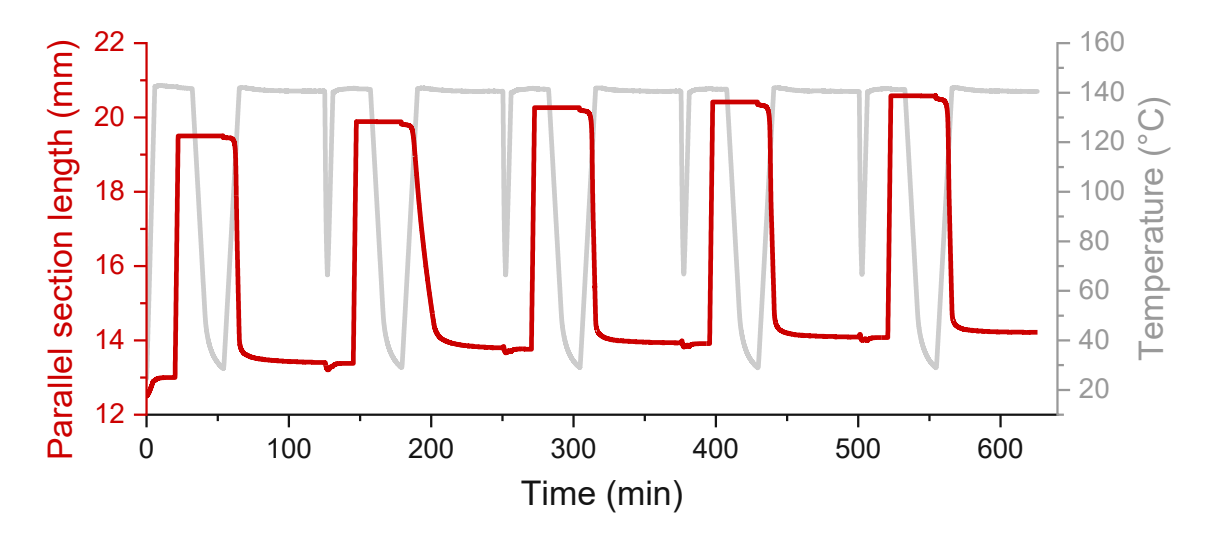


Figure S 2: First shape memory test of sample 1. Five cycles were tested with elongations of 6.5 mm. An unintended temperature drop during the shape recovery phase caused a minor artifact in the gap widths during this measurement.

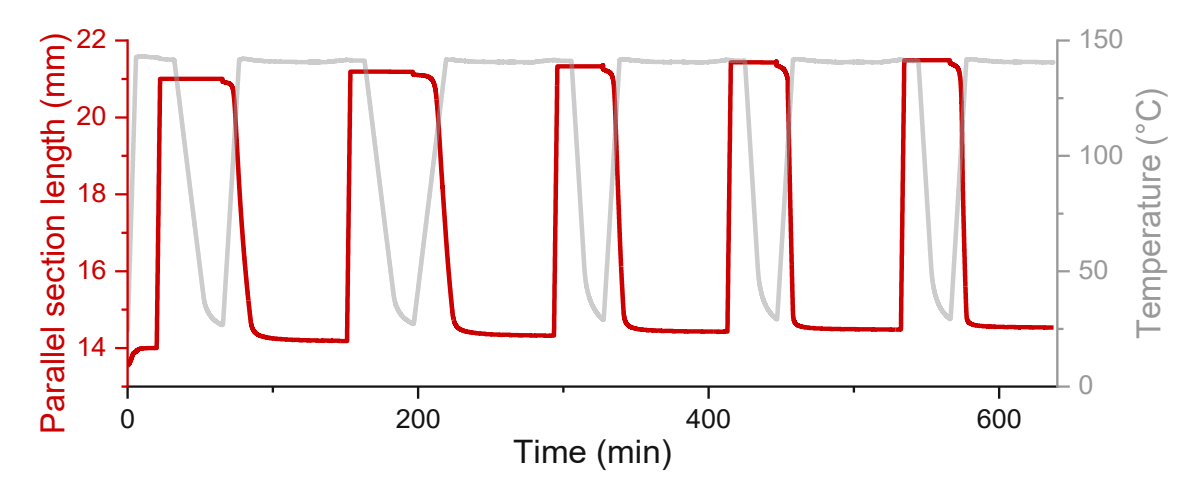


Figure S 3: Second shape memory test of sample 1. Five cycles were tested with elongations of 7 mm.

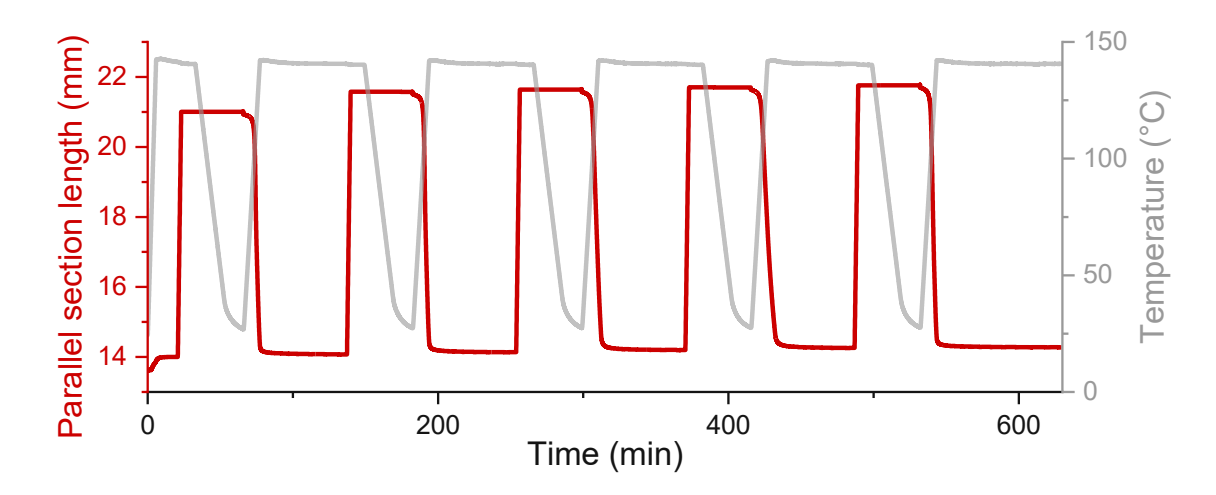


Figure S 4: Third shape memory test of sample 1. Five cycles were tested with elongations of 7 mm during the first cycle and 7.5 mm during subsequent cycles.

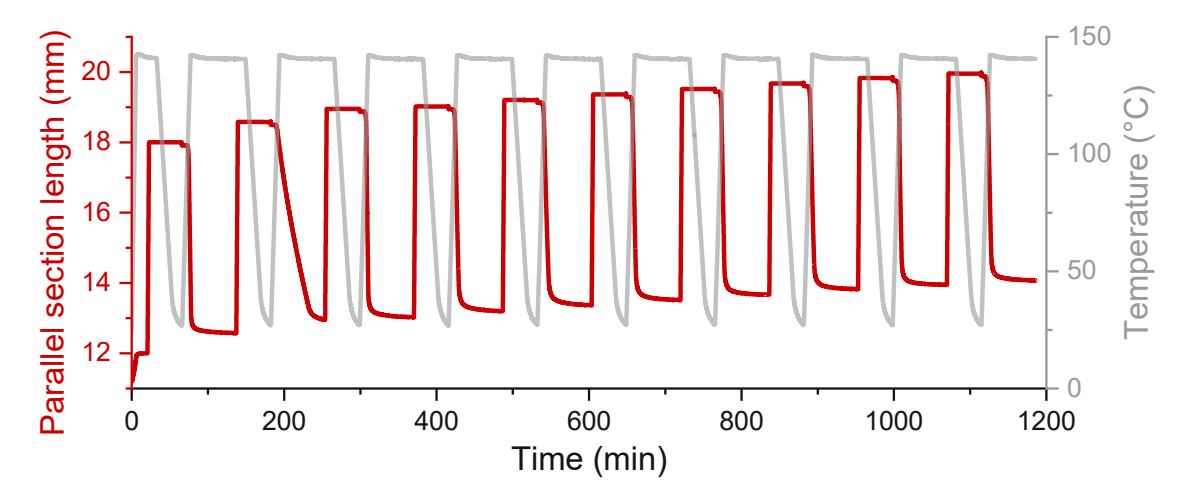


Figure S 5: First shape memory test of sample 2. Ten cycles were tested with elongations of 6 mm.

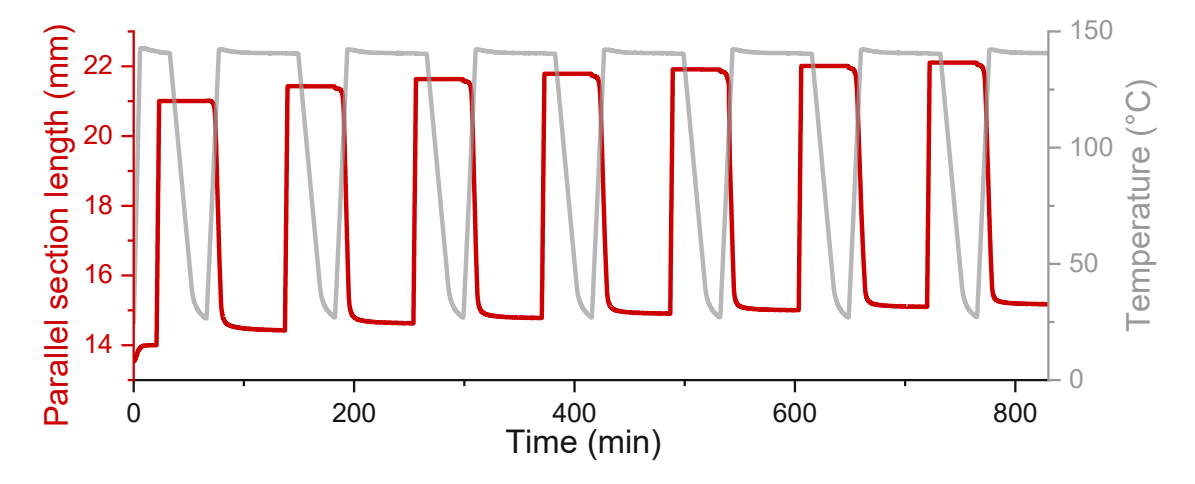


Figure S 6: Second shape memory test of sample 2. Seven cycles were tested with elongations of 7 mm.

3 Liquid crystalline molecule list

Melting points are abbreviated as "mp". Where multiple phase transitions are present, they are described in the common notation of Cr n LC n I with n being the temperature in °C and the following abbreviations for the different phases:

Cr... Crystalline phase

LC... Liquid crystalline phase

N... Nematic phase

Sm... Smectic phase

S_N... Smectic N phase, e.g., S_A for smectic A phase

I ... Isotropic molten phase

Monotropic liquid crystalline phases, which are only present during cooling, are given in brackets. When a melting point is given in the form of "mp=X °C", no information about the existence of a liquid crystalline phase could be found.

Biphenyl mesogens

Compound	Phase transition(s)
HO	mp=280 °C ¹⁵²
· Un	n=0: mp=175 °C ¹⁰⁷
	n=1: mp=181 °C ¹⁰⁸
	n=2: mp=159 °C ¹⁰⁹
	n=3: mp=146 °C ¹¹⁰
	n=4: mp=132 °C ¹⁵³
√ \0.	n=5: mp=126 °C ¹¹²
the contraction of the contracti	n=6: mp=121 °C ¹¹³
	n=7: mp=117 °C ¹¹²
\sim of \uparrow_n	n=8: mp=115 °C ¹¹³
	n=9: mp=114 °C ¹¹³
	n=10: mp=115 °C ¹¹³
	n=11: mp=114 °C ¹¹³
	n=12: mp=116 °C ¹¹³
	n=13: mp=114 °C ¹¹³
	n=0: mp=162 °C ⁹⁵
	n=1: mp=148 °C ⁹⁵
	n=2: mp=123 °C ⁹⁵
	n=3: Cr 92 LC 111 I ⁹⁶
	n=4: Cr 117 LC 118 I ⁹⁷
()	n=5: Cr 106 LC 118 I ⁹⁷
	n=6: Cr 95 LC 122 I ⁹⁷
	n=7: Cr 95 LC 120 I ⁹⁷
	n=8: Cr 98 LC 122 I ⁹⁷
,	n=9: Cr 98 LC 122 I ⁹⁷
	n=10: Cr 101 LC 122 I ⁹⁷
	n=11: Cr 101 LC 121 I ⁹⁷
	n=12: Cr 104 LC 121 I ⁹⁷
	n=13: Cr 105 LC 119 I ⁹⁷
	n=14: Cr 107 LC 119 I ⁹⁷
	n=0: mp=125 °C ⁹⁸
	$n=1: mp = 81 °C^{98}$
(a)	$n=2: mp = 60 °C^{99}$
	$n=3: mp=58 °C^{100}$
	n=4: Cr 25 Sm 46 I ¹⁰¹
\sim \swarrow_n	n=5: Cr 34 S _E 52 I ¹⁰¹
	n=6: Cr < 19 S _E 40 S _B 61 I ¹⁰¹
	$n=7: mp=65 °C^{102}$
	n=8: mp=49 °C ¹⁰³

	n=1: Cr 63 I ¹⁰⁶ n=3: Cr -36 Sm 29 I ¹⁰⁶ n=6: Cr 18 Sm 43 I ¹⁰⁶
	n=1: Cr 144 I ¹⁵⁴ n=7: Cr 105 I ¹⁵⁵
HS () O () SH	n=3: Cr 120 I ¹⁵⁶ n=4: LC phase exists, no temperatures given ¹⁵⁷ n=8: Cr 116 I ¹⁵⁸
	n=8: Cr 78 S _X 110 I ¹²⁹
	n=9: Cr 96 I ¹²⁹

Three-ring phenylester mesogens

Compound	Phase transition(s)
	n=0: Cr 213 LC 297 I ⁹⁰
	n=1: Cr 226 LC 287 I ⁹⁰
	n=2: Cr 175 LC 249 I ⁹⁰
() -	n=3: Cr 153 LC 241 I ⁹⁰
	n=4: Cr 125 LC 188 I ⁹⁰
	n=5: Cr 127 N 213 ⁹⁰
	n=6: Cr 121 LC 198 I ⁹⁰
\\\\\\\\\\\\\\\\\\\\\\\\\\\\\\\\\\\\\\	n=7: Cr 118 LC 195 ⁹⁰
\ \frac{1}{11}	n=9: Cr 122 LC 178 I ⁹⁰
	n=10: Cr 111 Sm 151 N 175 I ⁹¹
	n=11: Cr 111 Sm 151 N 175 I ⁹¹
	n=13: Cr 109 Sm 163 I ⁹⁰
	n=0: Cr 170 N 254 I ⁸⁹
\ 0\\	n=1: Cr 187 N 248 I ⁸⁹
	n=2: Cr 138 N 209 I ⁸⁹
	n=3: Cr 112 N 203 I ⁸⁹
	n=4: Cr 90 N 179 I ⁸⁹
	n=5: Cr 88 N 172 I ⁸⁹
	n=6: Cr 85 N 159 I ⁸⁹
	n=7: Cr 72 N 156 I ⁸⁹

	n=8: Cr 75 N 148 I ⁸⁹ n=9: Cr 80 N 144 I ⁸⁹
(continued)	n=0: Cr 205 N 277 I ⁹⁰
	n=1: Cr 216 N 266.5 I ⁹⁰ n=2: Cr 198 N 238 I ⁹⁰ n=3: Cr 183 N 229 I ⁹⁰ n=5: Cr 161 N 201 I ⁹⁰ n=6: Cr 153 N 188 I ⁹⁰
	n=1: Cr 167 LC 230 I ⁹² n=9: Cr 111 Sm 130 N 168 I ¹⁰⁵
	n=1: Cr 142 LC 217 I (own measurement) n=3: Cr 100.6 LC 186 I ¹⁰⁵ n=9: Cr 76 LC 137 I ¹⁰⁵
	n=9: Cr 91 LC 129 I ¹⁰⁵
	n=3: Cr 72 N 112 I ¹⁵⁹
	n=m=6: Cr 117 N 185 I ¹¹⁶
	n=m=6: Cr 87 N 148 I ¹¹⁶
HS () O () SH	n=6: Cr 100 N 194 I ¹⁶⁰

HS ()0 () SH	n=6 (heating): Cr 81 N 163 I ¹⁶¹
	n=1: Cr 181 LC 229 I ⁹² n=2: Cr 153 N 244 I ¹¹⁶ n=4: Cr 119 N 213 I ¹¹⁶ n=7: Cr 111 N 168 I ¹¹⁶ n=9: Cr 110 N 165 I ¹⁶²
	n=9: Cr 87 S _A 143 N 162 I ¹⁶²
	n=m=2: Cr 124 N 186 I ¹¹⁶ n=m=3: Cr 99 N 153 I ¹¹⁶
	n=m=3: Cr 68 N 100 I ¹¹⁶
	n=m=4: Cr 107 N 165 I ¹¹⁶ n=m=5: Cr 92 N 170 I ¹¹⁶ n=m=6: Cr 115 N 155 I (S _C 87 N) ¹¹⁶ n=m=8: Cr 82 S _C 108 N 148 I ¹¹⁶ n=m=10: Cr 87 S _C 112 N 137 I ¹¹⁶ n=m=11: Cr 67 S _X 88 S _C 114 N 133 I ¹¹⁶ n=11, m=6: Cr 68 S _X 79 S _C 105 N 144 I ¹¹⁶
	n=6: Cr 76 S _A 138 N 150 I ¹¹⁶ n=11: Cr 64 S _X 81 S _A 131 N 134 I ¹¹⁶
	n=6: Cr 117 S _A 140 N 145 I ¹¹⁶ n=11: Cr 117 S _A 128 N 130 I (S _X 88 S _A) ¹¹⁶
	n=m=4: Cr 80 N 165 I ¹¹⁶ n=m=5: Cr 93 N 124 I ¹¹⁶ n=m=6: Cr 86 N 116 I ¹¹⁶ n=m=11: Cr 79 N 104 I ¹¹⁶

	n=6: Cr 95 N 135 I ¹¹⁶
To CI	n=6: Cr 99 N 110 I ¹¹⁶
	n=6: Cr 106 N 138 I ¹¹⁶
CN CN CN CN	n=6: Cr 101 N 111 I (S _X 86 N) ¹¹⁶

Two- and four-ring phenylester mesogens

Compound	Phase transition(s)
	n=m=1: Cr 69 I ⁹² n=m=2: Cr 52 I ¹¹⁵ n=m=4: Cr 49 N 62 I ¹¹⁷
+ 0 () () () m	n=m=0 mp= 123 °C ¹⁶³ n=m=1 mp=113 °C ¹⁶⁴ n=1, m=2: mp=107 °C ¹⁶⁴ n=2, m=1: mp=88 °C ¹⁶⁴ n=m=2 mp=92 °C ¹⁶⁴ n=m=3 Cr 69 N 93 I ⁸⁷ n=4, m=3: Cr 68 N 84 I ⁸⁷ n=4, m=7: mp=50 °C ¹⁶⁵ n=5, m=3: mp=69 °C ¹⁶⁶ n=m=5 mp= 61 °C ¹⁶⁶ n=5, m=6: mp=55 °C ¹⁶⁷ n=5, m=7: mp=59 °C ¹⁶⁵ n=7, m=5: mp=53 °C ¹⁶⁵ n=m=7 Cr 62 Sm 72 N 90 I ⁸⁷ n=9, m=5: mp=62 °C ¹⁶⁸ n=9, m=7: Cr 71 Sm 88 N 91 I ¹⁶⁹ n=m=9 Cr 71 Sm 89 N 90 I ¹⁷⁰

	n=7, m=6: Cr 99 S _A 121 I ⁸⁹
	n=7, m=5: Cr 53 S _A 70 I ⁸⁹
	n=7, m=5: Cr 51 S _A 117 I ⁸⁹
	n=m=0: mp=90 ⁸⁵ n=m=2: Cr 15 N 32 I ⁸⁶ n=2, m=4: Cr 15 N 19 I ⁸⁷ n=4, m=3: Cr 23 I ⁸⁶ n=m=4: Cr 26 N 35 I ⁸⁸ n=m=7: Cr 54 S _A 65 N 67 I ⁸⁹
	n=m=6: Cr 56 S _A 72 N 82 I ¹¹⁶
	n=1: Cr 79 LC 93 I ⁹² n=2: Cr 45 LC 61 I ¹¹⁵
	n=m=4: Cr 85 I ¹¹⁶ n=m=4: Cr 60 I (S _A 35 N 46 I) ¹¹⁶ n=m=6: Cr 54 I (S _A 45 N 48 I) ¹¹⁶ n=m=11: Cr 56 S _A 62 I (S _X 50 S _A) ¹¹⁶ n=6, m=11: Cr 50 I (S _A 48 I) ¹¹⁶ n=11, m=6: Cr 57 I (S _X 38 S _A 55 I) ¹¹⁶
	n=m=2: Cr 45 N 61 I ¹¹⁶ n=m=4: Cr 56 N 66 I ¹¹⁶ n=m=7: Cr 77 I (S _A 66 N 74 I) ¹¹⁶
	n=m=2: Cr 43 I ¹¹⁶
HS () O () SH	n=4, m=6: Cr 62 N 77 I ¹⁶¹

n=1: Cr 184 N 278 I ⁹³ n=9: Cr 133 LC 264 I ⁹⁴
Cr 192 LC 271 I ⁹²

Naphthyl-containing mesogens	
Compound	Phase transition(s)
	n=0: Cr 180 N 229 I ¹⁷¹ n=5: Cr 153 N 168 I ¹⁷¹
	n=0: Cr 216 N 235 I ¹⁷¹ n=5: Cr 169.5 N 170.5 I ¹⁷¹
	n=5: Cr 122 N 230 I ¹⁷¹
	Substitution pattern 2,7: n=11: Cr 122 S _C P 170 I ¹²¹ n=13: Cr 88 S _C P 116 I ¹²¹ Substitution pattern 1,3: n=13: Cr 105 I ¹²¹ Substitution pattern 1,6: n=11: Cr 86 S _{CA} P _A 135 I ¹²¹ n=13: Cr 95 S _{CA} P _A 145 I ¹²¹ Substitution pattern 1,2: n=13: Cr 34 S _A 153 I ¹²¹ Substitution pattern 2,3: n=11: Cr 63 S _A 210 N 217 I ¹²¹ n=13: Cr 75 S _A 210 N 211 I ¹²¹ Substitution pattern 1,7: n=11: Cr 149 I ¹²¹ n=13: Cr 133 I ¹²¹ (properties given during cooling)

Compound	Phase transition(s)
	n=0: Cr 185 N 269 I ¹¹⁸
£)0. ^	n=1: Cr 171 N 273 I ¹¹⁸
(%)	n=2: Cr 161 N 236 I ¹¹⁸
	n=3: Cr 152 N 221 I ¹¹⁸
	n=5: Cr 141 N 191 I ¹¹⁸
♥ 0(/n	n=6: Cr 124 N 176 I ¹¹⁸
	n=7: Cr 119 N 171 I ¹¹⁸
	n=m=2: Cr 67 I ⁸⁸
	n=2, m=3: Cr 57 I (N 44 I) ⁸⁸
	n=2, m=4: Cr 39 N 56 I ⁸⁸
	n=2, m=5: Cr 48 I (N 46 I) ⁸⁸
	n=2, m=6: Cr 53 N 53 I ⁸⁸
	n=2, m=7: Cr 8 N 53 I ⁸⁸
	n=3, m=1: Cr 49 I (N 36 I) ⁸⁸
	n=3, m=2: Cr 50 I (N 47 I) ⁸⁸
	n=m=3: Cr 39 I (N 38 I) ⁸⁸
	n=3, m=4: Cr 30 N 49 I ⁸⁸
	n=3, m=5: Cr 29 N 43 I ⁸⁸
	n=3, m=6: Cr 23 N 52 I ⁸⁸
	n=3, m=7: Cr 27 N 51 I ⁸⁸
	n=4, m=1: Cr 48 N 55 I ⁸⁸
	n=4, m=2: Cr 60 N 67 I ⁸⁸
	n=4, m=3: Cr 39 N 54 I ⁸⁸
	n=m=4: Cr 31 N 65 I ⁸⁸
\ / _m	n=4, m=5: Cr 24 N 59 I ⁸⁸
	n=4, m=6: Cr 35 N 65 I (S _B 30.5 N) ⁸⁸
	n=4, m=7: Cr 41 S _B 42 N 63 I ⁸⁸
	n=5, m=1: Cr 45 N 48 I ⁸⁸
	n=5, m=2: Cr 41 N 60 I ⁸⁸
	n=5, m=3: Cr 47 N 51 I ⁸⁸
	n=5, m=4: Cr 38 N 55 I ⁸⁸
	n=m=5: Cr 40 N 54 I (S _B 33 N) ⁸⁸
	n=5, m=6: Cr 44 N 57 I (S _B 36 N) ⁸⁸
	n=5, m=7: Cr 48 N 60 I (S _B 53 N) ⁸⁸
	n=6, m=2: Cr 59 N 71 I ⁸⁸
	n=6, m=3: Cr 34 N 53 I ⁸⁸
	n=6, m=4: Cr 33 N 62 I ⁸⁸
	n=6, m=5: Cr 27 S _B 43 N 60 I ⁸⁸
	n=m=6: Cr 35 S _B 54 N 69 I ⁸⁸

	20
	n=6, m=7: Cr 34 S _B 61 N 67 I ⁸⁸
	n=m=2: Cr 61 N 89 I ⁸⁸
	n=2, m=3: Cr 48 N 94 I ⁸⁸
	n=2, m=4: Cr 40 N 87 I ⁸⁸
	n=2, m=5: Cr 74 N 91 I ⁸⁸
	n=2, m=6: Cr 50 N 85 I ⁸⁸
	n=2, m=7: Cr 52 N 88 I ⁸⁸
	n=3, m=2: Cr 49 N 82 I ⁸⁸
	n=3, m=3: Cr 33 N 85 I ⁸⁸
	n=3, m=4: Cr 52 N 85 I ⁸⁸
	n=3, m=5: Cr 46 N 88 I ⁸⁸
	n=3, m=6: Cr 53 N 84 I ⁸⁸
	n=3, m=7: Cr 45 N 83 I ⁸⁸
A	n=4, m=2: Cr 41 N 95 I ⁸⁸
	n=4, m=3: Cr 42 N 100 I ⁸⁸
	n=m=4: Cr 51 N 94 I ⁸⁸
o √ _m	n=4, m=5: Cr 55 N 97 I ⁸⁸
	n=4, m=6: Cr 57 N 93 I ⁸⁸
	n=4, m=7: Cr 54 N 96 I (S _C 37 S _A 50 N) ⁸⁸
	n=5, m=2: Cr 63 N 88 I ⁸⁸
	n=5, m=3: Cr 48 N 94 I ⁸⁸
	n=5, m=4: Cr 47 N 84 I ⁸⁸
	n=m=5: Cr 48 N 86 I ⁸⁸
	n=5, m=6: Cr 59 N 89 I (S _A 57 N) ⁸⁸
	n=5, m=7: Cr 54 S _A 66 N 90 I (S _C 27 S _A) ⁸⁸
	n=6, m=2: Cr 57 N 93 I ⁸⁸
	n=6, m=3: Cr 51 N 98 N ⁸⁸
	n=6, m=4: Cr 42 N 92 I ⁸⁸
	n=6, m=5: Cr 51 S _A 52 N 96 I ⁸⁸
	n=m=6: Cr 54 S _A 67 N 92 I ⁸⁸
	n=6, m=7: Cr 58 S _A 77 N 94 I ⁸⁸

Cyclohexane-containing mesogens		
Compound	Phase transition(s)	
	n=6: Cr 72 S _X 106 I ¹¹⁶	
√ m	n=1, m=2: Cr -3 S _B 68.2 I ¹¹⁹ n=1, m=4: Cr -16 S _B 77 I ¹¹⁹ n=4, m=2: Cr 22 S _B 98 I ¹¹⁹ n=m=4: Cr 41 S _B 114 I ¹¹⁹	

H_{n}	n=1, m=2: Cr 9 S _B 80 I ¹¹⁹ n=1, m=4: Cr ? S _B 95 I ¹¹⁹ n=2, m=1: Cr 31 S _B 80 I ¹¹⁹ n=4, m=2: Cr 52 S _B 109 I ¹¹⁹
F F m	n=4, m=2: Cr 142 I ¹¹⁹ n=m=4: Cr 100 S _B 153 I ¹¹⁹
	n=0: Cr 197 I ¹¹⁸ n=3: Cr 129 N 157 I ¹¹⁸ n=5: Cr 122 N 136 I ¹¹⁸
()° (), (), (), (), (), (), (), (), (), (),	n=5: LC phase present ¹⁷² n=7: LC phase present ¹⁷³

Long lateral chain phenylester mesogens	
Compound	Phase transition(s)
	n=5, m=0: Cr 80 N 87 I ⁸⁹
	n=5, m=1: Cr 84 I (N 58 I) ⁸⁹
/ \	n=5, m=2: Cr 90 I ⁸⁹
	n=5, m=3: Cr 87 I ⁸⁹
	n=5, m=4: Cr 60 I (N 43 I) ⁸⁹
ö	n=5, m=5: Cr 60 I (N 39 I) ⁸⁹
	n=5, m=6: Cr 67 I (N 40 I) ⁸⁹
	n=5, m=7: Cr 73 I ⁸⁹
	n=5, m=8: Cr 77 I ⁸⁹
	n=6, m=0: Cr 63 N 94 I ⁸⁹
	n=1, m=9: Cr 119 I (N 85 I) ⁸⁹
	n=1, m=11: Cr 112 I ⁸⁹
⟨ ⟩	n=2, m=9: Cr 94 I (N 63 I) 89
	n=2, m=11: Cr 81 I ⁸⁹
	n=3, m=9: Cr 76 I (N 73 I) ⁸⁹
	n=3, m=11: Cr 77 I (N 68 I) ⁸⁹
	n=4, m=9: Cr 76 I (N 65 I) ⁸⁹
	n=4, m=11: Cr 75 I (N 60 I) ⁸⁹
	n=m=7: Cr 59 N 78 I ⁸⁹
HOYO OFF	n=0, m=10: Cr 100 I (N 61 I) ⁸⁹
\\\\\\\\\\\\\\\\\\\\\\\\\\\\\\\\\\\\\\	n=3, m=0: Cr 110 N 155 I ⁸⁹
" \\\	n=4, m=0: Cr 90 N 135 I ⁸⁹
"\\o(\)	n=5, m=0: Cr 104 N 136 I ⁸⁹

(continued)

n=5, m=1: Cr 77 N 108 I⁸⁹ n=5, m=2: Cr 101 I (N 97 I)⁸⁹ n=5, m=3: Cr 100 I (N 87 I)⁸⁹ n=5, m=4: Cr 89 I (N 86 I)⁸⁹ n=5, m=5: Cr 81 N 88 I⁸⁹ n=5, m=6: Cr 81 N 87 I⁸⁹ n=5, m=7: Cr 91 I (N 83 I)⁸⁹ n=5, m=8: Cr 92 I (N 82 I)⁸⁹ n=5, m=9: Cr 96 I (N 80 I)⁸⁹ n=5, m=10: Cr 90 I (N 77 I)⁸⁹ n=6, m=0: Cr 97 N 129 I⁸⁹ n=6, m=1: Cr 88 N 102 I⁸⁹ n=6, m=2: Cr 102 I (N 93 I)⁸⁹ n=6, m=3: Cr 101 I (N 85 I)⁸⁹ n=6, m=4: Cr 92 I (N 85 I)⁸⁹ n=6, m=5: Cr 81 N 83 I⁸⁹ n=6, m=6: Cr 85 I (N 84 I)⁸⁹ n=6, m=7: Cr 89 I (N 79 I)⁸⁹ n=6, m=8: Cr 86 I (N 81 I)⁸⁹ n=6, m=9: Cr 89 I (N 78 I)⁸⁹ n=6, m=10: Cr 85 I (N 77 I)⁸⁹ n=7, m=0: Cr 102 N 124 I⁸⁹ n=7, m=1: Cr 90 N 102 I⁸⁹ n=7, m=2: Cr 83 N 94 I⁸⁹ n=7, m=3: Cr 87 I (N 85 I)⁸⁹ n=7, m=4: Cr 84 N 85 I⁸⁹ n=7, m=5: Cr 76 N 87 I⁸⁹ n=7, m=6: Cr 77 N 87 I⁸⁹ n=7, m=7: Cr 81 N 84 I⁸⁹ n=7, m=8: Cr 72 N 85 I⁸⁹ n=7, m=9: Cr 76 N 83 I⁸⁹ n=7, m=10: Cr 74 N 81 I⁸⁹ n=8, m=0: Cr 102 N 118 I⁸⁹ n=8, m=1: Cr 78 N 96 I⁸⁹ n=8, m=2: Cr 86 I (N 85 I)⁸⁹ n=8, m=3: Cr 82 I (N 79 I)⁸⁹ n=8, m=4: Cr 81 N 79 I⁸⁹ n=8, m=5: Cr 60 N 82 I⁸⁹ n=8, m=6: Cr 74 N 83 I⁸⁹ n=8, m=7: Cr 77 N 82 I⁸⁹ n=8, m=8: Cr 73 N 81 I⁸⁹ n=8, m=9: Cr 74 N 79 I⁸⁹ n=8, m=10: Cr 64 N 78 I⁸⁹

Die appı	The app
ibliothek	r knowledge hub
	WIEN

	n=7, m=2: Cr 90 N 100 I ⁸⁹ n=7, m=3: Cr 82 N 99 I ⁸⁹ n=7, m=5: Cr 60 N 98 I ⁸⁹ n=7, m=6: Cr 54 N 95 I ⁸⁹ n=7, m=7: Cr 52 N 93 I ⁸⁹
"	n=7, m=8: Cr 50 N 92 I ⁸⁹ n=7, m=9: Cr 54 N 90 I ⁸⁹
	n=7, m=5: Cr 62 N 79 I ⁸⁹ n=7, m=9: Cr 67 N 69 I ⁸⁹
	n=4, m=1: Cr 47 N 136 I ⁸⁹ n=4, m=7: Cr 48 N 48 I ⁸⁹ n=4, m=8: Cr 58 N 47 I ⁸⁹ n=4, m=9: Cr 44 N 46 I ⁸⁹
	n=4, m=0: Cr 67 N 138 I ⁸⁹ n=4, m=1: Cr 66 N 97 I ⁸⁹ n=4, m=2: Cr 72 N 74 I ⁸⁹ n=4, m=3: Cr 79 I ⁸⁹ n=4, m=4: Cr 70 I (N 52 I) ⁸⁹ n=4, m=5: Cr 72 I ⁸⁹ n=4, m=6: Cr 77 I ⁸⁹ n=4, m=7: Cr 71 I ⁸⁹ n=4, m=8: Cr 68 I (N 46 I) ⁸⁹

References

- Saed, M. O. et al. Molecularly-Engineered, 4D-Printed Liquid Crystal Elastomer 1 Actuators. Advanced **Functional Materials** 29 (2019).https://doi.org:10.1002/adfm.201806412
- Herbert, K. M. et al. Synthesis and alignment of liquid crystalline elastomers. Nature 2 Reviews Materials 7, 23-38 (2021). https://doi.org:10.1038/s41578-021-00359-z
- Wermter, H. & Finkelmann, H. Liquid crystalline elastomers as artificial muscles. 1 3 (2001). https://doi.org:doi:10.1515/epoly.2001.1.1.111
- 4 Hisano, K. et al. Mechano-Optical Sensors Fabricated with Multilayered Liquid Crystal Elastomers Exhibiting Tunable Deformation Recovery. Advanced Functional Materials 31 (2021). https://doi.org:10.1002/adfm.202104702
- 5 Li, Z., Olson, G., Patel, D. K., Yao, L. & Majidi, C. Electrically Controlled Liquid Crystal Elastomer Surfaces for Dynamic Wrinkling. Advanced Intelligent Systems 6 (2023). https://doi.org:10.1002/aisy.202200402
- 6 Martinez, A. M., McBride, M. K., White, T. J. & Bowman, C. N. Reconfigurable and Spatially Programmable Chameleon Skin-Like Material Utilizing Light Responsive Covalent Adaptable Cholesteric Liquid Crystal Elastomers. Advanced Functional Materials (2020). https://doi.org:10.1002/adfm.202003150
- 7 Barnes, M. et al. Reactive 3D Printing of Shape-Programmable Liquid Crystal Elastomer Actuators. ACS Appl Mater Interfaces 12, 28692-28699 (2020). https://doi.org:10.1021/acsami.0c07331
- 8 Lopez-Valdeolivas, M., Liu, D., Broer, D. J. & Sanchez-Somolinos, C. 4D Printed Actuators with Soft-Robotic Functions. Macromol Rapid Commun 39 (2018). https://doi.org:10.1002/marc.201700710
- 9 Javed, M. et al. Programmable Shape Change in Semicrystalline Liquid Crystal Elastomers. **ACS** Appl Mater Interfaces 14, 35087-35096 (2022).https://doi.org:10.1021/acsami.2c07533
- Westbrook, K. K. et al. Two-way reversible shape memory effects in a free-standing 10 composite. polymer Smart Materials and **Structures** 20 (2011).https://doi.org:10.1088/0964-1726/20/6/065010
- Behl, M. & Lendlein, A. Actively moving polymers. Soft Matter 3, 58-67 (2006). 11 https://doi.org:10.1039/b610611k
- 12 Hebner, T. S., Korner, K., Bowman, C. N., Bhattacharya, K. & White, T. J. Leaping Science **Advances** eade1320 liquid crystal elastomers. 9, https://doi.org:10.1126/sciadv.ade1320
- 13 Buruiana, T., Melinte, V., Costin, G. & Buruiana, E. C. Synthesis and properties of liquid crystalline urethane methacrylates for dental composite applications. *Journal*

- of Polymer Science Part A: Polymer Chemistry 49, 2615-2626 (2011). https://doi.org:10.1002/pola.24693
- Tai, Y. Y., Hsu, S. H., Chen, R. S., Su, W. F. & Chen, M. H. Liquid crystalline epoxy 14 nanocomposite material for dental application. J Formos Med Assoc 114, 46-51 (2015). https://doi.org:10.1016/j.jfma.2014.01.018
- 15 Ritter, H. D., Georg; Moszner, Norbert; Salz, Ulich; Rheinberger, Volker. Dental materials on basis of liquid crystal monomers. (1997).
- 16 Liu, W. et al. Synthesis of a liquid-crystalline resin monomer with the property of shrinkage polymerization. Dent Mater J **32**, 550-556 https://doi.org:10.4012/dmj.2013-018
- 17 Gebhardt, A. & Hötter, J.-S. in Additive Manufacturing (eds Andreas Gebhardt & Jan-Steffen Hötter) I-XX (Hanser, 2016).
- Jain, P. K. & Jain, P. K. Use of 3D printing for home applications: A new generation 18 concept. Materials Today: **Proceedings** 605-607 (2021).**43**, https://doi.org:https://doi.org/10.1016/j.matpr.2020.12.145
- Kafle, A. et al. 3D/4D Printing of Polymers: Fused Deposition Modelling (FDM), 19 Selective Laser Sintering (SLS), and Stereolithography (SLA). Polymers 13 (2021). https://doi.org:10.3390/polym13183101
- 20 Gmeiner, R., Mitteramskogler, G., Stampfl, J. & Boccaccini, A. R. Stereolithographic Ceramic Manufacturing of High Strength Bioactive Glass. International Journal of Applied Ceramic Technology 12, 38-45 (2015). https://doi.org:10.1111/ijac.12325
- Steyrer, B., Busetti, B., Harakály, G., Liska, R. & Stampfl, J. Hot Lithography vs. room 21 temperature DLP 3D-printing of a dimethacrylate. Additive Manufacturing 21, 209-214 (2018). https://doi.org:10.1016/j.addma.2018.03.013
- 22 Taschner, R. et al. Evaluation of Sulfonium Borate Initiators for Cationic Photopolymerization and Their Application in Hot Lithography. ACS Applied Polymer Materials 5, 3023-3033 (2023). https://doi.org:10.1021/acsapm.3c00191
- 23 Haslinger, C., Zahoranova, A. & Baudis, S. Synthesis of coumarin-containing poly(2oxazoline)s and light-induced crosslinking for hydrogel formation. Monatsh Chem 154, 459-471 (2023). https://doi.org:10.1007/s00706-022-03013-8
- Ligon-Auer, S. C., Schwentenwein, M., Gorsche, C., Stampfl, J. & Liska, R. 24 Toughening of photo-curable polymer networks: a review. Polymer Chemistry 7, 257-286 (2016). https://doi.org:10.1039/c5py01631b
- 25 Segurola, J., Allen, N. S., Edge, M., McMahon, A. & Wilson, S. Photoyellowing and discolouration of UV cured acrylated clear coatings systems: influence of photoinitiator type. Polymer Degradation and Stability 64, 39-48 (1999). https://doi.org/https://doi.org/10.1016/S0141-3910(98)00169-4

- 26 Ahmad, N. M. et al. Chain Transfer to Polymer and Branching in Controlled Radical Polymerizations of n-Butyl Acrylate. Macromol Rapid Commun 30, 2002-2021 (2009). https://doi.org:10.1002/marc.200900450
- 27 Crivello, J. V. & Reichmanis, E. Photopolymer Materials and Processes for Advanced Technologies. of Materials 26, 533-548 (2013).Chemistry https://doi.org:10.1021/cm402262g
- 28 Pierrel, J., Ibrahim, A., Croutxé-Barghorn, C. & Allonas, X. Effect of the oxygen affected layer in multilayered photopolymers. Polymer Chemistry 8, 4596-4602 (2017). https://doi.org:10.1039/c7py00974g
- Furuncuoğlu, T., Uğur, İ., Değirmenci, İ. & Aviyente, V. Role of Chain Transfer Agents 29 in Free Radical Polymerization Kinetics. Macromolecules 43, 1823-1835 (2010). https://doi.org:10.1021/ma902803p
- 30 Gorsche, C., Koch, T., Moszner, N. & Liska, R. Exploring the benefits of β-allyl sulfones for more homogeneous dimethacrylate photopolymer networks. *Polymer* Chemistry 6, 2038-2047 (2015). https://doi.org:10.1039/c4py01582g
- 31 Henríquez, C., Bueno, C., Lissi, E. A. & Encinas, M. V. Thiols as chain transfer agents in free radical polymerization in aqueous solution. *Polymer* 44, 5559-5561 (2003). https://doi.org:10.1016/s0032-3861(03)00581-0
- 32 Hoyle, C. E. & Bowman, C. N. Thiol-ene click chemistry. Angew Chem Int Ed Engl 49, 1540-1573 (2010). https://doi.org:10.1002/anie.200903924
- 33 Moad, G., Rizzardo, E. & Thang, S. H. Radical addition-fragmentation chemistry in polymer synthesis. Polymer 49, 1079-1131 (2008).https://doi.org/https://doi.org/10.1016/j.polymer.2007.11.020
- Gorsche, C., Griesser, M., Gescheidt, G., Moszner, N. & Liska, R. \(\beta Allyl Sulfones as \) 34 Addition-Fragmentation Chain Transfer Reagents: A Tool for Adjusting Thermal and Mechanical Properties of Dimethacrylate Networks. Macromolecules 47, 7327-7336 (2014). https://doi.org:10.1021/ma501550b
- 35 Gorsche, C. et al. Difunctional vinyl sulfonate esters for the fabrication of tough methacrylate-based photopolymer networks. Polymer 158, 149-157 (2018). https://doi.org:10.1016/j.polymer.2018.10.024
- 36 Fairbanks, B. D. et al. Photoclick Chemistry: A Bright Idea. Chem Rev 121, 6915-6990 (2021). https://doi.org:10.1021/acs.chemrev.0c01212
- Hoyle, C. E., Lee, T. Y. & Roper, T. Thiol-enes: Chemistry of the past with promise 37 for the future. Journal of Polymer Science Part A: Polymer Chemistry 42, 5301-5338 (2004). https://doi.org:10.1002/pola.20366
- 38 Chatani, S., Kloxin, C. J. & Bowman, C. N. The power of light in polymer science: photochemical processes to manipulate polymer formation, structure, and properties. Polym. Chem. 5, 2187-2201 (2014). https://doi.org:10.1039/c3py01334k

- 39 Jersek, M., Jovanovski, G., Boev, B. & Makreski, P. Intriguing minerals: corundum in the world of rubies and sapphires with special attention to Macedonian rubies. ChemTexts 7 (2021). https://doi.org:10.1007/s40828-021-00143-0
- 40 Shao, J., Huang, Y. & Fan, Q. Visible light initiating systems for photopolymerization: status, development and challenges. Polymer Chemistry 5, 4195-4210 (2014). https://doi.org:10.1039/C4PY00072B
- Qin, X.-H., Ovsianikov, A., Stampfl, J. & Liska, R. Additive manufacturing of 41 photosensitive hydrogels for tissue engineering applications. 15, 49-70 (2014). https://doi.org:doi:10.1515/bnm-2014-0008
- Yagci, Y., Jockusch, S. & Turro, N. J. Photoinitiated Polymerization: Advances, 42 and Opportunities. *Macromolecules* **43**, 6245-6260 (2010).https://doi.org:10.1021/ma1007545
- 43 Bagheri, A. & Jin, J. Photopolymerization in 3D Printing. ACS Applied Polymer Materials 1, 593-611 (2019). https://doi.org:10.1021/acsapm.8b00165
- 44 Moszner, N. H., T.; Burtscher, P.; Vogel, K.; Todd, J. C.; Siegward, H.; Peschke,; A. in Ivoclar Vivadent Report Vol. 19 (2013).
- 45 Anderson, T. L. Fracture Mechanics: Fundamentals and Application. (2005).
- 46 Strong, A. B. *Plastics: materials and processing*. (Prentice Hall, 2006).
- 47 Ahmadi, M., Ehrmann, K., Koch, T., Liska, R. & Stampfl, J. From Unregulated Networks to Designed Microstructures: Introducing Heterogeneity at Different Length Scales in Photopolymers for Additive Manufacturing. Chem Rev 124, 3978-4020 (2024). https://doi.org:10.1021/acs.chemrev.3c00570
- 48 Hasa, E., Stansbury, J. W. & Guymon, C. A. Manipulation of crosslinking in photoinduced phase separated polymers to control morphology and thermo-mechanical properties. Polymer 202. 122699 (2020).https://doi.org/10.1016/j.polymer.2020.122699
- 49 Courtney, T. H. Mechanical Behavior of Materials. (Waveland Press, 2005).
- Hsiao, B. S. in *Encyclopedia of Materials: Science and Technology* (eds K. H. Jürgen 50 Buschow et al.) 1-6 (Elsevier, 2002).
- Sycks, D. G., Safranski, D. L., Reddy, N. B., Sun, E. & Gall, K. Tough Semicrystalline 51 Thiol-Ene Photopolymers Incorporating Spiroacetal Alkenes. Macromolecules 50, 4281-4291 (2017). https://doi.org:10.1021/acs.macromol.7b00628
- Rylski, A. K. et al. Digital Light Processing 3D Printing of Soft Semicrystalline 52 Acrylates with Localized Shape Memory and Stiffness Control. ACS Appl Mater Interfaces (2023). https://doi.org:10.1021/acsami.3c07172
- Alim, M. D. et al. A photopolymerizable thermoplastic with tunable mechanical 53 performance. Materials Horizons (2020). https://doi.org:10.1039/c9mh01336a

- 54 Childress, K. K. et al. Systematic Modulation and Structure–Property Relationships in Photopolymerizable Thermoplastics. ACS Applied Polymer Materials (2021). https://doi.org:10.1021/acsapm.0c01393
- 55 Qin, Q. H. in Toughening Mechanisms in Composite Materials (eds Qinghua Qin & Jiangiao Ye) 1-32 (Woodhead Publishing, 2015).
- 56 Mao, H., Jia, W., Leung, Y.-S., Jin, J. & Chen, Y. Multi-material stereolithography using curing-on-demand printheads. Rapid Prototyping Journal 27, 861-871 (2021). https://doi.org:10.1108/RPJ-05-2020-0104
- 57 Subedi, S. et al. Multi-material vat photopolymerization 3D printing: a review of mechanisms and applications. npj Advanced Manufacturing 1, 9 (2024). https://doi.org:10.1038/s44334-024-00005-w
- 58 Wang, H., Xia, Y., Zhang, Z. & Xie, Z. 3D gradient printing based on digital light Chemistry B 11, 8883-8896 processing. Journal of Materials https://doi.org:10.1039/D3TB00763D
- 59 Kuang, X. et al. Grayscale digital light processing 3D printing for highly functionally materials. Science eaav5790 graded **Advances** 5, https://doi.org:10.1126/sciadv.aav5790
- Cazin, I. et al. Spatially controlling the mechanical properties of 3D printed objects 60 by dual-wavelength vat photopolymerization. Additive Manufacturing 57, 102977 (2022). https://doi.org:https://doi.org/10.1016/j.addma.2022.102977
- 61 Palffy-Muhoray, P. The diverse world of liquid crystals. Physics Today 60, 54-60 (2007). https://doi.org:10.1063/1.2784685
- 62 Martin, J. D. et al. Metallotropic liquid crystals formed by surfactant templating of molten halides. Nature Materials 271-275 (2006).metal 5. https://doi.org:10.1038/nmat1610
- 63 Mingos, D. M. Vol. 162 1-65 (2014).
- 64 Kamarudin, M. A. et al. Self-assembled liquid crystalline nanotemplates and their incorporation in dye-sensitised solar cells. *Electrochimica Acta* **222**, 657-667 (2016). https://doi.org/https://doi.org/10.1016/j.electacta.2016.11.021
- 65 An, J.-G., Hina, S., Yang, Y., Xue, M. & Liu, Y. CHARACTERIZATION OF LIQUID CRYSTALS: A LITERATURE REVIEW. Reviews on Advanced Materials Science 44 (2016).
- Bera, M. K., Bu, W. & Uysal, A. in Physical Chemistry of Gas-Liquid Interfaces 66 167-194 (2018).
- Ciofani, G., Menciassi, Arianna. Piezoelectric Nanomaterials for Biomedical 67 Applications. (2012).
- 68 Turcott, E., Nguyen, K. & Garcia-Rejon, A. Microstrcture development during the injection molding of PET/LCP blends. Polymer Engineering and Science - POLYM ENG SCI 41, 603-617 (2001). https://doi.org:10.1002/pen.10757

- 69 Yang, Q., Hirata, M., Hsu, Y.-I., Lu, D. & Kimura, Y. Improved thermal and mechanical properties of poly(butylene succinate) by polymer blending with a thermotropic liquid crystalline polyester. Journal of Applied Polymer Science 131 (2014). https://doi.org:10.1002/app.39952
- 70 Ye, P., Hong, Z., Loy, D. A. & Liang, R. UV-curable thiol-ene system for broadband infrared transparent objects. Nature Communications 14, 8385 (2023). https://doi.org:10.1038/s41467-023-44273-0
- 71 Chen, L., Wu, Q., Wei, G., Liu, R. & Li, Z. Highly stable thiol-ene systems: from their structure-property relationship to DLP 3D printing. Journal of Materials Chemistry C 6, 11561-11568 (2018). https://doi.org:10.1039/C8TC03389G
- 72 Cook, C. C. et al. Highly Tunable Thiol-Ene Photoresins for Volumetric Additive Manufacturing. Advanced Materials 2003376 (2020).32, https://doi.org:https://doi.org/10.1002/adma.202003376
- Podgorski, M., Huang, S. & Bowman, C. N. Additive Manufacture of Dynamic Thiol-73 ene Networks Incorporating Anhydride-Derived Reversible Thioester Links. ACS Interfaces Appl Mater **13**, 12789-12796 (2021).https://doi.org:10.1021/acsami.0c18979
- 74 Sölle, B., Schmallegger, M., Schlögl, S. & Rossegger, E. Wavelength-Dependent Dynamic Behavior in Thiol-Ene Networks Based on Disulfide Exchange. Journal of **American** Chemical 146, 34152-34157 (2024).the Society https://doi.org:10.1021/jacs.4c13735
- 75 Ware, T. H. & White, T. J. Programmed liquid crystal elastomers with tunable actuation strain. Polymer Chemistry 4835-4844 (2015).6, https://doi.org:10.1039/c5py00640f
- 76 Ohm, C., Brehmer, M. & Zentel, R. Liquid crystalline elastomers as actuators and sensors. Adv Mater 22, 3366-3387 (2010). https://doi.org:10.1002/adma.200904059
- 77 Fleischmann, E.-K., Forst, F. R., Köder, K., Kapernaum, N. & Zentel, R. Microactuators from a main-chain liquid crystalline elastomer via thiol-ene "click" chemistry. Journal of Materials Chemistry C 1 (2013). https://doi.org:10.1039/c3tc30272e
- Liu, M., Yin, L. & Zhao, Y. Effect of Spacer and Mesogen in Side-Chain Liquid Crystal 78 Elastomer Structure on Reversible Actuation Behavior. Macromolecules 56, 9431-9442 (2023). https://doi.org:10.1021/acs.macromol.3c01310
- 79 White, T. J. & Broer, D. J. Programmable and adaptive mechanics with liquid crystal polymer networks and elastomers. Nat Mater 14, 1087-1098 (2015). https://doi.org:10.1038/nmat4433
- Fowler, H. E., Pearl, H. M., Hoang, J. D. & White, T. J. Liquid Crystal Elastomers 80 Prepared by Thiol-Ene Photopolymerization Amenable to Surface-Enforced Macromolecules 2619-2627 Alignment. **57**, (2024).https://doi.org:10.1021/acs.macromol.3c02291

- Ware, T. H., Perry, Z. P., Middleton, C. M., Iacono, S. T. & White, T. J. Programmable 81 Liquid Crystal Elastomers Prepared by Thiol-Ene Photopolymerization. ACS Macro Letters 4, 942-946 (2015). https://doi.org:10.1021/acsmacrolett.5b00511
- 82 Becker, R., Kuenstler, A. S. & Bowman, C. N. Photopolymerizable semi-crystalline polymers for thermally reversible, 3D printable cast molds. Dent Mater (2024). https://doi.org:10.1016/j.dental.2024.05.009
- 83 Childress, K. K., Alim, M. D., Hernandez, J. J., Stansbury, J. W. & Bowman, C. N. Additive manufacture of lightly crosslinked semicrystalline thiol-enes for enhanced (2020).mechanical performance. Polymer Chemistry 11, 39-46 https://doi.org:10.1039/c9py01452g
- 84 Sycks, D. G., Wu, T., Park, H. S. & Gall, K. Tough, stable spiroacetal thiol-ene resin Journal of Applied Polymer Science for printing. 135 (2018).https://doi.org:10.1002/app.46259
- Kirsch & et al. Journal of Organic Chemistry 33, 85 127,128 (1968).https://doi.org:10.1021/jo01265a023
- Osman, M. A. MESOMORPHIC PROPERTIES OF SOME 4-CYCLOHEXYL PHENYL 86 ESTERS. Molecular Crystals and Liquid Crystals (1969-1991) 82, 323 - 330 (1982).
- 87 Klingbiel, R. T., Genova, D. J., Criswell, T. R. & Van Meter, J. P. Comparison of the dielectric behavior of several Schiff-base and phenyl benzoate liquid crystals. American Chemical Society 7651-7655 (1974).Journal of the 96, https://doi.org:10.1021/ja00832a009
- Gray, G. W. & Kelly, S. M. The Liquid Crystal Properties of 4-n-Alkyl- and 4-n-88 Alkoxy-phenyl 4-n-Alkylbicyclo (2.2.2) octane-1-carboxylates. Molecular Crystals and Liquid Crystals 75, 95-108 (1981). https://doi.org:10.1080/00268948108073606
- Weissflog, W. & Demus, D. Thermotropic liquid crystalline compounds with lateral 89 long-chain substituents (II). Synthesis and liquid crystalline properties of 1,4-bis[4substituted-benzoyloxy]-2-n-alkylbenzenes. Cryst. Res. Technol. 19, 55-69 (1984). https://doi.org:10.1002/crat.2170190112
- 90 Dewar, M. J. S. & Goldberg, R. S. Effects of central and terminal groups on nematic mesophase stability. J. Org. Chem. **35**, 2711 (1970).https://doi.org:10.1021/jo00833a051
- Arora, S., Fergason, J. & Taylor, T. Molecular Structure and Liquid Crystallinity. 91 Phenylene Bis(alkoxybenzoates). The Journal of Organic Chemistry 35, 4055-4058 (1970). https://doi.org:10.1021/jo00837a708
- 92 Lee, J. Y. & Jang, J. The effect of mesogenic length on the curing behavior and properties of liquid crystalline epoxy resins. Polymer 47, 3036-3042 (2006). https://doi.org:10.1016/j.polymer.2006.03.009
- Koßmehl, G., Gerecke, B., Harmsen, N., Schröder, F. & Vieth, H. M. Liquid Crystalline 93 Main Chain Polysiloxane Esters and their Monomers Part I: Synthesis of some di(ω-

- unsaturated esters) and their thermal behaviour. Molecular Crystals and Liquid Crystals Science and Technology. Section A. Molecular Crystals and Liquid Crystals **269**, 39-53 (1995). https://doi.org:10.1080/10587259508037320
- 94 Xu, X.-X., Hong, Z. & Liu, F. New Liquid-Crystalline Elastomers: 1. Synthesis, Structure, and Phase Behavior of a Series of Mesogenic Crosslinking Agents Containing Reactive Bifunctional Groups. Molecular Crystals and Liquid Crystals **533**, 52-62 (2010). https://doi.org:10.1080/15421406.2010.526561
- 95 Pakkal, R., Thomas, F. D., II & Fernelius, W. C. Study of the double Fries rearrangement. II. Rearrangement of diesters of 4,4'-biphenol. J. Org. Chem. 25, 282 (1960). https://doi.org:10.1021/jo01072a618
- 96 Li, Y. et al. Liquid crystalline texture and hydrogen bond on the thermal conductivities of intrinsic thermal conductive polymer films. Journal of Materials 82, Science Technology 250-256 (2021).& https://doi.org:https://doi.org/10.1016/j.jmst.2021.01.017
- 97 Jang, K.-S. & Korley, L. T. J. Phase diagrams of thermally stable, polymer-dispersed liquid crystals: Exploring the impact of chain length and chemical structure. Polymer Engineering Science **56**, 388-393 (2016).& https://doi.org/https://doi.org/10.1002/pen.24264
- 98 Agrahari, B. et al. Synthesis, characterization and crystal structure of Cu(II) complex of trans-cyclohexane-1,2-diamine: Application in synthesis of symmetrical biaryls. of Journal Molecular Structure 1134, 85-90 (2017).https://doi.org:https://doi.org/10.1016/j.molstruc.2016.12.053
- 99 Nemoto, F., Ishizu, K. & Hasegawa, H. EXCEPTIONAL HINDERED INTERNAL ROTATION OF THE ALKYL GROUP IN THE 4,4'-DI-N-PROPYL BIPHENYL ANION. Chemistry Letters 1, 267-268 (1972). https://doi.org:10.1246/cl.1972.267
- Boedtker, E. Some homologs of biphenyl. Bull. Soc. Chim. Fr. 45, 645 (1929). 100
- 101 Watanabe, G. & Tabe, Y. Tilted and Non-tilted Liquid Crystalline Langmuir Monolayers: Analogy to Bulk Smectic Phases. Journal of the Physical Society of Japan **76** (2007). https://doi.org:10.1143/jpsj.76.094602
- 102 Kaplan, E. P., Kazakova, Z. I. & Petrov, A. D. Synthesis and properties of 4-alkyl- and 4,4'-dialkylbiphenyls and their hydrogenates with C16-32 compositions. Zh. Obshch. Khim. 30, 369 (1960).
- Annamalai, S. & Aidhen, I. S. Novel synthetic strategy for biphenyl-spaced sugars 103 towards heparinoid mimetics. Trends Carbohydr. Res. 3, 33-43 (2011).
- Sluckin, T., Dunmur, D. & Stegemeyer, H. Crystals that flow. (Taylor & Francis 104 London, 2004).
- Ren, W. STRUCTURE-PROPERTY RELATIONS IN SILOXANE-BASED MAIN CHAIN 105 LIQUID CRYSTALLINE ELASTOMERS AND RELATED LINEAR POLYMERS. (2007).

- 106 Joo, S.-H. & Jin, J.-I. All hydrocarbon main-chain thermotropic liquid crystalline polymers, poly(1,1?-biphenylene-4,4?-alkenediyl)s, prepared by the ADMET method their hydrogenated polymers, poly(1,1?-biphenylene-4,4?alkanediyl)s. Journal of Polymer Science Part A: Polymer Chemistry 42, 1335-1349 (2004). https://doi.org:10.1002/pola.11061
- 107 Kaluszyner, A., Reuter, S. & Bergmann, E. D. Synthesis and biological properties of diaryl(trifluoromethyl)carbinols. J. Am. Chem. Soc. **77**, 4164 (1955).https://doi.org:10.1021/ja01620a064
- 108 Nishimura, N., Yoza, K. & Kobayashi, K. Guest-Encapsulation Properties of a Self-Assembled Capsule by Dynamic Boronic Ester Bonds. J. Am. Chem. Soc. 132, 777-790 (2010). https://doi.org:10.1021/ja9084918
- 109 Cui, L., Sapagovas, V. & Lattermann, G. Synthesis and thermal behavior of liquid crystalline pyridinium bromides containing a biphenyl core. Lig. Cryst. 29, 1121-1132 (2002). https://doi.org:10.1080/02678290210155589
- 110 Holec, J., Rybacek, J., Budesinsky, M., Pospisil, L. & Holy, P. Electron-rich ligands with multiple tetrathiafulvalene arms. Monatsh. Chem. 142, 821-826 (2011). https://doi.org:10.1007/s00706-011-0520-8
- 111 Wirth & et al. Molecular Crystals 4, 321 (1968).
- 112 Sannasi, V., Jose, T. P. & Jeyakumar, D. Synthesis and optical properties of poly(2,7-(9,9-dihexylfluorene)-3,3'(4,4'-dialkoxybiphenyl)). Designed **Monomers** and Polymers 18, 51-63 (2014). https://doi.org:10.1080/15685551.2014.947553
- Kidowaki, M., Moriyama, M., Wada, M. & Tamaoki, N. Molecular Mechanism of 113 Anomalous Increase in the Helical Pitch of Cholesteric Liquid Crystals Induced by Achiral **107**, Dopants. J. Phys. Chem. В 12054-12061 (2003).https://doi.org:10.1021/jp034916e
- Destrade, C., Huu Tinh, N. & Gasparoux, H. Mesogenic and Non Mesogenic Central 114 Rigid Cores. Molecular Crystals and Liquid Crystals 59, 273-288 (1980). https://doi.org:10.1080/00268948008071428
- 115 Broer, D. J., Lub, J. & Mol, G. N. Synthesis and photopolymerization of a liquidcrystalline diepoxide. Macromolecules 26, 1244-1247 (1993).https://doi.org:10.1021/ma00058a007
- LUB, R. A. M. H. a. J. ANISOTROPIC NETWORKS AND GELS OBTAINED BY 116 PHOTOPOLYMERISATION IN THE LIQUID CRYSTALLINE STATE: SYNTHESIS AND APPLICATIONS. (1996).
- Kaese, T., Wöhrle, D., Hartwig, A. & Schnurpfeil, G. Syntheses of dialkenes and 117 diepoxides, and the influence of their structural parameters on liquid crystalline properties. Liquid Crystals 32, 921-931 (2005).https://doi.org:10.1080/02678290500183664

- 118 Dewar, M. J. S. & Goldberg, R. S. Role of p-phenylene groups in nematic liquid crystals. J. Amer. Chem. Soc. 92, 1582 (1970). https://doi.org:10.1021/ja00709a026
- 119 Kirsch, P. & Tarumi, K. A Novel Type of Liquid Crystals Based on Axially Fluorinated Cyclohexane Units. Angewandte Chemie International Edition 37, 484-489 (1998). https://doi.org:10.1002/(sici)1521-3773(19980302)37:4<484::Aidanie484>3.0.Co;2-6
- Seidler, K. et al. Vinyl Sulfonate Esters: Efficient Chain Transfer Agents for the 3D 120 Printing of Tough Photopolymers without Retardation. Angew Chem Int Ed Engl 57, 9165-9169 (2018). https://doi.org:10.1002/anie.201803747
- Kozmík, V. et al. Mesogens with central naphthalene core substituted at various 121 positions. Liguid Crystals 45, 746-756 (2017).https://doi.org:10.1080/02678292.2017.1380238
- 122 Kovářová, A. et al. Naphthalene-based bent-shaped liquid crystals with a semifluorinated terminal chain. Liquid Crystals **39**, 755-767 (2012).https://doi.org:10.1080/02678292.2012.678396
- Li, Y. et al. Liquid crystalline networks based on photo-initiated thiol-ene click 123 chemistry. Soft Matter (2019). https://doi.org:10.1039/c9sm01818b
- 124 Wilderbeek, H. T. A. et al. Synthesis and properties of phenyl benzoate-based and biphenyl-based liquid crystalline thiol-ene monomers. Liquid Crystals 30, 93-108 (2003). https://doi.org:10.1080/0267829021000001746
- Percec, V. & Tomazos, D. in Comprehensive Polymer Science and Supplements (eds. 125 Geoffrey Allen & John C. Bevington) 299-383 (Pergamon, 1989).
- 126 Tokushige, N., Mihara, T. & Koide, N. Thermal Properties and Photo-Polymerization of Diepoxy Monomers with Mesogenic Group. Molecular Crystals and Liquid Crystals 428, 33-47 (2006). https://doi.org:10.1080/154214090892681
- 127 Huo, L., Gao, J., Du, Y. & Chai, Z. Synthesis and characterization of the two novel liquid crystalline epoxy resins based on bisphenol-s mesogen. Journal of Applied Polymer Science 110, 3671-3677 (2008). https://doi.org:10.1002/app.28973
- Imae, I., Tsukimori, M., Fujimoto, T., Tsukiyama, K. & Harima, Y. Orientation control 128 of anchored molecules on metal-oxide substrates. *Inorganic Chemistry* Communications 82, 44-47 (2017). https://doi.org:10.1016/j.inoche.2017.05.009
- Białecka-Florjańczyk, E., Śledzińska, I., Stolarzewicz, I., Makal, A. & Górecka, E. 129 Synthesis and study of new liquid crystalline compounds with an epoxy group. Liquid Crystals 36, 67-73 (2009). https://doi.org:10.1080/02678290802663298
- Fuerstner, A., Leitner, A., Mendez, M. & Krause, H. Iron-Catalyzed Cross-Coupling 130 Reactions. J. Am. Chem. Soc. 124, 13856-13863 (2002).https://doi.org:10.1021/ja027190t
- Fürstner, A. L., Andreas; Seidel, Günter. 4-nonylbenzoic acid. Organic syntheses 81, 131 33 (2005). https://doi.org:10.15227/orgsyn.081.0033

- 132 Zhang, G. Y., Lu, H. B. & Xu, W. B. Synthesis and Application of a Novel Liquid Crystal 1,4-di-[4-(3-acryloyloxyhexyloxy)benzoyloxy]-2-methyl Benzene. 875-877. Advanced Materials Research 3-8 (2014).https://doi.org:10.4028/www.scientific.net/AMR.875-877.3
- 133 Jordan, A., Whymark, K. D., Sydenham, J. & Sneddon, H. F. A solvent-reagent selection guide for Steglich-type esterification of carboxylic acids. *Green Chemistry* 23, 6405-6413 (2021). https://doi.org:10.1039/d1gc02251b
- Liverton, N. J. et al. Preparation of N-substituted nonaryl heterocyclyl amides as 134 NMDA/NR2B antagonists for relieving pain. WO2002080928 (2002).
- Lee, H., Sylvester, K., Derbyshire, E. R. & Hong, J. Synthesis and Analysis of Natural-135 Product-Like Macrocycles by Tandem Oxidation/Oxa-Conjugate Addition Chemistry Reactions. 6500-6504 25, (2019).https://doi.org:10.1002/chem.201900620
- Denolf, K., Cordoyiannis, G., Glorieux, C. & Thoen, J. Effect of nonmesogenic 136 impurities on the liquid crystalline phase transitions of octylcyanobiphenyl. Phys Nonlin Rev Ε Stat Soft Matter Phys 76, 051702 (2007).https://doi.org:10.1103/PhysRevE.76.051702
- 137 Van Damme, J. et al. Anthracene-Based Thiol-Ene Networks with Thermo-Degradable and Photo-Reversible Properties. Macromolecules 50, 1930-1938 (2017). https://doi.org:10.1021/acs.macromol.6b02400
- Li, Z. et al. A Dual Wavelength Polymerization and Bioconjugation Strategy for High 138 Throughput Synthesis of Multivalent Ligands. J Am Chem Soc 141, 19823-19830 (2019). https://doi.org:10.1021/jacs.9b09899
- 139 Han, C.-C. & Balakumar, R. Mild and efficient methods for the conversion of benzylic bromides to benzylic thiols. Tetrahedron Letters 47, 8255-8258 (2006). https://doi.org:10.1016/j.tetlet.2006.09.093
- 140 Fast, D. E. et al. Wavelength-Dependent Photochemistry of Oxime Ester Photoinitiators. Macromolecules **50**, 1815-1823 (2017).https://doi.org:10.1021/acs.macromol.7b00089
- 141 PerkinElmer, I. DSC - Frequently asked questions, a beginner's guide. (2013).
- Saed, M. O. et al. Thiol-acrylate main-chain liquid-crystalline elastomers with 142 tunable thermomechanical properties and actuation strain. Journal of Polymer Science **Part** В: Polymer **Physics 55**, 157-168 (2016).https://doi.org:10.1002/polb.24249
- Utroša, P., Onder, O. C., Žagar, E., Kovačič, S. & Pahovnik, D. Shape Memory 143 Synthesized **Emulsion-Templated** Poly(ε-Caprolactone) Behavior Organocatalyzed Ring-Opening Polymerization. Macromolecules 52, 9291-9298 (2019). https://doi.org:10.1021/acs.macromol.9b01780

- 144 Defize, T. et al. Thermoreversibly crosslinked poly(epsilon-caprolactone) as recyclable shape-memory polymer network. Macromol Rapid Commun 32, 1264-1269 (2011). https://doi.org:10.1002/marc.201100250
- 145 Bonetti, L. et al. 4D printing of semi-crystalline crosslinked polymer networks with two-way shape-memory effect. Materials & Design 238, 112725 (2024). https://doi.org/https://doi.org/10.1016/j.matdes.2024.112725
- Chen, G. et al. A Triple-Shape Memory Material via Thermal Responsive Behavior 146 of Liquid Crystalline Network Incorporating Main-Chain/Side-Chain LC Units. Macromolecular Chemistry and **Physics** 220 (2019).https://doi.org:10.1002/macp.201900059
- 147 Geelhaar, T., Griesar, K. & Reckmann, B. 125 years of liquid crystals--a scientific revolution in the home. Angew Chem Int Ed Engl 52, 8798-8809 (2013). https://doi.org:10.1002/anie.201301457
- Chen, M. et al. Recent Advances in 4D Printing of Liquid Crystal Elastomers. Adv 148 Mater 35, e2209566 (2023). https://doi.org:10.1002/adma.202209566
- Jalili, A. R. et al. Liquid Crystal-Mediated 3D Printing Process to Fabricate Nano-149 Ordered Layered Structures. ACS Appl Mater Interfaces 13, 28627-28638 (2021). https://doi.org:10.1021/acsami.1c05025
- 150 Ambulo, C. P. et al. Four-dimensional Printing of Liquid Crystal Elastomers. ACS *Interfaces* 37332-37339 (2017).Appl Mater 9, https://doi.org:10.1021/acsami.7b11851
- Laa, D. Voxel-based representation of digital materials for additive manufacturing 151 MSc thesis, TU Wien, (2022).
- 152 Du, F. et al. Dimerization of Aromatic Compounds Using Palladium-Carbon-Catalyzed Suzuki-Miyaura Cross-Coupling by One-Pot Synthesis. Synlett 29, 779-784 (2018). https://doi.org:10.1055/s-0036-1591892
- 153 Li, C. et al. High thermal conductivity of liquid crystalline monomer-poly (vinyl alcohol) dispersion films containing microscopic-ordered structure. Journal of Polymer Science 49791 Applied 138, (2021).https://doi.org:https://doi.org/10.1002/app.49791
- P. et al. Hydroxylated biphenyls as 154 tyrosinase spectrophotometric and electrochemical study. Eur. J. Med. Chem. 126, 1034-1038 (2017). https://doi.org:10.1016/j.ejmech.2016.12.028
- Mohana, K. & Umadevi, S. Side-chain polysiloxane liquid crystalline elastomers 155 from non-mesogenic components. New Journal of Chemistry 43, 15968-15978 (2019). https://doi.org:10.1039/c9nj03482j
- Kamiński, R. et al. The Role of the C–H···π Interactions in the Cyclisation Reactions 156 Leading to New Aryl-Bridged Tetraazamacrocyclic Complexes of Copper and

- Nickel. European Journal of Inorganic Chemistry 2011, 479-488 (2010). https://doi.org:10.1002/ejic.201000818
- 157 Kang, S. U., Oh, S. Y., Lee, S. H. & Lee, M. H. Liquid crystal display device with improved optical and electrooptical properties and its manufacturing method. KR2014001044 (2014).
- Luttringhaus, A., Cramer, F., Prinzbach, H. & Henglein, F. M. Cyclization of long-158 chain dithiols. Attempted preparation of linked rings with the aid of inclusion compounds. Ann. 613, 185 (1958).
- 159 Hessberger, T., Braun, L. & Zentel, R. Microfluidic Synthesis of Actuating Microparticles from a Thiol-Ene Based Main-Chain Liquid Crystalline Elastomer. Polymers (Basel) 8 (2016). https://doi.org:10.3390/polym8120410
- Lub, J., Broer, D. J. & van den Broek, N. Synthesis and Polymerization of Liquid 160 Crystals Containing Vinyl and Mercapto Groups. Liebigs Annalen 1997, 2281-2288 (1997). https://doi.org:10.1002/jlac.199719971116
- 161 Lupi, F. et al. Dithiols as Liquid Crystalline Building Blocks for Smart Polymers via Thiol-yne Click Chemistry. ACS Appl. Polym. Mater. 3, 1602-1609 (2021). https://doi.org:10.1021/acsapm.0c01423
- 162 reaTokushige, N., Mihara, T. & Koide, N. Thermal Properties and Photo-Polymerization of Diepoxy Monomers with Mesogenic Group. *Molecular Crystals* and Liquid Crystals 428, 33-47 (2006). https://doi.org:10.1080/154214090892681
- Cavill, G. W. K. & Solomon, D. H. Organic oxidation processes. III. Reaction of lead 163 tetraacetate with phenyl ethers. J. Chem. Soc., 1404 (1955).https://doi.org:10.1039/jr9550001404
- 164 Hashimoto, K. & Yanagi, T. Cellulose acylate formulation for manufacture of optical films for liquid crystal displays. JP2005325258 (2005).
- Gnilomedova & et al. Journal of applied chemistry of the USSR 49, 1365,1366 (1976). 165
- 166 Steinstraesser, R. Zeitschrift fur Naturforschung. Teil B: Chemie, Biochemie, Biophysik, Biologie 27, 774 - 779 (1972).
- Burmistrov, V. A., Aleksandriiskii, V. V. & Koifman, O. I. The orientational properties 167 of hydrogen-bonded non-mesomorphic component-liquid crystal complexes. III. Nematic esters. Russian Journal of Physical Chemistry 63, 678 - 680 (1989).
- Demus, D., Krieg, C. & Weissflog, W. Cholesterinische Gemische fuer die 168 Thermographie. Zeitschrift fur Chemie 22, 385 - 386 (1982).
- Buivydas, M., Adomenas, P., Adomeniene, O. & Beganskiene, A. INFLUENCE OF 169 ACHIRAL Sc HOST ON THE VALUES OF SPONTANEOUS POLARIZATION AND ROTATIONAL VISCOSITY OF FERROELECTRIC MIXTURES. Molecular Crystals and Liquid Crystals (1969-1991) 191, 407 - 411 (1990).
- 170 Neubert, M. E. et al. THE EFFECT OF CARBONYL CONTAINING SUBSTITUENTS IN THE TERMINAL CHAINS ON MESOMORPHIC PROPERTIES IN AROMATIC ESTERS

- AND THIOESTERS, 2. ACYLOXY GROUPS ON THE PHENOLIC END. Molecular Crystals and Liquid Crystals (1969-1991) **145**, 111 - 158 (1987).
- 171 Jackson, W. J., Jr. Liquid crystalline polymers. 5. Liquid crystalline polyesters containing naphthalene rings. *Macromolecules* **16**, 1027-1033 (1983). https://doi.org:10.1021/ma00241a001
- Hornung, B., Jungbauer, D. & Manero, J. Alkyl-substituted hydroquinone 172 derivatives and ferroelectric liquid-crystal mixtures and electrooptical devices containing them. EP603786 (1994).
- 173 Yoshida, A., Tanaka, S. & Hisakado, Y. Cellulose composition, optical film, retardation sheet, polarizing plate and liquid crystal display device. US20100245744 (2010).